Synthesis of Perovskite Nanocrystals and Their Applications in Perovskite Solar Cells

Liang, Xinxing

Award date:
2018

Awarding institution:
University of Bath

Synthesis of Perovskite Nanocrystals and Their Applications in Perovskite Solar Cells

Xinxing Liang

A thesis submitted for the degree of Doctor of Philosophy

University of Bath

Department of Chemistry

September 2018

COPYRIGHT

Declaration of any previous submission of the work

The material presented here for examination for the award of a higher degree by research has not been incorporated into a submission for another degree.

Candidate's signature

. . . . . .

Declaration of authorship

I am the author of this thesis, and the work described herein was carried out by myself personally, with the exception of the following work which was carried out in collaboration with other researchers:

The design of the flow reactor for the synthesis of perovskite nanocrystals in Chapter 6 was done with the help of Dr. Kejun Wu in Laura Torrente-Murciano's group at the University of Cambridge. The reproducibility study in Chapter 6 (**Fig. 6.6**) was conducted by Robert Baker. The application of $CH_3NH_3PbI_3$ nanocrystals as interlayers in perovskite solar cells (**section 7.3**) were conducted by Isabella Poli.

Candidate's signature

. . . . . .

Abstract

Perovskite solar cells are a very promising photovoltaic technology which was first reported in 2009 and developed very rapidly. The crystallisation within perovskite films is highly dependent on processing environments, such as temperature, humidity, atmosphere, even light, which makes the fabrication of perovskite solar cells rather lab-dependent and poorly reproducible. One strategy to overcome this problem is to develop a controlled synthesis of perovskite nanocrystals which can then be ordered into films in a separate step.

In this thesis, optimisation of planar perovskite solar cells is carried out by the engineering of perovskite film fabrication methods. Different deposition methods along with different process factors such as solvents, temperature and precursor recipes are compared. One step spin-coating method with the recipe of MAI:$PbCl_2$=3:1 gives the best PCE of 12.1 ± 0.7 % in air with controlled humidity of $< 35\%$, showing high reliability and reproducibility.

Doping of TiO_2 layers with Zn^{2+}, Sn^{4+} and Nb^{5+} ions are carried out to investigate the impacts of doping ions in different valence states on the electron-transporting properties of TiO_2 ETLs. The different doping ions shift the flat band potential differently. Zn^{2+} largely negatively shifts the flat band potential, whereas Nb^{5+} positively shifts and Sn^{4+} barely changes the flat band potential of TiO_2. the Zn-doping of the TiO_2 ETL decreases the performance of the cells. However, when a thin layer of Zn-doped TiO_2 is deposited on top of the pristine TiO_2 layer as interlayer, the cell efficiency is slightly improved.

Following the cell optimisation, to achieve better control over the crystallisation process, a facile flow reactor is developed for the synthesis of $MAPbX_3$ perovskite nanocrystals at low temperature, which are further used for perovskite solar cells. The nanocrystals show narrow size distribution, good emissive properties and high stability. The bandgap of the nanocrystals was easily tuned between 485-745 nm by changing the halide compostion. The photoluminescence of the $MAPbI_3$ NCs in the first supernatant can also be tuned by changing the process parameters such as temperature, residence time and ligand concentration. However the impacts are more complex in the second supernatant

in toluene with the appearance of multiple peaks in the PL spectra. It could be resulted from the formation of smaller NCs due to the reprecipitation of the incompletely removed reactants when added into toluene, or the fragmentation of the NCs upon dispersion in toluene, but better understanding is still needed.

In the last part of the thesis, the synthesised $MAPbI_3$ nanocrystals are investigated in perovskite solar cell applications. They have been applied as interlayers at the perovskite-HTM interface, where they improved the stability of the devices towards moisture. The nanocrystals and their bulk by-products are also used as active light-absorbing layers for perovskite solar cells, delivering the the best PCEs of 0.51% and 1.2% respectively, and notably showing outstanding water resistance. Further improvements in the cell performance could potentially be achieved by the removal of the insulating long chain ligands using effective ligand exchange treatments.

Acknowledgements

Firstly I would like to thank my supervisor Dr. Petra Cameron for her strong support. Her supervision was crucial for me to plan and finish my PhD, and her supports to my applications for fundings were highly helpful. I also thank her for having the courage and patience to read every page of my thesis, trying to understand what exactly I want to say and giving comments. I know it's not easy! Great thanks to all the group members in Petra's group, Adam, Ralf, Wentao, Pete, Sam, Dom, Isabella, Rob and Rodrigo, for their friendship and kind help with my research.

I also would like to thank Kejun and Laura in Cambridge for their help with the flow reactor design and setup; Ursula and Phil in MAS for their help with the SEM and TEM imaging; Yaomin in UCL for the help with XPS measurements. Thanks are also due to Prof. Frank Marken for providing fumehood space for my flow setup, Prof. Tony James for providing access to his fluorescence spectrophotometer, and Asel Sartbaeva and Simon Lewis for providing seating space in their office, so that I had the chance to meet many very nice office mates to whom great thanks should also be given.

Thank the university of Bath for funding through the 50th anniversary excellence studentship for overseas students to support my three year tuition fee and stipend. Thanks to Leche Trust and the Great Britian-China Educational Trust (GBCET) for extra funding support and Santander Mobility Award for the travel grant to support me attending the AP-HOPV18 conference.

I also thank Daping, Nick, Haobo, Andi, Yuanyang and all other friends in Bath. It was very nice meeting you here, far away from home. I had a wonderful time with you. Doing PhD in a different country is tough, but things get much easier with you guys around.

I also would like to say great thanks to my family. I was far away from home, but your support was always around me, and I can never be here without it. Finally, greatest thanks to Wentao, the one who came to UK before me and had everything settled so that I had less to worry about, who shared all my achievements and failures, my happiness and sorrow, and who is always by my side whatever happens.

Symbols and Abbreviations

PV: photovoltaic

PCE: power conversion efficiency

V_{OC}: open-circuit voltage

J_{SC} short-circuit current density

FF: fill factor

DSSC: dye-sensitised solar cell

ETL: electron-transporting layer

HTL: hole-transporting layer

MA: methylammonium

FA: formamidinium

FTO: fluorine-doped tin oxide

NC: nanocrystal

QD: quantum dot

HTM: hole-transporting material

FWHM: full width at half maximum

PL: photoluminescence

HI: hot injection

LARP: ligand-assisted reprecipitation

LED: light-emitting diode

ODE: octadecene

OLA: oleylamine

OA: oleic acid

DMF: N,N-dimethylformamide

DMSO: dimethyl sulfoxide

CB: conduction band

VB: valence band

XRD: X-ray diffraction

AFM: atomic force microscopy

TEM: transmission electron microscopy

XPS: X-ray photoelectron spectroscopy

E_F: Fermi level

E_g: band-gap

Re: Reynolds number

n_i: intrinsic carrier concentration

k_B: Boltzmann's constant

T: temperature

h: Planck constant

$\hbar$: reduced Planck constant

I_0: dark saturation current

q: elementary charge

τ: carrier lifetime

W_{SC}: width of space charge region

N_d: doping density

C_{SC}: capacitance of space charge region

V_{FB}: flat band potential

Z: impedance

ε: relative permittivity

ε_0: vacuum permittivity

a_B: exciton Bohr radius

μ: reduce exciton mass

R_s: series resistance

R_{rec}: recombination resistance

List of Publications

1. X. Liang, R.W. Baker, K. Wu, W. Deng, D. Ferdani, P.S. Kubiak, F. Marken, L. Torrente-Murciano and P.J. Cameron, Continuous Low Temperature Synthesis of $MAPbX_3$ Perovskite Nanocrystals in a Flow Reactor, *Reaction Chemistry & Engineering*, DOI: 10.1039/C8RE00098K, 2018.

2. I. Poli, X. Liang, R. Baker, S. Eslava and P.J. Cameron, Enhancing the Hydrophobicity of Perovskite Solar Cells using C18 Capped $CH_3NH_3PbI_3$ Nanocrystals. *Journal of Materials Chemistry C*, 6(26): 7149-7156, 2018.

3. W. Deng, X. Liang, P.S. Kubiak and P.J. Cameron, Molecular Interlayers in Hybrid Perovskite Solar Cells. *Advanced Energy Materials*, 8(1):1701544, 2018

Contents

Chapter 1

Introduction

With the development of an industrial society, the ever-increasing demand for energy by mankind and the non-renewability of fossil fuels have pulled human beings into an Energy Crisis. The use of fossil fuels is generally believed to be responsible for air pollution and climate change, which have serious global implications. To rectify this, people are seeking clean renewable energies to replace fossil fuels. Renewable energies such as wind, solar energy, hydroenergy and biomass have been greatly developed over the last few years, as shown by the figures for UK electricity generation by renewables during 2003-2016 in **Fig. 1.1**[1]. Of all the renewable energies, solar energy is believed to be the source of almost all energy on the earth. It is so abundant that the energy from sunlight hit on the earth in a year is as high as 1.5×10^{18} kWh, which is more than a hundred times the total energy of known fossil fuel reserves all over the world[2]. Therefore developing an efficient way to make use of solar energy would be highly promising for fulfilling societal demand. Photovoltaic cells are one way to harvest this solar energy.

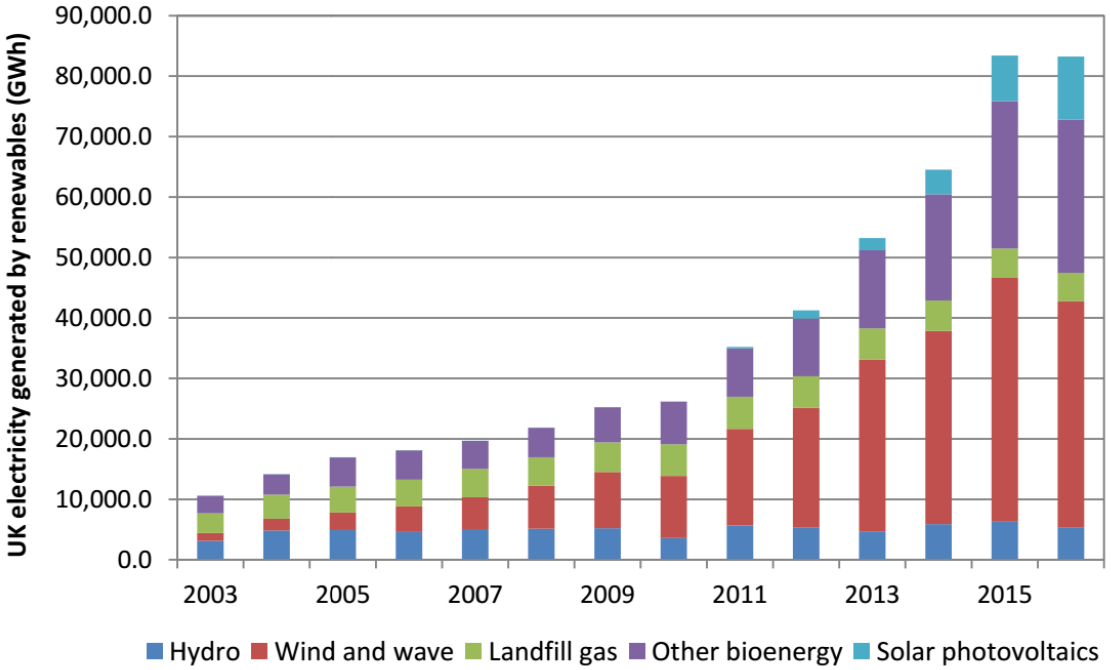

Fig. 1.1 Electricity generation by renewable sources in UK during 2003-2016. Reproduced from data provided by National Statistics.[1]

1.1 Solar cell overview

A solar cell is a device which can convert solar energy directly into electricity. Since the first discovery of the photovoltaic (PV) effect by Edmond Becquerel in 1839[3] and the first production of a 6% crystalline silicon solar cell by Chapin et al. in 1954[4], this technology has been greatly developed. Now crystalline silicon based PV technology is very mature and widely commercialised. By the end of 2016, the global installed PV power capacity has increased to 315 GW, and is predicted to double by 2019[5]. The global PV cell/module production in 2016 has also reached over 80 GW as shown in **Fig. 1.2**.

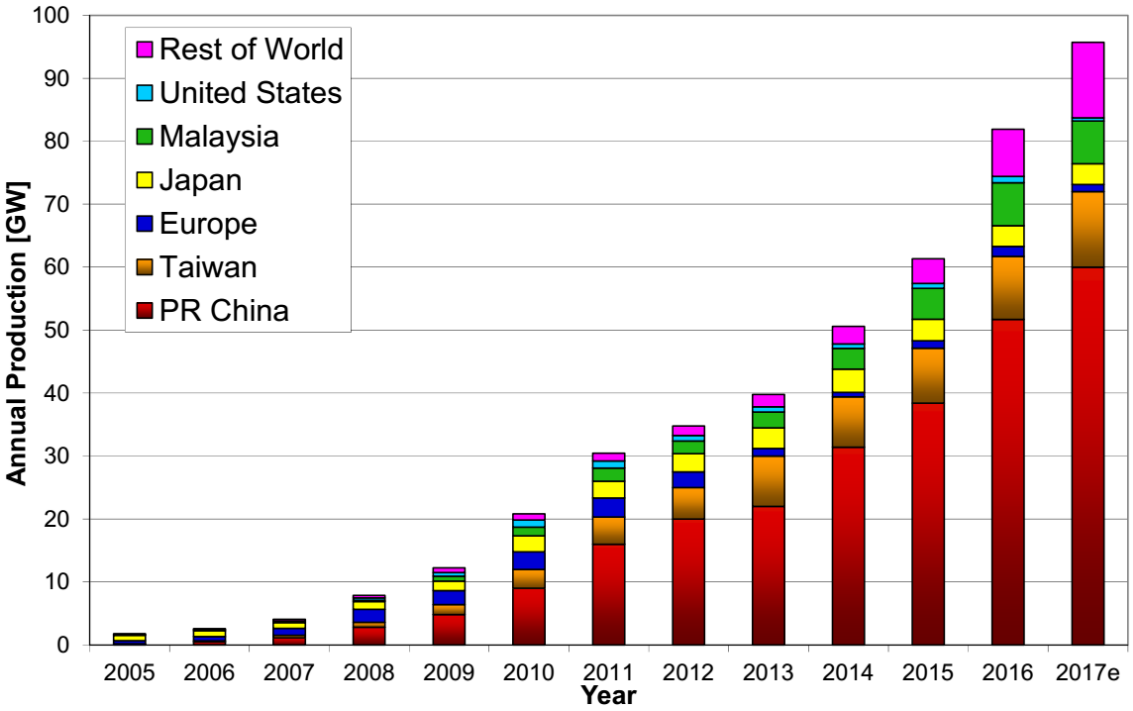

Fig. 1.2 World PV cell/module production from 2005 to 2017 (estimate).[5]

The development of solar cell technology has gone through three stages, which are known as three generations, as shown in **Fig. 1.3**[6].

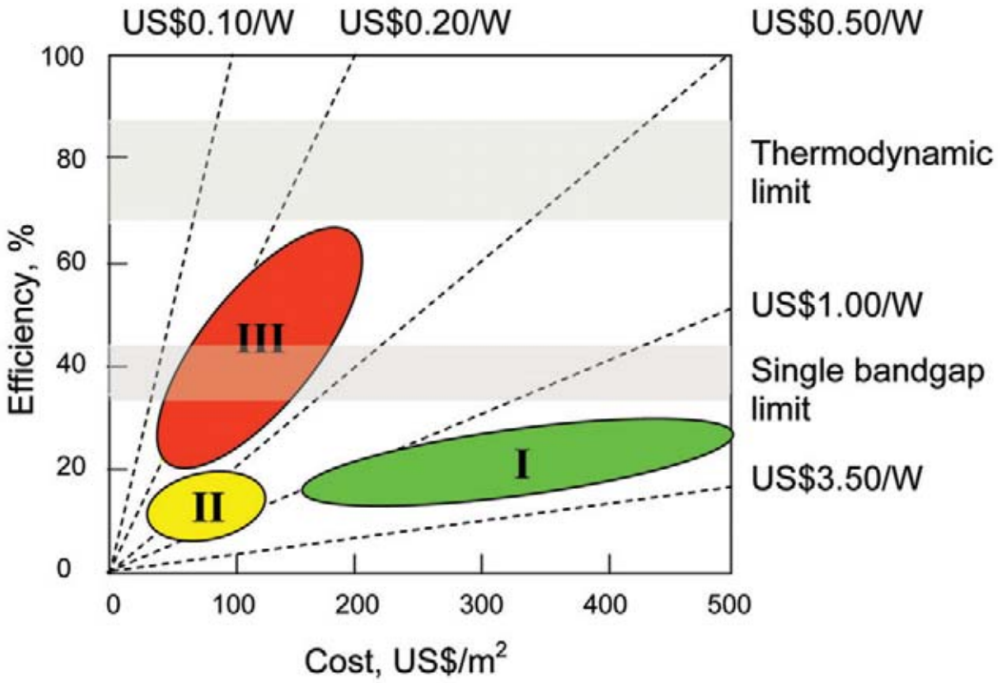

Fig. 1.3 Diagram showing the efficiencies and costs for three generations of PV technologies.[6]

First generation

The so-called 'first generation' solar cells are based on silicon wafers. This technology is now the most mature and still dominates the photovoltaic market. Most solar cells and modules sold today are made of crystalline silicon, both single-crystalline and polycrystalline silicon wafers with high purity. The efficiencies for these solar cells are typically close to 20%[7], but they also suffer from relatively high cost for large scale production as well as negative environmental impacts due to stringent processing conditions, which can increase their energy payback time[8].

Second generation

The second generation solar cells are based on thin film technology. In this approach, a thin layer of active material, for example, cadmium telluride (CdTe)[9] or copper indium gallium selenide (CIGS)[10], is deposited onto a substrate, which not only reduces the usage of the active material and consequently the cost, but also makes the cells more flexible and lower in weight. This technology is operational, and the efficiency can also be around 20%[7], but it is still facing difficulties in large-scale production including the availability of Te, In, and Ga sources as well as the toxicity of heavy metals such as Cd[11].

Third Generation

The third generation solar cells refer to different emerging technologies which aim at producing solar cells with lower cost and higher efficiency. The third generation technologies normally include organic solar cells, quantum dots solar cells, dye-sensitised solar cells (DSSCs), perovskite solar cells as well as multi-junction solar cells such as tandem solar cells. Although these technologies are mostly not mature enough for industrial commercialization, they are still believed to be very promising and attract much research interest worldwide.

Organic solar cells

In organic solar cells, organic polymers or small organic molecules are used for light absorption and charge transport. Organic materials are normally flexible and lightweight, allowing organic solar cells to be the same. In addition, molecular engineering makes

the band-gap of organic materials tunable, and the thickness can be reduced to $\sim 100\,\text{nm}$ due to optical absorption coefficients as high as $10^5\,\text{cm}^{-1}$.[12] However, since the band-gap of most organic materials are large (above 2 eV for many cases), the harvesting of the incident light can be quite limited[13], which makes organic solar cells less efficient. The highest record efficiency for organic solar cells is still only $\sim 11\%$[7]. Apart from low efficiency, poor stability is another problem for organic solar cells. Photo-oxidation or degradation can easily occur under illumination and continuous exposure to oxygen or moisture, which results in the short lifetime of the organic solar devices and hinders their practical application[14].

Quantum dots solar cells

Quantum dots are nanocrystals of semiconducting materials. The diameter of the quantum dots is typically a few nanometres, which is so small that electrons are confined in all three dimensions due to the quantum confinement effect. The band-gap of quantum dots can be tuned simply by changing the dots size. As a result, photons with different wavelengths can be harvested at the same time using mixtures of quantum dots with different sizes, which can potentially make multi-junctional solar cells. Using $CsPbI_3$ perovskite quantum dots (coated with formamidinium iodide (FAI) to enhance the carrier mobility) as the absorbing material, a solar cell with a certified efficiency of 13.4% has been achieved, and a high open-circuit voltage (V_{OC}) of 1.2 V has been abtained[15].

Dye-sensitised solar cells

A DSSC is based on a 5-20 μm layer of a mesoporous oxide (normally TiO_2) formed between an anode and an electrolyte as shown in **Fig. 1.4**[16]. The wide band-gap of TiO_2 nanoparticles (3.2 eV) means they can only absorb light in ultraviolet region[17]. Therefore, in DSSCs, to enable the absorption towards sunlight in the visible region, a dye monolayer is adsorbed on the mesoporous TiO_2 layer. Photo-generated electrons in the dye molecules are rapidly injected into the conduction band of TiO_2 and then collected by the anode. The oxidised dye is then regenerated by a redox couple, normally the iodide/triiodide couple in the organic electrolyte which is further regenerated at the cathode. Overall, the device generates electric power from sunlight continuously without consuming the electrode materials or the electrolyte.

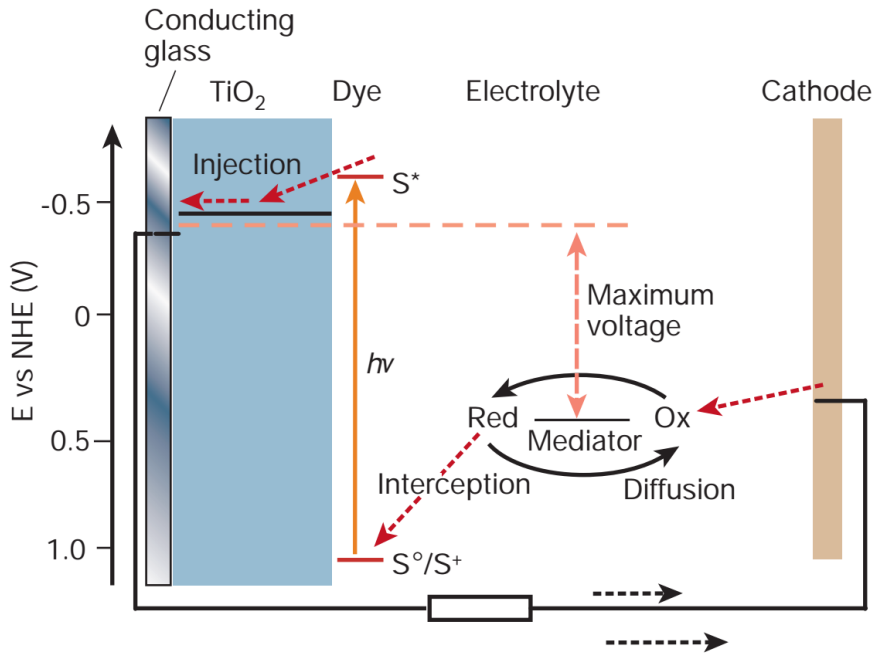

Fig. 1.4 Schematic diagram of operational principle of dye-sensitised solar cells.[16]

Since the report of the first highly efficient DSSC by Brian O'Regan and Michael Grätzel in 1991 with an efficiency of 7.1-7.9%[18], the efficiency has reached 13% in 2014[19]. Though the efficiency is still relatively low compared with silicon-based solar cells, DSSCs do show some advantages[20]. They can be produced using low-energy-consuming roll-to-roll techniques, on flexible substrates. They can also work under low light intensity condition due to the scattering effect of the mesoporous TiO_2 nanoparticles in the film. The main problem hindering the application of DSSCs is their instability, mainly arising from the leaking of the liquid eletrolyte[20,21]. The electrolyte solution is made up of volatile organic solvents which are hazardous to human health and the environment, and the corrosive nature of the redox couple to plastic sealants also makes the sealing of the electrolyte a big challenge. Alternatively, a solid p-type organic semiconductor with hole-transporting property is used to replace the liquid electrolyte, providing a solid-state DSSC. The most commonly used hole transporting material is Spiro-OMeTAD[22,23]. However since the optimal film thickness of the mesoporous TiO_2 layer is 2-3 μm which is not sufficient for efficient optical absorption[24], it ended up with no big improvement in the efficiency[25], until perovskite materials replaced dyes as the sensitizer.

1.2 Perovskite solar cells

Since the first use of perovskite in solar cells in 2009[26], the efficiency of perovskite-based solar cells has rocketed from 3.81% to ~23%[7]. Their development was so quick that they were named as a new type of solar cells - 'perovskite solar cells'.

1.2.1 Structure of perovskite

Perovskite refers to a crystal structure originally found for $CaTiO_3$. Compounds with perovskite structure normally have a generic chemical formula of ABX_3, in which an A cation resides at the eight corners of the cubic cell and the B cation is located at the body centre, surrounded by six X anions (located at the face centres), forming a BX_6 octahedron, as shown in **Fig. 1.5**. Typically, the A cation can be Ca^{2+}, Cs^{+}, organoammonium ions such as methylammonium (MA) and formamidinium (FA), etc., the B site cation, which is smaller than the A cation, could be Ti^{4+}, Pb^{2+}, Sn^{2+}, etc., and the C anion could be halide ions or oxygen. To form a stable cubic perovskite structure, the size of the ions should meet some certain requirement, i.e. the tolerance factor Γ defined as Equation 1.1 should lie between $0.813 < \Gamma < 1.107$[27,28].

$$\Gamma = \frac{r_A + r_X}{\sqrt{2}(r_B + r_X)} \tag{1.1}$$

where r_A, r_B and r_X are the effective ionic radii for A, B and X ions, respectively. For solar cell applications, the most used perovskite is organoammonium lead (or tin) halide perovskite, for example methylammonium lead iodide ($MAPbI_3$), of which the tolerance factor is calculated as 0.83[28].

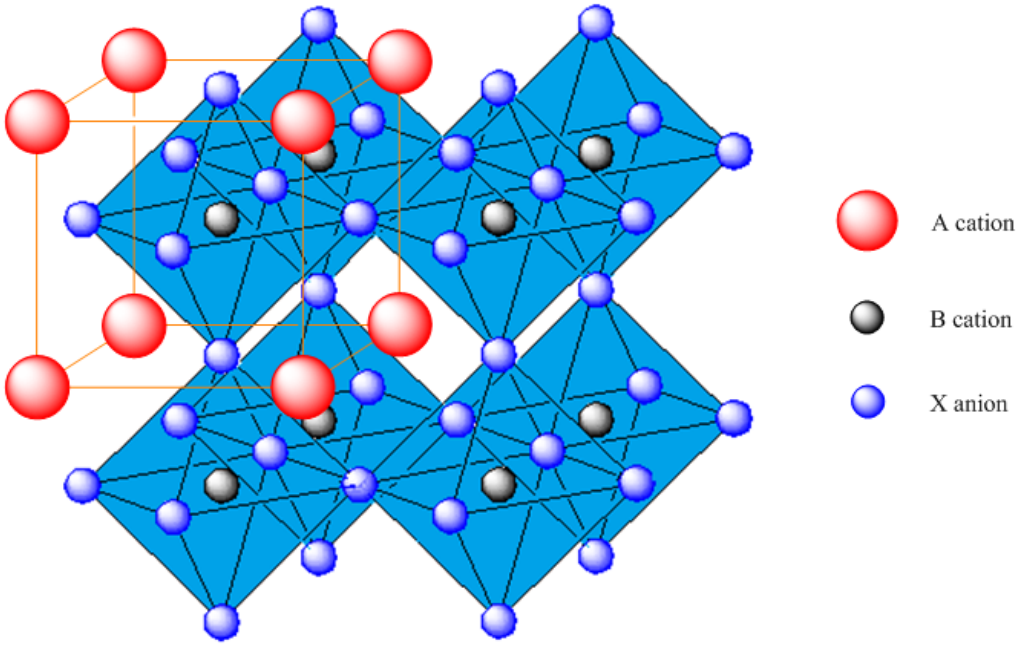

Fig. 1.5 Crystal structure of perovskite ABX_3.

1.2.2 History of perovskite solar cells

Studies of perovskite solar cells first appeared in 2009 and evolved from DSSC technology. In DSSCs, the normal dyes only form a monolayer, thus the thickness of the mesoporous layer has to be around 10 μm in order for sufficient light absorption[24]. To enhance the light-absorbing ability, people were trying to develop alternative sensitizers. In 2009, Miyasaka and coworkers[26] reported the utilization of $MAPbI_3$ and $MAPbBr_3$ perovskites as sensitizers in a DSSC with solution electrolyte. The perovskite materials absorbed light strongly and broadly in the visible range, so that complete light absorption can be achieved in films even as thin as 500 nm[29]. An efficiency as high as 3.81% was achieved for the $MAPbI_3$ based cell, and a high photovoltage of 0.96 V was obtained for the $MAPbBr_3$ based device. N.G. Park and co-workers[30] optimized the TiO_2 thickness, perovskite precursor concentration and TiO_2 surface in 2011 based on a similar device structure, and further improved the efficiency to 6.54% with 3.6 μm-thick TiO_2 films. However, the instability of perovskite in liquid electrolyte is fatal for these electrolyte-based cells. 80% degradation occurred in about 10 min under continuous illumination as the $MAPbI_3$ perovskite was dissolved gradually by the redox electrolyte.

A breakthrough in the efficiency and stability of perovskite solar cells came with the use of solid state hole transporting material (HTM) 2,2,7,7-tetrakis(N,N-p-dimethoxyphenylamino)-9,90-spirobifluorene (spiro-OMeTAD) in 2012. Park, Grätzel and coworkers[31] reported a solid-state perovskite solar cell with $MAPbI_3$ on a 0.6 μm m-TiO_2 layer and spiro-MeOTAD as HTM, which showed a power conversion efficiency (PCE) of 9.7%. The use of spiro-OMeTAD also greatly improved the device stability compared to liquid electrolyte-based cells. Long-term stability for over 500 h was achieved, with the devices being stored in air without encapsulation. At a similar time, Snaith and coworkers[32] reported a mixed-halide $MAPbI_{3-x}Cl_x$ perovskite solar cells with the same device structure, as shown in **Fig. 1.6**, delivering a PCE of ~ 8%. They also replaced the mesoporous n-type TiO_2 with mesoporous Al_2O_3. Al_2O_3 is an insulator (band-gap 7-9 eV), and cannot transport electrons. Surprisingly the device still worked and the electron transport in the Al_2O_3-based device was even much faster than in the TiO_2-based device, and the V_{OC} was also increased by a few hundred millivolts with the insulating Al_2O_3 scaffold, leading to a PCE of 10.9%. Even a planar-junction device FTO/c-TiO_2/$MAPbI_2Cl$/spiro-OMeTAD/Ag without a mesoporous layer also exhibited an efficiency of 1.8%. These results mean that the perovskite layer can not only absorb light but also transport electrons out of the device. Since then, an explosion of research activities was triggered, and a variety of device configurations, deposition methods and material sets have been employed.

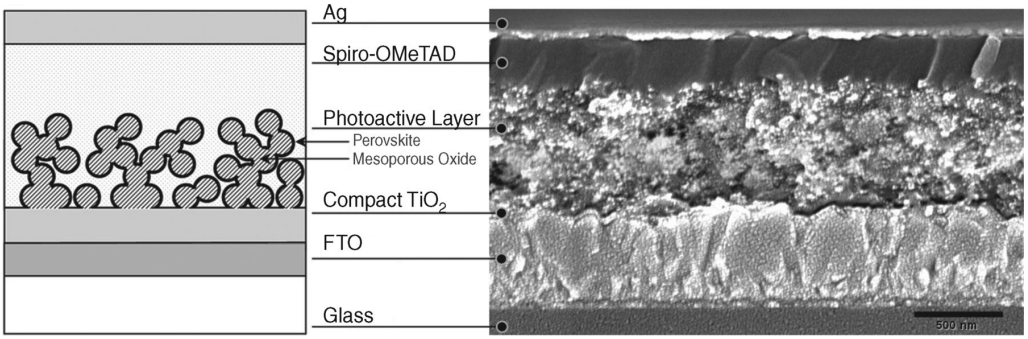

Fig. 1.6 Schematic diagram and SEM image of the cross-section of a mesoporous structured perovskite solar cell[32].

Grätzel and coworkers[33] investigated a mesoscopic $MAPbI_3$/TiO_2 heterojunction solar cell without an HTM layer, which still showed remarkable photovoltaic performance. An PCE of 5.5% was obtained with a short-circuit current density (J_{SC}) of 16.1 mA cm^{-2}, a

V_{OC} of 0.63 V, and a fill factor (FF) of 0.57. It shows that $MAPbI_3$ can also work as the HTM in a heterojunction solar cell.

Snaith[34] configured a planar FTO/c-TiO_2/$MAPbI_{3-x}Cl_x$/spiro-OMeTAD/Ag device without a mesoporous layer utilizing a highly uniform $MAPbI_{3-x}Cl_x$ layer synthesized via a dual-source vapour deposition route. The perovskite films showed extreme uniformity without pinholes, and thus avoided direct contacts between the spiro-OMeTAD and c-TiO_2 layers which could form shunting paths lowering the cell performance. An efficiency of over 15% was achieved, with an V_{OC} of 1.07 V.

Generally, mixed halide perovskite $MAPbI_{3-x}Cl_x$ showed better performance than pure iodide perovskite $MAPbI_3$[35–37], though no significant content of chloride in the lattice had been detected experimentally. The introduction of chloride is believed to improve the uniformity of perovskite films, as well as increase the carrier lifetime and diffusing length.

Grätzel's group reported a mixed-cation perovskite[38] based on mixed organic cations of MA and FA. It was found that the band-gap of perovskite $(MA)_x(FA)_{1-x}PbI_3$ can be tuned by changing the FA content in the composition. The increase of FA content resulted in a red shift of absorption onset which means a smaller optical band-gap, while the light absorbing ability was decreased. Optimal absorption was obtained from $MA_{0.6}FA_{0.4}PbI_3$, with a best efficiency of 14.9%. Saliba and coworkers further added a small amount of Cs into the binary mixed cations[39], forming a triple cation configuration $Cs_x(MA_{0.17}FA_{0.83})_{(100-x)}Pb(I_{0.83}Br_{0.17})_3$. The triple cation cells delivered stabilized PCEs up to 21.1%, and an PCE of 18% was still retained even after continuous aging for 250 hours under operational conditions. The triple cation configuration is now still giving the highest efficiency in perovskite family. F. Hao and M. G. Kanatzidis et al.[40] substituted lead with tin, and found that the band-gap of $MASn_{1-x}Pb_xI_3$ can also be tuned by changing the content of Sn. For $MASn_{0.5}Pb_{0.5}I_3$, the smallest band-gap of 1.17 eV was obtained, smaller than both $MAPbI_3$ (1.55 eV) and $MASnI_3$ (1.3 eV), showing an PCE of 7.27%.

1.2.3 Deposition methods of perovskite films

As the key absorber material for perovskite solar cells, the quality of the perovskite layer is vital for the device performance. The deposition of the perovskite films is mainly based on the reaction of the organic ammonium MAX and the inorganic lead halide PbX_2 components, where X = I, Cl, Br.

$$PbX_2 + MAX \xrightarrow{\triangle} MAPbX_3 \tag{1.2}$$

Up to now, various deposition processes have been investigated for the fabrication of organometal halide perovskite films, which are mainly classified as one-step methods and two-step methods through solution processes, vapour processes, or a combination thereof.

One-step methods

One-step methods are based on the co-deposition of both the organic and inorganic precursors through a solution process or a vapour process.

Initially, most $MAPbI_3$ or $MAPbI_{3-x}Cl_x$ perovskite films were deposited by spin-coating a mixed solution of PbX_2 (X=I, Cl) and MAI in organic solvents (DMF, DMSO, GBL), followed by thermal annealing. For $MAPbI_3$, stoichiometric MAI and PbI_2 (1:1) are dissolved in organic solvent for spin-coating deposition[31,41]. While for $MAPbI_{3-x}Cl_x$, a molar ratio of MAI: $PbCl_2$ of 3:1 is normally used[32,42]. In order to obtain perovskite films with higher surface coverage and better uniformity, much work has been done to control the crystallization of perovskite. Snaith's group[43] investigated the morphology of $MAPbI_{3-x}Cl_x$ annealed at different temperature, and found that surface coverage dropped as the annealing temperature increased. Coverage of $\sim 93\%$ was obtained for the planar $MAPbI_{3-x}Cl_x$ film annealed at 90 °C, delivering an improved efficiency of 11.4%. Po-Wei Liang, Alex K.-Y. Jen et al.[44] added 1,8-diiodooctane (DIO) to the perovskite precursor as an additive, and found that the perovskite films prepared with 1 wt% DIO additive were much smoother and better covered than the prestine films, leading to a PCE $\sim 12\%$ in a planar perovskite solar cell. Jeon and Seok et al. developed a solvent engineering technique to improve the film quality[45], by toluene dripping while spin-coating of the perovskite precursor in the mixture of GBL and DMSO. This toluene dripping treatment

enabled extremely uniform and dense perovskite layers and achieved a certified 16.2% PCE.

Apart from solution processed one-step methods, a vapour based one-step method was also developed for the fabrication of high quality perovskite films. Snaith and coworkers[34] successfully synthesized a uniform film of $MAPbI_{3-x}Cl_x$ perovskite with a dual-source vapour deposition method. MAI and $PbCl_2$ were evaporated simultaneously under vacuum with with a molar ratio of 4:1, and deposited on FTO substrates with compact TiO_2. Fully crystallized perovskite layers were obtained after annealing. With this vapour-deposition method, efficient perovskite devices with an efficiency of 15.4% were yielded, with a J_{SC} of 21.5 mA cm^{-2}, a V_{OC} of 1.07 V and a FF of 0.68.

Two-step methods

Two-step methods, or sequential methods, are based on the formation of PbX_2 films, normally by spin-coating, and their subsequent transformation into perovskite films. The transformation process can be done in different ways, as shown in **Fig. 1.7**: 1) dipping the PbX_2 films into MAX solution[46,47]; 2) spin-coating MAX solution on top of the PbX_2 films[48,49]; 3) evaporating MAX powder at elevated temperature and exposing the PbX_2 films into the vapour[50].

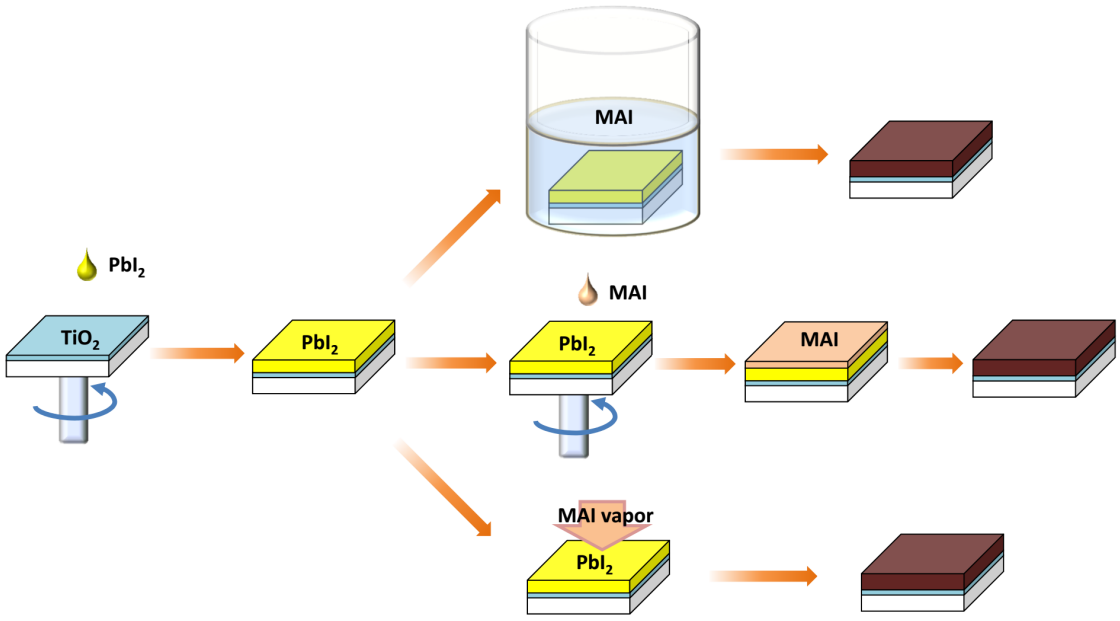

Fig. 1.7 Schematic diagram of two-step methods for perovskite film preparation.

Two-step deposition methods allow for independent control in the deposition conditions of each precursor and hence their reaction thereafter, which eventually enables a better control over the perovskite film formation process. Julian Burschka and Michael Grätzel et al.[46] spin-coated PbI_2 film on a 350-nm-thick mesoporous TiO_2 layer, and subsequently dipped it in a solution of 10 mg ml^{-1} MAI in IPA. The conversion of yellow PbI_2 into dark brown perovskite occurred within seconds, and resulted in a PCE of approximately 15% with excellent reproducibility. In contrast, it takes much longer for complete conversion in planar devices, as it is harder for MAI to diffuse into a planar PbI_2 film. A dipping duration of approximately 20 min has been reported[51], or a higher reaction temperature (70 °C) is needed[52]. Qi Chen and Huanping Zhou et al. developed a vapour-assisted solution process (VASP)[50] for the fabrication of perovskite film, in which PbI_2 was first spin-coated from solution and subsequently annealed in MAI vapour to form $MAPbI_3$ films with microscale grain size, highly smooth surface and full coverage. The obtained optimum planar device showed a PCE of 12.1%. Chang-Wen Chen and Hao-Wu Lin et al.[53] prepared $MAPbI_{3-x}Cl_x$ films through a layer-by-layer sequential vacuum deposition process. Extremely smooth $PbCl_2$ films were thermally sublimed onto PEDOT:PSS-coated indium tin oxide (ITO) glass, followed by the sublimation of MAI, which resulted in ultra-smooth $MAPbI_{3-x}Cl_x$ films with full surface coverage. The champion cell performed a high PCE of 15.4%, with a J_{SC} of 20.9 mA cm^{-2}, an V_{OC} of 1.02 V and a high FF of 0.72.

1.2.4 The bright side of perovskite solar cells

The band-gap for $MAPbI_3$ perovskite is $\sim$ 1.5 eV, corresponding to an absorption onset of $\sim$ 800 nm, which makes it a good absorber over the whole wavelength range of visible light. The high absorption coefficient of 1.5×10^4 cm^{-1} at 550 nm and 0.5×10^4 cm^{-1} at 700 nm allows sufficient absorption even with a small film thickness[28]. And the high carrier mobilities (11.6 cm^2 V^{-1} s^{-1} for $MAPbI_{3-x}Cl_x$ and $\sim$ 8 cm^2 V^{-1} s^{-1} for $MAPbI_3$ [54]) along with the long carrier lifetime (hundreds of nanoseconds) result in a long carrier diffusion length (ranging between 100 nm and 1,000 nm[55]). These together greatly decrease the possibility of recombination within the bulk.

Typically, perovskite solar cells employ a n-i-p or p-i-n junction structure in which a perovskite layer (intrinsic semiconductor layer) is sandwiched between an n-type electron-transporting layer (ETL, normally TiO_2 or PCBM) and a p-type hole-transporting layer (HTL, normally spiro-OMeTAD, NiO or PEDOT:PSS). The energy level alignment as shown in **Fig. 1.8** is favourable for charge separation[31]. After excitation, the photoelectrons can be fast injected into the conduction band of TiO_2, while the holes are transported into the HOMO of spiro-OMeTAD. In this way the charge carriers are separated and recombination can be alleviated.

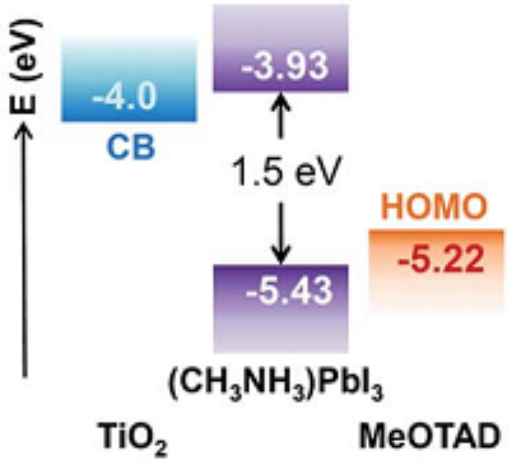

Fig. 1.8 Energy diagram in a typical n-i-p structured perovskite solar cell.[31] (Assuming the Spiro acts as a semiconductor rather than a redox couple.)

The preparation methods of perovskite, both one-step and two-step, are simple, low-energy-consuming and capable of producing high quality perovskite films. Roll-to-roll processes such as spray-coating and blade-coating also make the production of perovskite devices easy to scale up. These factors, along with the abundance of raw materials, mean perovskite solar cells have a short energy payback time (EPBT, defined as the ratio of the total primary energy consumption to the annual electricity generation), which is estimated to be 0.3 years, much shorter than silicon-based devices, as shown in **Fig. 1.9**[56].

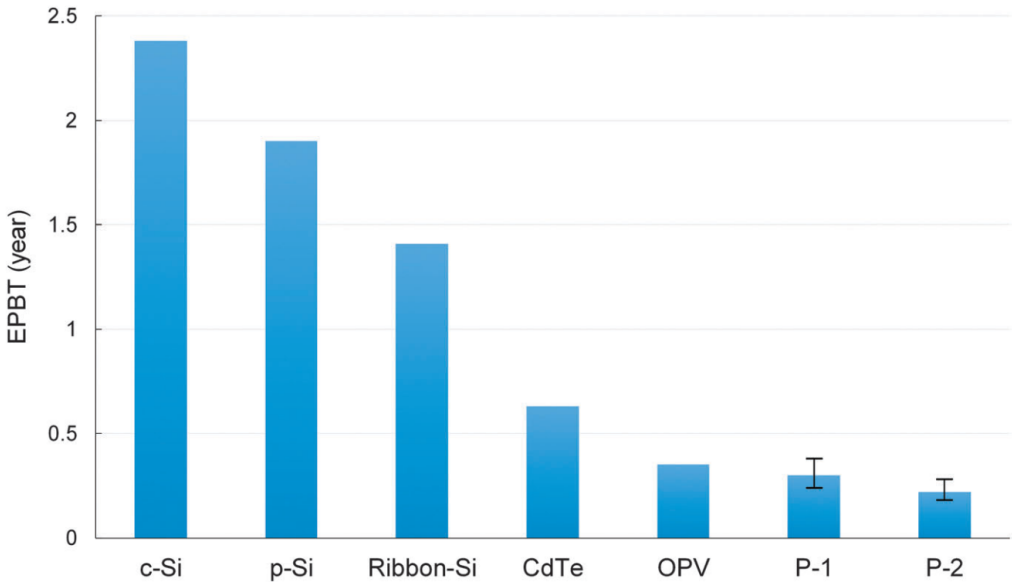

Fig. 1.9 Comparison in the energy payback time of typical PV modules. P-1 and P-2 are perovskite modules based on TiO_2 and ZnO, respectively. The error bars show the 95% confidence intervals.[56]

The rapid development of perovskite solar cells has sparked the hope of their practical application. Dar and Grätzel used cheap inorganic CuSCN as HTMs for perovskite solar cells[57], which achieved stabilized PCEs exceeding 20%. By incorporating a reduced graphene oxide interlayer between the CuSCN and gold layers, over 95% of the initial efficiency of the cells was successfully retained after 1000 hours aging at the maximum power point at 60 °C. Nazeeruddin's group[58] developed a 2D/3D $(HOOC(CH_2)_4NH_3)_2PbI_4/MAPbI_3$ perovskite junction, and fabricated 10×10 cm^2 solar modules through a fully printable route. The large area modules delivered stable 11.2% efficiency with no efficiency decrease for over 10000 h. Furthermore, there have been numerous industrial companies worldwide, such as Solar-Tectic, Oxford PV, Frontier Energy Solution and Microquanta Semiconductor, dedicated to the commercialisation of the perovskite technology. Hopefully, perovskite solar cells will find their real applications in the near future.

1.2.5 Issues to be addressed

Though organometallic halide perovskite based solar cells have shown many extraordinary properties and promising efficiency, there are still some issues to be addressed before their large-scale application.

Hysteresis

Hysteresis is a phenomenon commonly observed during the performance tests of perovskite solar cells. When scanned from different directions during current-voltage behaviour tests, different J-V curves can be obtained, as illustrated in **Fig.1.10**[59]. The current-voltage curve taken with decreasing voltage (reverse scan) tends to exhibit higher currents at each voltage than the curve taken with increasing voltage (forward scan). As a result, the performance of perovskite devices can be overestimated. Several ideas have been proposed as the cause of this phenomenon, including trap states[60], ferroelectricity[61,62] and ion migration[63–66]. The idea that it is caused by ion migration is being accepted by more and more researchers, but more work is still needed for better understanding and the avoidance of hysteresis.

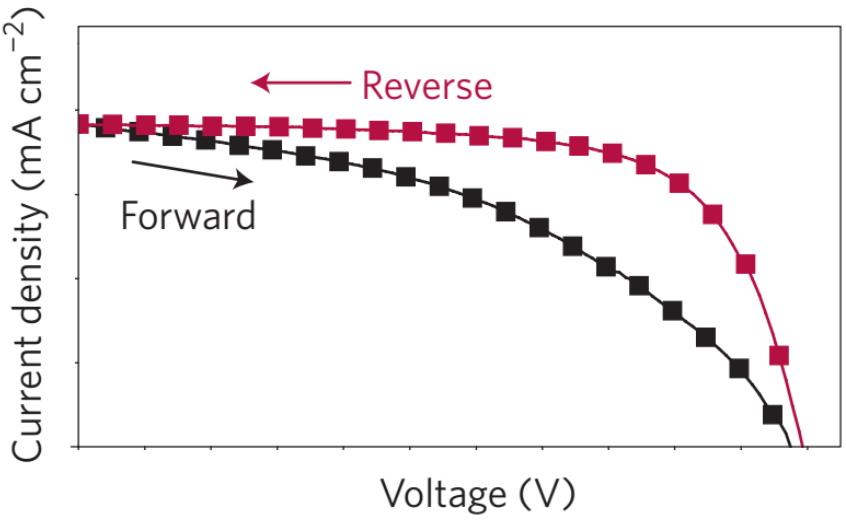

Fig. 1.10 J-V curves with forward and reverse scans showing hysteresis.[59]

Hysteresis has been found to be much more severe in planar devices than in mesoporous devices, and strongly dependent on the scan speed, light-soaking and pre-biasing conditions[67,68], temperature[69], perovskite crystal size[70] and contacts used[71].

For the accurate measurement of perovskite solar cells, it is generally required to include the data of both forward and reverse J-V curves at various scan rates as well as the steady-state photocurrent at voltages near the maximum power point (P_{max}) when efficiencies are reported[72].

Stability

Stability is probably the biggest challenge preventing practical applications of perovskite solar cells. For the decomposition reaction

$$\mathrm{MAPbI_3} \rightleftharpoons \mathrm{PbI_2} + \mathrm{MAI} \tag{1.3}$$

the change in the Gibbs free energy at 300K is $\Delta G^{\circ}_{300\mathrm{K}} = 0.16\,\mathrm{eV}$ per formula unit[73], indicating the perovskite structure is chemically stable under standard conditions, but the small magnitude suggests the stability is very fragile and can be shifted easily, especially with the existence of water. Since MAI is highly water soluble, the saturation concentration to suppress the decomposition of $\mathrm{MAPbI_3}$ is estimated to be as high as $\sim 8\,\mathrm{g/L}$[73], which means a small amount of water can result in serious decomposition of the perovskite phase. Besides, further decomposition can occur through reaction 1.4 which can be further accelerated by oxygen or UV light due to the consumption of the HI[74] through the reactions illustrated in Equation 1.5 and Equation 1.6, respectively. It was found that $\mathrm{MAPbI_3}$ would be degraded completely into $\mathrm{PbI_2}$ after 18 h exposuse in air with a humidity of 60% at 35 °C[74]. As a result, optimised device architecture and proper encapsulation are required for the long-term stability of perovskite solar cells.

$$\mathrm{MAI\,(aq)} \rightleftharpoons \mathrm{CH_3NH_2\,(aq)} + \mathrm{HI\,(aq)} \tag{1.4}$$

$$4\mathrm{HI\,(aq)} + \mathrm{O_2\,(g)} \rightleftharpoons 2\mathrm{I_2\,(s)} + 2\mathrm{H_2O\,(l)} \tag{1.5}$$

$$2\mathrm{HI\,(aq)} \rightleftharpoons \mathrm{H_2\,(g)} + \mathrm{I_2\,(s)} \tag{1.6}$$

Toxicity

Lead compounds are very hazardous for the environment, and the impact of lead-based perovskite devices on the environment is a big concern for their large-scale application. Several researchers have tried to replace Pb with other less toxic elements such as Sn[75,76]. Though $\mathrm{MASnI_3}$ also showed good semiconductive properties with a bandgap of $\sim 1.3\,\mathrm{eV}$, $\mathrm{Sn^{2+}}$ is easily oxidized into $\mathrm{Sn^{4+}}$ which can cause p-type doping to the material[75]. Partial replacement of Pb with Sn has also been investigated to reduce the

use of lead[77–79], but the highest PCE so far reported for Sn-Pb alloy-based perovskite solar cell is only 15.2% for $MASn_{0.25}Pb_{0.75}I_3$ [78], and stability is still a problem. So until now, the most efficient perovskite solar cells still have to be based on lead, but with proper encapsulation and the development of lead recycling processes which is also extremely important for lead acid batteries, the harm of lead content to the environment could be minimised.

1.3 Perovskite Nanocrystals

Along with the rapid development of bulk perovskite materials in solar cells, their nanocrystals (NCs) have also attracted significant interest. When the size of crystalline semiconductors is reduced into the nanoscale dimension, the materials can exhibit distinct properties from their bulk forms. Due to the quantum confinement effect, quantum dots of PbS, CdSe etc. show size-dependent band-gaps, which provide for tunable light emission by control of the particle size. As a result, these quantum dots have shown promising applications in displays and lighting[80], as well as solar cells[81]. On the basis of the facile solution processability, as well as the high carrier mobility, long carrier lifetime and low trap density shown in solar cell applications of bulk perovskite materials, people have also prepared NCs of a variety of $APbX_3$ perovskite materials, and found promising applications, in both light emitting diodes (LEDs) and solar cells.

Perovskite NCs have shown bright and narrow-band photoluminescence (PL) that is easily tunable from ultraviolet to near-infrared wavelengths by changing either the halide composition or NC size. Pérez-Prieto and co-workers[82] reported the preparation of 6 nm-sized $MAPbBr_3$ NCs as stable colloidal solutions and made electroluminescent devices using them. Both the solutions and thin films showed bright green emission at ~ 530 nm, and the quantum yield reached 23%. Rogach's group[83] demonstrated the size-tunable bandgap of $MAPbBr_3$ NCs by changing the processing temperature. The emission peaks of the $MAPbBr_3$ NCs was tuned in the region of 475-520 nm when the temperature was changed from 0 to 60 °C, all with narrow emission linewidths of 28-36 nm, and very high quantum yields of 74%-93% were achieved. Zhong et al.[84] reported the synthesis of brightly luminescent $MAPbX_3$ (X = Cl, Br and I) NCs with a simple ligand assisted

repricipitation strategy, and demonstrated the fine tunability of the PL wavelength from 407 nm to 734 nm by changing the halide composition, with an absolute PL quantum yield of up to 70%. Kovalenko and co-workers[85] also managed to synthesize monodisperse NCs of fully inorganic perovskite $CsPbX_3$. The band-gap of the NCs showed both compositional dependance and size tunability, and covered the the whole visible spectral region of 410-700 nm. The PL spectra also exhibited narrow emission peak widths of 12-42 nm and high quantum yields of 50-90%. Perovskite NCs based on other organic cations have also been synthesised. The same group further demonstrated the fabrication of highly monodisperse $FAPbBr_3$ NCs[86], and managed to tune the PL peaks in the range of 470-540 nm by controlling the size of the NCs (5-12 nm). High quantum yield of up to 85% and narrow PL peak width of <22 nm were also achieved. Scholes et al.[87] have successfully synthesized layered 2D perovskites $R_2(MA)_{n-1}Pb_nI_{3n+1}$, where R is a long-chain organic ammonium ion, and n is the number of layers. The PL emission was dependent on not only the size of the NCs, but also the number of layers n which can be tuned by the molar ratio between RI and MAI.

In addition to promising applications in LEDs, perovskite NCs have also been investigated in solar cell applications. Zheng and Wang[88] used $MAPbBr_{0.9}I_{2.1}$ NCs as interlayers for perovskite solar cells, where the NCs were placed between the $MAPbI_3$ layer and HTL. The NCs improved hole transfer at the interface and consequently improved the PCE of the device from 10.3% to 13.3%. Perovskite NCs have also been used as the absorber layers for solar cells. Petrozza and Manna[89] reported the fabrication of perovskite solar cells based on $CsPbBr_3$ NCs. The cells with active layers of 550 ± 50 nm delivered an ultra high V_{OC} of 1.5 V, but due to the large band-gap of the $CsPbBr_3$ NCs (2.38 eV), and possibly poor band alignments of the charge transporting layers, a PCE of only 5.4% was achieved. Luther, on the other hand, reported[90] the use of 9 nm $CsPbI_3$ NCs with a much smaller band-gap of ~ 1.9 eV as the absorbing layers for perovskite solar cells. The cells exhibited a high PCE of 10.77% and a V_{OC} of 1.23 V. The cells also worked as LEDs, giving red emission with low turn-on voltage. The same group further treated the $CsPbI_3$ NCs with FAI[15], and pushed the PCE to 13.4%, a certified record for quantum dots based solar cells[91]. The FAI treatment doubled the charge carrier mobility of the $CsPbI_3$ NC film from 0.23 to 0.50 $cm^2\ V^{-1}\ s^{-1}$ and increased the photocurrent.

Up to now, solution approaches for the synthesis of perovskite NCs are mainly based on two strategies: hot-injection (HI) and ligand-assisted reprecipitation (LARP), as shown in **Fig. 1.11**.

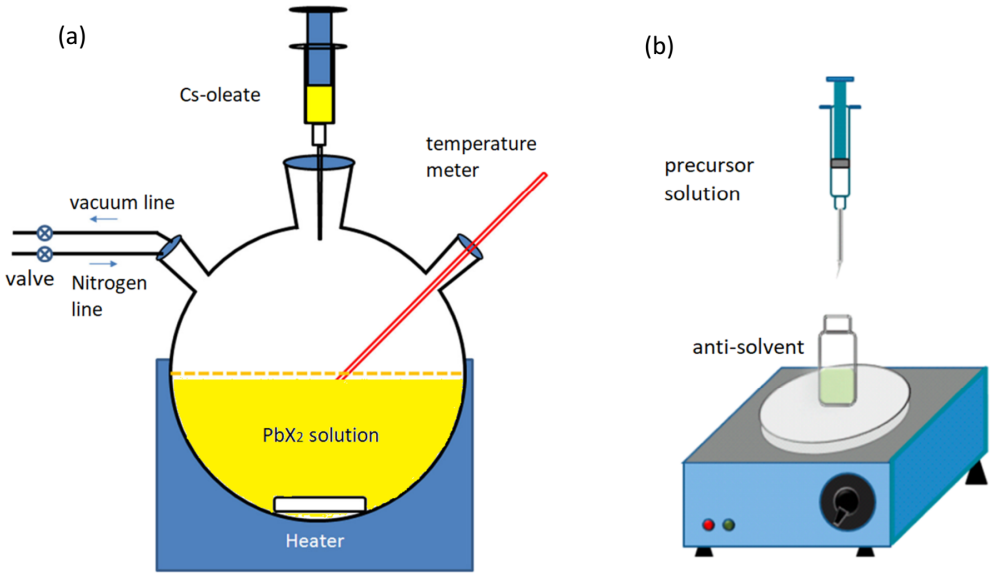

Fig. 1.11 Schematic diagram of synthesizing strategies of perovskite NCs: (a) HI method[92]; (b) LARP approach[84].

The HI route is a fabrication process of $APbX_3$ perovskite NCs which involves the injection of (typically) the A source into a PbX_2 solution at elevated temperature. The HI procedure had been commonly used for the synthesis of metal chalcogenide or fluoride NCs[93–96] such as PbS, CdSe and $NaYF_4$, based on which Kovalenkos group[85] pioneered the fabrication of $CsPbX_3$ NCs. Cs-oleate solution was made through the reaction of Cs_2CO_3 with oleic acid, and was quickly injected into the PbX_2 solution in octadecene at high temperatures (140-200 °C), with 1:1 mixture of oleic acid (OA) and oleylamine (OLA). The OA and OLA worked as ligands to dissolve PbX_2 and stabilize the as-obtained perovskite NCs. Highly luminescent colloidal 4-15 nm cubic $CsPbX_3$ NCs were obtained through the reaction in Equation.1.7, with high quantum yield of 50-90%, and the PL was tunable by both particle size and halide composition.

$$3\,PbX_2 + 2\,\text{Cs-oleate} \xrightarrow{\triangle} 2\,CsPbX_3 + Pb(\text{oleate})_2 \tag{1.7}$$

Following their work, the HI method has been widely used for the synthesis of $CsPbX_3$ NCs. Zhang and Jiang[97] investigated ethers as the solvent for the synthesis and found

that the growth of $CsPbX_3$ NCs could be better controlled in less polar solvents. Zeng and coworks[98] replaced the Cs-oleate with Cs-stearate and successfully synthesised 2D $CsPbBr_3$ nanosheets with a thickness of around 3.3 nm. The nanosheets showed good dispersibility, high flexibility and excellent photo-detecting properties. Due to the ability to achieve high-quality perovskite NCs, the HI approach has been the most widely adopted procedure for the fabrication of $CsPbX_3$ NCs. However, this method normally requires a protective atmosphere and high temperatures of over 100 °C, and the reaction temperature and time are hard to control during the injection of the reagent, resulting in poor reproducibility between batches and users[99,100]. Besides, the HI process normally suffers from localised mixing of the reactants, which makes it hard to scale up.

The LARP approach is another important process for the synthesis of perovskite NCs, which typically involves the addition of a perovskite precursor solution in a polar solvent (e.g. DMF or DMSO) into a nonpolar solvent such as toluene or hexane. Perovskite crystals precipitate out with the assistance of stabilising capping ligands. In 2015, Zhong and coworkers[84] developed the LARP technique for the preparation of $MAPbBr_3$ NCs by dropping a precursor solution of MABr and $PbBr_2$ in DMF with OA and OLA as ligands into toluene with vigorous stirring. $MAPbBr_3$ NCs were obtained with a mean diameter of 3.3 nm and a narrow size distribution. The PL spectrum peaked sharply at 515 nm with a small peak width of only 21 nm, and PL quantum yields of 50-70% were achieved. Halide composition was also easily tuned by using appropriate halide ratios in the precursor solution. Since then, the LARP method has been widely used for the synthesis of $APbX_3$ NCs. Deng's group[101] applied the LARP stragety in the preparation of $CsPbX_3$ NCs. $CsPbX_3$ NCs of different morpholopies were prepared by changing the organic acid and amine ligands. By tuning the shape, size and composition of the NCs, PL emission peaks covering the visible range from 380 to 693 nm were achieved, with PL quantum yields up to over 80%. Levchuk et al.[102] reported the LARP synthesis of brightly emitting $FAPbX_3$ nanoplatelets. A high quantum yield of up to 85% was achieved, and luminescence was tuned by simply changing the halide composition, covering a wide visible range between 415 and 740 nm. The thickness of the nanoplatelets was also tailored by the ligand ratio. The LARP approach can be carried out at room temperature and is easy to conduct, but bulk material is formed as a by-product together with the nanoparticles, which limits the synthetic yield[84].

Although both these two methods result in the formation of highly emissive perovskite NCs, they are typically focused on conventional batch systems which are characterized by poor heat and mass transport. The nucleation rates for perovskite NCs, however, is very fast[103]. As a result, the low speed of homogeneous mixing of reagents and heat transfer in the batch system, especially in large-scale production, makes the synthesis difficult, and therefore limits their scale-up. A promising alternative to the batch system is flow chemistry.

1.4 Flow chemistry

Flow chemistry is a process in which the use of flow reactors comprising channels or tubing are involved to conduct a chemical reaction in a continuous stream rather than in a static container[104]. Flow chemistry has provided a very useful tool for both the industrial scale-up of a variety of reactions as well as laboratory researches into small scale material production, and has received remarkable attention[105–107].

Flow reactors are modular toolboxes for synthetic chemistry, and are typically comprised of multiple interconnected units as shown in **Fig. 1.12**: delivery, mixing, reactor, quenching, collection, and optionally pressure regulation, analysis and purification units[104]. A delivery unit (typically feeding pumps) accurately feed the reactants into the flow system. Mixing of the reactants is conducted in a mixing unit before they enter the reactor unit which is further connected to a quenching unit to terminate the reaction, and the product is collected in the collection unit. Pressure regulation is also needed if high pressure is involved in the system, and optional analysis and purification units can also be incorporated where required.

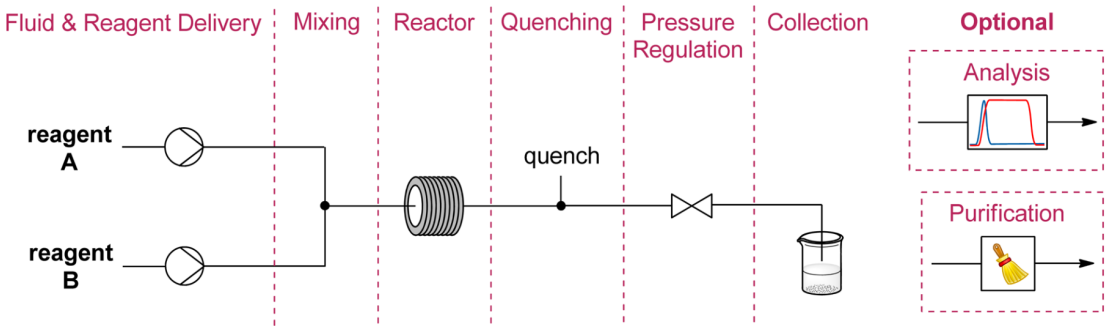

Fig. 1.12 Schematic diagram of a typical flow reactor.[104]

The reactor unit is where chemical reactions occur, and is the core of a flow reactor system. The reactor could be a chip reactor based on channels formed in silicon, glass, ceramics or stainless steel, or a coil reactor comprising low cost tubings made from polymers (e.g. PFA, PTFE) or stainless steel. The reactors are normally set up in combination with temperature-controlling facilities to maintain the temperature during the reaction. The length of the reactor, together with the flow rate of the flow medium, determines the residence time of the reactant mixture in the reactor, which is also the reaction time, a most important parameter of a flow system. Bawendi and co-workers[108] reported the synthesis of CdSe NCs of different sizes using a flow microcapillary reactor, and demonstrated higher reaction yields and larger particle sizes obtained at longer residence time or higher temperature. The scale of a reactor can range from 10 μm up to a few milimeters in inner diameter (i.d.). Mesofluidic reactors[106] (typical i.d. 500 μm up to several milimeters) provide large flow capacity, less pressure drop and less tendency to block, and are therefore normally used for industrial large-scale manufacturing. Whereas microfluidic reactors (typical i.d. 10-500 μm) possess better heat transfer capability due to their larger heat transfer area per unit volume, while suffering from limited flow capacity and high pressure drop, thus are mainly used in laboratories for analytical and diagnostic applications[106]. Alivisatos[109] demonstrated chip-based microfluidic reactors for the synthesis of CdSe NCs with controllable sizes by changing the reaction time, temperature and precursor concentration, and highlighted the flexibility of microreactors for kinetic studies and fine tuning of product properties.

Putting chemical reactions into fluids flowing in long thin channels have several intrinsic advantages over conventional batch systems, which have made the technology attractive

for chemical synthesis in both industry and academia.

Better mixing

Mixing of reactants is normally of great importance for chemical reactions, especially for fast reactions. When the rate of the reaction is higher than the speed of mixing, the concentration gradients or localised distribution of the reactants could result in the formation of by-products, or uneven size-distribution of nanomaterials. The flow pattern of liquids can be predicted using the Reynolds number (*Re*) defined as:

$$Re = \frac{\rho d v}{\eta} \tag{1.8}$$

where ρ is the density of the liquid, η is the dynamic viscosity of the liquid, d is the characteristic dimension of the container, and v is the velocity of the flow. Low Re describes laminar flow, whereas high Re values normally mean turbulent flows, and transitional flow forms in between. In laboratory batch reactors, mixing is typically turbulent near the stirring bar while laminar at outlying areas where reactants mixing is generally based on diffusion[104]. Fluids in flow reactors normally have low Reynolds numbers (below 250) and are also within the laminar flow regime[107]. Since the diameter of the flow channel is very small, the diffusion time is inherently smaller and mixing can be achieved much faster than in batch. In addition, various mixers can be easily integrated into the flow system, which can make uniform mixing achievable within seconds.

Faster heat transfer

Due to the small dimensions of flow reactors, their area to volume ratios are large, which facilitate the heat transfer between the liquid and the temperature-controlling facility in the flow system. For endothermic and exothermic reactions, the heat consumed or generated by the reaction could decrease or increase the temperature of the reaction medium, and consequently cause problem, such as the formation of side-products, decomposition of chemicals or phase transition of solvents[105]. The change of temperature can also make kinetics studies impossible, as the reaction kinetics is highly dependent on temperature. Therefore, efficient heat transfer of flow reactors provides a good solution to keeping the temperature constant, allowing efficient control over the reaction.

Increased safety

Flow reactors are better at running dangerous chemistry than batch systems due to their intrinsic advantages in safety[110]. The small dimension of the flow reactors means that any toxic chemicals are used in small amounts and are easier to handle. The reactions are confined in the channels of robust materials, which make the chemicals less likely to spill or be unintentionally exposed to the environment during the reaction. More importantly, the fast heat transfer discussed above makes the heat management more efficient, thus avoiding thermal runaway and dangerous safety issues such as boiling of solvents, and even explosion.

Online analysis

Chemical reactions take place along with the reactants flowing through the reactor, therfore, different stages of the reactions happen at different positions in the flow reactor. This makes online analysis of the reaction, such as the intermediates and mechanism investigations, very feasible, especially for fast reactions. Kovalenko and deMello[111] reported a droplet microfluidic platform for the synthesis of $FAPbX_3$ perovskite NCs. An end-point fluorescence detector and an in-line fluorescence detector were incorporated, allowing them to conduct mechanistic and optimising studies. Online PL analysis of the NCs identified optimal synthesis conditions, and revealed the different growth mechanisms for $FAPbX_3$ NCs with different halide compositions.

Automation

As all the components (i.e. feeding pumps, valves, temperature controller, pressure regulator, etc.) are easy for automation, flow reactions can be automated easily, even remotely[112], allowing for unattended operation and experimental planning. By coupling the reactor with a detecting system, it is possible to further automate the screening of a range of possible reaction parameters (stoichiometry, residence time and temperature, etc.) with little or no intervention. Automatic feedback optimization can also be carried out so that the parameters can be adjusted in real-time, saving significant time and money for the chemists[104].

Due to these advantages, flow systems have been successfully used to synthesize a variety

of nanomaterials[113], including metal nanoparticles[114], metal oxides[115,116] and colloidal semiconductors[117,118]. Torrente-Murciano and coworkers demonstrated[114] the synthesis of silver nanoparticles with narrow size distributions in a helical microreactor without the assistance of capping ligands. Lee and Jeon developed[118] a thermoplastic-based microreactor for the synthesis of ZnSe/ZnS core/shell NCs. The formation of the core and the shell layers were achieved in a single step and the size of the NCs were easily tunable by changing the flow rates of the precursors.

Flow chemistry has also been applied in the synthesis of perovskite NCs. The nucleation and growth of perovskite NCs are typically fast due to the ionic metathesis nature of the reaction[103]. Therefore, flow systems are particularly useful in terms of fast mixing and heat transfer. deMello and Kovalenko[103] reported an elegant flow synthesis of $CsPbX_3$ NCs using a droplet-based microfluidic platform in 2016. Online optical measurements were conducted to perform ultrafast kinetic studies and reaction optimization, revealing the fast growth time of $\leqslant 3$ s. The same group carried out[111] further mechanistic investigation and reaction optimisation to the preparation of $FAPbX_3$ NCs using the droplet microfluidic system, and developed[119] an automated droplet microfluidic platform for the controlled synthesis of $FAPb(Cl_{1-x}Br_x)_3$ NCs with blue emission. However we could not find any reports of flow chemistry being used to synthesize MA-based perovskite NCs. In addition, the reported flow synthesis of perovskite NCs are developed from the HI technique, and require not only high temperatures of 120-180 °C, but also the use of an oil carrier fluid which increased the system complexity.

Reference

[1] U. National Statistics. Regional statistics 2003-2016: Generation. `https://www.gov.uk/government/statistics/regional-renewable-statistics`, 2017. Online; Accessed 19 April 2018.

[2] T.C. Sum and N. Mathews. Advancements in perovskite solar cells: Photophysics behind the photovoltaics. *Energy & Environmental Science*, 7(8):2518–2534, 2014.

[3] A.-E. Becquerel. Recherches sur les effets de la radiation chimique de la lumiere

solaire au moyen des courants electriques. *Comptes Rendus de L'Academie des Sciences*, 9:145–149, 1839.

[4] D.M. Chapin, C.S. Fuller, and G.L. Pearson. A new silicon pn junction photocell for converting solar radiation into electrical power. *Journal of Applied Physics*, 25(5):676–677, 1954.

[5] A. Jger-Waldau. PV status report 2017. Report ISBN 978-92-79-74071-8, European Commission, 2017.

[6] G. Conibeer. Third-generation photovoltaics. *Materials Today*, 10(11):42–50, 2007.

[7] M.A. Green, Y. Hishikawa, E.D. Dunlop, D.H. Levi, J. HohlEbinger, and A.W.Y. HoBaillie. Solar cell efficiency tables (version 51). *Progress in Photovoltaics: Research and Applications*, 26(1):3–12, 2018.

[8] S. Kazim, M.K. Nazeeruddin, M. Grätzel, and S. Ahmad. Perovskite as light harvester: A game changer in photovoltaics. *Angewandte Chemie. International Edition in English*, 53(11):2812–24, 2014.

[9] X. Wu. High-efficiency polycrystalline cdte thin-film solar cells. *Solar Energy*, 77(6):803–814, 2004.

[10] P. Jackson, D. Hariskos, E. Lotter, S. Paetel, R. Wuerz, R. Menner, W. Wischmann, and M. Powalla. New world record efficiency for Cu(In,Ga)Se_2 thin-film solar cells beyond 20%. *Progress in Photovoltaics: Research and Applications*, 19(7):894–897, 2011.

[11] V. Fthenakis. Sustainability of photovoltaics: The case for thin-film solar cells. *Renewable and Sustainable Energy Reviews*, 13(9):2746–2750, 2009.

[12] H. Bin, L. Gao, Z.G. Zhang, Y. Yang, Y. Zhang, C. Zhang, S. Chen, L. Xue, C. Yang, M. Xiao, and Y. Li. 11.4% efficiency non-fullerene polymer solar cells with trialkylsilyl substituted 2D-conjugated polymer as donor. *Nature Communications*, 7:13651, 2016.

[13] S. Gnes, H. Neugebauer, and N.S. Sariciftci. Conjugated polymer-based organic solar cells. *Chemical reviews*, 107(4):1324–1338, 2007.

[14] N. Grossiord, J.M. Kroon, R. Andriessen, and P.W.M. Blom. Degradation mechanisms in organic photovoltaic devices. *Organic Electronics*, 13(3):432–456, 2012.

[15] E.M. Sanehira, A.R. Marshall, J.A. Christians, S.P. Harvey, P.N. Ciesielski, L.M. Wheeler, P. Schulz, L.Y. Lin, M.C. Beard, and J.M. Luther. Enhanced mobility $CsPbI_3$ quantum dot arrays for record-efficiency, high-voltage photovoltaic cells. *Science Advances*, 3(10):eaao4204, 2017.

[16] M. Grätzel. Photoelectrochemical cells. *Nature*, 414(6861):338–344, 2001.

[17] C. Dette, M.A. Prez-Osorio, C.S. Kley, P. Punke, C.E. Patrick, P. Jacobson, F. Giustino, S.J. Jung, and K. Kern. TiO_2 anatase with a bandgap in the visible region. *Nano Letters*, 14(11):6533–6538, 2014.

[18] B. O'Regan and M. Grätzel. A low-cost, high-efficiency solar cell based on dye-sensitized colloidal TiO_2 films. *Nature*, 353(6346):737–740, 1991.

[19] S. Mathew, A. Yella, P. Gao, R. Humphry-Baker, F.E. CurchodBasile, N. Ashari-Astani, I. Tavernelli, U. Rothlisberger, K. NazeeruddinMd, and M. Grätzel. Dye-sensitized solar cells with 13% efficiency achieved through the molecular engineering of porphyrin sensitizers. *Nature Chemistry*, 6(3):242–247, 2014.

[20] J. Gong, K. Sumathy, Q. Qiao, and Z. Zhou. Review on dye-sensitized solar cells (dsscs): Advanced techniques and research trends. *Renewable and Sustainable Energy Reviews*, 68:234–246, 2017.

[21] P.M. Sommeling, M. Spth, H.J.P. Smit, N.J. Bakker, and J.M. Kroon. Long-term stability testing of dye-sensitized solar cells. *Journal of Photochemistry and Photobiology A: Chemistry*, 164(1):137–144, 2004.

[22] F. Fabregat-Santiago, J. Bisquert, L. Cevey, P. Chen, M. Wang, S.M. Zakeeruddin, and M. Grätzel. Electron transport and recombination in solid-state dye solar cell with spiro-ometad as hole conductor. *Journal of the American Chemical Society*, 131(2):558–562, 2009.

[23] H.J. Snaith, A.J. Moule, C. Klein, K. Meerholz, R.H. Friend, and M. Grätzel. Efficiency enhancements in solid-state hybrid solar cells via reduced charge recombination and increased light capture. *Nano Letters*, 7(11):3372–3376, 2007.

[24] H.J. Snaith and L. Schmidt-Mende. Advances in liquid-electrolyte and solid-state dye-sensitized solar cells. *Advanced Materials*, 19(20):3187–3200, 2007.

[25] H.M. Upadhyaya, S. Senthilarasu, M.-H. Hsu, and D.K. Kumar. Recent progress and the status of dye-sensitised solar cell (dssc) technology with state-of-the-art conversion efficiencies. *Solar Energy Materials and Solar Cells*, 119(0):291–295, 2013.

[26] A. Kojima, K. Teshima, Y. Shirai, and T. Miyasaka. Organometal halide perovskites as visible-light sensitizers for photovoltaic cells. *Journal of the American Chemical Society*, 131(17):6050–6051, 2009.

[27] C. Li, X. Lu, W. Ding, L. Feng, Y. Gao, and Z. Guo. Formability of ABX_3 (X = F, Cl, Br, I) halide perovskites. *Acta Crystallographica Section B*, 64(6):702–707, 2008.

[28] N.-G. Park. Perovskite solar cells: An emerging photovoltaic technology. *Materials Today*, 18(2):65–72, 2015.

[29] H.J. Snaith. Perovskites: The emergence of a new era for low-cost, high-efficiency solar cells. *The Journal of Physical Chemistry Letters*, 4(21):3623–3630, 2013.

[30] J.H. Im, C.R. Lee, J.W. Lee, S.W. Park, and N.G. Park. 6.5% efficient perovskite quantum-dot-sensitized solar cell. *Nanoscale*, 3(10):4088–93, 2011.

[31] H.-S. Kim, C.-R. Lee, J.-H. Im, K.-B. Lee, T. Moehl, A. Marchioro, S.-J. Moon, R. Humphry-Baker, J.-H. Yum, J.E. Moser, M. Grätzel, and N.-G. Park. Lead iodide perovskite sensitized all-solid-state submicron thin film mesoscopic solar cell with efficiency exceeding 9%. *Scientific Reports*, 2(1):591, 2012.

[32] M.M. Lee, J. Teuscher, T. Miyasaka, T.N. Murakami, and H.J. Snaith. Efficient hybrid solar cells based on meso-superstructured organometal halide perovskites. *Science*, 338(6107):643–647, 2012.

[33] L. Etgar, P. Gao, Z. Xue, Q. Peng, A.K. Chandiran, B. Liu, M.K. Nazeeruddin, and M. Grätzel. Mesoscopic $CH_3NH_3PbI_3/TiO_2$ heterojunction solar cells. *Journal of the American Chemical Society*, 134(42):17396–17399, 2012.

[34] M. Liu, M.B. Johnston, and H.J. Snaith. Efficient planar heterojunction perovskite solar cells by vapour deposition. *Nature*, 501(7467):395–398, 2013.

[35] S. Colella, E. Mosconi, P. Fedeli, A. Listorti, F. Gazza, F. Orlandi, P. Ferro, T. Besagni, A. Rizzo, G. Calestani, G. Gigli, F. De Angelis, and R. Mosca. $MAPbI_{3-x}Cl_x$ mixed halide perovskite for hybrid solar cells: The role of chloride as dopant on the transport and structural properties. *Chemistry of Materials*, 25(22):4613–4618, 2013.

[36] Y. Tidhar, E. Edri, H. Weissman, D. Zohar, G. Hodes, D. Cahen, B. Rybtchinski, and S. Kirmayer. Crystallization of methyl ammonium lead halide perovskites: Implications for photovoltaic applications. *Journal of the American Chemical Society*, 136(38):13249–13256, 2014.

[37] D. Wang, Z. Liu, Z. Zhou, H. Zhu, Y. Zhou, C. Huang, Z. Wang, H. Xu, Y. Jin, B. Fan, S. Pang, and G. Cui. Reproducible one-step fabrication of compact $MAPbI_{3-x}Cl_x$ thin films derived from mixed-lead-halide precursors. *Chemistry of Materials*, 26(24):7145–7150, 2014.

[38] N. Pellet, P. Gao, G. Gregori, T.-Y. Yang, M.K. Nazeeruddin, J. Maier, and M. Grätzel. Mixed-organic-cation perovskite photovoltaics for enhanced solar-light harvesting. *Angewandte Chemie International Edition*, 53(12):3151–3157, 2014.

[39] M. Saliba, T. Matsui, J.Y. Seo, K. Domanski, J.P. Correa-Baena, M.K. Nazeeruddin, S.M. Zakeeruddin, W. Tress, A. Abate, A. Hagfeldt, and M. Grätzel. Cesium-containing triple cation perovskite solar cells: Improved stability, reproducibility and high efficiency. *Energy & Environmental Science*, 9(6):1989–1997, 2016.

[40] F. Hao, C.C. Stoumpos, R.P.H. Chang, and M.G. Kanatzidis. Anomalous band gap behavior in mixed Sn and Pb perovskites enables broadening of absorption spectrum in solar cells. *Journal of the American Chemical Society*, 136(22):8094–8099, 2014.

[41] C. Chen, C. Li, F. Li, F. Wu, F. Tan, Y. Zhai, and W. Zhang. Efficient perovskite solar cells based on low-temperature solution-processed $CH_3NH_3PbI_3$ perovskite/$CuInS_2$ planar heterojunctions. *Nanoscale Research Letters*, 9(1):1–8, 2014.

[42] J. You, Z. Hong, Y. Yang, Q. Chen, M. Cai, T.-B. Song, C.-C. Chen, S. Lu, Y. Liu, H. Zhou, and Y. Yang. Low-temperature solution-processed perovskite solar cells with high efficiency and flexibility. *ACS Nano*, 8(2):1674–1680, 2014.

[43] G.E. Eperon, V.M. Burlakov, P. Docampo, A. Goriely, and H.J. Snaith. Morphological control for high performance, solution-processed planar heterojunction perovskite solar cells. *Advanced Functional Materials*, 24(1):151–157, 2014.

[44] P.W. Liang, C.Y. Liao, C.C. Chueh, F. Zuo, S.T. Williams, X.K. Xin, J. Lin, and A.K. Jen. Additive enhanced crystallization of solution-processed perovskite for highly efficient planar-heterojunction solar cells. *Advanced Materials*, 26(22):3748–3754, 2014.

[45] N.J. Jeon, J.H. Noh, Y.C. Kim, W.S. Yang, S. Ryu, and S.I. Seok. Solvent engineering for high-performance inorganic-organic hybrid perovskite solar cells. *Nature Materials*, 13(9):897–903, 2014.

[46] J. Burschka, N. Pellet, S.-J. Moon, R. Humphry-Baker, P. Gao, M.K. Nazeeruddin, and M. Grätzel. Sequential deposition as a route to high-performance perovskite-sensitized solar cells. *Nature*, 499(7458):316–319, 2013.

[47] S. Pang, H. Hu, J. Zhang, S. Lv, Y. Yu, F. Wei, T. Qin, H. Xu, Z. Liu, and G. Cui. $NH_2CH{=}NH_2PbI_3$: An alternative organolead iodide perovskite sensitizer for mesoscopic solar cells. *Chemistry of Materials*, 26(3):1485–1491, 2014.

[48] J.-H. Im, H.-S. Kim, and N.-G. Park. Morphology-photovoltaic property correlation in perovskite solar cells: One-step versus two-step deposition of $CH_3NH_3PbI_3$. *APL Materials*, 2(8):081510, 2014.

[49] Z. Xiao, C. Bi, Y. Shao, Q. Dong, Q. Wang, Y. Yuan, C. Wang, Y. Gao, and J. Huang. Efficient, high yield perovskite photovoltaic devices grown by inter-

diffusion of solution-processed precursor stacking layers. *Energy & Environmental Science*, 7(8):2619–2623, 2014.

[50] Q. Chen, H. Zhou, Z. Hong, S. Luo, H.-S. Duan, H.-H. Wang, Y. Liu, G. Li, and Y. Yang. Planar heterojunction perovskite solar cells via vapor-assisted solution process. *Journal of the American Chemical Society*, 136(2):622–625, 2014.

[51] S. Dharani, H.K. Mulmudi, N. Yantara, P.T. Thu Trang, N.G. Park, M. Grätzel, S. Mhaisalkar, N. Mathews, and P.P. Boix. High efficiency electrospun TiO_2 nanofiber based hybrid organic-inorganic perovskite solar cell. *Nanoscale*, 6(3):1675–1679, 2014.

[52] L. Hu, J. Peng, W. Wang, Z. Xia, J. Yuan, J. Lu, X. Huang, W. Ma, H. Song, W. Chen, Y.-B. Cheng, and J. Tang. Sequential deposition of $CH_3NH_3PbI_3$ on planar NiO film for efficient planar perovskite solar cells. *ACS Photonics*, 1(7):547–553, 2014.

[53] C.W. Chen, H.W. Kang, S.Y. Hsiao, P.F. Yang, K.M. Chiang, and H.W. Lin. Efficient and uniform planar-type perovskite solar cells by simple sequential vacuum deposition. *Advanced Materials*, 26(38):6647–6652, 2014.

[54] C. Wehrenfennig, G.E. Eperon, M.B. Johnston, H.J. Snaith, and L.M. Herz. High charge carrier mobilities and lifetimes in organolead trihalide perovskites. *Advanced Materials*, 26(10):1584–1589, 2014.

[55] S.D. Stranks, G.E. Eperon, G. Grancini, C. Menelaou, M.J.P. Alcocer, T. Leijtens, L.M. Herz, A. Petrozza, and H.J. Snaith. Electron-hole diffusion lengths exceeding 1 micrometer in an organometal trihalide perovskite absorber. *Science*, 342(6156):341–344, 2013.

[56] J. Gong, S.B. Darling, and F. You. Perovskite photovoltaics: Life-cycle assessment of energy and environmental impacts. *Energy & Environmental Science*, 8(7):1953–1968, 2015.

[57] N. Arora, M.I. Dar, A. Hinderhofer, N. Pellet, F. Schreiber, S.M. Zakeeruddin, and M. Grätzel. Perovskite solar cells with CuSCN hole extraction layers yield stabilized efficiencies greater than 20%. *Science*, 358(6364):768–771, 2017.

[58] G. Grancini, C. Roldan-Carmona, I. Zimmermann, E. Mosconi, X. Lee, D. Martineau, S. Narbey, F. Oswald, F. De Angelis, M. Grätzel, and M.K. Nazeeruddin. One-year stable perovskite solar cells by 2D/3D interface engineering. *Nature Communications*, 8:15684, 2017.

[59] M.D. McGehee. Perovskite solar cells: Continuing to soar. *Nature Materials*, 13(9):845–846, 2014.

[60] H.J. Snaith, A. Abate, J.M. Ball, G.E. Eperon, T. Leijtens, N.K. Noel, S.D. Stranks, J.T.-W. Wang, K. Wojciechowski, and W. Zhang. Anomalous hysteresis in perovskite solar cells. *The Journal of Physical Chemistry Letters*, 5(9):1511–1515, 2014.

[61] H.-W. Chen, N. Sakai, M. Ikegami, and T. Miyasaka. Emergence of hysteresis and transient ferroelectric response in organo-lead halide perovskite solar cells. *The Journal of Physical Chemistry Letters*, 6(1):164–169, 2015.

[62] J. Wei, Y. Zhao, H. Li, G. Li, J. Pan, D. Xu, Q. Zhao, and D. Yu. Hysteresis analysis based on the ferroelectric effect in hybrid perovskite solar cells. *The Journal of Physical Chemistry Letters*, 5(21):3937–3945, 2014.

[63] C. Eames, J.M. Frost, P.R. Barnes, B.C. O'Regan, A. Walsh, and M.S. Islam. Ionic transport in hybrid lead iodide perovskite solar cells. *Nature Communications*, 6(1):7497, 2015.

[64] P. Calado, A.M. Telford, D. Bryant, X. Li, J. Nelson, B.C. ORegan, and P.R.F. Barnes. Evidence for ion migration in hybrid perovskite solar cells with minimal hysteresis. *Nature Communications*, 7:13831, 2016.

[65] S. Meloni, T. Moehl, W. Tress, M. Franckeviius, M. Saliba, Y.H. Lee, P. Gao, M.K. Nazeeruddin, S.M. Zakeeruddin, U. Rothlisberger, and M. Grätzel. Ionic polarization-induced current-voltage hysteresis in $CH_3NH_3PbX_3$ perovskite solar cells. *Nature Communications*, 7:10334, 2016.

[66] C. Li, S. Tscheuschner, F. Paulus, P.E. Hopkinson, J. Kieβling, A. Khler, Y. Vaynzof, and S. Huettner. Iodine migration and its effect on hysteresis in perovskite solar cells. *Advanced Materials*, 28(12):2446–2454, 2016.

[67] E.L. Unger, E.T. Hoke, C.D. Bailie, W.H. Nguyen, A.R. Bowring, T. Heumller, M.G. Christoforo, and M.D. McGehee. Hysteresis and transient behavior in currentvoltage measurements of hybrid-perovskite absorber solar cells. *Energy & Environmental Science*, 7(11):3690–3698, 2014.

[68] C. Zhao, B. Chen, X. Qiao, L. Luan, K. Lu, and B. Hu. Revealing underlying processes involved in light soaking effects and hysteresis phenomena in perovskite solar cells. *Advanced Energy Materials*, 5(14):1500279, 2015.

[69] L.K. Ono, S.R. Raga, S. Wang, Y. Kato, and Y. Qi. Temperature-dependent hysteresis effects in perovskite-based solar cells. *Journal of Materials Chemistry A*, 3(17):9074–9080, 2015.

[70] H.-S. Kim and N.-G. Park. Parameters affecting IV hysteresis of $CH_3NH_3PbI_3$ perovskite solar cells: Effects of perovskite crystal size and mesoporous TiO_2 layer. *The Journal of Physical Chemistry Letters*, 5(17):2927–2934, 2014.

[71] G.A. Sepalage, S. Meyer, A. Pascoe, A.D. Scully, F. Huang, U. Bach, Y.-B. Cheng, and L. Spiccia. Copper(i) iodide as hole-conductor in planar perovskite solar cells: Probing the origin of J-V hysteresis. *Advanced Functional Materials*, 25(35):5650–5661, 2015.

[72] J.A. Christians, J.S. Manser, and P.V. Kamat. Best practices in perovskite solar cell efficiency measurements. Avoiding the error of making bad cells look good. *The Journal of Physical Chemistry Letters*, 6(5):852–857, 2015.

[73] E. Tenuta, C. Zheng, and O. Rubel. Thermodynamic origin of instability in hybrid halide perovskites. *Scientific Reports*, 6:37654, 2016.

[74] G. Niu, W. Li, F. Meng, L. Wang, H. Dong, and Y. Qiu. Study on the stability of $CH_3NH_3PbI_3$ films and the effect of post-modification by aluminum oxide in all-solid-state hybrid solar cells. *Journal of Materials Chemistry A*, 2(3):705–710, 2014.

[75] F. Hao, C.C. Stoumpos, D.H. Cao, R.P.H. Chang, and M.G. Kanatzidis. Lead-free solid-state organicinorganic halide perovskite solar cells. *Nature Photonics*, 8(6):489–494, 2014.

[76] N.K. Noel, S.D. Stranks, A. Abate, C. Wehrenfennig, S. Guarnera, A.-A. Haghighirad, A. Sadhanala, G.E. Eperon, S.K. Pathak, M.B. Johnston, A. Petrozza, L.M. Herz, and H.J. Snaith. Lead-free organicinorganic tin halide perovskites for photovoltaic applications. *Energy & Environmental Science*, 7(9):3061–3068, 2014.

[77] M.M. Tavakoli, S.M. Zakeeruddin, M. Grätzel, and Z. Fan. Large-grain tin-rich perovskite films for efficient solar cells via metal alloying technique. *Advanced Materials*, 30(11):1705998, 2018.

[78] H.L. Zhu, J. Xiao, J. Mao, H. Zhang, Y. Zhao, and W.C.H. Choy. Controllable crystallization of $CH_3NH_3Sn_{0.25}Pb_{0.75}I_3$ perovskites for hysteresisfree solar cells with efficiency reaching 15.2%. *Advanced Functional Materials*, 27(11):1605469, 2017.

[79] Y. Zong, N. Wang, L. Zhang, M.G. Ju, X.C. Zeng, X.W. Sun, Y. Zhou, and N.P. Padture. Homogenous alloys of formamidinium lead triiodide and cesium tin triiodide for efficient idealbandgap perovskite solar cells. *Angewandte Chemie. International Edition in English*, 129(41):12832–12836, 2017.

[80] T. Frecker, D. Bailey, X. Arzeta-Ferrer, J. McBride, and S.J. Rosenthal. Review - Quantum dots and their application in lighting, displays, and biology. *ECS Journal of Solid State Science and Technology*, 5(1):R3019–R3031, 2016.

[81] G.H. Carey, A.L. Abdelhady, Z. Ning, S.M. Thon, O.M. Bakr, and E.H. Sargent. Colloidal quantum dot solar cells. *Chemical reviews*, 115(23):12732–12763, 2015.

[82] L.C. Schmidt, A. Pertegs, S. Gonzlez-Carrero, O. Malinkiewicz, S. Agouram, G. Mnguez Espallargas, H.J. Bolink, R.E. Galian, and J. Prez-Prieto. Nontemplate synthesis of $CH_3NH_3PbBr_3$ perovskite nanoparticles. *Journal of the American Chemical Society*, 136(3):850–853, 2014.

[83] H. Huang, A.S. Susha, S.V. Kershaw, T.F. Hung, and A.L. Rogach. Control of emission color of high quantum yield $CH_3NH_3PbBr_3$ perovskite quantum dots by precipitation temperature. *Advanced Science*, 2(9):1500194, 2015.

[84] F. Zhang, H. Zhong, C. Chen, X. g. Wu, X. Hu, H. Huang, J. Han, B. Zou, and Y. Dong. Brightly luminescent and color-tunable colloidal $CH_3NH_3PbX_3$ (X =

Br, I, Cl) quantum dots: Potential alternatives for display technology. *ACS Nano*, 9(4):4533–4542, 2015.

[85] L. Protesescu, S. Yakunin, M.I. Bodnarchuk, F. Krieg, R. Caputo, C.H. Hendon, R.X. Yang, A. Walsh, and M.V. Kovalenko. Nanocrystals of cesium lead halide perovskites ($CsPbX_3$, X = Cl, Br, and I): Novel optoelectronic materials showing bright emission with wide color gamut. *Nano Letters*, 15(6):3692–3696, 2015.

[86] L. Protesescu, S. Yakunin, M.I. Bodnarchuk, F. Bertolotti, N. Masciocchi, A. Guagliardi, and M.V. Kovalenko. Monodisperse formamidinium lead bromide nanocrystals with bright and stable green photoluminescence. *Journal of the American Chemical Society*, 138(43):14202–14205, 2016.

[87] Y. Hassan, Y. Song, R.D. Pensack, A.I. Abdelrahman, Y. Kobayashi, M.A. Winnik, and G.D. Scholes. Structure-tuned lead halide perovskite nanocrystals. *Advanced Materials*, 28(3):566–573, 2016.

[88] M. Cha, P. Da, J. Wang, W. Wang, Z. Chen, F. Xiu, G. Zheng, and Z.-S. Wang. Enhancing perovskite solar cell performance by interface engineering using $CH_3NH_3PbBr_{0.9}I_{2.1}$ quantum dots. *Journal of the American Chemical Society*, 138(27):8581–8587, 2016.

[89] Q.A. Akkerman, M. Gandini, F. Di Stasio, P. Rastogi, F. Palazon, G. Bertoni, J.M. Ball, M. Prato, A. Petrozza, and L. Manna. Strongly emissive perovskite nanocrystal inks for high-voltage solar cells. *Nature Energy*, 2(2):16194, 2016.

[90] A. Swarnkar, A.R. Marshall, E.M. Sanehira, B.D. Chernomordik, D.T. Moore, J.A. Christians, T. Chakrabarti, and J.M. Luther. Quantum dotinduced phase stabilization of α-$CsPbI_3$ perovskite for high-efficiency photovoltaics. *Science*, 354(6308):92–95, 2016.

[91] N.R.E.L. (NREL). NREL efficiency chart. `https://www.nrel.gov/pv/assets/images/efficiency-chart.png`, 2017. Online; Accessed 21 April 2018.

[92] D.-C. Nguyen, S. Ito, K. Fukatsu, and K. Tanimoto. Making nanoparticle ink for compound solar cells. *SPIE, January. http://spie. org*, 2013.

[93] D.V. Talapin, A.L. Rogach, A. Kornowski, M. Haase, and H. Weller. Highly luminescent monodisperse cdse and cdse/zns nanocrystals synthesized in a hexadecylaminetrioctylphosphine oxidetrioctylphospine mixture. *Nano Letters*, 1(4):207–211, 2001.

[94] J. Zhang, R.W. Crisp, J. Gao, D.M. Kroupa, M.C. Beard, and J.M. Luther. Synthetic conditions for high-accuracy size control of pbs quantum dots. *The Journal of Physical Chemistry Letters*, 6(10):1830–1833, 2015.

[95] M.A. Hines and G.D. Scholes. Colloidal pbs nanocrystals with sizetunable near-infrared emission: Observation of postsynthesis selfnarrowing of the particle size distribution. *Advanced Materials*, 15(21):1844–1849, 2003.

[96] Q. Tian, K. Tao, W. Li, and K. Sun. Hot-injection approach for two-stage formed hexagonal nayf4:Yb,er nanocrystals. *The Journal of Physical Chemistry C*, 115(46):22886–22892, 2011.

[97] G. Li, H. Wang, T. Zhang, L. Mi, Y. Zhang, Z. Zhang, W. Zhang, and Y. Jiang. Solvent-polarity-engineered controllable synthesis of highly fluorescent cesium lead halide perovskite quantum dots and their use in white light-emitting diodes. *Advanced Functional Materials*, 26(46):8478–8486, 2016.

[98] J. Song, L. Xu, J. Li, J. Xue, Y. Dong, X. Li, and H. Zeng. Monolayer and fewlayer allinorganic perovskites as a new family of twodimensional semiconductors for printable optoelectronic devices. *Advanced Materials*, 28(24):4861–4869, 2016.

[99] X. He, Y. Qiu, and S. Yang. Fully-inorganic trihalide perovskite nanocrystals: A new research frontier of optoelectronic materials. *Advanced Materials*, 29(32):1700775, 2017.

[100] J. van Embden, A.S.R. Chesman, and J.J. Jasieniak. The heat-up synthesis of colloidal nanocrystals. *Chemistry of Materials*, 27(7):2246–2285, 2015.

[101] S. Sun, D. Yuan, Y. Xu, A. Wang, and Z. Deng. Ligand-mediated synthesis of shape-controlled cesium lead halide perovskite nanocrystals via reprecipitation process at room temperature. *ACS Nano*, 10(3):3648–3657, 2016.

[102] I. Levchuk, A. Osvet, X. Tang, M. Brandl, J.D. Perea, F. Hoegl, G.J. Matt, R. Hock, M. Batentschuk, and C.J. Brabec. Brightly luminescent and color-tunable formamidinium lead halide perovskite $FAPbX_3$ (x = Cl, Br, I) colloidal nanocrystals. *Nano Letters*, 17(5):2765–2770, 2017.

[103] I. Lignos, S. Stavrakis, G. Nedelcu, L. Protesescu, A.J. deMello, and M.V. Kovalenko. Synthesis of cesium lead halide perovskite nanocrystals in a droplet-based microfluidic platform: Fast parametric space mapping. *Nano Letters*, 16(3):1869–1877, 2016.

[104] M.B. Plutschack, B. Pieber, K. Gilmore, and P.H. Seeberger. The hitchhikers guide to flow chemistry. *Chemical reviews*, 117(18):11796–11893, 2017.

[105] R.L. Hartman, J.P. McMullen, and K.F. Jensen. Deciding whether to go with the flow: Evaluating the merits of flow reactors for synthesis. *Angewandte Chemie International Edition*, 50(33):7502–7519, 2011.

[106] J. Wegner, S. Ceylan, and A. Kirschning. Ten key issues in modern flow chemistry. *Chemical Communications*, 47(16):4583–4592, 2011.

[107] K.S. Elvira, X.C. i Solvas, R.C.R. Wootton, and A.J. deMello. The past, present and potential for microfluidic reactor technology in chemical synthesis. *Nature Chemistry*, 5(11):905–915, 2013.

[108] B.K.H. Yen, N.E. Stott, K.F. Jensen, and M.G. Bawendi. A continuousflow microcapillary reactor for the preparation of a size series of cdse nanocrystals. *Advanced Materials*, 15(21):1858–1862, 2003.

[109] E.M. Chan, R.A. Mathies, and A.P. Alivisatos. Size-controlled growth of cdse nanocrystals in microfluidic reactors. *Nano Letters*, 3(2):199–201, 2003.

[110] M. Movsisyan, E.I.P. Delbeke, J.K.E.T. Berton, C. Battilocchio, S.V. Ley, and C.V. Stevens. Taming hazardous chemistry by continuous flow technology. *Chemical Society Reviews*, 45(18):4892–4928, 2016.

[111] R.M. Maceiczyk, K. Dumbgen, I. Lignos, L. Protesescu, M.V. Kovalenko, and A.J. deMello. Microfluidic reactors provide preparative and mechanistic insights into

the synthesis of formamidinium lead halide perovskite nanocrystals. *Chemistry of Materials*, 29(19):8433–8439, 2017.

[112] D.E. Fitzpatrick, C. Battilocchio, and S.V. Ley. A novel internet-based reaction monitoring, control and autonomous self-optimization platform for chemical synthesis. *Organic Process Research & Development*, 20(2):386–394, 2016.

[113] Y. Song, J. Hormes, and C.S. Kumar. Microfluidic synthesis of nanomaterials. *Small*, 4(6):698–711, 2008.

[114] K.-J. Wu, G.M. De Varine Bohan, and L. Torrente-Murciano. Synthesis of narrow sized silver nanoparticles in the absence of capping ligands in helical microreactors. *Reaction Chemistry & Engineering*, 2(2):116–128, 2017.

[115] E.Y. Erdem, J.C. Cheng, F.M. Doyle, and A.P. Pisano. Multi-temperature zone, droplet-based microreactor for increased temperature control in nanoparticle synthesis. *Small*, 10(6):1076–1080, 2014.

[116] Y. Roig, S. Marre, T. Cardinal, and C. Aymonier. Synthesis of exciton luminescent ZnO nanocrystals using continuous supercritical microfluidics. *Angewandte Chemie International Edition*, 50(50):12071–12074, 2011.

[117] S. Marre, J. Park, J. Rempel, J. Guan, M.G. Bawendi, and K.F. Jensen. Supercritical continuous-microflow synthesis of narrow size distribution quantum dots. *Advanced Materials*, 20(24):4830–4834, 2008.

[118] B.H. Kwon, K.G. Lee, T.J. Park, H. Kim, T.J. Lee, S.J. Lee, and D.Y. Jeon. Continuous in situ synthesis of ZnSe/ZnS core/shell quantum dots in a microfluidic reaction system and its application for light-emitting diodes. *Small*, 8(21):3257–3262, 2012.

[119] I. Lignos, L. Protesescu, D.B. Emiroglu, R. Maceiczyk, S. Schneider, M.V. Kovalenko, and A.J. deMello. Unveiling the shape evolution and halide-ion-segregation in blue-emitting formamidinium lead halide perovskite nanocrystals using an automated microfluidic platform. *Nano Letters*, 18(2):1246–1252, 2018.

Chapter 2

Theory

In this chapter, the main theories used in this thesis are introduced, including the basic theories of the working principle of a solar cell, from the primary principles of semiconductors to the processes of charge generation, charge separation and charge recombination. The theories behind some important characterisation techniques such as the Mott-Schottky test and the impedance spectroscopy are also included, to assist the understanding towards the results of the work.

2.1 Semiconductor

Semiconductors are materials with electronic conductivity that lies between conductors and insulators. According to band theory, the valence band (VB) is the allowed energy band where all of the valence electrons reside, while the conduction band (CB) is the energy band with higher energy in which electrons can move freely in the material. The VB and CB are separated by a forbidden region and the energy difference between them is called the band-gap. Electrons in a full VB are unable to move and cannot contribute to conduction unless they absorb enough energy to overcome the band-gap and are excited into CB. For conductors, the VB and CB touch or overlap, so the electrons can move easily, but in insulators, the band-gap is so wide that the excitation of electron is normally not possible, as seen in **Fig. 2.1**, while semiconductors have small band-gap so that excitation of carriers across the band-gap is possible.

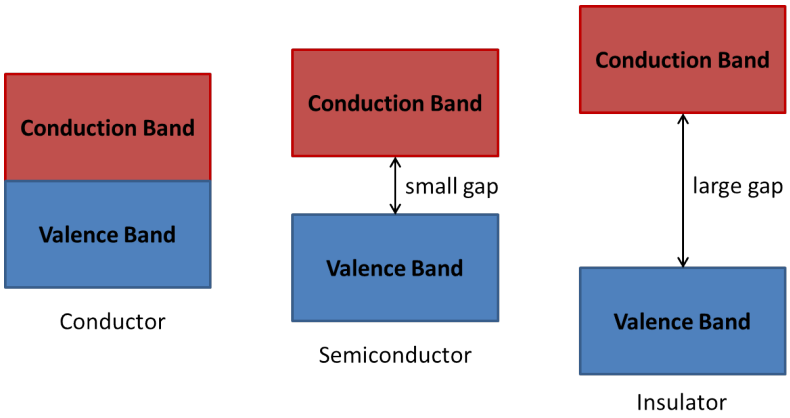

Fig. 2.1 Valence and conduction bands in conductor, semiconductor and insulator.

According to the type of majority charge carrier, semiconductors can be classified into n-type, p-type and intrinsic semiconductors. An intrinsic semiconductor is a pure semiconductor without any significant dopant species present. The charge carriers in intrinsic semiconductors are electrons that have been excited into the CB and holes which remain in the VB, and the number of electrons and holes are equal. When an intrinsic semiconductor is doped with donor impurities (e.g. nitrogen in silicon) or acceptor impurities (e.g. boron in silicon), an n-type or p-type semiconductor is formed. In n-type semiconductors, due to the existence of donor states, the electrons have a higher concentration than holes, and serve as majority charge carrier and minority charge carrier, respectively. In p-type semiconductors the situation is the opposite, in which holes are majority and electrons are minority charge carriers.

2.1.1 Fermi level

The probability of an electron occupying an energy level with energy E is given by the Fermi-Dirac distribution function:

$$f(E) = \frac{1}{1 + \exp((E - E_F)/(k_B T))} \tag{2.1}$$

where k_B is Boltzmann's constant, T is the temperature, and E_F is called the Fermi energy or Fermi level which is the energy level where the probability of occupancy by an electron

is exactly 50%, i.e.

$$f(E_F) = \frac{1}{2} \tag{2.2}$$

When $E >> E_F$, equation 2.1 can be simplified to the Boltzmann approximation.

$$f(E) = \exp\Big(- \frac{E - E_F}{k_B T} \Big) \tag{2.3}$$

In an intrinsic semiconductor, the Fermi level lies in the middle of the band-gap, as shown in **Fig.2.2**. But in an n-type semiconductor, there are more electrons in the conduction band than holes in the valence band, which means the probability of finding an electron near the conduction band edge is larger than the probability of finding a hole at the valence band edge, therefore the Fermi level is closer to the conduction band. Contrarily, for a p-type semiconductor, as the number of holes in the valence band is higher than that of electrons in conduction band, the probability of finding an electron near the conduction band edge is smaller than the probability of finding a hole at the valence band edge, and the Fermi level is closer to the valence band.

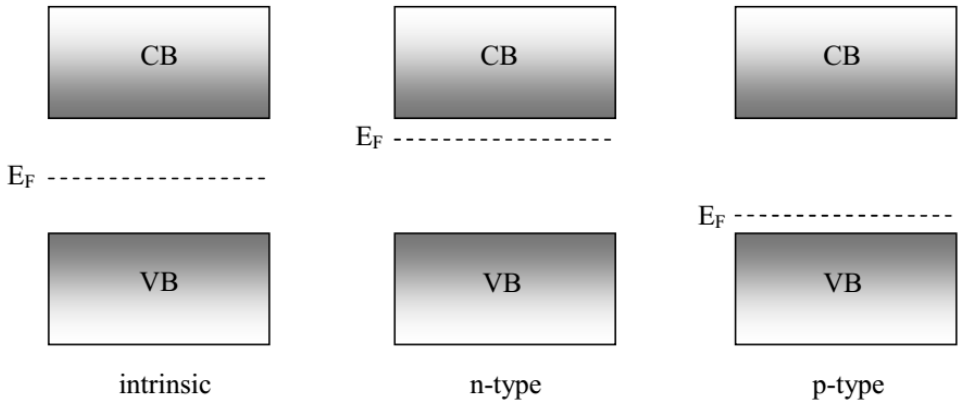

Fig. 2.2 Energy levels of intrinsic, n-type and p-type semiconductors.

2.1.2 Equilibrium carrier concentration

In intrinsic semiconductors in darkness, as electrons in conduction bands and holes in valence bands are always created in pairs, the concentrations of electrons n_0 and holes p_0

are the same and are called the intrinsic carrier concentration, denoted as n_i.

$$n_0 = p_0 = n_i \tag{2.4}$$

The intrinsic carrier concentration is material dependent and is ralated to the band-gap of the material and temperature. Silicon for instance, the intrinsic carrier concentration is described by Misiakos as a function of temperature T[1,2]:

$$n_i(T) = 5.29 \times 10^{19}(T/300)^{2.54}\exp(-6726/T) \tag{2.5}$$

For n-type or p-type semiconductors, as the concentration of the dopant introduced is normally much higher than the intrinsic carrier concentration, the concentration of majority charge carriers approximately equals to the concentration of the donor N_D or acceptor N_A, assuming the dopants are fully ionised. And according to the law of mass action, at equilibrium,

$$n_0 p_0 = n_i^2 \tag{2.6}$$

Therefore, the equilibrium carrier concentrations are expressed as:
For n-type,

$$n_0 = N_D, \quad p_0 = \frac{n_i^2}{N_D} \tag{2.7}$$

For p-type,

$$p_0 = N_A, \quad n_0 = \frac{n_i^2}{N_A} \tag{2.8}$$

2.2 Photovoltaic effect

When a semiconductor is exposed to light of certain wavelengths, electrons in the valence band can absorb the energy of the photons and get excited into the conduction band, leaving holes in the valence band. When the electrons and the holes are separated, e.g. by a p-n junction, a voltage can be measured in the external circuit. This phenomenon is called photovoltaic effect, which is the basis of a solar cell.

2.2.1 Charge generation

In photovoltaics, the most important charge generation process is photogeneration which means charge generation through light absorption. The light absorption of a semiconductor depends on the band-gap of the semiconductor material and the wavelength of the light, i.e. only the photons with energy equal to or higher than the band-gap can be absorbed. Photons with energy the same as the band-gap of the semiconductor can be absorbed and excite electrons from the valence band edge into exactly the edge of the conduction band. Photons with energy higher than the band-gap of the semiconductor can also be absorbed and generate charge carriers with higher kinetic energy. But the carriers quickly lose the extra energy, usually by thermalisation through interacting with the lattice and eventually relax to the band edge, producing a phonon[3]. Semiconductor materials have an onset in their absorption spectra, as shown in the absorption profile of $CH_3NH_3PbI_3$ perovskite in **Fig. 2.3**, since light with less energy than the band-gap cannot be absorbed.

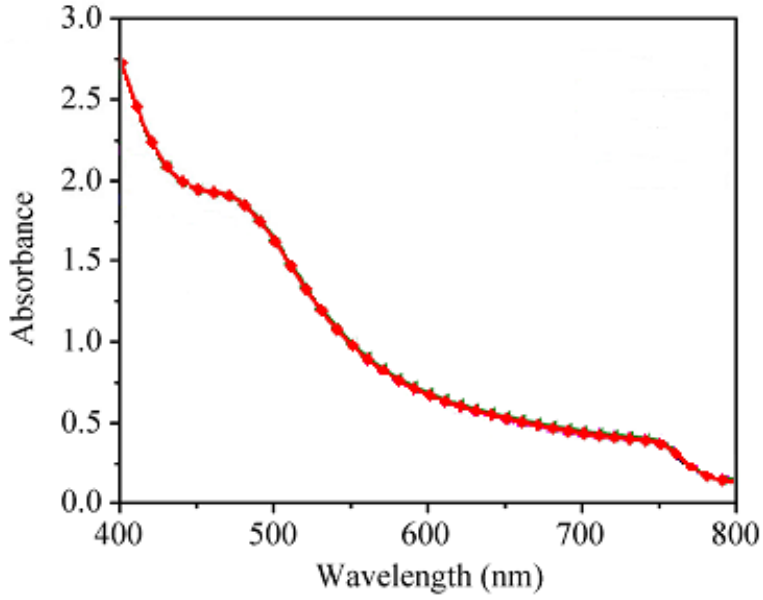

Fig. 2.3 Absorption spectra of a $CH_3NH_3PbI_3$ perovskite film[4].

The absorbing ability of a material towards light is defined by the absorption coefficient, which is related to the absorption depth (the penetration distance needed for a certain of absorption). The absorption coefficient is dependent on the energy of the photon, and

their relations are different for direct semiconductors and indirect semiconductors. During the band transition following light absorption, in addition to the requirement about the photon energy, momentum must also be conserved. For direct band gap semiconductors, the minimal energy state in the conduction band and the maximal energy state in the valence band have the same crystal momentum (k-vector), therefore, the band transition can happen directly, as shown in **Fig. 2.4**a. The absorption rate is high and the absorption coefficient α is proportional to the square root of the difference between the photon energy and the band gap[5].

$$\alpha = A(h\nu - E_g)^{1/2} \tag{2.9}$$

where A is a constant depending on the material, and ν is the frequency of the photon. While for indirect band gap semiconductors, the k-vectors of the valence band maxima and conduction band minima are different, so the band transition is not possible due to the conservation of momentum unless the momentum is changed by interacting with the lattice. Thus, the absorption or emission of a phonon must also be involved, which makes the process less likely to happen. The absorption coefficient α is proportional to the square of the difference between the photon energy and the band gap[5].

$$\alpha \propto \frac{(h\nu + E_p - E_g)^2}{\exp(E_p/k_BT) - 1} + \frac{(h\nu - E_p - E_g)^2}{1 - \exp(-E_p/k_BT)} \propto (h\nu - E_g)^2 \quad \text{when } h\nu - E_g \gg E_P \tag{2.10}$$

where E_p is the energy of the phonon.

Compared with direct band gap semiconductors, the absorption coefficient is normally smaller in indirect band gap semiconductors, so a thicker film is generally needed if an indirect band gap semiconductor is used for photovoltaic applications to achieve sufficient light absorption. Therefore, direct semiconductors are more preferable for thin film solar cells.

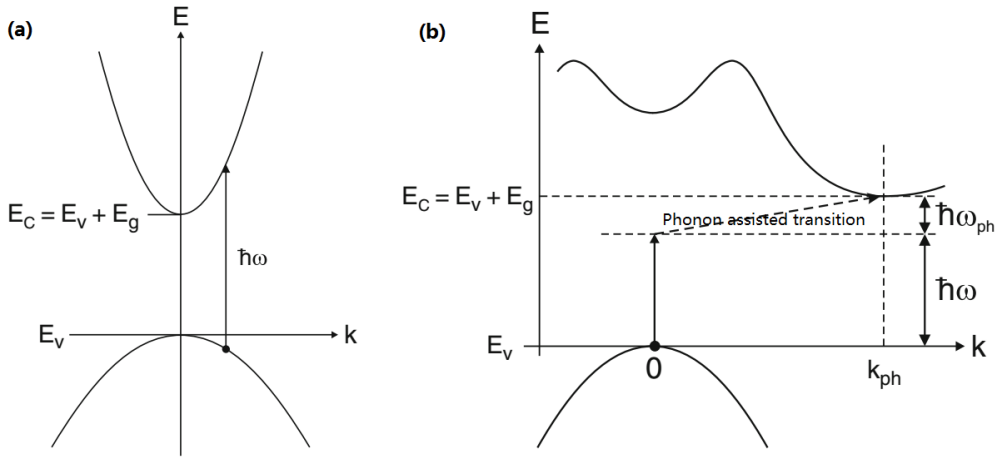

Fig. 2.4 Electron transitions during light absorption in (a) direct and (b) indirect band gap semiconductors.[6]

2.2.2 Charge separation

Charge separation in photovoltaics is normally carried out using a p-n junction. A p-n junction is formed when a p-type semiconductor and an n-type semiconductor join together. Due to the higher electron concentration in the n-type material and the higher hole concentration in the p-type material, electrons diffuse from the n-side to the p-side, and holes diffuse from the p-type side to the n-type side, as shown in **Fig. 2.5**a, creating a diffusion current I_{dif}. As a result of this diffusion, the p-side of the junction becomes negatively charged and the n-side is positively charged, forming a 'built-in' voltage. The built-in voltage will cause the holes in the n-side to move towards the p-side and electrons from the p-side to the n-side, achieving charge separation and a drift current I_{dr}. Any charge carriers present are quickly wiped away, so the region is called a depletion region. At equilibrium, the diffusion current and drift current are the same magnitude in opposite directions, and equal dark saturation current I_0, as shown in **Fig. 2.5**b.

$$I_{dif} = I_{dr} = I_0 \tag{2.11}$$

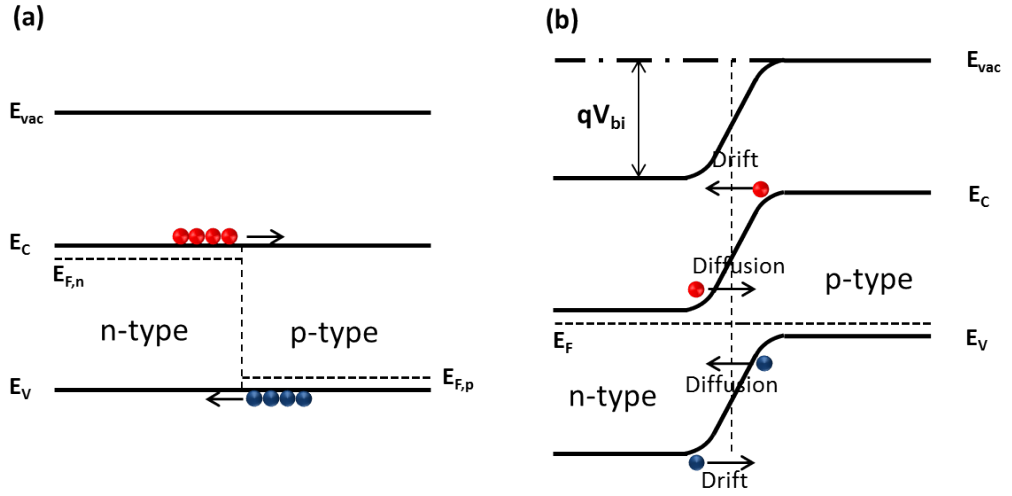

Fig. 2.5 Energy band diagrams of a P-N junction under no bias in the dark: (a) at the first contact; (b) at equilibrium.

When an external bias is applied across the p-n junction, the Fermi levels in p- and n-sides are split, as shown in **Fig. 2.6**. The external bias changes the diffusion barrier of charge carriers across the junction and changes the diffusion current I_{dif}. On the other hand, the drift current I_{dr} stays essentially the same since it depends on the number of minority carriers generated near or within the depletion region which is relatively not changed by the external bias[2]. As a result, the equilibrium between diffusion current and drift current shown in equation 2.11 is broken, and a net dark current I_d forms, which is expressed as the diode equation:

$$I_d = I_0(e^{\frac{qV}{nk_BT}} - 1) \tag{2.12}$$

, where V is the bias voltage applied across the junction, q is the absolute charge value of an electron, k_B is the Boltzmann's constant, T is the temperature, and n is ideality factor which serves as a measure of how close a diode is to an ideal diode.

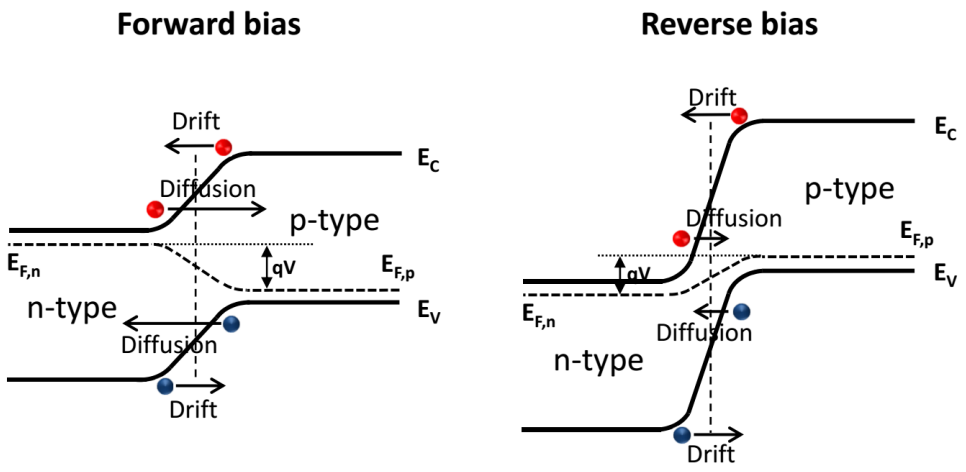

Fig. 2.6 Energy band diagrams of a P-N junction under forward and reverse bias in the dark.

Under illumination, the p- and n- semiconductors absorbs the energy of photons and generate charge carrier pairs, and the Fermi levels for electrons and holes are split. The photogenerated minority charge carriers (holes in the n-type semiconductor and electrons in the p-type semiconductor) reaching the P-N junction are swept across the junction by the electric field in the junction and become majority carriers on the other side, forming a photocurrent I_L which is in the opposite direction to the dark current I_d. In this way, the photo-generated carriers are spatially separated by the P-N junction, preventing their recombination. The overall current is given as

$$I = I_L - I_d = I_L - I_0\left(e^{\frac{qV}{nk_BT}} - 1\right) \tag{2.13}$$

Therefore, by scanning the bias voltage and measuring the current, an I-V curve can be obtained, as illustrated in **Fig. 2.7**, which is the normal way of testing the performance of a solar cells device. From the I-V curve, the short circuit current (I_{SC}, the current at $V = 0$), the open circuit voltage (V_{OC}, the bias voltage where $I = 0$) and the fill factor (FF, the ratio of the maximum power P_{max} to the product of I_{SC} and V_{OC}) can be determined, and the power conversion efficiency PCE is given as

$$PCE(\%) = \frac{P_{\text{max}}}{P_{\text{in}}} = \frac{V_{\text{mp}}I_{\text{mp}}}{P_{\text{in}}} = \frac{V_{\text{OC}}I_{\text{SC}}FF}{P_{\text{in}}} \tag{2.14}$$

where P_{in} is the incident power, V_{mp} and I_{mp} are the bias voltage and current at the maxi-

mum power point respectively.

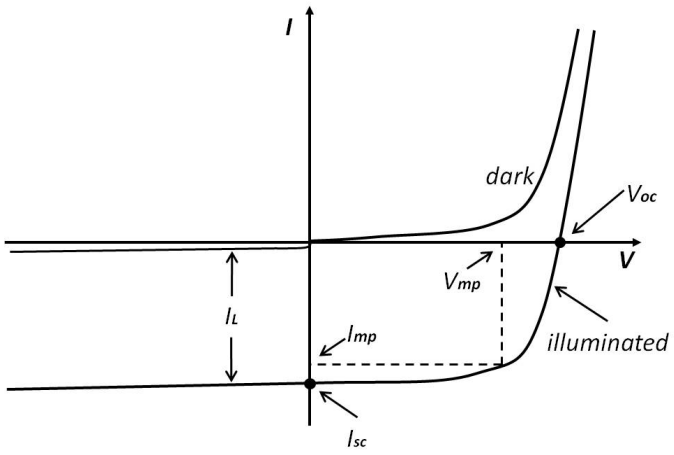

Fig. 2.7 I-V curves of a typical solar cell under dark and illumination[7].

2.3 Recombination

After being excited into conduction bands, the electrons can also jump back into valence bands and combine with holes, releasing energy. The recombination is the reverse process of excitation, and leads to the elimination of charge carriers. According to the mechanisms, there are three types of recombinations.

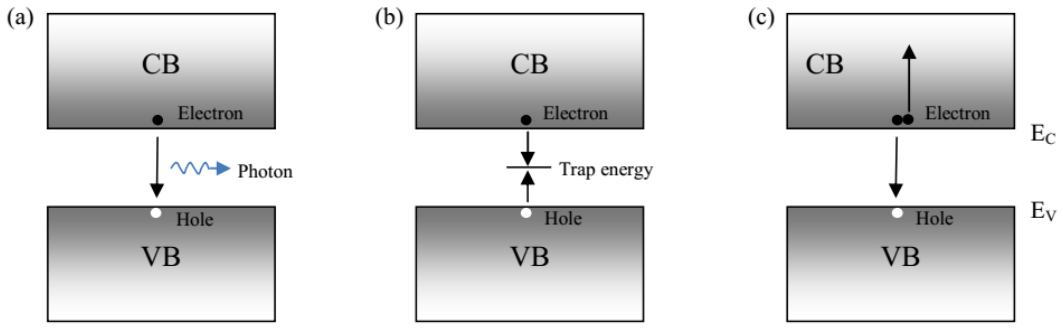

Fig. 2.8 Schematic diagram of (a) radiative, (b) SRH and (c) auger recombinations.

2.3.1 Radiative recombination

Radiative recombination is the reverse process of the light absorption, which is the recombination of an electron from the conduction band directly with a hole at the valence band, releasing a photon, as shown in **Fig. 2.8**a. Since the energy of the photon is close to the band-gap of the material, it can only be weakly absorbed and is emitted out of the material. Radiative recombination normally occurs in direct band-gap semiconductors and is the basis of LEDs.

2.3.2 Shockley-Read-Hall recombination

Shockley-Read-Hall (SRH) recombination, also called trap-assisted recombination, is a recombination process which involves two steps. Recombination occurs via defects in the crystal lattices, as shown in **Fig.2.8**b. Firstly, an electron (or a hole) is trapped at an energy level within the forbidden region which is caused by dopants or defects in the crystal lattice. The trapped carrier can again be released by thermal activation. Otherwise, if the defect traps another opposite charge carrier before releasing the first trapped charge carrier, the two carriers recombine. As the concentration of defects are high at the surface or grain boundaries due to the disruption of crystal lattices, the SRH recombination is more profound at these areas, and is generally important in photovoltaic applications.

2.3.3 Auger Recombination

Auger recombination is a recombination process in which three charge carriers are involved. An electron in the conduction band recombines with a hole in the valence band, but instead of emitting a photon, the energy is given to a another electron in the conduction band. This excites the electron into a higher energy level in the conduction band, as shown in **Fig.2.8**c. Eventually the electron relaxes back to the valance band edge and thermally releases its excess energy. Due to the involvement of three charge carriers, auger recombination is an important recombination process only where carrier densities are very high, such as in highly doped materials, at high temperature or under strong illumination.

In solar cell applications, recombination should be prevented as much as possible so that more carriers can be collected by the electrodes and more electricity can be obtained. Two important parameters relating to recombination rates are carrier lifetime and diffusion length.

The lifetime of an electron or hole in a given material, denoted by τ_n or τ_p, is the average time which a minority carrier can exist before it recombines. The carrier lifetime takes into account all different types of recombinations.

$$\frac{1}{\tau} = \frac{1}{\tau_{Rad}} + \frac{1}{\tau_{SRH}} + \frac{1}{\tau_{Aug}} \tag{2.15}$$

Carrier diffusion length L is the average distance a carrier can move before it recombines. It depends on the carrier lifetime τ and the diffusivity D through the equation

$$L_n = \sqrt{D_n \tau_n} \text{ for electrons}, \quad \mathrm{L_p} = \sqrt{D_p \tau_p} \text{ for holes} \tag{2.16}$$

The diffusion length is closely related to the probability of a carrier being collected by the electrode in solar cells. With higher diffusion length, carriers can move longer distance before recombination and thus are more likely to be collected and contribute to the photocurrent. In solar cell architectures, the thickness of active layer is normally smaller than or similar to the carrier diffusion length, such that the charge carriers can be collected effectively.

2.4 Mott-Schottky relationship

When a semiconductor contacts with an electrolyte, charges also transfer in a similar way as in a p-n junction, forming a semiconductor-electrolyte junction. Due to differences between the redox potential of the electrolyte ($E_{F,redox}$) and the Fermi level of the semiconductor (E_F), charge flows between the electrolyte and the semiconductor. As a result, the energy bands bend in the semiconductor at the interface until equilibrium is reached ($E_F = E_{F,redox}$ when no external potential is applied), leaving a space charge region in the semiconductor side[8,9]. The net charge is compensated by the opposite ionic charge in

the electrolyte side. According to the direction of the charge transfer, the space charge region can be a depletion region or an accumulation region. As shown in **Fig.2.9**, for the case of an n-type semiconductor, if the redox potential of the electrolyte is lower than the Fermi level of the semiconductor before contact ($E_{F,redox} < E_F$), electrons flow from the semiconductor to the electrolyte, leaving a space charge region positively charged. As the majority charge carriers are depleted, the space charge region is called a depletion region. In contrast, if the redox potential of the electrolyte is higher than the Fermi level of the semiconductor before contact ($E_{F,redox} > E_F$), electrons flow from the solution to the semiconductor, making the majority carrier density at the surface larger than in the bulk of the semiconductor, and the space charge region is called an accumulation region.

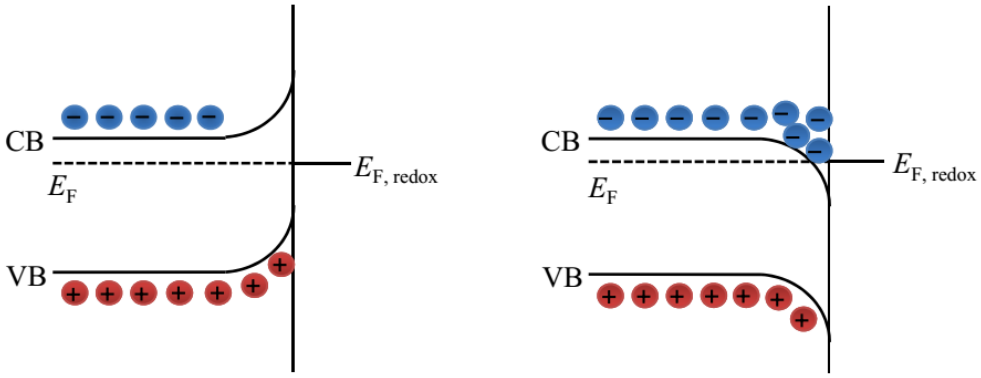

Fig. 2.9 Types of space charge regions in n-type semiconductors. a) Depletion layer. b) Accumulation layer.

The degree of band bending can also be changed by applying an external bias. At a specific applied bias, there is no excess charge on the semiconductor side of the junction. At this potential, which is denoted as the flat-band potential V_{FB}, no band bending occurs. If the potential is made more positive than V_{FB}, electrons are withdrawn from the semiconductor, leaving a positive depletion region. The distribution of charge, electric field, potential and band energy are as shown in **Fig.2.10**.

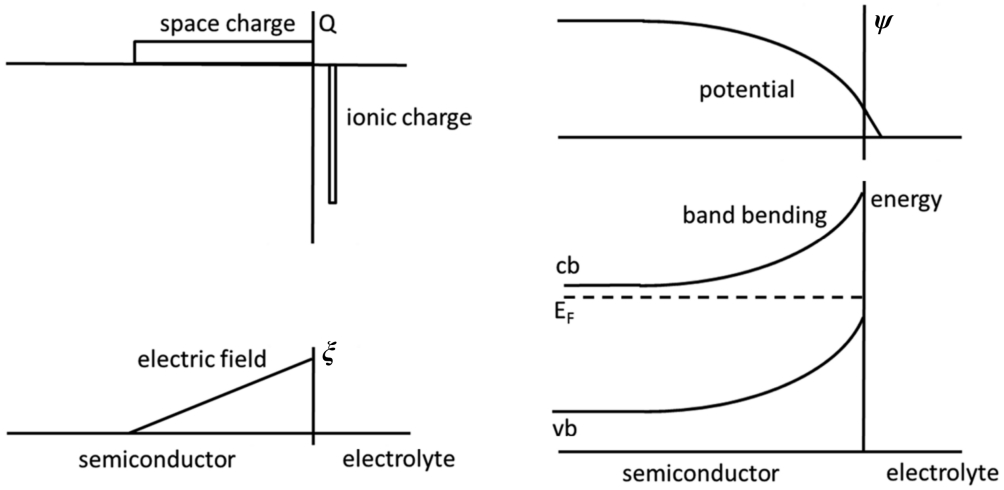

Fig. 2.10 Distribution of charge (Q), electric field (ξ), potential (ψ) and band energy across the n-type semiconductor-electrolyte junction[8].

Under the assumption of being only distance dependent in the x direction, the potential distribution in the space charge region is described according to the Poisson's law in one dimension as

$$\frac{\mathrm{d}^2\psi(x)}{\mathrm{d}x^2} = -\frac{\sigma(x)}{\varepsilon\varepsilon_0} \tag{2.17}$$

where $\psi(x)$ is the potential at x, $\sigma(x)$ is the charge density, ε is the relative permittivity of the material and ε_0 is the vacuum permittivity.

Using the abrupt approximation that all the electrons in the space charge region ($0 \leq x \leq W_{SC}$, where W_{SC} is the width of the space charge region) are depleted, $\sigma(x)$ is given by the doping density N_d, i.e.

$$\frac{\mathrm{d}^2\psi(x)}{\mathrm{d}x^2} = -\frac{\sigma(x)}{\varepsilon\varepsilon_0} = -\frac{qN_d}{\varepsilon\varepsilon_0} \tag{2.18}$$

If 2.18 is integrated, with boundary conditions that when $x = W_{SC}$, the electric field $\xi(x) = \mathrm{d}\psi(x)/\mathrm{d}x = 0$ and $\psi(x) = \phi_b$, then

$$\psi(x) = \frac{qN_d}{\varepsilon\varepsilon_0}\left(W_{SC}x - \frac{1}{2}x^2 - \frac{1}{2}W_{SC}^2\right) + \phi_b \tag{2.19}$$

in which ϕ_b is the potential in the bulk of the semiconductor and q is the elementary charge. At the semiconductor surface, $\psi(x = 0) = \phi_b - \Delta\phi_{SC}$, therefore,

$$W_{SC} = \left(\frac{2\varepsilon\varepsilon_0\Delta\phi_{SC}}{qN_d}\right)^{1/2} \tag{2.20}$$

where $\Delta\phi_{SC}$ is the potential drop across the space charge region and $\Delta\phi_{SC} = V_{applied} - V_{\mathrm{FB}}$. The total charge of the space charge region Q_{SC} is given as

$$Q_{SC} = qN_dAW_{SC} \tag{2.21}$$

where A is the area of the semiconductor electrode, and the differential capacitance of the space charge region C_{SC} is

$$C_{SC} = \frac{\mathrm{d}Q_{SC}}{\mathrm{d}\Delta\phi_{SC}} \tag{2.22}$$

Substituting equation 2.20 and 2.21 into equation 2.22 gives the Mott-Schottky relationship as equation 2.23

$$C_{SC}^{-2} = \frac{2\Delta\phi_{SC}}{qN_dA^2\varepsilon\varepsilon_0} = \frac{2}{qN_dA^2\varepsilon\varepsilon_0}\left(V_{applied} - V_{\mathrm{FB}}\right) \tag{2.23}$$

In a more accurate approach, the thermal distribution of electrons n_e is taken into account, the charge density in the space charge region is given as

$$\sigma(x) = q[N_d - n_e(x)] \tag{2.24}$$

According to equation 2.3,

$$n_e(x) = n_e^0 \exp\left[\frac{q}{k_BT}\left(\psi(x) - \phi_b\right)\right] \tag{2.25}$$

where n_e^0 is the electron concentration in the bulk of the semiconductor, and for n-type semiconductors $n_e^0 \approx N_d$.

Substituting equations 2.24 and 2.25 into equation 2.17 gives

$$\frac{\mathrm{d}^2\psi(x)}{\mathrm{d}x^2} = \frac{qN_d}{\varepsilon\varepsilon_0}\left\{\exp\left[\frac{q}{k_BT}\left(\psi(x) - \phi_b\right)\right] - 1\right\} \tag{2.26}$$

Using the transformation

$$\frac{\mathrm{d}^2\psi(x)}{\mathrm{d}x^2} = \frac{\mathrm{d}\psi}{\mathrm{d}x}\frac{\mathrm{d}\psi/\ \mathrm{d}x}{\mathrm{d}\psi} \tag{2.27}$$

and integrating equation 2.26, the electric field in the space charge region can be derived

as

$$\xi(x) = \frac{\mathrm{d}\psi(x)}{\mathrm{d}x} = \left(\frac{2qN_d}{\varepsilon\varepsilon_0}\right)^{1/2} \left\{\frac{k_BT}{q}\exp\left[\frac{q}{k_BT}\left(\psi(x) - \phi_b\right)\right] - \left(\psi(x) - \phi_b\right) - \frac{k_BT}{q}\right\}^{1/2} \tag{2.28}$$

According to Gauss' law,

$$Q_{SC} = \varepsilon\varepsilon_0 A\xi(x = 0) \tag{2.29}$$

Thus

$$Q_{SC} = \left(2\varepsilon\varepsilon_0 A^2 qN_d\right)^{1/2} \left[\frac{k_BT}{q}\exp\left(\frac{-q}{k_BT}\Delta\phi_{SC}\right) + \Delta\phi_{SC} - \frac{k_BT}{q}\right]^{1/2} \tag{2.30}$$

For depletion layer $-q\Delta\phi_{SC}/k_BT < -1$, therefore neglecting the exponential term gives

$$Q_{SC} = \left(2\varepsilon\varepsilon_0 A^2 qN_d\right)^{1/2} \left(\Delta\phi_{SC} - \frac{k_BT}{q}\right)^{1/2} \tag{2.31}$$

Substituting equation 2.31 into equation 2.22 gives the Mott-Schottky relationship with an extra term k_BT/q

$$C_{SC}^{-2} = \frac{2}{qN_dA^2\varepsilon\varepsilon_0}\left(\Delta\phi_{SC} - \frac{k_BT}{q}\right) = \frac{2}{qN_dA^2\varepsilon\varepsilon_0}\left(V_{applied} - V_{\mathrm{FB}} - \frac{k_BT}{q}\right) \tag{2.32}$$

From the Mott-Schottky relationship, the plot of C_{SC}^{-2} according to the applied potential $V_{applied}$ is linear. The Mott-Schottky plot can be made by carrying out impedance measurements on the semiconductor electrode immersed in the electrolyte at different applied potentials. The slope of the plot gives the doping density of the semiconductor N_d, and the flat band potential V_{FB} can be obtained from the intercept on the x axis.

2.5 Photoluminescence

Photoluminescence (PL) is an embodiment of radiative recombination, and is the reverse process of absorption, in which photon-excited electrons and holes in semiconductors recombine and emit light.

There are various mechanisms involved in radiative recombination processes, and the band to band transition is one of the most important. After excitation, electrons are excited from valence bands to conduction bands. The energy of the excitation photons may be higher than the band gap and the electrons are excited into higher energy levels than the conduction band edge. These carriers with higher kinetic energy then quickly relax to the band edge by releasing phonons to cool down. The electrons at the conduction band edge can return to the valence band and recombine with holes at the valence band edge, releasing photons.

In direct band gap semiconductors, the k-vectors of the valence band maxima and conduction band minima are the same, as shown in **Fig. 2.11**, and the transition can happen directly. Only an electron and a hole are involved in the recombination process, so the rate is high, which results in a high radiative efficiency. The energy of the photons emitted is

$$\hbar\omega = E_C - E_V = E_g \tag{2.33}$$

where $\hbar$ is the Dirac constant, ω is the angular frequency of the photon.

While in indirect band gap semiconductors, the k-vectors of the valence band maxima and conduction band minima are different, and a direct transition is not possible due to conservation of momentum. For the transition to occur in an indirect band gap material, the absorption or emission of a phonon must also be involved, which makes the process less likely to happen. Thus the emission intensities of indirect band gap semiconductors are normally low. This is the reason why direct band gap semiconductors are more favourable in light emitting and lasing applications. The energy of the photons emitted for indirect band gap semiconductors is

$$\hbar\omega = E_C - E_V \pm E_p \tag{2.34}$$

where E_P is the energy of the phonon.

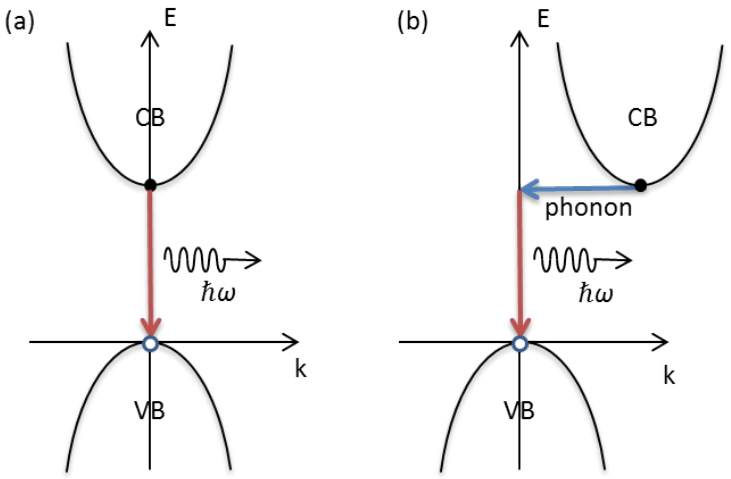

Fig. 2.11 Electron transitions during band to band recombination in (a) direct and (b) indirect band gap semiconductors.

In band to band recombination, both the recombining electrons and holes have well-defined energies, as a result the photoluminescence spectra of semiconductors give sharp peaks, which are very useful for the measurement of band gaps.

Apart from the band to band recombination, photoluminescence can also be induced by other recombination mechanisms[6] such as the recombination of excitons which are bound electron-hole pairs, the recombination via impurities, and so on. Careful analysis of these data provides an important way to spot the impurities and check the crystalline quality of semiconductors.

As discussed in section **2.3**, there are other recombination processes which do not emit photons and compete with radiative recombination. Due to these non-radiative recombinations, not all excited charge carriers are available for light emission. The parameter to present the efficiency of photoluminescence is the quantum yield Φ, which is a most important parameter for materials for LED applications.

$$\Phi = \frac{Number\ of\ photons\ emitted}{Number\ of\ photons\ absorbed} \tag{2.35}$$

Photoluminescence spectroscopy is a very useful technique to investigate carrier recombination processes. It has been widely used to determine the band gap of semiconductors, to study charge separation in solar cells, and to measure the quantum yield of emitting ma-

terials for LEDs. By combining it with microscopy, it is also a powerful tool to probe the purity and quality of semiconductor samples. Besides, time-resolved photoluminescence (TRPL), in which the sample is excited with a light pulse and the decay of the emission is measured, is a useful method to measure minority carrier lifetimes.

2.6 Quantum confinement effects

For bulk semiconductor particles, the conduction electrons are unconfined in the boundless crystal lattice. As a result the energy bands are continuous. When electrons in the conduction band move to the valence band and radiatively recombine with holes, as discussed previously in section 2.5, the energy of the photons emitted is near the band gap E_g of the bulk semiconductor. However, when the size of the semiconductor crystal is very small, typically several nanometers and comparable with the exciton Bohr radius a_B, the excitons are confined by the dimensions of the crystal, and the energy bands become discrete. The energy gap between the conduction bands and valence bands ΔE becomes size-dependent and larger than the bulk band gap E_g. The exciton Bohr radius a_B is given as

$$a_B = \varepsilon \left(\frac{m_e}{\mu} \right) a_0 \tag{2.36}$$

where ε is the relative permittivity of the material, m_e is the electron rest mass, μ is the reduced mass of the exciton which is given by the electron effective mass m_e^* and hole effective mass m_h^* as $1/\mu = 1/m_e^* + 1/m_h^*$, and a_0 is the Bohr radius which is 0.53 Å. This size-dependent effect is called the quantum confinement effect, and the semiconductor nanoparticles showing quantum confinement are called quantum dots.

The quantum confinement effect can be understood by the particle-in-a-box model, also known as an infinite potential well. Firstly, a simple one dimensional system is considered, wherein the particle is confined in one dimension in a box with a length of L, as shown in **Fig. 2.12**.

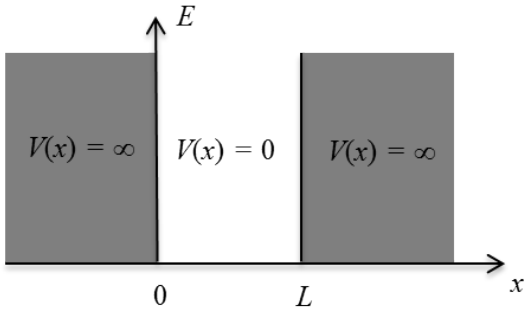

Fig. 2.12 Schematic diagram of a one dimension quantum well.

Within the box, the potential energy $V(x)$ is zero, and the particle can move freely. However, at the walls of the box, the potential energy is infinite, which prevents the particle from escaping from the box. That is,

$$V(x) = \begin{cases} 0, & 0 < x < L \\ \infty, & x \geq L, x \leq 0 \end{cases} \tag{2.37}$$

The time-independent Schrödinger wave equation is given as

$$E\Psi(x) = -\frac{\hbar^2}{2m}\frac{\partial^2}{\partial x^2}\Psi(x) + V(x)\Psi(x) \tag{2.38}$$

where E is the total energy of the particle, $\hbar$ is the reduced Planck constant, m is the mass of the particle, and $\Psi(x)$ is the time-independent wavefunction. Inside the box, as the particle moves freely, it behaves like a free particle. Solving the Schrödinger equation 2.38 gives the wavefunction in the form of

$$\Psi(x) = A\sin(kx) + B\cos(kx) \tag{2.39}$$

where $k^2 = \frac{2mE}{\hbar^2}$. Using the boundary conditions of Ψ being continuous and $\Psi(x = 0) = \Psi(x = L) = 0$, the constants k and B are calculated to be

$$k = \frac{n\pi}{L}, \qquad n = 1, 2, 3 \ldots$$

$$B = 0$$

As the probability of finding the particle in the box is equal to 1, normalizing the integral of the wavefunction to 1 gives

$$A = \sqrt{\frac{2}{L}}$$

Therefore, the wavefunction is given as

$$\Psi(x) = \begin{cases} \frac{2}{L}\sin\left(\frac{n\pi}{L}x\right), & 0 < x < L \\ 0, & x \geq L, x \leq 0 \end{cases} \tag{2.40}$$

and the energy of the particle E is

$$E_n = \frac{n^2\pi^2\hbar^2}{2mL^2} \tag{2.41}$$

Thus, the energy of the particle in the quantum well is not continuous, but can only take up discrete values which increase with n^2, and the minimum of the energy is

$$E_1 = \frac{\pi^2\hbar^2}{2mL^2} \tag{2.42}$$

In quantum dots, the situation is not the same. The box is three dimensional and spherical is shape. But the confinement energy equation of excitons is similar, which is given as

$$E_{\text{dot}} = \frac{\pi^2\hbar^2}{2\mu r^2} \tag{2.43}$$

where r is the radius of the quantum dots. Therefore, the band gap of quantum dots is equal to the band gap of the bulk material E_g plus the energy derived from confinement E_{dot}. Further considering the Coulombic interaction between the confined electron and hole, the band gap of quantum dots ΔE is given as the Brus equation[10]

$$\Delta E = E_g + \frac{\pi^2\hbar^2}{2\mu r^2} - \frac{1.8q^2}{4\pi\varepsilon\varepsilon_0 r} \tag{2.44}$$

where ε is the relative permittivity of the material, ε_0 is the vacuum permittivity and q is the elementary charge. As the Coulombic term is normally small, the band gap of quantum dots is approximately inversely proportional to the square of the radius of the quantum dots r^2.

As a result of the quantum confinement effect, the band gap of the quantum dots are size dependent, and the optical properties can be continuously tuned by changing their particle sizes through changing the conditions of synthesis. This unique property of quantum dots makes them very promising for LED and lasing applications.

2.7 Impedance spectroscopy

Impedance spectroscopy measures the response of a system to an applied small amplitude voltage. Based on the nature of a system, the current output can have a different magnitude and phase to the input signal. Analysis of the response at different frequencies can provide information about the system.

In impedance spectroscopy, a sinusoidal perturbation signal is normally applied, i.e.

$$V_t = V_\mathrm{m} \sin(\omega t) \tag{2.45}$$

where V_m is the signal amplitude, ω is the angular frequency ($\omega = 2\pi f$, where f is the signal frequency) and t is time. The response signal, I_t, is also sinusoidal with the same angular frequency ω, shifted in phase (ϕ) and has a different amplitude I_m,

$$I_t = I_\mathrm{m} \sin(\omega t + \phi) \tag{2.46}$$

if the following criteria are met[11,12]:

Causality. The response of the system must be determined entirely by the perturbation signal. This requires the system to be shielded from outside noises and the system conditions such as temperature need to be kept constant during the measurement.

Linearity. The perturbation/response characteristics of the system must be linear. For electrochemical systems, the relationship between voltage and current is intrinsically not linear, but if the perturbation is small enough, it can be pseudo-linear.

Stability. The system being measured must remain in a stationary state during the measurement. Once the perturbation has been removed, the system must return to its original

state. Therefore measurement conditions have to be properly chosen in order to avoid any long term drift of the system.

According to Euler's formula, for any real number x

$$e^{jx} = \cos x + j \sin x \tag{2.47}$$

where j is the imaginary unit. Therefore, the sinusoidal signals can be written in complex notation as:

$$\begin{aligned} V_t &= V_\mathrm{m}\, e^{j\omega t} \\ I_t &= I_\mathrm{m}\, e^{j(\omega t+\phi)} \end{aligned} \tag{2.48}$$

Then the impedance Z can be defined as:

$$\begin{aligned} Z = \frac{V_t}{I_t} &= \frac{V_\mathrm{m}\, e^{j\omega t}}{I_\mathrm{m}\, e^{j(\omega t+\phi)}} = \frac{V_\mathrm{m}}{I_\mathrm{m}}\, e^{-j\phi} \\ &= Z_0\, e^{-j\phi} = Z_0 \cos\phi - jZ_0 \sin\phi = Z' + jZ'' \end{aligned} \tag{2.49}$$

in which Z_0 is the magnitude, ϕ is the phase angle, Z' is the real part, Z'' is the imaginary part of the impedance, and $Z_0^2 = Z'^2 + Z''^2$, $\tan\phi = Z''/Z'$. The impedance spectra can be obtained by plotting $-Z''$ versus Z' (Nyquist plot) or Z_0 and ϕ versus frequency f (Bode plot).

The impedance of some basic circuit elements can be derived as follows:

For a resistor R, according to Ohms law,

$$I_t = \frac{E_t}{R} = \frac{V_\mathrm{m}\, e^{j\omega t}}{R} \tag{2.50}$$

The impedance of the resistor is given as

$$Z_R = \frac{V_t}{I_t} = \frac{V_\mathrm{m}\, e^{j\omega t}}{\frac{V_\mathrm{m}\, e^{j\omega t}}{R}} = R \tag{2.51}$$

Therefore, the impedance of a resistor is simply its resistance R, independent of frequency.

For a capacitor C,

$$I_t = C\frac{\mathrm{d}V_t}{\mathrm{d}t} = C\frac{\mathrm{d}\left(V_\mathrm{m}\, e^{j\omega t}\right)}{\mathrm{d}t} = jC\omega V_\mathrm{m}\, e^{j\omega t} \tag{2.52}$$

The impedance of the capacitor is given as

$$Z_C = \frac{V_t}{I_t} = \frac{V_\mathrm{m}\, e^{j\omega t}}{jC\omega V_\mathrm{m}\, e^{j\omega t}} = \frac{1}{j\omega C} = -j\frac{1}{\omega C} \tag{2.53}$$

For an inductor L, the impedance can be calculated in a similar way.

$$V_t = L\frac{\mathrm{d}I_t}{\mathrm{d}t} = L\frac{\mathrm{d}\left(I_\mathrm{m}\, e^{j\omega t}\right)}{\mathrm{d}t} = jL\omega I_\mathrm{m}\, e^{j\omega t} \tag{2.54}$$

$$Z_L = \frac{V_t}{I_t} = \frac{jL\omega I_\mathrm{m}\, e^{j\omega t}}{I_\mathrm{m}\, e^{j\omega t}} = j\omega L \tag{2.55}$$

When these basic circuit elements are connected together to form a electrical circuit, the total impedance is the combination of the impedances of the individual elements. For elements in series, the total impedance is the sum of the individual impedances, i.e. $Z = Z_1 + Z_2 + \ldots$, while for elements in parallel, the inverse of the total impedance equal to the sum of the inverse of the individual impedances, that is, $1/Z = 1/Z_1 + 1/Z_2 + \ldots$. In this way, the impedance of a more complex system can be calculated.

Real systems can be modelled as different equivalent circuits comprised of a series of basic circuit elements according to the process and interface properties of the system. A typical electrochemical electrode system for instance, can be modelled with a simplified Randles circuit[13] as shown in **Fig. 2.13**, which includes a double layer capacitor C_{dl} in parallel with a charge transfer resistance R_{ct} and a solution resistance R_s in series with the parallel recombination[14].

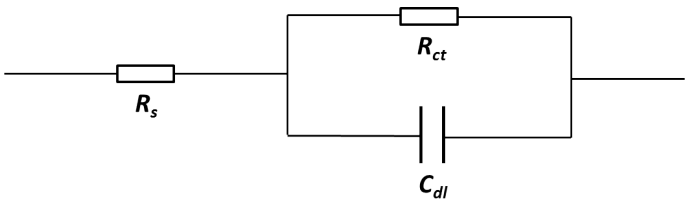

Fig. 2.13 Schematic diagram of the simplified Randles circuit.

The total impedance of the system is given as

$$\begin{aligned} Z = R_s + \frac{1}{\frac{1}{R_{ct}} + j\omega C_{dl}} &= R_s + \frac{R_{ct}}{1 + j\omega C_{dl} R_{ct}} \\ &= R_s + \frac{R_{ct}}{1 + (\omega C_{dl} R_{ct})^2} - j\,\frac{\omega C_{dl} R_{ct}^2}{1 + (\omega C_{dl} R_{ct})^2} \end{aligned} \tag{2.56}$$

Thus, the real part Z' and imaginary part Z'' of the impedance are

$$Z' = R_s + \frac{R_{ct}}{1 + (\omega C_{dl} R_{ct})^2} \tag{2.57}$$

$$Z'' = -\frac{\omega C_{dl} R_{ct}^2}{1 + (\omega C_{dl} R_{ct})^2} \tag{2.58}$$

It is easy to get

$$\left(Z' - R_s - \frac{R_{ct}}{2}\right)^2 + Z''^2 = \left(\frac{R_{ct}}{2}\right)^2 \tag{2.59}$$

Therefore, the Nyquist plot of the simplified Randles circuit gives a semicircle centering at point $(R_s + R_{ct}/2,\ 0)$ with a diameter of R_{ct}, as shown in **Fig. 2.14**

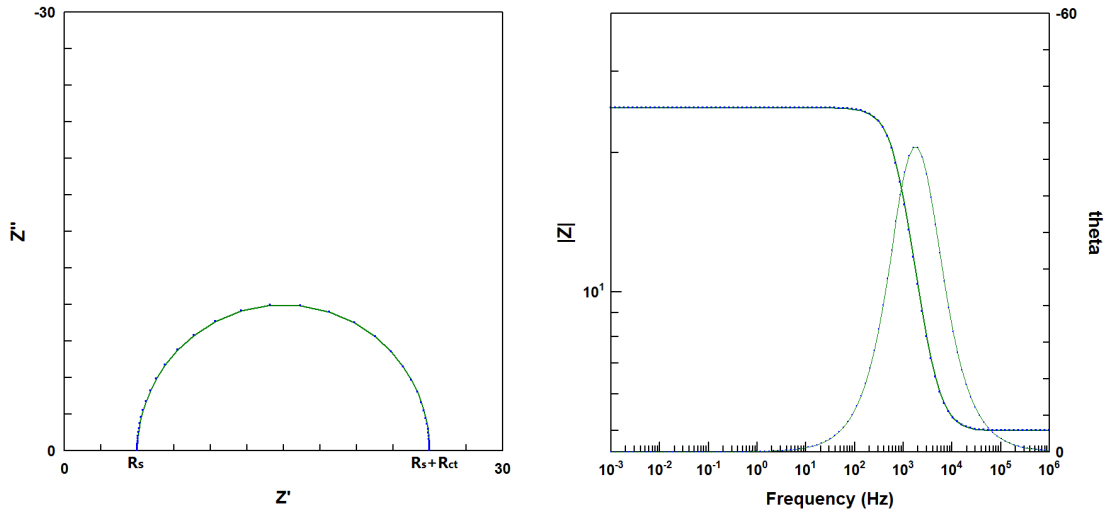

Fig. 2.14 Nyquist and Bode plots for the simplified Randles circuit with $R_s = 5\,\Omega$, $R_{ct} = 20\,\Omega$ and $C_{dl} = 1 \times 10^{-5}$ F

For an unknown system, the impedance properties at different frequencies reflect the process and interfacial behaviours inside the system. Therefore, collecting the impedance data and fitting them with proper equivalent circuits is an effective way to retrieve information about the system. For perovskite solar cells, impedance spectrum has been widely

used for the investigation of carrier recombination and ion diffusion processes[15–18].

Reference

[1] K. Misiakos and D. Tsamakis. Accurate measurements of the silicon intrinsic carrier density from 78k to 340k. *Journal of Applied Physics*, 74(5):3293–3297, 1993.

[2] C. Honsberg and S. Bowden. PVCDROM. `https://pveducation.org/`. Online; Accessed 01 May 2018.

[3] J. Nelson. *The physics of solar cells*. World Scientific Publishing Co Inc, 2003.

[4] L. Chen, F. Tang, Y. Wang, S. Gao, W. Cao, J. Cai, and L. Chen. Facile preparation of organometallic perovskite films and high-efficiency solar cells using solid-state chemistry. *Nano Research*, 8(1):263–270, 2015.

[5] T.S. Moss, G.J. Burrell, and B. Ellis. *Chapter 3 - absorption processes in semiconductors*, pages 48–94. Butterworth-Heinemann, 1973.

[6] M. Grundmann. *The physics of semiconductors: An introduction including nanophysics and applications*. Springer Berlin Heidelberg, 2010.

[7] P.S. Priambodo, N.R. Poespawati, and D. Hartanto. *Solar cell*. InTech, 2011.

[8] L.M. Peter. *Chapter 1 photoelectrochemistry: From basic principles to photocatalysis*, pages 1–28. The Royal Society of Chemistry, 2016.

[9] R. Memming. *Solid-liquid interface*, pages 81–111. Wiley-VCH Verlag GmbH, 2007.

[10] L. Brus. Electronic wave functions in semiconductor clusters: Experiment and theory. *The Journal of Physical Chemistry*, 90(12):2555–2560, 1986.

[11] B.J. Dougherty and S.I. Smedley. *Validation of experimental data from high impedance systems using the kramers-kronig transforms*. ASTM International, 1993.

[12] A. Sacco. Electrochemical impedance spectroscopy: Fundamentals and application in dye-sensitized solar cells. *Renewable and Sustainable Energy Reviews*, 79:814–829, 2017.

[13] A. Lasia. *Electrochemical impedance spectroscopy and its applications*, pages 143–248. Springer US, Boston, MA, 2002.

[14] N. Sekar and R. Ramasamy. Electrochemical impedance spectroscopy for microbial fuel cell characterization. *Journal of Microbial and Biochemical Technology*, 5(Special Issue (S6)), 2013.

[15] A. Pockett, G.E. Eperon, T. Peltola, H.J. Snaith, A. Walker, L.M. Peter, and P.J. Cameron. Characterization of planar lead halide perovskite solar cells by impedance spectroscopy, open-circuit photovoltage decay, and intensity-modulated photovoltage/photocurrent spectroscopy. *The Journal of Physical Chemistry C*, 119(7):3456–3465, 2015.

[16] A.R. Pascoe, N.W. Duffy, A.D. Scully, F. Huang, and Y.-B. Cheng. Insights into planar $CH_3NH_3PbI_3$ perovskite solar cells using impedance spectroscopy. *The Journal of Physical Chemistry C*, 119(9):4444–4453, 2015.

[17] I. Zarazua, G. Han, P.P. Boix, S. Mhaisalkar, F. Fabregat-Santiago, I. Mora-Ser, J. Bisquert, and G. Garcia-Belmonte. Surface recombination and collection efficiency in perovskite solar cells from impedance analysis. *The Journal of Physical Chemistry Letters*, 7(24):5105–5113, 2016.

[18] A. Pockett, G.E. Eperon, N. Sakai, H.J. Snaith, L.M. Peter, and P.J. Cameron. Microseconds, milliseconds and seconds: Deconvoluting the dynamic behaviour of planar perovskite solar cells. *Physical Chemistry Chemical Physics*, 19(8):5959–5970, 2017.

Chapter 3

Experimental

In this chapter, the materials used for the synthesis of perovskite nanocrystals and the fabrication of perovskite solar devices are listed, general methods are introduced, and typical characterisation techniques are included. Further more, each results chapter of this thesis also includes an individual brief experimental section, stating experimental processes specifically applied in that chapter, so that the exact procedure used for a specific experiment can be referred to more easily.

3.1 Materials

All the materials used in this thesis are listed in **Table. 3.1**. All reagents and solvents are used as received without further purification.

Table 3.1 Chemicals and solvents used in this thesis.

Materials	Purity	Supplier
Lead (II) iodide (PbI_2)	99%	Sigma-Aldrich
Lead (II) bromide ($PbBr_2$)	99.999%	Sigma-Aldrich
Methylammonium iodide (MAI)	-	Dyesol
Methylammonium bromide (MABr)	-	Dyesol
N,N-dimethylformamide (DMF)	anhydrous, 99.8%	Sigma-Aldrich
Isopropanol (IPA)	anhydrous, 99.5%	Sigma-Aldrich

Materials	Purity	Supplier
Titanium (IV) diisopropoxide bis(acetylacetonate)	75 wt% in IPA	Sigma-Aldrich
Ethanol absolute	99.8%, AnalaR ACS Reagent	VWR Chemicals
Chlorobenzene	anhydrous, 99.8%	Sigma-Aldrich
TiO_2 paste (18NR-T)	-	Dyesol
Lithium bis(trifluoromethylsulphonyl)-imide (Li-TFSI)	99.95%	Sigma-Aldrich
Spiro-OMeTAD	99%	Sigma-Aldrich
Dimethyl sulfoxide (DMSO)	anhydrous, 99.9%	Sigma-Aldrich
4-tert-butylpyridine (tBP)	99%	Sigma-Aldrich
Gold	Premion 99.9985%	Alfa Aesar
Tin (IV) isopropoxide	99%, 10% w/v in IPA	Sigma-Aldrich
Zinc nitrate hexahydrate ($Zn(NO_3)_2 \cdot 6\,H_2O$)	98%	Sigma-Aldrich
Niobium (V) ethoxide	99.95%	Sigma-Aldrich
Octadecene (ODE)	90%	Acros Organics
1-butanol (BuOH)	99%	Acros Organics
Oleylamine (OLA)	80-90%	Acros Organics
Oleic acid (OA)	90%	Alfa Aesar
Toluene	ACS Reagent	VWR Chemicals
n-hexane	97% HPLC	VWR Chemicals
Diethyl ether	99% GPR	VWR Chemicals
Azetidinium iodide (AzI)	-	-
tert-butylammonium iodide (tBAI)	98%	Sigma-Aldrich

3.2 Methods

3.2.1 Perovskite film preparation

The preparation of perovskite films was conducted using three different methods:

Vapour-assisted sequential deposition method. the vapour-assisted sequential deposition of perovskite films was carried out in ambient atmosphere with room humidity of less than 35 %. Firstly a solution of 400 mg mL^{-1} PbI_2 in DMF was spin-coated at 4000 rpm for 30 s, followed by annealing at 100 °C for 1 h. Then the PbI_2 films were put on a hotplate, surrounded with MAI powder and covered with a lid. The chamber was evacuated with an Edwards vacuum pump by continuously pumping for 2 min and sealed. The setup of the experiment is illustrated in **Fig. 3.1**. The hotplate was heated at 70 °C for 20 min to remove moisture adsorbed in the MAI powder, after which the chamber was re-evacuated for another 2 min and the temperature was raised to 150 °C to sublime the MAI powder and transform the PbI_2 into $MAPbI_3$ perovskite. After 1 h reaction, the perovskite film was taken out and cooled to room temperature.

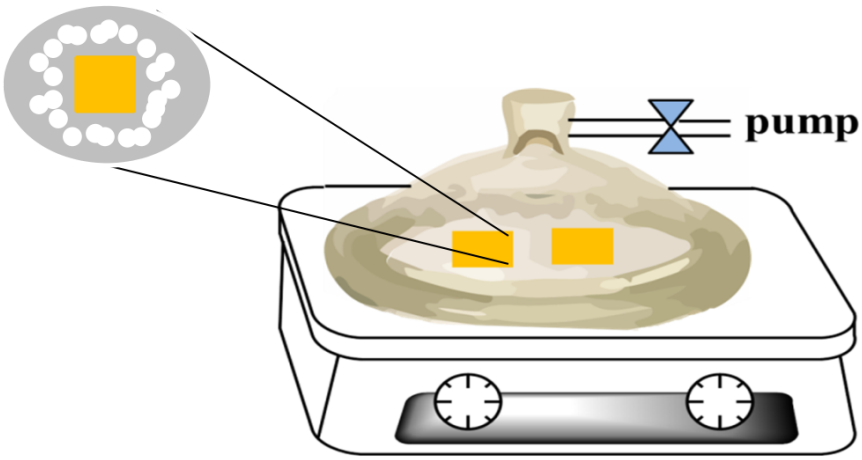

Fig. 3.1 Schematic diagram of the setup for the vapour assisted two step method[1].

Sequential spin-coating method. Firstly PbI_2 films were formed by spin-coating a solution of 461 mg mL^{-1} PbI_2 in DMF at 6000 rpm for 30 s, followed by annealing at 70 °C for 10 min. Then a solution of MAI in IPA with different concentrations was sequentially

spin-coated onto the PbI_2 films at 6000 rpm for 30 s with a loading time of 10 s. The wet films were kept at room temperature for 10 min before being annealed at 110 °C for 60 min. The interdiffusion and reaction of the two layers resulted in the formation of dark brown perovskite phase. The sequential spin-coating deposition of perovskite films was carried out in a nitrogen-filled dry box with controlled humidity of less than 10 %.

One-step spin-coating method. Precursor solutions of 40 wt% were made by dissolving MAI, PbI_2 and $PbCl_2$ (in the mixed lead source recipe) with the molar ratio of MAI : PbI_2 : $PbCl_2$ = 4 : 1 : 1 or MAI and $PbCl_2$ (in the $PbCl_2$ source recipe) with the molar ratio of MAI : $PbCl_2$ = 3 : 1 in DMF at 60 °C. The precursors were spin-coated onto hot substrates of 100 °C at 4000 rpm for 30 s, followed by annealing at 100 °C for 100 min. The deposition process was carried out and compared in ambient atmosphere with humidity of less than 35 % and in the dry box with controlled humidity of less than 10 %.

3.2.2 Device fabrication

Perovskite cells with a n-i-p architecture were fabricated layer by layer on glass substrates coated with FTO conducting layers. The structure of planar and mesoporous devices, along with a photo of a typical device, are depicted in **Fig. 3.2**.

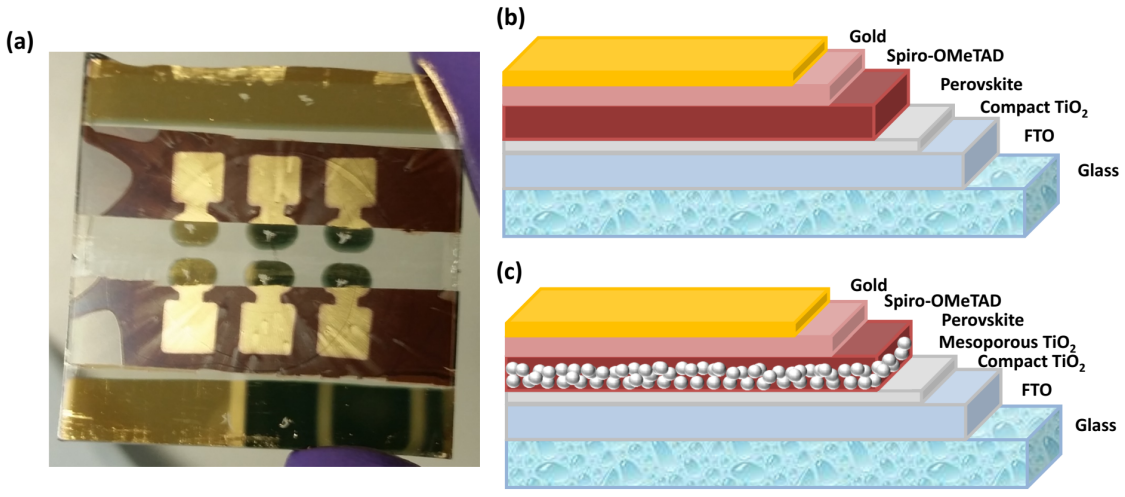

Fig. 3.2 (a) Photo image of a typical device with six small pixel cells. Each pixel is comprised of multiple-layer structures shown in (b) planar or (c) mesoporous.

Substrate pretreatment. FTO substrates (2.5 cm × 2.5 cm) were etched with Zn powder

and hydrochloric acid, and cleaned sequentially with 2% Hellmanex detergent, deionised water, IPA, acetone and absolute ethanol under ultrasonication (50 Hz, 100 W) for 10 min respectively. After being blow dried, the substrates were treated with UV-ozone for 10 min.

ETL deposition. Compact TiO_2 hole blocking layers (c-TiO_2) were deposited using a spray pyrolysis method. A 50 mL solution of titanium diisopropoxide bis(acetylacetonate) (0.2 M) was obtained by dissolving 4.9 mL of it in ethanol absolute. The precursor solution was then sprayed onto the cleaned FTO substrates kept on a hotplate at 450 °C using a hand-held atomiser. The spraying process was carried out every half minute and repeated 10 times to achieve a thickness of ~ 50 nm. The substrates were further post-annealed for 20 min to get anatase TiO_2 films. In planar devices, the c-TiO_2 blocking layer alone served as the ETL, whereas another mesoporous TiO_2 (m-TiO_2) layer was deposited on top of the compact layer in mesoporous devices. The deposition of the mesoporous layer was conducted by spin-coating a 18NR-T TiO_2 paste at 3000 rpm for 30 s after it being diluted into ethanol with a weight ratio of 2 : 7. The film was dried at 150 °C for 30 min, followed by calcination at 500 °C for 30 min. After the ETLs were cooled to room temperature, perovskite layers were deposited on top with the methods described in **3.2.1**.

HTL deposition. After the perovskite layers had been deposited on top of the ETLs, Spiro-OMeTAD layers were deposited on top serving as HTLs. A solution was prepared by dissolving 96.6 mg Spiro-OMeTAD in 1 mL chlorobenzene at 60 °C for 30 min, followed by the addition of 9.6 μL tBP and 30.2 μL Li-TFSI solution (175 mg mL^{-1} in acetonitrile). The solution was spin-coated on top of the perovskite layers at 3000 rpm for 30 s after a loading time of 10 s. The films were kept overnight in dry air to allow the Spiro to become partially oxidised and hence to increase the doping density of the Spiro layer.

Deposition of back contacts. Full devices were finished with the deposition of gold back contacts through thermal evaporation. ~ 200 mg of gold wire was evaporated using a nanoPVD T15A bench-top physical vapour deposition system at the pressure of 1×10^{-5} mBar and a current of ~ 60 A. A shadow mask was used to define six pixels on one device, each with an active area of 0.09 cm^2.

3.2.3 Flow synthesis of perovskite NCs

A flow reactor setup was developed for the continuous flow synthesis of perovskite NCs, which comprised of two syringe pumps, a PFA T-junction and PTFE tubing, as illustrated in **Fig. 3.3**. The formation of perovskite NCs resulted from the reaction of a lead halide (PbX_2) solution and a methylammonium halide (MAX) solution. The PbX_2 solution was prepared by dissolving 0.8 mmol PbI_2 or $PbBr_2$ in 8 mL ODE with 1.2 mL OLA and 1.2 mL OA at 100 °C. The MAX solution was made by dissolving 0.8 mmol MAI or MABr in the mixture of 8 mL BuOH and 4 mL ODE with 1 mL OA. Both the solutions were cooled to room temperature before use. For $MAPbI_3$ NC synthesis, the PbI_2 solution and MAI solution were pumped using the syringe pumps and mixed in the T-juction before being flown through a 3 meter PTFE tubing (internal diameter: 1.5 mm) submerged in a water bath at 30 °C. The flow rates of the two solutions were set to be 236 μL/min and 294 μL/min respectively, resulting in the molar ratio of $PbX_2 : MAX = 1 : 1$ and a residence time of 10 min. The mixture was collected in a container sitting inside an ice bath to help quench the reaction. The final product was centrifuged and the supernatant containing any unreacted precursors was discarded. The solid was re-dispersed in toluene, and a second centrifugation step was used to remove any larger aggregates. The NCs remained in the second supernatant, and kept for further characterisations or applications. For $MAPbI_xBr_{3-x}$ NCs, the PbI_2 solution was replaced by a mixture of PbI_2 solution and $PbBr_2$ solution, and/or the MAI solution was replaced by a mixture of MAI solution and MABr solution, according to the ratio of I : Br = x : (3-x).

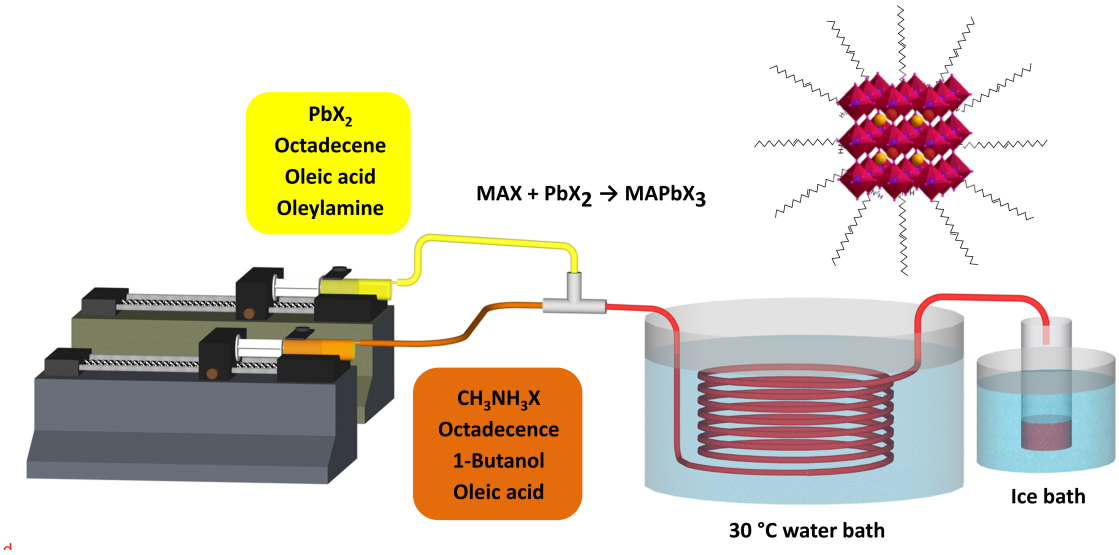

Fig. 3.3 Schematic diagram of the flow reactor system used for the synthesis of $MAPbX_3$ NCs.

3.3 Characterisation techniques

X-ray diffraction (XRD). XRD spectra of thin films were measured using a BRUKER D8-Advance Powder X-Ray Diffractometer using a Cu Kα radiation source ($\lambda = 1.5406$ Å) at a voltage of 40 kV and 40 mA, and a PSD:VANTEC-1 detector. The diffraction pattern was scanned with a step size of 0.023 ° and a rotation speed of 15 rpm, at room temperature. To measure the XRD patterns of the perovskite NCs, clean silicon wafers were immersed in the dispersion of the NCs in toluene. After 48 h, the wafers were taken out, blow-dried with nitrogen and measured on the X-Ray Diffractometer.

UV-visible spectroscopy (UV-vis). UV-vis spectra of the $MAPbX_3$ NCs dispersed in toluene and perovskite thin films were measured. For $MAPbX_3$ NCs, the solutions were put in a quartz cuvette, and the UV-vis spectra were measured on a Varian Cary 50 UV-Visible spectrophotometer. Scans were carried out at a rate of 300 nm/min at room temperature. For perovskite thin films, both the reflectance R% and transmittance T% were measured using a Perkin-Elmer Lambda 750S UV/Vis spectrometer with an integrating sphere. The absorptance A% was calculated by A%=1-T%-R%. Scans were conducted from 900 nm to 300 nm.

Photoluminescence (PL). PL spectra of the perovskite NCs were measured on a Gilden

photonics fluoroSENS fluorimeter under emission mode. The dispersions of $MAPbX_3$ NCs in toluene were put in a 1-cm quartz cuvette. The excitation wavelength was set at 365 nm which is commonly used in PL studies for perovskite nanocrystals[2,3], and the integrating time of the measurement was 100 ms. All data were obtained at room temperature and under air atmosphere.

Atomic Force Microscopy (AFM). The morphology of thin films were studied with AFM on a Nanosurf Easyscan 2 atomic force microscope under the "Phase Contrast" mode using tap190 AFM probes. The scan speed was 1 second per line.

Transmission electron microscopy (TEM). TEM measurements were carried out to investigate the micromorphology of the $MAPbX_3$ NCs. The samples were prepared by dropping the toluene dispersions of the NCs onto carbon supported copper grids followed by drying overnight under vacuum. The TEM measurements were performed on a JEOL JEM-2100Plus transmission electron microscope with an acceleration voltage of 200 kV.

Current density voltage tests (J - V). J-V curves of perovskite cells were measured on a Keithley 2601 System SourceMeter under simulated AM 1.5 sunlight at 100 mW cm^{-2} irradiation generated by an Abet sun 2000 solar simulator. The light intensity was calibrated using a Si reference cell. Cells were masked with a dark aperture to define an illumination area of 0.0625 cm^2. A Bias potential was applied across the cell and it was scanned from 1.2 V to 0 V and back to 1.2 V after being pre-biased at 1.2 V for 5 seconds. The scan rate was 200 mV/s.

X-ray photoelectron spectroscopy (XPS). XPS analysis of the TiO_2 films were carried out using a Thermo Scientific K-Alpha spectrometer fitted with a monochromatic Al-Kα source to investigate the elemental constituents. Survey scans were conducted in the binding energy range of 0-1350 eV at a pass energy of 40 eV.

Mott-Schottky tests. Mott-Schottky measurements of compact TiO_2 hole blocking layers were carried out on a Modulab potentiostat. Copper wires were attached to the exposed FTO at the top of the substrates with copper tape. The coated FTO slides served as the working electrodes, and Kapton tapes were used to define an area of $\sim 50\,mm^2$. The electrodes were photographed and the actual areas were measured using ImageJ soft-

ware. During Mott-Schottky measurements, three electrode electrochemical cells were constructed, with a Pt wire counter electrode and a Ag/AgCl reference electrode. A solution of 0.1 M Na_2SO_4 in water with the pH = 3 (adjusted by H_2SO_4) was used as the electrolyte. Capacitances were retrieved through single frequency (27 Hz, where the space charge capacitance C_{SC} dominates the measured capacitance[4]) impedance tests at different bias voltage between -0.1 V and 1 V, and were used for the Mott-Schottky plots, from which the doping density and flat band potential of the TiO_2 films were calculated.

Electrochemical impedance spectroscopy (EIS). Impedance spectra were measured on a ModulabXm (Solartron analytical) in a Faraday cage at room temperature. Cells were held at the open circuit voltage under illumation. A blue LED (470 nm) was used as the light source. Measurements were carried out at different light intensities by changing the current input of the LED. The frequency range was 1 MHz to 10 mHz and the AC amplitude was 10 mV.

Reference

[1] Wentao Deng. Small molecules for applications in solar cells, 2017.

[2] D.N. Minh, J. Kim, J. Hyon, J.H. Sim, H.H. Sowlih, C. Seo, J. Nam, S. Eom, S. Suk, S. Lee, E. Kim, and Y. Kang. Room-temperature synthesis of widely tunable formamidinium lead halide perovskite nanocrystals. *Chemistry of Materials*, 29(13):5713–5719, 2017.

[3] M.C. Weidman, M. Seitz, S.D. Stranks, and W.A. Tisdale. Highly tunable colloidal perovskite nanoplatelets through variable cation, metal, and halide composition. *ACS Nano*, 10(8):7830–7839, 2016.

[4] O. Almora, C. Aranda, E. Mas-Marzá, and G. Garcia-Belmonte. On mott-schottky analysis interpretation of capacitance measurements in organometal perovskite solar cells. *Applied Physics Letters*, 109(17):173903, 2016.

Chapter 4

Synthesis Optimisation of Perovskite Solar Cells

With an n-i-p structure made up of multi layers as shown in **Fig. 4.1**, the performance of perovskite solar cells is highly dependent on the properties of each layer, among which the quality of the perovskite layer is one of the most important. As the light-absorbing layer, the light harvesting ability of the perovskite layer is linked directly to the number of charge-carriers generated and subsequently the current of the device. The perovskite layer is sandwiched between an n-type TiO_2 electron-transporting layer and a p-type spiro-OMeTAD hole-transporting layer, thus discontinuities (pinholes) in the perovskite film can form shunt paths due to the direct contact of these two layers and cause the loss of photocurrent. In addition, trap states caused by poor crystallization of the perovskite can serve as recombination centres and result in poor performance[1,2]. Many strategies have been developed to improve the quality of the perovskite layer, including solvent engineering[3–6], solvent annealing[7,8] and additives[9–11]. But due to the sensitivity of the perovskite crystallisation to environmental conditions such as humidity[12,13], atmosphere[14,15], temperature[16,17], even light[18], the quality of the perovskite films are still rather lab-dependent and process-dependent. In this chapter, both one-step and two-step methods are adapted, and different conditions such as solvents, annealing temperature and precursor recipes are optimised to find a robust way of making high-quality perovskite films in our lab in air or with the assistance of a nitrogen drybox. The work in this chapter is the foundation of research works on perovskite solar cells to be discussed in the following chapters.

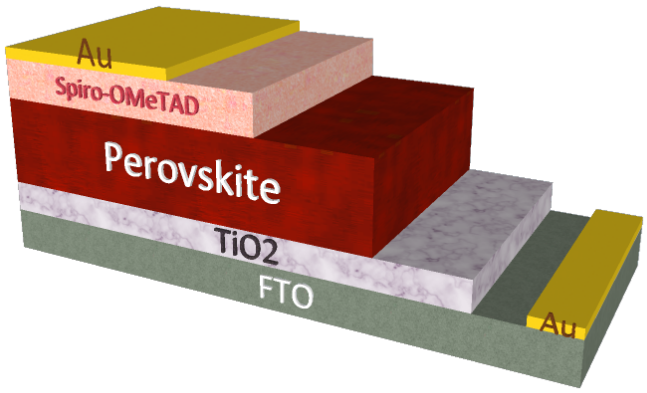

Fig. 4.1 Schematic diagram of the cell architecture. Thickness of different layers: TiO_2: ~50 nm, perovskite: 200-300 nm, Spiro-OMeTAD: ~200 nm, Au: 80-100 nm.

4.1 Experimental

In this chapter, different methods were studied for the preparation of perovskite layers, including a vapour-assisted sequential deposition method, a sequential spin-coating method and a one-step method. The detailed processes used in each of these methods can be found in the main experimental chapter 3.

For the vapour-assisted sequential deposition method, different annealing temperatures of 115 °C, 130 °C and 150 °C, different solvents of DMF and DMSO, different lead sources of PbI_2 and $PbCl_2$ and the effect of chlorobenzene dripping during PbI_2 spin-coating were compared. In chlorobenzene dripping during the spin-coating of PbI_2 solution, 120 µL of chlorobenzene was quickly dripped on the center of the substrate 8 seconds after the spinning started. For the sequential spin-coating method, different MAI concentrations of 10 mg/mL, 30 mg/mL and 50 mg/mL were compared. For the one-step method, different precursor recipes of MAI:$PbCl_2$=3:1 and MAI:PbI_2:$PbCl_2$=4:1:1 were compared in air and in a dry box.

4.2 Vapour-assisted sequential deposition method

The vapour-assisted sequential deposition synthesis of perovskite thin films involves the crystallisation of PbI_2 and its conversion into perovskite through heterogeneous reaction with MAI vapour. The reaction temperature and the morphology of the PbI_2 films are of great importance for the formation of high quality perovskite films. Here, the influences of annealing temperature, anti-solvent dripping, solvents and lead sources were investigated, as shown in **Fig. 4.2**.

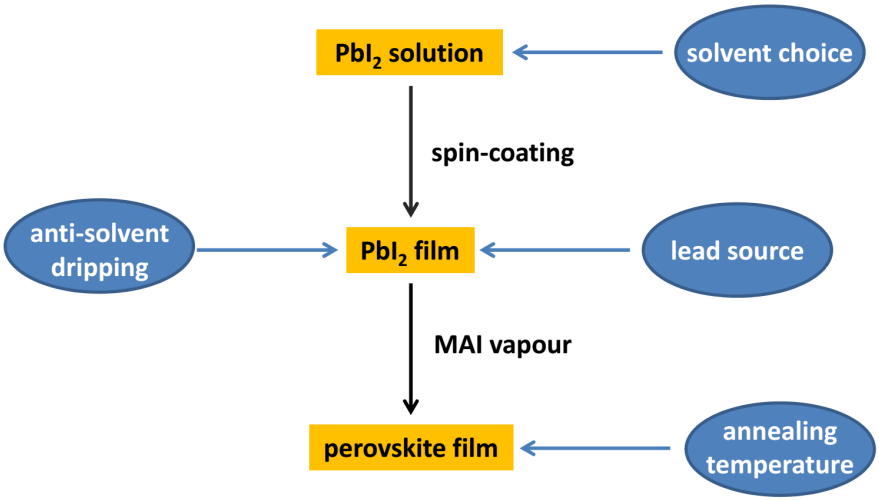

Fig. 4.2 Diagram showing the factors investigated in the vapour-assisted sequential deposition of perovskite films.

4.2.1 Annealing temperature

Temperature is of great importance for the conversion of PbI_2 into perovskite in the vapour-assisted sequential method. It affects not only the generation of MAI vapour, but also the infiltration of MAI in the film, as well as the growth of perovskite crystals.

Fig. 4.3 shows the XRD patterns of perovskite films synthesised at 115 °C, 130 °C and 150 °C. At 115 °C, after 1 h reaction, the appearance of peaks at 13.9°, 28.2° and 31.7° in the XRD pattern shows the formation of tetragonal perovskite, corresponding to the (110), (220) and (310) facets respectively[19]. However, a set of strong diffraction peaks at 12.5°, 25.7° and 34.1° still remained, which are assigned to the (001), (101) and (102)

facets of PbI_2, indicating the incomplete conversion of PbI_2. For the sample synthesised at 130 °C, the peaks of perovskite were enhanced, indicating better conversion at a higher temperature. But the existence of characteristic peaks of PbI_2, though much lower in intensity, implied that 130 °C for 1 h was still not enough for the complete conversion of PbI_2. When the reaction temperature was further raised to 150 °C, the diffraction peaks of PbI_2 fully disappeared and the peaks of tetragonal perovskite phase were further enhanced, suggesting the full conversion of PbI_2 and the formation of a perovskite film with high crystallinity.

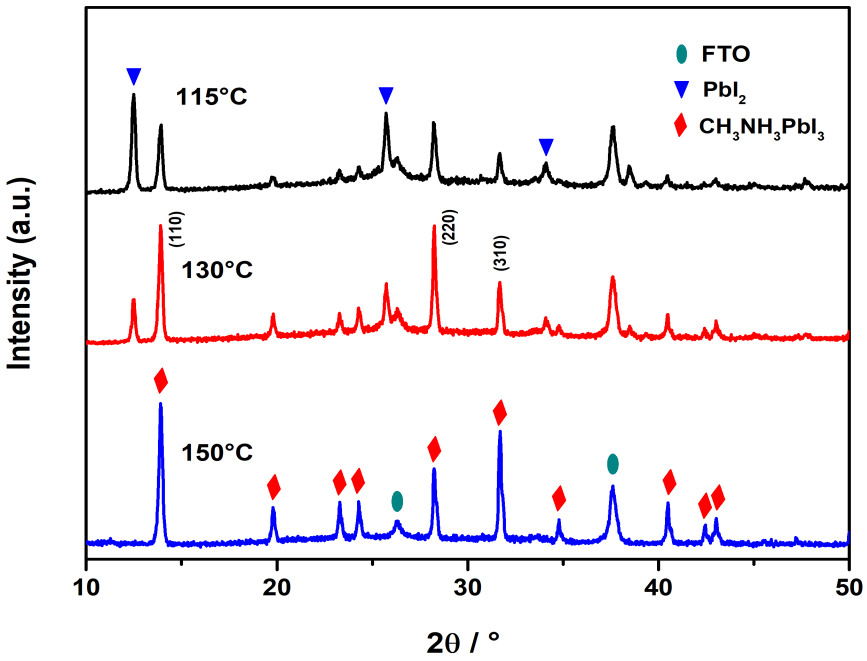

Fig. 4.3 XRD patterns of perovskite films synthesized with the vapour-assisted sequential method at different temperatures.

AFM images of perovskite films synthesised at different temperatures are shown in **Fig. 4.4**. For the sample prepared at 115 °C for 1 h, the film consisted of many small particles and some larger particles, with a rough surface. As the reaction temperature increased, the amount of smaller particles decreased and more larger particles were formed. The surface smoothness was also improved. When the reaction temperature was increased to 150 °C, the particles grew into many large particles with a diameter of ~ 1 μm, packing densely on the surface, forming a uniform film with good smoothness and high coverage. The morphology changes may be ascribed to the high MAI vapour concentration in the system and fast formation of crystals at high temperatures serving as seed crystals for perovskite

growth[17].

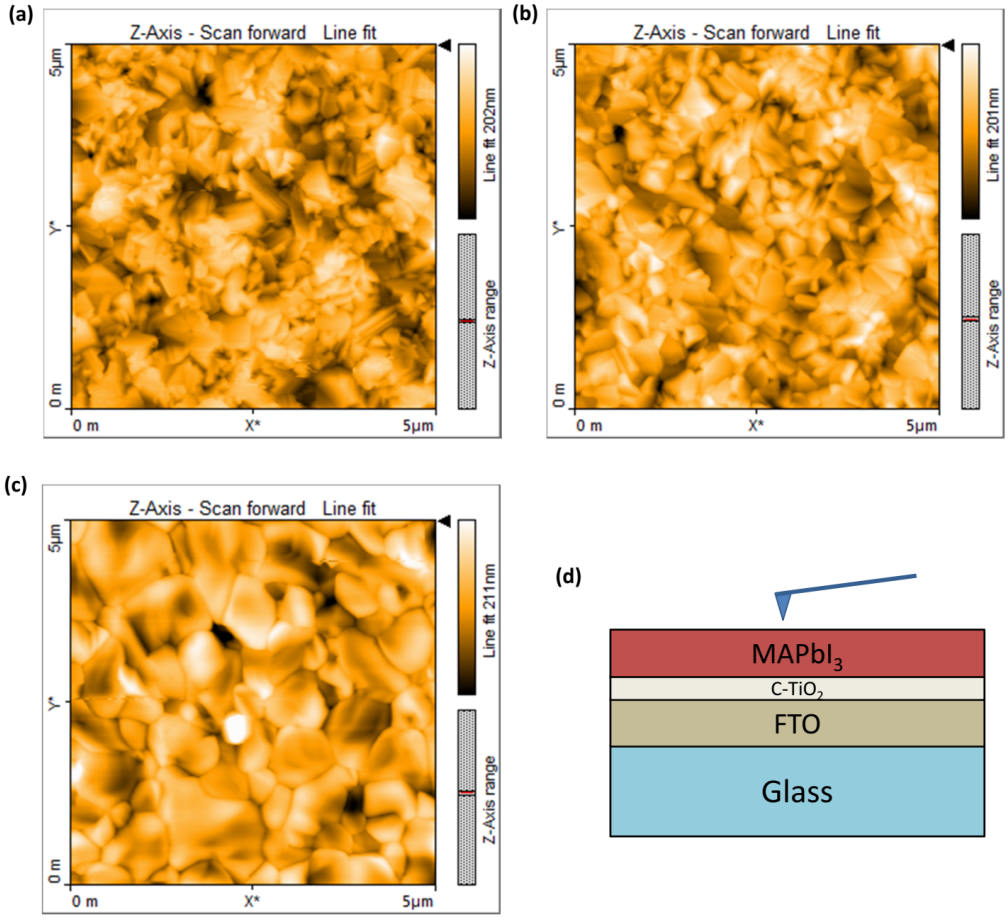

Fig. 4.4 AFM images of $MAPbI_3$ perovskite films synthesized at (a) 115 °C, (b) 130 °C and (c) 150 °C on c-TiO_2 blocking layers; (d) Schematic diagram of the structure of the half device for AFM tests.

Solar cell devices with the structure of FTO/c-TiO_2/perovskite/Spiro-OMeTAD/Au were made, and J-V tests were carried out. The cell performances are shown in the box plots in **Fig. 4.5** and listed in **Table. 4.1**. The cells with perovskite layers made at 115 °C showed PCEs of $1.52 \pm 0.37\%$, with the V_{OC} of 0.84 ± 0.04 V, J_{SC} of 2.50 ± 0.45 mA $\cdot$ cm^{-2} and FF of 0.74 ± 0.19. The low PCE is mainly due to the low current which is believed to be due to the poor conversion of PbI_2 as shown in the XRD spectra, as well as recombination at the grain boundaries due to the small particle size[20]. When the annealing temperature was increased to 130 °C, as a result of the enhanced conversion of PbI_2 to perovskite, and the increased particle size, the J_{SC} increased to 7.48 ± 2.05 mA $\cdot$ cm^{-2}, and the PCE increased to $3.46 \pm 1.30\%$. When the annealing temperature was increased further to 150 °C, the J_{SC} decreased to 3.22 ± 1.16 mA $\cdot$ cm^{-2} and the PCE decreased to $1.73 \pm 0.81\%$, though the

perovskite films showed complete phase conversion and larger particle sizes. The better performance of the cells with perovskite layers made at 130 °C than 150 °C may be due to the existence of the small amount of PbI_2 in the perovskite films which has previously been reported to passivate the grain boundaries and decrease recombination when it is present in small amounts at the interface[21,22].

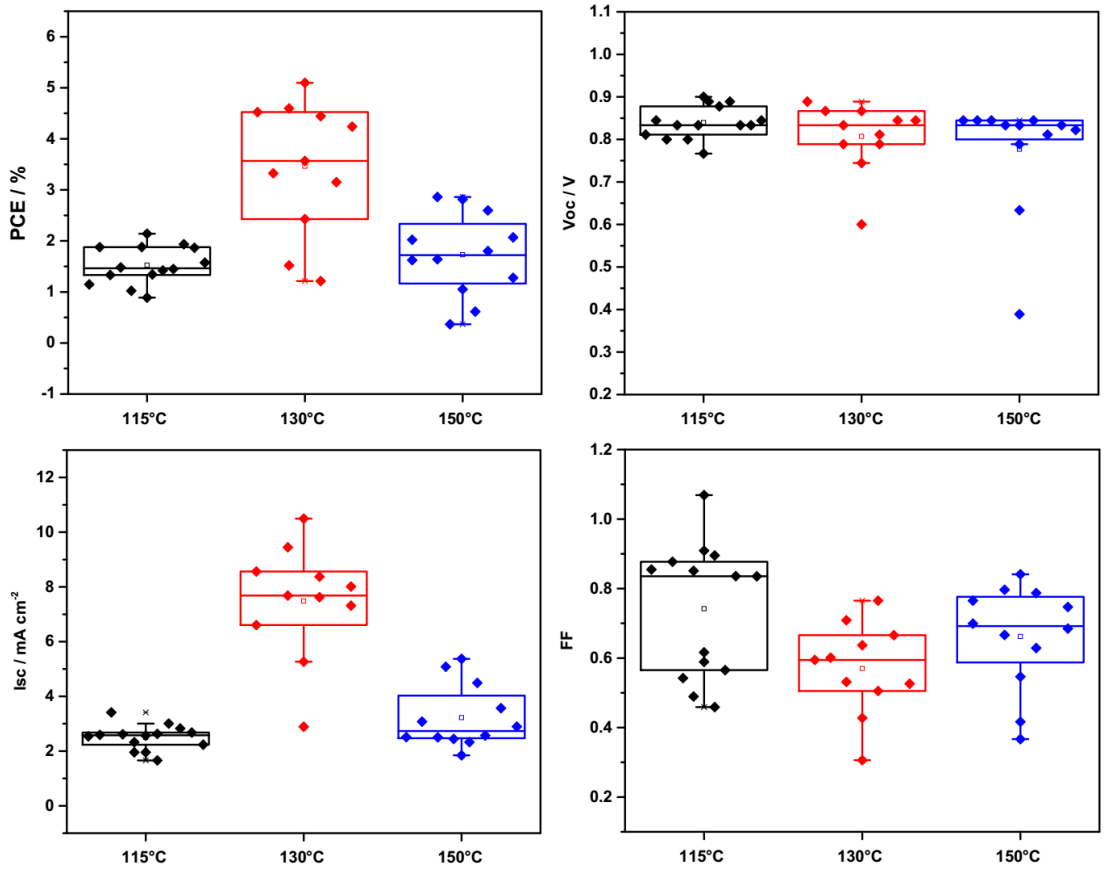

Fig. 4.5 Box plots of PCE, V_{OC}, I_{SC} and FF of devices with $MAPbI_3$ films synthesis at 115 °C, 130 °C and 150 °C. The box edges represent the 25/75 percentiles. The square symbols (□) inside the boxes show the mean value, and the lines across the boxes stand for the median.

Table 4.1 Performance parameters in reverse scans for cells with perovskite layers made at different temperatures.

Temperature [°C]	V_{OC} [V]	J_{SC} [mA·cm^{-2}]	FF	PCE [%]
115	0.84 ± 0.04	2.50 ± 0.45	0.74 ± 0.19	1.52 ± 0.38
130	0.81 ± 0.08	7.48 ± 2.05	0.57 ± 0.13	3.46 ± 1.30
150	0.78 ± 0.13	3.22 ± 1.16	0.66 ± 0.15	1.73 ± 0.81

Although the cells with perovskite films made at 130 °C showed the best performance, the reproducibility was considerably poorer, as seen from the wide distribution of PCEs in **Fig. 4.5**. Therefore, 150 °C was used for the preparation of perovskite films in the following investigations about the vapour-assisted sequential method.

4.2.2 Chlorobenzene dripping

Antisolvent dripping has been widely applied for the one-step preparation of perovskite films, and it has been shown that the introduction of antisolvents such as chlorobenzene, toluene or ethyl acetate during the spin-coating of perovskite precursors can accelerate the crystallization of perovskite and result in the formation of highly uniform perovskite thin films with high coverage[3,4,6]. Therefore, in order to control the morphology of PbI_2 precursor and investigate its effect on the perovskite film, chlorobenzene dripping was conducted during the spin-coating process of the PbI_2 solution.

Due to the insolubility of PbI_2 in chlorobenzene, the addition of chlorobenzene helps with the crystallization of PbI_2. As shown in **Fig. 4.6**a and **Fig. 4.6**b, after the addition of chlorobenzene, due to the accelerated nucleation speed, the particle size of PbI_2 was greatly decreased, and the surface coverage was significantly improved. After the phase conversion, the resulting perovskite films both showed increases in particle sizes and better coverage than the PbI_2 films due to volume expansion[23]. The sample with chlorobenzene dripping also showed smaller particle size than that without.

However, XRD patterns of the perovskite films showed the existence of remaining PbI_2 in the film prepared with chlorobenzene dripping. As shown in **Fig. 4.7**, both the samples with and without chlorobenzene dripping exhibited strong diffraction peaks of tetragonal $MAPbI_3$ perovskite, indicating the high crystalline nature of the perovskite phase. But there is also a weak peak at 12.5 ° in the spectrum of the perovskite film synthesised with chlorobenzene dripping, which is the characteristic diffraction peak of the PbI_2 phase. The incomplete conversion of the chlorobenzene dripped PbI_2 could be caused by the increased compactness of the PbI_2 film which hindered the infiltration of MAI vapour into the film. Therefore, though the chlorobenzene dripping treatment during the spin-coating process can improve the quality of PbI_2 precursor films and consequently the morphology

of perovskite films, a higher temperature or longer reaction time is necessary for the full conversion of PbI_2.

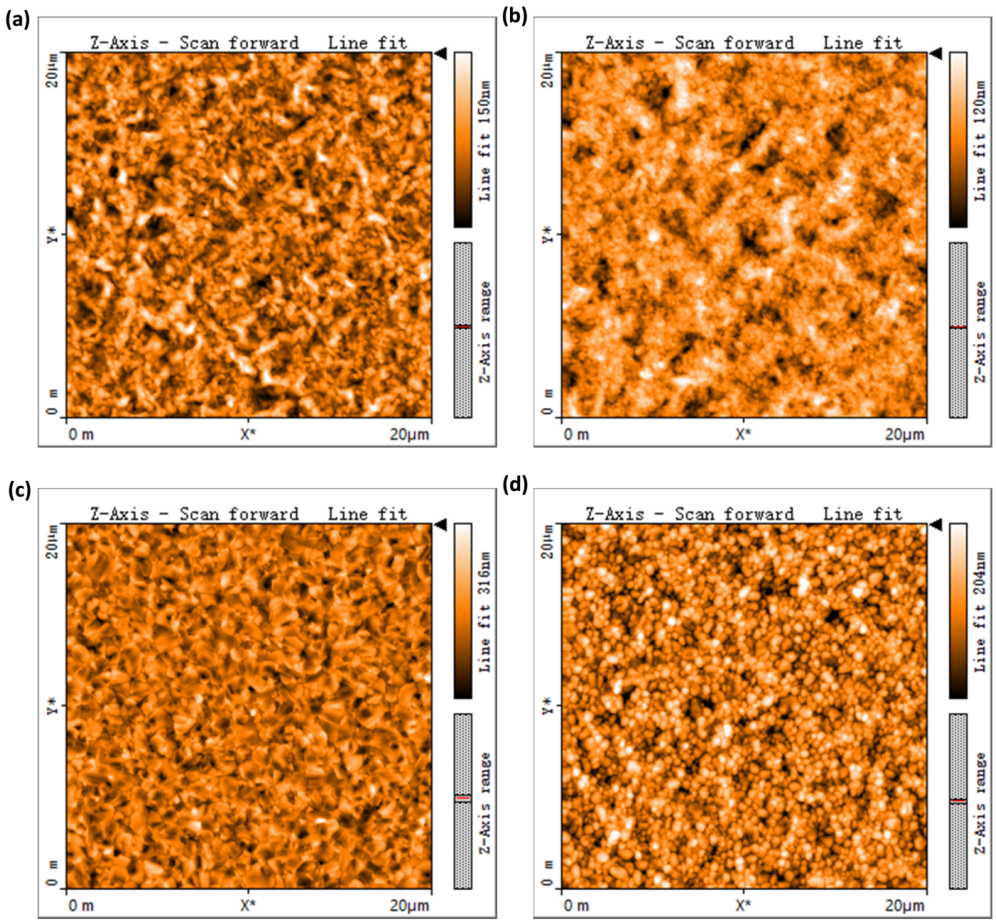

Fig. 4.6 AFM images of PbI_2 films (a) without and (b) with chlorobenzene dripping and (c, d) the obtained $MAPbI_3$ perovskite films on c-TiO_2 blocking layers. The AFM image of the c-TiO_2 film can be found in **Fig. 5.4**.

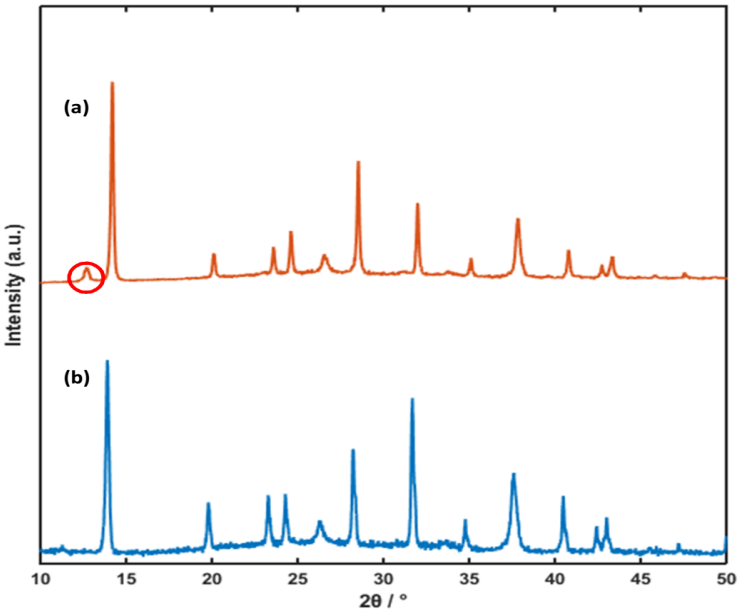

Fig. 4.7 XRD spectra of perovskite films synthesised from PbI_2 films (a) with and (b) without chlorobenzene dripping.

The performance of devices based on the $MAPbI_3$ films prepared from PbI_2 layers with and without chlorobenzene dripping are shown in **Fig. 4.8**. For the devices without chlorobenzene dripping, V_{OC} of 0.81 ± 0.09 V, J_{SC} of 7.28 ± 3.53 mA·cm^{-2} and FF of 0.27 ± 0.05 were obtained, leading to PCEs of 1.70 ± 1.17 %. Whereas for the devices with chlorobenzene dripping, the photovoltaic performances were even worse, with PCEs of as low as 0.64 ± 0.21 %. The inferior performance is believed to be caused by the incomplete phase conversion of PbI_2 into perovskite. It has been discussed previously that small amount of unconverted PbI_2 can passivate the grain boundaries and reduce recombination. However, in this case, the unreacted PbI_2 due to the hindered infiltration of MAI by the the highly compact PbI_2 film would be most likely to accumulate at the bottom of the perovskite film, rather than being uniformly distributed at grain boundaries in the layer. Because of its wide bandgap, PbI_2 accumulating at the interface of TiO_2/perovskite may impede the charge transfer to the ETL[21,24] as illustrated in **Fig. 4.9**. As a result, the V_{OC}, J_{SC} and FF all dropped comparing with the devices without chlorobenzene dripping.

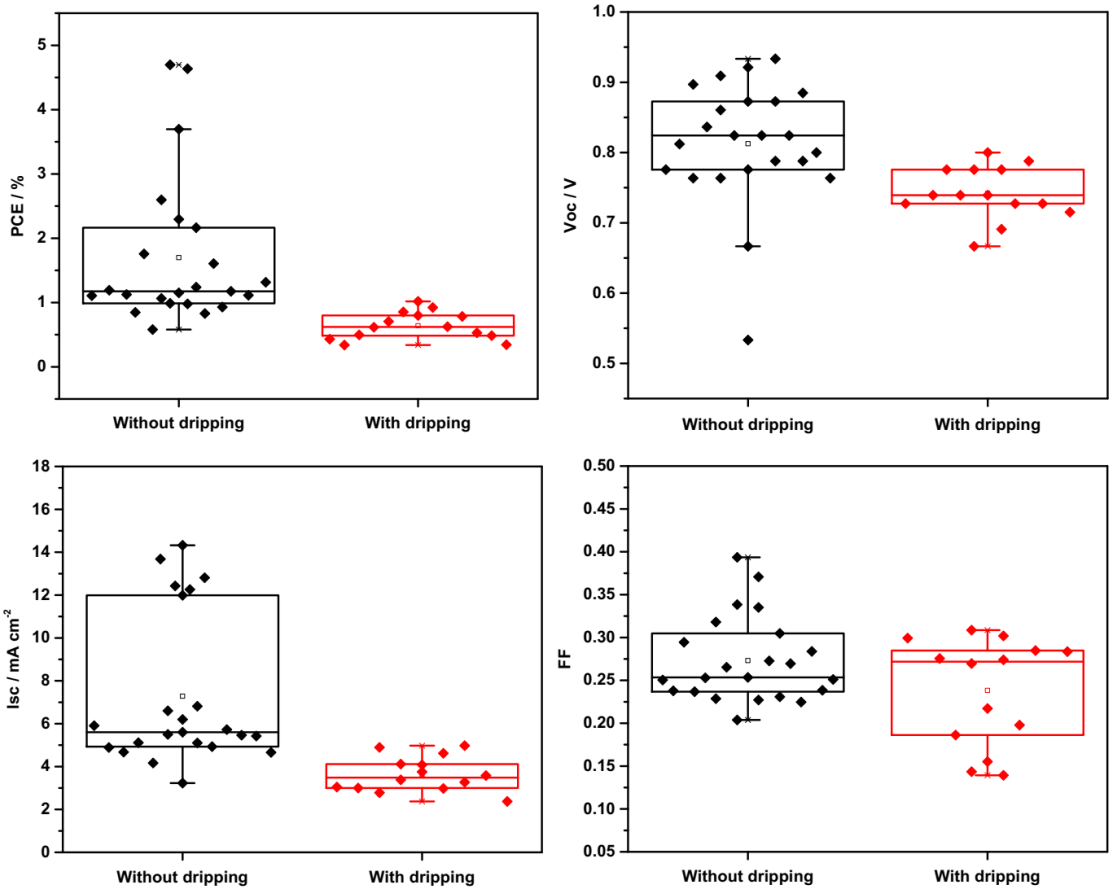

Fig. 4.8 Box plots of cell performance of devices with perovskite films synthesised from PbI_2 layers with and without chlorobenzene dripping.

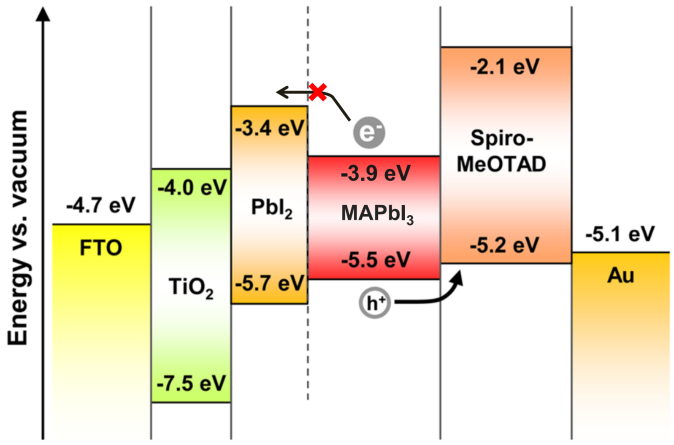

Fig. 4.9 Approximate band diagram of the device showing the presence of a PbI_2 layer in the incompletely converted perovskite layer would form an energy barrier hindering electron injection from perovskite into TiO_2.[24]

4.2.3 Solvents

Due to the differences in the solubility of PbI_2 in different solvents, the interaction between PbI_2 and solvent molecules, and the volatility properties of different solvents, the choice of solvents for the spin-coating solution is also important for the PbI_2 film obtained. DMF and DMSO are both common solvents for the dissolution of PbI_2. Here, they were introduced as the solvents for the spin-coating of PbI_2 films and their effects on the morphology of the films were investigated.

As shown in the AFM images of PbI_2 and perovskite films in **Fig. 4.10**, the DMF-based PbI_2 film was made up of particles packing loosely and irregularly, and the surface coverage was poor. While in the case of DMSO, the particle size was much smaller and the packing of particles was denser, with very good coverage. The improvement in surface coverage may be ascribed to the stronger coordination between sulfoxide oxygen with Pb^{2+} [25], and the lower volatility of DMSO, such that crystallization was initiated at a higher onset concentration[26]. After phase conversion, the particle sizes increased and surface coverage was improved for both samples compared with the PbI_2 films due to volume expansion. Particles in the perovskite film synthesised from DMSO-based PbI_2 were much smaller than that from DMF-based PbI_2 film, with excellent surface coverage. The area roughness of the film was as small as 12.1 nm, which is much smaller than the 28.1 nm of the DMF perovskite film, indicating the ultra smoothness of the DMSO films.

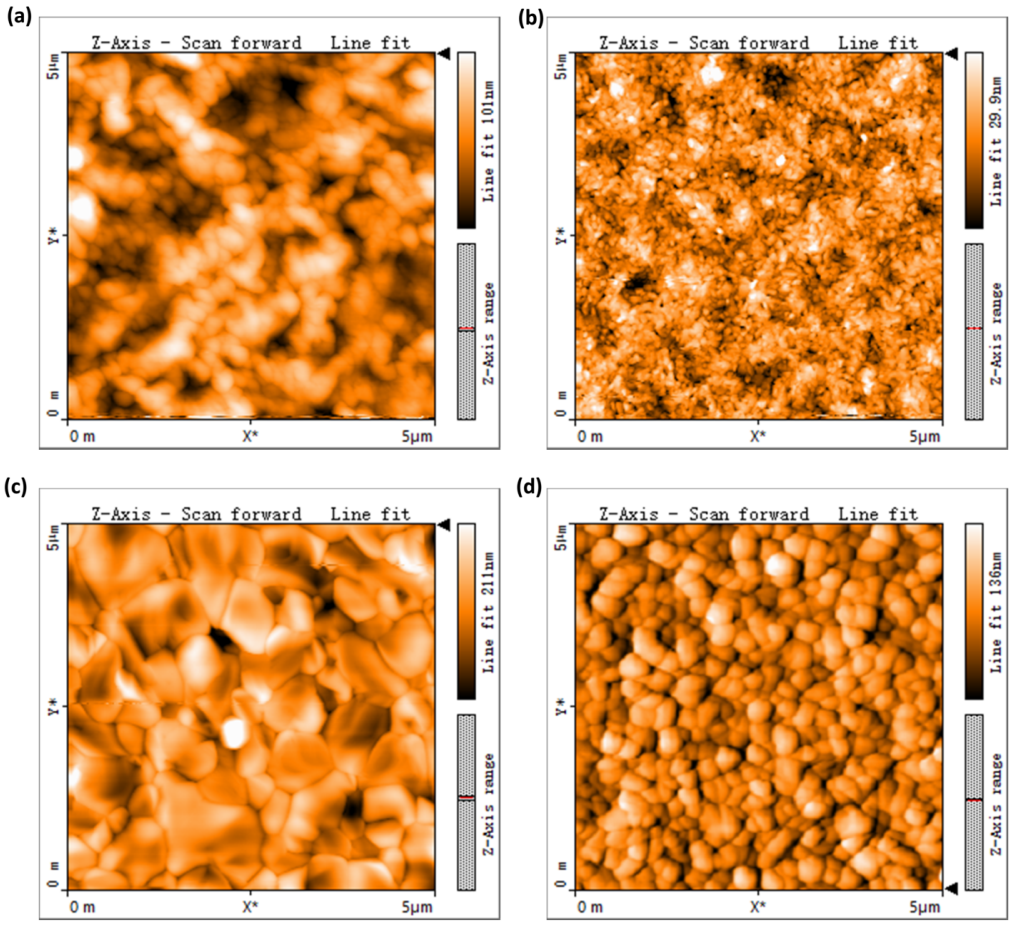

Fig. 4.10 AFM images of PbI_2 films deposited from DMF (a) and DMSO (b) and the obtained $MAPbI_3$ perovskite films (c, d) on TiO_2 blocking layers.

The effect of DMF and DMSO as solvents for PbI_2 deposition on the device performance are illustrated in the box plots of cell performance in **Fig. 4.11**. The DMF devices showed a PCE of 1.70 ± 1.17 %, with the V_{OC} of 0.81 ± 0.09 V, the J_{SC} of 7.28 ± 3.53 mA·cm^{-2} and the FF of 0.27 ± 0.07. While with DMSO as the solvent for PbI_2 deposition, the PCE of the cells was improved to 2.34 ± 0.60 %. The narrower distribution of the PCE is believed to be due to the high uniformity of the perovskite film. The V_{OC} of the cells with DMSO as the solvent was 0.81 ± 0.08 V, practically unchanged comparing with the DMF devices, and the increase of the efficiency was mainly resulted from the enhanced J_{SC} (8.61 ± 0.81 mA·cm^{-2}) and FF (0.34 ± 0.10), which could be ascribed to the better contact with the hole-transporting and electron-transporting layers due to the ultra smoothness of the perovskite film as seen from the AFM images.

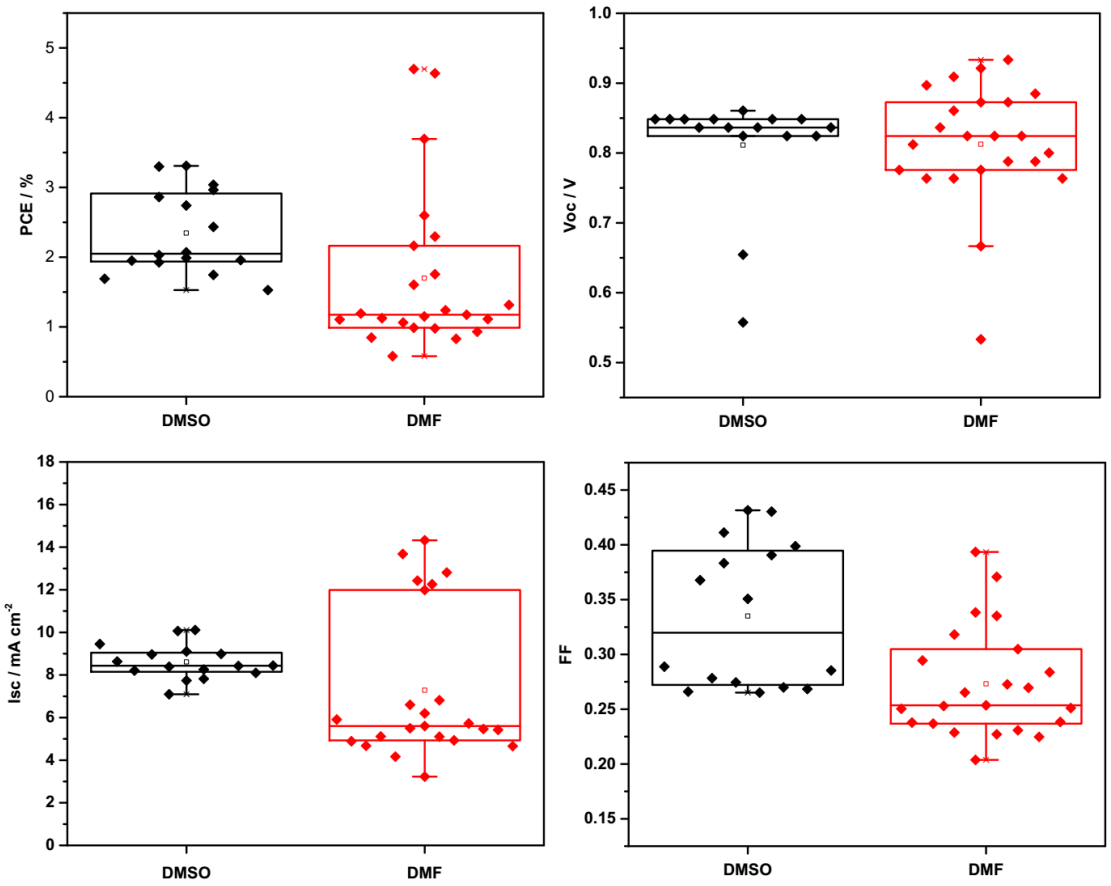

Fig. 4.11 Box plots of cell performance of devices with perovskite films synthesised from PbI_2 layers with DMF and DMSO as the solvents.

4.2.4 Lead sources

Introducing chlorine in the precursor for perovskite film deposition is a widely accepted way to improve the cell performance. Though only trace amounts of Cl can incorporate into the $MAPbI_3$ perovskite film due to the large difference between the ionic radii of Cl and I[27] and the high sublimation of MACl[28,29], the addition of Cl can not only result in the formation of perovskite films with better morphology, but more importantly it is argued that they greatly increase the carrier diffusion length of perovskite from ~ 100 nm for $MAPbI_3$ to over 1 µm for $MAPbI_{3-x}Cl_x$[30]. Here different lead salts of PbI_2 and $PbCl_2$ were used as precursors for the fabrication of perovskite films. Due to the poor solubility of $PbCl_2$ in DMF, DMSO was used as the solvent for all the samples.

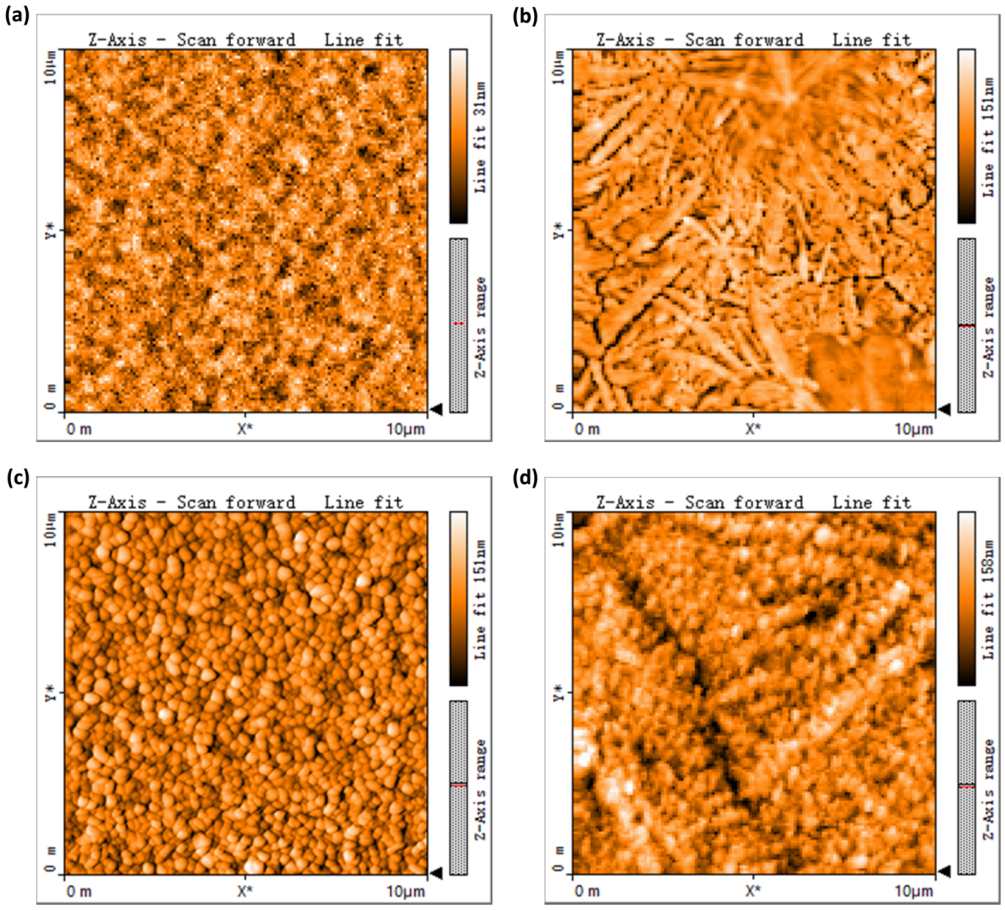

Fig. 4.12 AFM images of PbI_2 (a) and $PbCl_2$ (b) films deposited from DMSO and the obtained $MAPbI_3$ (c) and $MAPbI_{3-x}Cl_x$ (d) perovskite films on TiO_2 blocking layers.

The AFM images of PbI_2, $PbCl_2$ films and the corresponding perovskite films are shown in **Fig. 4.12**. The films showed distinctly different mophologies. The PbI_2 film was composed of very small particles in the scale of nanometres, with small pin-holes in the film. Whereas for the $PbCl_2$ film, the particles grew into bigger tree-like particles with branches and the surface coverage was relatively low, with many cracks observed in the film. After the phase conversion into perovskite, the particles in the $MAPbI_3$ film were larger than those in the PbI_2 film and packed neatly on the surface forming a highly uniform film with area roughness of 11.8 nm and superb coverage. While for the $MAPbI_{3-x}Cl_x$ film, the particle sizes were smaller than that of the $PbCl_2$ film. This may be because of the emission of MACl from the bulk of the film during the reaction which broke the grains into smaller particles. The area roughness of the film was 21.4 nm and the cracks in the $PbCl_2$ film were still observed though less significant.

The performances of the $MAPbI_3$ and $MAPbI_{3-x}Cl_x$ devices with PbI_2 and $PbCl_2$ as lead sources are shown in the box plots in **Fig. 4.13**. For the $MAPbI_3$ perovskite devices, the PCE was 2.34 ± 0.60 %, with the V_{OC} of 0.81 ± 0.08 V, the J_{SC} of 8.61 ± 0.81 mA·cm^{-2} and the FF of 0.34 ± 0.10. While for the $MAPbI_{3-x}Cl_x$ devices, the cell performances were largely improved. The PCE was increased to 3.41 ± 0.69 %, with the V_{OC} increased to 0.85 ± 0.04 V, the J_{SC} enhanced to 8.91 ± 2.59 mA·cm^{-2} and the FF increased to 0.47 ± 0.08. The performance enhancement in spite of the poorer morphology comparing with the $MAPbI_3$ film as shown in the AFM images could be attributed to the suppressed recombination. $MAPbI_{3-x}Cl_x$ perovskite has shown much longer diffusion length than $MAPbI_3$ [30] after the introduction of Cl, as a result, the possibility of recombination was greatly reduced.

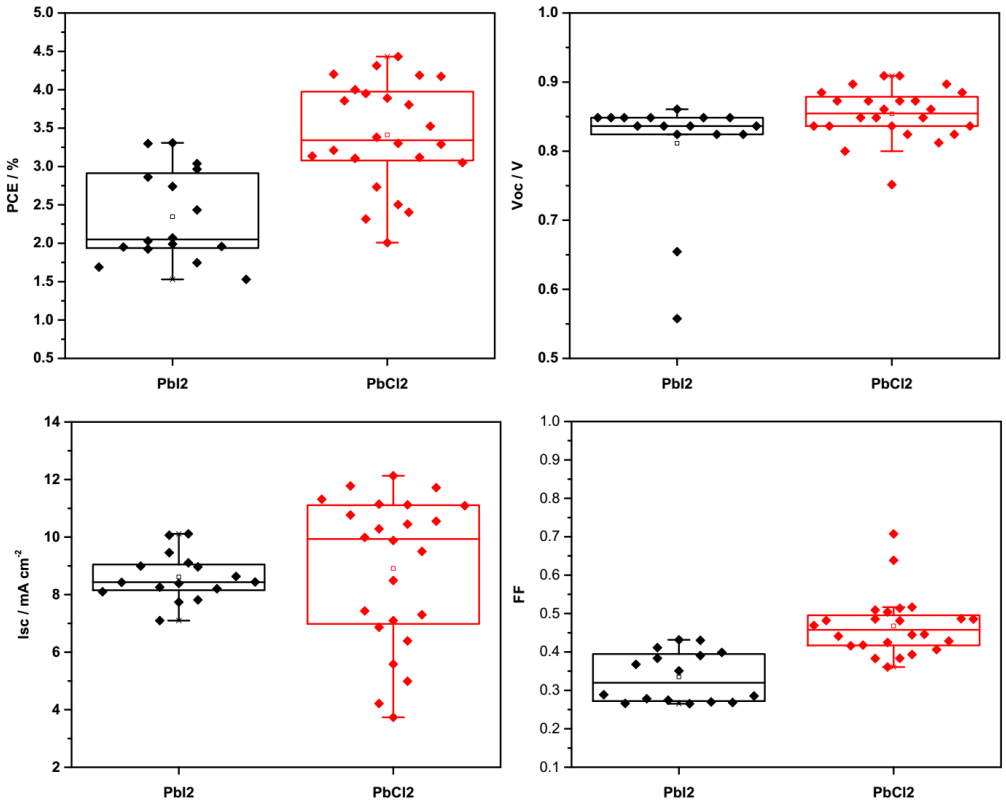

Fig. 4.13 Box plots of cell performance of devices with $MAPbI_3$ and $MAPbI_{3-x}Cl_x$ perovskite films synthesised from PbI_2 and $PbCl_2$ as the lead sources.

Although the vapour assisted sequential method has been reported to give decent efficiencies in literature[31,32], it did not in these experiments, so other techniques were investigated.

4.3 Sequential spin-coating method

The sequential spin-coating method is another two-step processing method for the synthesis of perovskite thin films which involves the spin-coating of MAI solution on top of PbI_2 films. The interdiffusion and reaction of the two stacking layers result in the formation of $MAPbI_3$ perovskite films. Sequential spin-coating deposition can also achieve a better control of the perovskite crystal growth, and compared with the vapour-assisted sequential deposition process, it only requires simple spin-coating operations and does not require special experiment setups. In the sequential spin-coating process, the concentration of MAI solution is a very important factor influencing the conversion of PbI_2 into perovskite. It determines not only the thickness of the MAI layer, but also the diffusion of MAI into the PbI_2 layer and the nucleation of perovskite during the loading time[33]. Thus, different MAI concentrations of 10 mg/mL, 30 mg/mL and 50 mg/mL were investigated for the sequential spin-coating deposition of $MAPbI_3$ films.

As seen from the AFM images of the $MAPbI_3$ films in **Fig. 4.14**, MAI concentration made no big differences to the grain sizes of the perovskite films. All the films showed particles sizes of 200-300 nm. The trend was consistent with Nam-Gyu Park *et al*.'s report[33] which showed the perovskite particle size decreased exponentially to an asymptotic plateau with the increase of MAI concentration. The particle sizes of our perovskite films are larger than that in the report (90 nm for MAI concentration of 10 mg/mL), which is believed to be due to the formation of $MAPbI_3 \cdot H_2O$ intermediate during the air exposure process before annealing[34]. Notably, the films made with 30 mg/mL and 50 mg/mL MAI showed remarkable compactness and better surface coverage than that with 10 mg/mL MAI, and the film made with 30 mg/mL MAI exhibited the lowest area roughness (15.4 ± 2.3 nm) comparing with 21.4 ± 4.8 nm of that with 10 mg/mL MAI and 20.5 ± 1.5 nm of that with 50 mg/mL MAI. However, the conversion of PbI_2 was complete only when the MAI concentration was as high as 50 mg/mL, as illustrated in the XRD spectra in **Fig. 4.14**d. The diffraction peaks at 12.5 ° indicated the existence of PbI_2 in the films made with MAI concentrations of 10 mg/mL and 30 mg/mL, and the intensity was much stronger for the 10 mg/mL film, suggesting the very poor phase conversion. Due to the poor light-absorbing and charge-transferring ability of PbI_2 comparing with perovskite, the residue

of large amounts of PbI_2 in perovskite films would result in the poor performance of the photovoltaic devices.

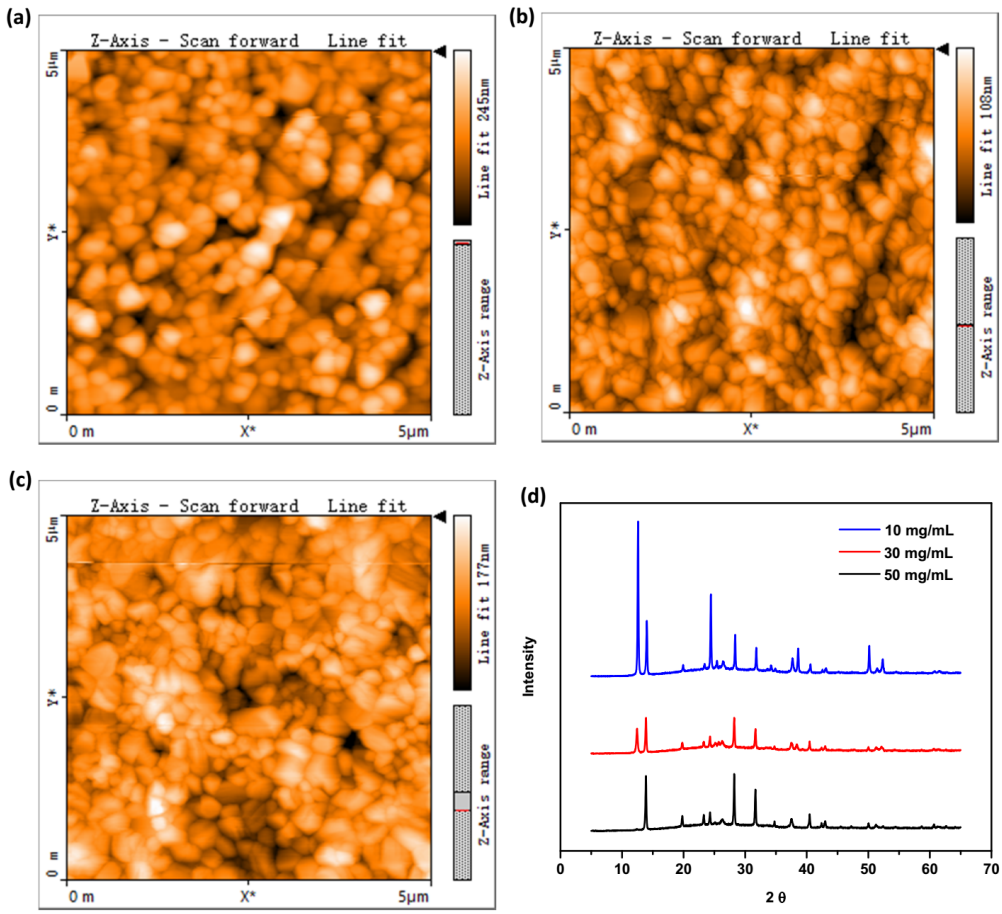

Fig. 4.14 AFM images of $MAPbI_3$ films synthesised with sequential spin-coating method with MAI concentrations of 10 mg/mL (a), 30 mg/mL (b) and 50 mg/mL (c), and XRD patterns (d) of the films on TiO_2 blocking layers.

Cell performances of devices with the $MAPbI_3$ films are shown in **Fig. 4.15**. The cells with perovskite films synthesised with MAI concentration of 30 mg/mL showed the best PCE of 5.1 ± 2.7 %, with the V_{OC} of 1.00 ± 0.02 V, the J_{SC} of 11.1 ± 2.5 mA·cm^{-2} and the FF of 0.44 ± 0.14 (champion: PCE 9.5%, J_{SC} 14.5 mA·cm^{-2}, V_{OC} 1.02 V and FF 0.64). When the MAI concentration was decreased to 10 mg/mL, the J_{SC} dropped to 6.12 ± 2.75 mA·cm^{-2} and the FF dropped to 0.34 ± 0.06, leading to the decrease of the PCE to 2.12 ± 1.21%. The poor cell performance is believed to be caused by the large amount of unconverted PbI_2 in the perovskite films. With the concentration of MAI increased to 50 mg/mL, however, the cell performance also became worse, even though the $MAPbI_3$ film showed good surface coverage and complete conversion of PbI_2 as shown in

Fig. 4.14. The PCE dropped to 1.09 ± 0.67 %, the J_{SC} decreased to 5.78 ± 3.95 mA·cm^{-2} and the FF decreased to 0.26 ± 0.12, even worse than that of the 10 mg/mL cells. The better performance of the 30 mg/mL cells than the 50 mg/mL cells could be due to the existence of the small amount of PbI_2 in the perovskite films as discussed previous, which passivated the grain boundaries and decreased recombination[21,22]. The very poor performance of the 50 mg/mL cells might be also because of the excess of the MAI in the perovskite films which hindered the charge transfer.

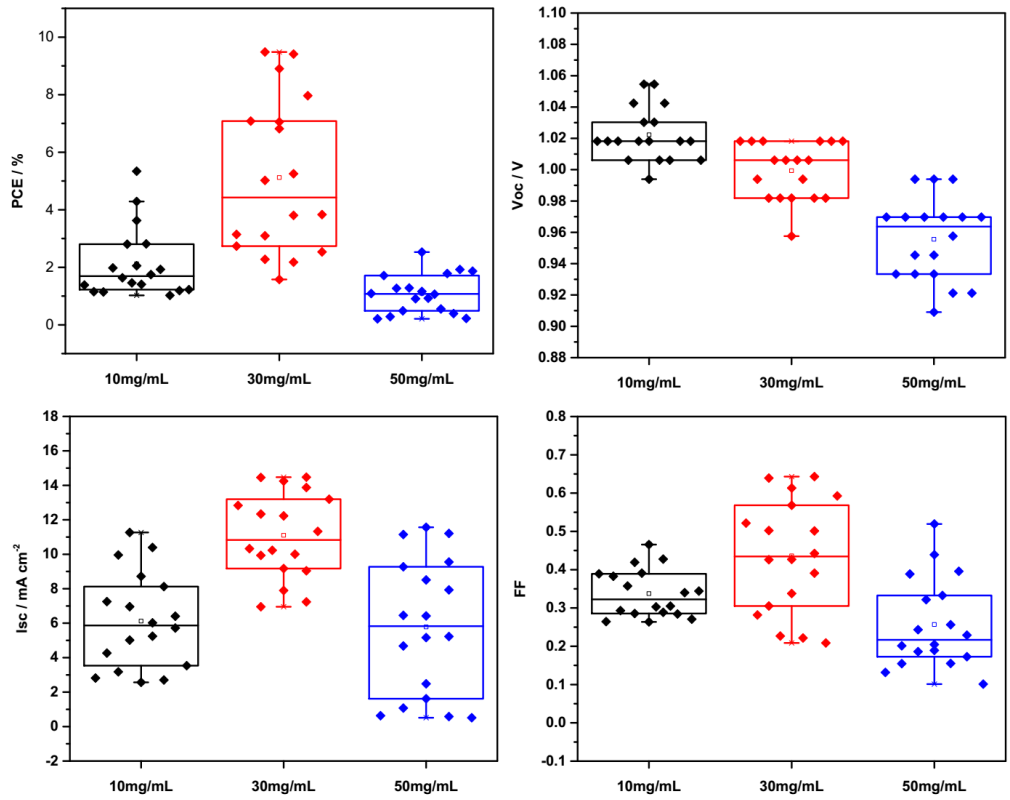

Fig. 4.15 Box plots of cell performance of devices with $MAPbI_3$ films synthesised with sequential spin-coating method with different MAI concentrations.

4.4 One-step method

One-step synthesis of perovskite films involves the straightforward deposition, mainly by spin-coating, of the perovskite precursor solution containing both the lead and ammonium ingredients. It is the simplest process for the preparation of perovskite thin films. However, the performance of the devices is strongly dependent on many factors, including humidity[12,13], atmosphere[14,15], lead sources[35,36] and precursor recipes[37]. In this

work, different recipes of MAI:$PbCl_2$=3:1 and MAI:PbI_2:$PbCl_2$=4:1:1 are studied as the precursors for perovskite deposition and syntheses carried out in air with humidity of below 35 % and in a nitrogen-filled dry box are compared.

Fig. 4.16 shows the XRD spectra of the $MAPbI_{3-x}Cl_x$ films. All the films showed high phase purities of perovskite structure. The strong diffraction peaks at 14.2 ° and 28.5 ° were assigned to the (110) and (220) facets of tetragonal perovskite crystals. No visible peaks of PbI_2 were observed, indicating the complete conversion of the reactants. The peak intensities of the 3:1 samples were much higher than that of the 4:1:1 samples, suggesting better crystallinity. It could be due to the faster crystallisation of the 4:1:1 samples which were observed to turn dark much faster than the 3:1 samples. The reaction of PbI_2 with MAI was much faster than $PbCl_2$, therefore $MAPbI_3$ perovskite crystallites formed very quickly in the 4:1:1 films and accelerated the growth of $MAPbI_{3-x}Cl_x$ [37]. Notably, for the recipe of 3:1, the films synthesised in the dry box showed better crystallinity than in air, whereas better crystallinity was achieved in air with the recipe of 4:1:1.

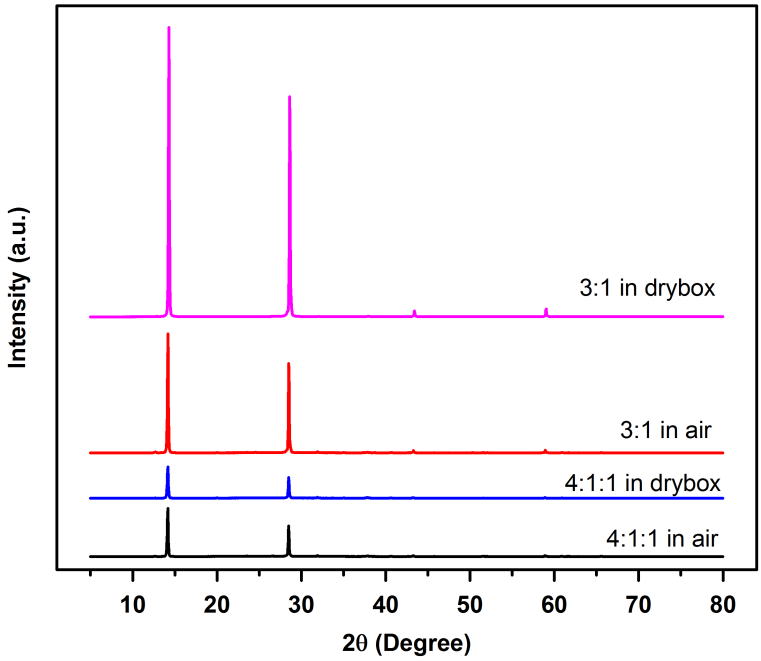

Fig. 4.16 XRD patterns of $MAPbI_{3-x}Cl_x$ films prepared through one-step spin-coating process with the recipes of 3:1 and 4:1:1 in air and in a dry box.

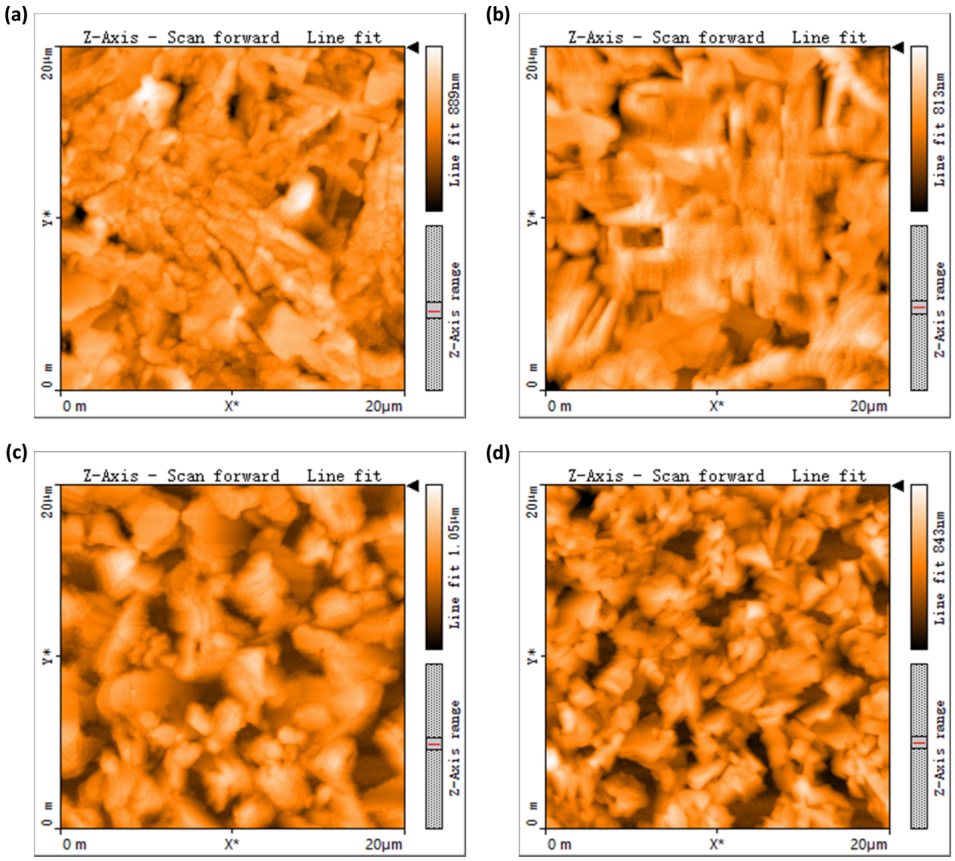

Fig. 4.17 AFM images of $MAPbI_{3-x}Cl_x$ films prepared via one-step spin-coating process with the recipes of: 3:1 in air (a) and in the dry box (b); and 4:1:1 in air (c) and in the dry box (d).

The morphologies of the $MAPbI_{3-x}Cl_x$ films are illustrated in **Fig. 4.17**. The films prepared with the recipe of 3:1 in air and in the dry box both showed high compactness and good surface coverage, whereas numerous voids were observed in the films synthesised with the recipe of 4:1:1. The films prepared with the 3:1 recipe showed a high coverage of 97-98%, as estimated with Matlab, whereas the 4:1:1 films exhibited a surface of $\sim$90%. It has been reported that the one-step deposition of $MAPbI_{3-x}Cl_x$ using 4:1:1 recipe can produce more uniform films than using 3:1 recipe[37], as the rapid reaction of MAI with PbI_2 preforms $MAPbI_3$ perovskite domains which help the sequential growth of the perovskite film. Our experiment, however, showed the contrary. It could be due to the different annealing process used during the deposition, as the formation of $MAPbI_{3-x}Cl_x$ film has been shown highly sensitive to the thermal annealing condition[38]. In our deposition, hot-casting was applied, in which the substrates were kept hot at 100 °C during spin-coating. The hot-casting process has been shown capable of producing uniform $MAPbI_{3-x}Cl_x$ films with large grains[39], but may not be ideal for the 4:1:1 recipe.

Similar trend with the surface coverage was seen for the absorption of the films, as shown in the UV-vis spectra in **Fig. 4.18**. All the films showed absorption onsets of ~ 800 nm, indicating a bandgap of 1.55 eV. The films prepared with the 3:1 recipe gave stronger absorption than those made with the 4:1:1 recipe, which could be likely due to their better surface coverage as discussed above. Another possible reason could be the difference in the thickness of the films due to the different compositions of the precursor solutions. In addition, for both the recipes, the films made in the dry box showed better light absorption properties than in air. Since the surface morphology and coverage of the films made in air and in the dry box were quite similar as shown in **Fig. 4.17**, the different absorption is most likely to be due to the difference in the film thickness. The different atmosphere, air flow and temperature in the dry box and in ambient may cause the different evaporation rate of the solvent during spin-coating, resulting in the different thickness of the perovskite films.

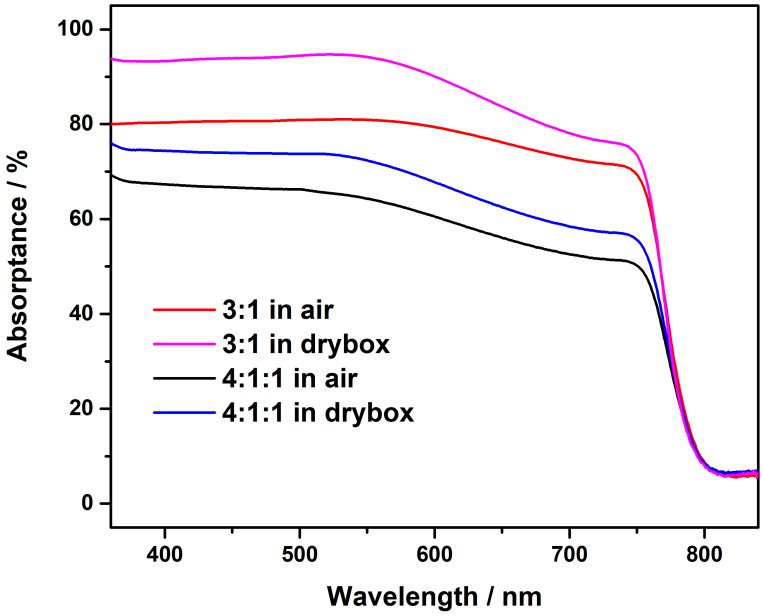

Fig. 4.18 UV-vis absorption spectra of FTO/c-TiO_2/$MAPbI_{3-x}Cl_x$ films prepared through one-step spin-coating process with the recipes of 3:1 and 4:1:1 in air and in the dry box. The absorptance A% is calculated by A%=1-T%-R% where T% and R% are the transmittance and reflectance respectively.

The cell performances of the devices with one-step processed$MAPbI_{3-x}Cl_x$ films are shown in **Fig. 4.19**. All the cells made with the 3:1 recipe showed better performance than those with 4:1:1 recipe, giving the PCEs of 12.1 ± 0.7 % and 10.8 ± 0.9 % for made in air and in the dry box respectively, comparing with 9.0 ± 0.6 % and 8.0 ± 0.7 % for those with the

4:1:1 recipe. Significantly better J_{SC} was observed for the 3:1 cells ($20.7 \pm 0.6\,mA{\cdot}cm^{-2}$ in air, and $20.4 \pm 0.9\,mA{\cdot}cm^{-2}$ in the dry box) compared with the 4:1:1 cells ($16.8 \pm 0.5\,mA{\cdot}cm^{-2}$ in air, and $16.3 \pm 0.7\,mA{\cdot}cm^{-2}$ in the dry box). The J_{SC} enhancements were due to the better surface coverage and the better light absorption as shown in **Fig. 4.17** and **Fig. 4.18**. Moreover, better cell performance was achieved for the cells made in air than in the dry box, mainly due to the enhanced V_{OC}. The cell made in air showed a V_{OC} of 0.97 ± 0.03 V with the 3:1 recipe and 0.91 ± 0.03 V with the 4:1:1 recipe, whereas those made in the dry box showed the V_{OC} of 0.92 ± 0.04 V (3:1 cells) and 0.85 ± 0.03 V (4:1:1 cells) respectively. This could be due to the suppressed recombination in the perovskite films made in the ambient air with controlled humidity. Yang and coworkers[14] have reported the annealing of perovskite films in ambient air with a humidity of $35 \pm 5\%$, and illustrated the increased PL lifetime of the films, indicating suppressed non-radiative recombination, which consequently improved the cell performance.

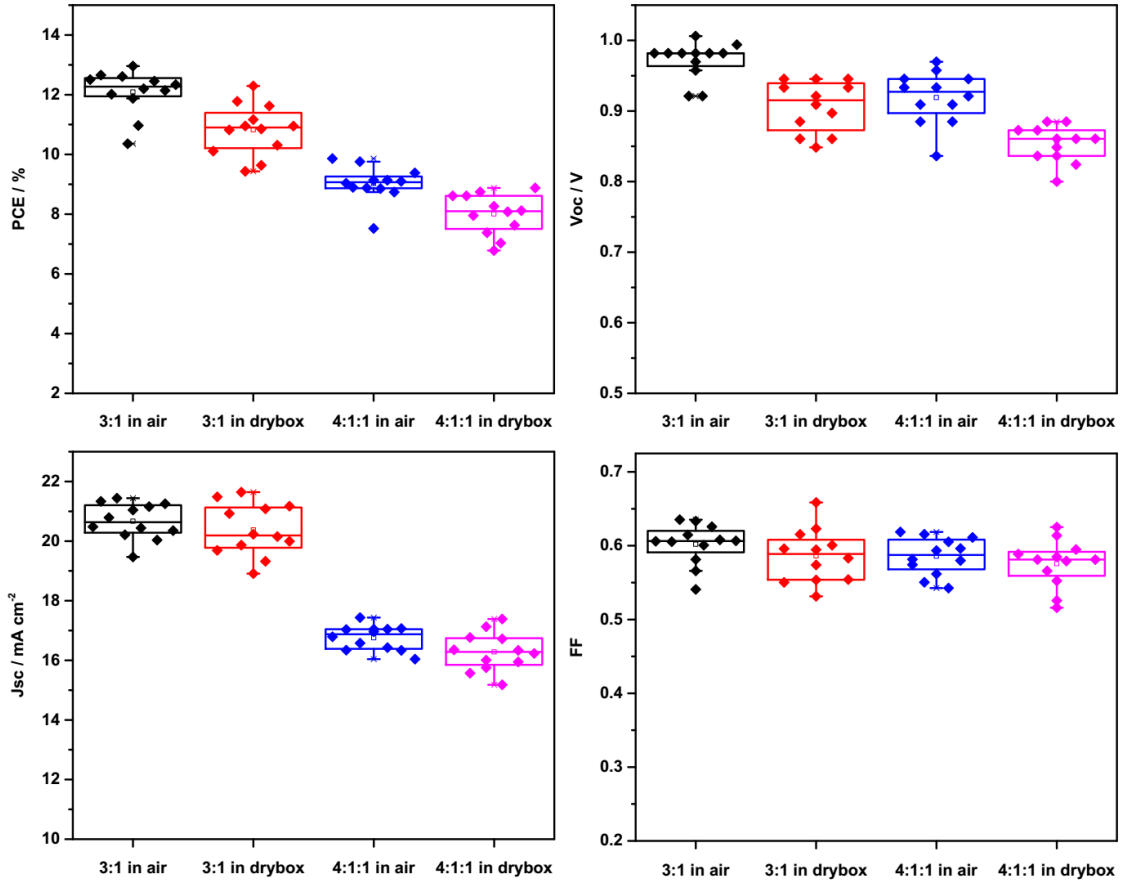

Fig. 4.19 Box plots of cell performance of devices made through one-step spin-coating process with the recipes of 3:1 and 4:1:1 in air and in the dry box.

Table 4.2 Performance parameters for cells made through one-step spin-coating process with the recipes of 3:1 and 4:1:1 in air and in the dry box.

Recipes	Atmosphere	V_{OC} [V]	J_{SC} [mA·cm^{-2}]	FF	PCE [%]
3:1	air	0.97 ± 0.03	20.7 ± 0.6	0.60 ± 0.03	12.1 ± 0.7
	drybox	0.91 ± 0.03	20.4 ± 0.9	0.59 ± 0.04	10.8 ± 0.9
4:1:1	air	0.92 ± 0.04	16.8 ± 0.5	0.58 ± 0.02	9.0 ± 0.6
	dry box	0.85 ± 0.03	16.3 ± 0.7	0.58 ± 0.03	8.0 ± 0.7

4.5 Conclusions

In this chapter, vapour-assisted sequential method, sequential spin-coating method and one-step spin-coating method were adapted for the synthesis of perovskite layers as absorbing layers for perovskite solar cells. Different factors such as solvents, temperature and precursor recipes were investigated, to establish a robust procedure for the fabrication of high quality perovskite layers, and set a foundation for the following works.

For the vapour-assisted sequential process, a high temperature of 150 °C was necessary for the complete conversion of PbI_2, but the trace amount of residual PbI_2 in the films made at 130 °C improved the cell performance by passivating the grain boundaries and reducing the recombination. Chlorobenzene dripping during the spin-coating of PbI_2 helped improving the coverage and compactness of the PbI_2 film, which may however have hindered the infiltration of MAI and caused the incomplete conversion of PbI_2 at the bottom. DMSO as the solvent for PbI_2 deposition resulted in smaller particles and better uniformity of the PbI_2 films, and consequently ultra smooth perovskite films and better cell performance. Perovskite films prepared with $PbCl_2$ as the lead source showed poorer surface coverage and uniformity than PbI_2, but better cell performance was still achieved due to the greatly improved carrier diffusion length.

For sequential spin-coating method, a concentration of 50 mg/mL for the MAI solution is required for the complete conversion of the PbI_2 precursor films, while the lower concen-

tration of 30 mg/mL gave better surface smoothness of the perovskite films and the trace PbI_2 residue passivated the grain boundaries and reduced the recombination, giving rise to the better PCEs of 5.12 ± 2.69 %.

For one-step spin-coating process, the recipe of MAI:$PbCl_2$=3:1 produced $MAPbI_{3-x}Cl_x$ with better surface coverage and light absorption than the recipe of MAI:PbI_2:$PbCl_2$=4:1:1, likely to be due to the slower crystallisation of $MAPbI_{3-x}Cl_x$ than $MAPbI_3$, and consequently better cell performance was achieved. Besides, improved cell performance was seen for the cells made in air with relative humidity of < 35 % than in the dry box, which could be due to the suppressed recombination in the perovskite films made in ambient air with the assistance of controlled humidity.

Finally, one-step spin-coating of MAI:$PbCl_2$=3:1 solution gave the best cell performance, with the PCE of 12.1 ± 0.7 % in air and 10.8 ± 0.9 % in the dry box, respectively, with high reliability and reproducibility. The process was set as the baseline for the cell fabrication in the studies of TiO_2 doping in the next chapter.

Reference

[1] W.G.J.A. H., S. Max, S.A. Miquel, M. Cristina, . Jorge, and B.H. J. Trap-assisted non-radiative recombination in organic-inorganic perovskite solar cells. *Advanced Materials*, 27(11):1837–1841, 2015.

[2] X. Wen, Y. Feng, S. Huang, F. Huang, Y.-B. Cheng, M. Green, and A. Ho-Baillie. Defect trapping states and charge carrier recombination in organic-inorganic halide perovskites. *Journal of Materials Chemistry C*, 4(4):793–800, 2016.

[3] M. Xiao, F. Huang, W. Huang, Y. Dkhissi, Y. Zhu, J. Etheridge, A. Gray-Weale, U. Bach, Y.B. Cheng, and L. Spiccia. A fast deposition-crystallization procedure for highly efficient lead iodide perovskite thin-film solar cells. *Angewandte Chemie International Edition*, 53(37):9898–903, 2014.

[4] N.J. Jeon, J.H. Noh, Y.C. Kim, W.S. Yang, S. Ryu, and S.I. Seok. Solvent engineer-

ing for high-performance inorganic-organic hybrid perovskite solar cells. *Nature Materials*, 13(9):897–903, 2014.

[5] Y. Zhou, M. Yang, W. Wu, A.L. Vasiliev, K. Zhu, and N.P. Padture. Room-temperature crystallization of hybrid-perovskite thin films via solventsolvent extraction for high-performance solar cells. *Journal of Materials Chemistry A*, 3(15):8178–8184, 2015.

[6] M. Yin, F. Xie, H. Chen, X. Yang, F. Ye, E. Bi, Y. Wu, M. Cai, and L. Han. Annealing-free perovskite films by instant crystallization for efficient solar cells. *Journal of Materials Chemistry A*, 4(22):8548–8553, 2016.

[7] Z. Xiao, Q. Dong, C. Bi, Y. Shao, Y. Yuan, and J. Huang. Solvent annealing of perovskite-induced crystal growth for photovoltaic-device efficiency enhancement. *Advanced Materials*, 26(37):6503–6509, 2014.

[8] W. Zhu, T. Yu, F. Li, C. Bao, H. Gao, Y. Yi, J. Yang, G. Fu, X. Zhou, and Z. Zou. A facile, solvent vapor-fumigation-induced, self-repair recrystallization of $CH_3NH_3PbI_3$ films for high-performance perovskite solar cells. *Nanoscale*, 7(12):5427–5434, 2015.

[9] Y. Chen, Y. Zhao, and Z. Liang. Non-thermal annealing fabrication of efficient planar perovskite solar cells with inclusion of nh4cl. *Chemistry of Materials*, 27(5):1448–1451, 2015.

[10] C.-C. Chen, Z. Hong, G. Li, Q. Chen, H. Zhou, and Y. Yang. One-step, low-temperature deposited perovskite solar cell utilizing small molecule additive. *Journal of Photonics for Energy*, 5(1):057405, 2015.

[11] P.W. Liang, C.Y. Liao, C.C. Chueh, F. Zuo, S.T. Williams, X.K. Xin, J. Lin, and A.K. Jen. Additive enhanced crystallization of solution-processed perovskite for highly efficient planar-heterojunction solar cells. *Advanced Materials*, 26(22):3748–3754, 2014.

[12] M.K. Gangishetty, R.W.J. Scott, and T.L. Kelly. Effect of relative humidity on crystal growth, device performance and hysteresis in planar heterojunction perovskite solar cells. *Nanoscale*, 8(12):6300–6307, 2016.

[13] D. Li, S.A. Bretschneider, V.W. Bergmann, I.M. Hermes, J. Mars, A. Klasen, H. Lu, W. Tremel, M. Mezger, H.-J. Butt, S.A.L. Weber, and R. Berger. Humidity-induced grain boundaries in $MAPbI_3$ perovskite films. *The Journal of Physical Chemistry C*, 120(12):6363–6368, 2016.

[14] J. You, Y. Yang, Z. Hong, T.-B. Song, L. Meng, Y. Liu, C. Jiang, H. Zhou, W.-H. Chang, G. Li, and Y. Yang. Moisture assisted perovskite film growth for high performance solar cells. *Applied Physics Letters*, 105(18):183902, 2014.

[15] S. Pathak, A. Sepe, A. Sadhanala, F. Deschler, A. Haghighirad, N. Sakai, K.C. Goedel, S.D. Stranks, N. Noel, M. Price, S. Httner, N.A. Hawkins, R.H. Friend, U. Steiner, and H.J. Snaith. Atmospheric influence upon crystallization and electronic disorder and its impact on the photophysical properties of organicinorganic perovskite solar cells. *ACS Nano*, 9(3):2311–2320, 2015.

[16] A. Dualeh, N. Ttreault, T. Moehl, P. Gao, M.K. Nazeeruddin, and M. Grätzel. Effect of annealing temperature on film morphology of organicinorganic hybrid pervoskite solid-state solar cells. *Advanced Functional Materials*, 24(21):3250–3258, 2014.

[17] X. Ren, Z. Yang, D. Yang, X. Zhang, D. Cui, Y. Liu, Q. Wei, H. Fan, and S. Liu. Modulating crystal grain size and optoelectronic properties of perovskite films for solar cells by reaction temperature. *Nanoscale*, 8(6):3816–3822, 2016.

[18] A. Ummadisingu, L. Steier, J.-Y. Seo, T. Matsui, A. Abate, W. Tress, and M. Grätzel. The effect of illumination on the formation of metal halide perovskite films. *Nature*, 545(7653):208–212, 2017.

[19] T. Oku. *Crystal structures of $CH_3NH_3PbI_3$ and related perovskite compounds used for solar cells*, page Ch. 03. InTech, Rijeka, 2015.

[20] D.W. deQuilettes, S.M. Vorpahl, S.D. Stranks, H. Nagaoka, G.E. Eperon, M.E. Ziffer, H.J. Snaith, and D.S. Ginger. Impact of microstructure on local carrier lifetime in perovskite solar cells. *Science*, 348(6235):683–686, 2015.

[21] Q. Chen, H. Zhou, T.-B. Song, S. Luo, Z. Hong, H.-S. Duan, L. Dou, Y. Liu, and Y. Yang. Controllable self-induced passivation of hybrid lead iodide perovskites toward high performance solar cells. *Nano Letters*, 14(7):4158–4163, 2014.

[22] Y.C. Kim, N.J. Jeon, J.H. Noh, W.S. Yang, J. Seo, J.S. Yun, A. Ho-Baillie, S. Huang, M.A. Green, J. Seidel, T.K. Ahn, and S.I. Seok. Beneficial effects of PbI_2 incorporated in organo-lead halide perovskite solar cells. *Advanced Energy Materials*, 6(4):1502104, 2016.

[23] T. Zhang, M. Yang, Y. Zhao, and K. Zhu. Controllable sequential deposition of planar $CH_3NH_3PbI_3$ perovskite films via adjustable volume expansion. *Nano Letters*, 15(6):3959–3963, 2015.

[24] D. Bae, A. Palmstrom, K. Roelofs, B. Mei, I. Chorkendorff, S.F. Bent, and P.C.K. Vesborg. Tailoring mixed-halide, wide-gap perovskites via multistep conversion process. *ACS Appl Mater Interfaces*, 8(23):14301–14306, 2016.

[25] Y. Wu, A. Islam, X. Yang, C. Qin, J. Liu, K. Zhang, W. Peng, and L. Han. Retarding the crystallization of PbI_2 for highly reproducible planar-structured perovskite solar cells via sequential deposition. *Energy & Environmental Science*, 7(9):2934–2938, 2014.

[26] J.H. Heo, D.H. Song, and S.H. Im. Planar $CH_3NH_3PbBr_3$ hybrid solar cells with 10.4% power conversion efficiency, fabricated by controlled crystallization in the spin-coating process. *Advanced Materials*, 26(48):8179–8183, 2014.

[27] Q. Chen, H. Zhou, Y. Fang, A.Z. Stieg, T.-B. Song, H.-H. Wang, X. Xu, Y. Liu, S. Lu, J. You, P. Sun, J. McKay, M.S. Goorsky, and Y. Yang. The optoelectronic role of chlorine in $CH_3NH_3PbI_3$(Cl)-based perovskite solar cells. *Nature Communications*, 6(1):7269, 2015.

[28] N. Yantara, F. Yanan, C. Shi, H.A. Dewi, P.P. Boix, S.G. Mhaisalkar, and N. Mathews. Unravelling the effects of cl addition in single step $CH_3NH_3PbI_3$ perovskite solar cells. *Chemistry of Materials*, 27(7):2309–2314, 2015.

[29] A. Dualeh, P. Gao, S.I. Seok, M.K. Nazeeruddin, and M. Grätzel. Thermal behavior of methylammonium lead-trihalide perovskite photovoltaic light harvesters. *Chemistry of Materials*, 26(21):6160–6164, 2014.

[30] S.D. Stranks, G.E. Eperon, G. Grancini, C. Menelaou, M.J.P. Alcocer, T. Leijtens, L.M. Herz, A. Petrozza, and H.J. Snaith. Electron-hole diffusion lengths

exceeding 1 micrometer in an organometal trihalide perovskite absorber. *Science*, 342(6156):341–344, 2013.

[31] Q. Chen, H. Zhou, Z. Hong, S. Luo, H.-S. Duan, H.-H. Wang, Y. Liu, G. Li, and Y. Yang. Planar heterojunction perovskite solar cells via vapor-assisted solution process. *Journal of the American Chemical Society*, 136(2):622–625, 2014.

[32] S. Casaluci, L. Cin, A. Pockett, P.S. Kubiak, R.G. Niemann, A. Reale, A. Di Carlo, and P.J. Cameron. A simple approach for the fabrication of perovskite solar cells in air. *Journal of Power Sources*, 297:504–510, 2015.

[33] J.-H. Im, I.-H. Jang, N. Pellet, M. Grätzel, and N.-G. Park. Growth of $CH_3NH_3PbI_3$ cuboids with controlled size for high-efficiency perovskite solar cells. *Nature Nanotechnology*, 9(11):927–932, 2014.

[34] B. Yang, O. Dyck, J. Poplawsky, J. Keum, A. Puretzky, S. Das, I. Ivanov, C. Rouleau, G. Duscher, D. Geohegan, and K. Xiao. Perovskite solar cells with near 100% internal quantum efficiency based on large single crystalline grains and vertical bulk heterojunctions. *Journal of the American Chemical Society*, 137(29):9210–9213, 2015.

[35] F.K. Aldibaja, L. Badia, E. Mas-Marz, R.S. Snchez, E.M. Barea, and I. Mora-Sero. Effect of different lead precursors on perovskite solar cell performance and stability. *Journal of Materials Chemistry A*, 3(17):9194–9200, 2015.

[36] W. Zhang, M. Saliba, D.T. Moore, S.K. Pathak, M.T. Horantner, T. Stergiopoulos, S.D. Stranks, G.E. Eperon, J.A. Alexander-Webber, A. Abate, A. Sadhanala, S. Yao, Y. Chen, R.H. Friend, L.A. Estroff, U. Wiesner, and H.J. Snaith. Ultrasmooth organic-inorganic perovskite thin-film formation and crystallization for efficient planar heterojunction solar cells. *Nature Communications*, 6(1):6142, 2015.

[37] D. Wang, Z. Liu, Z. Zhou, H. Zhu, Y. Zhou, C. Huang, Z. Wang, H. Xu, Y. Jin, B. Fan, S. Pang, and G. Cui. Reproducible one-step fabrication of compact $MAPbI_{3-x}Cl_x$ thin films derived from mixed-lead-halide precursors. *Chemistry of Materials*, 26(24):7145–7150, 2014.

[38] G.E. Eperon, V.M. Burlakov, P. Docampo, A. Goriely, and H.J. Snaith. Morphological control for high performance, solution-processed planar heterojunction perovskite solar cells. *Advanced Functional Materials*, 24(1):151–157, 2014.

[39] W. Nie, H. Tsai, R. Asadpour, J.-C. Blancon, A.J. Neukirch, G. Gupta, J.J. Crochet, M. Chhowalla, S. Tretiak, M.A. Alam, H.-L. Wang, and A.D. Mohite. High-efficiency solution-processed perovskite solar cells with millimeter-scale grains. *Science*, 347(6221):522–525, 2015.

Chapter 5

Doped-TiO_2 for Perovskite Solar Cells

Due to the fact that perovskite solar cells evolved from DSSCs, the most commonly used ETL for n-i-p perovskite solar cells has been TiO_2 due to its excellent optical transmittance and good chemical stability at high temperature in air. However, it has also been reported to possess a relatively low electron mobility[1,2] ($10^{-4}\,cm^2\,V^{-1}\,s^{-1}$) and poorer charge transfer[3,4] from perovskite layers when compared to other ETLs such as ZnO and PCBM. To facilitate charge transfer, a few approaches have been developed, including applying interlayers between perovskite and TiO_2 layers[5,6], surface treatments[2] and defect control[7,8] of TiO_2 layers.

TiO_2 generally displays n-type semiconducting properties due to the formation of oxygen vacancies or titanium interstitials during the film preparation which both are donor-type defects[9]. Therefore, controlling the defect states by varying the annealing atmosphere or introducing doping ions can significantly change the semiconductive properties. However, the effects of these defect states on the performance of the perovskite solar cells are rather inconsistent between reports, and sometimes even contrary. Yu-Che Ho et al.[8] reported reduced oxygen vacancies in TiO_2 films by annealing them in oxygen. They argued that trap-assisted recombination was significantly decreased due to the reduced defect states, which resulted in improved perovskite solar cell performance. However, Yanbo Li's work[7] showed deep trap states introduced by depositing the TiO_2 films in an oxygen-deficient environment could improve the photo-conductivity of the TiO_2 films and therefore improve the cell performance.

Doping of TiO_2 has been widely investigated to modify its semiconductive electronic

properties in dye sensitised solar cells[10], and has also been reported to be able to greatly improve the performance of perovskite solar cells. Zhou et al.[11] reported Y-doped TiO_2 as an effcient ETL and managed to achieve a high PCE of 19.3% for planar $MAPbI_3$ perovskite solar cells. Giordano et al.[12] reported the n-doping of TiO_2 with lithium which partially reduced Ti^{4+} to Ti^{3+}; they believed that this passivated trap states acting as non-radiative recombination centres. Using Li-doped mesoporous TiO_2 electrodes, the PCE of the perovskite solar cells was successfully improved from 17% to over 19% with negligible hysteresis. Peng et al.[13] used indium-doped TiO_2 as an ETL for pervoskite solar cells, which they argued exhibited increased carrier density and better aligned band energies, and successfully improved the steady-state efficiency of the $MAPbI_3$ based cells from 13.5% to 17.9%. However, the effect of metal doping on the electronic properties of TiO_2 are not always clear. Zn-doping, for instance, has been reported to negatively shift the flat band potential V_{FB} of TiO_2 in some works[14,15], but to positively shift the V_{FB} in others[10,16].

It has been argued that doping can affect the energy levels of TiO_2 in two different ways[10] according to the influence on the number of trap states, as shown in **Fig. 5.1**. In n-type doping, as shown in **Fig. 5.1**b, doping decreases the number of deep trap states, causing an upward shift of E_F and CB . Whereas in p-type doping shown in **Fig. 5.1**c, more deep traps are formed, resulting in the downward shift of the CB and E_F.

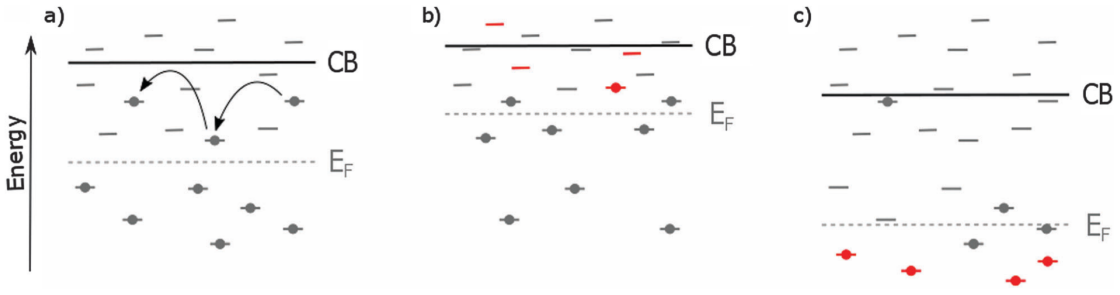

Fig. 5.1 The effect of doping on the CB and E_F of TiO_2. States induced by the doping are shown in red. (a) pristine TiO_2; (b) n-type doping; (c) p-type doping.[10]

In this work, metal ions with different oxidation states were investigated as dopants for TiO_2 films, and the impacts of the dopants on the morphology, optical and semiconductive electronic properties and also the performance of the perovskite solar cells were studied.

5.1 Experimental

Deposition of TiO_2 ETLs were conducted via a spray pyrolysis process. 0.2 M titanium diisopropoxide bis(acetylacetone) solution in ethanol was sprayed onto clean FTO substrates placed on a hot plate at 450 °C using a hand held atomizer. Spraying was carried out every half minute and repeated 10 times to achieve the desired thickness of ~ 50 nm. The films were further annealed on the hot plate for another 20 min before being removed and air cooled. To dope the TiO_2 films, $Zn(NO_3)_2 \cdot 6\,H_2O$, tin(IV) isopropoxide, or niobium(V) ethoxide was added to the titanium precursor with the desired molar ratio to the Ti^{4+} ion. The deposition processes of the films were the same with that of the undoped TiO_2 films.

Device fabrication. The synthesis of perovskite films were carried out with the one-step spin-coating method with the precursor recipe of MAI:$PbCl_2$=3:1. The detailed film deposition and device fabrication processes can be found in Chapter 3. All the cell fabrication were conducted in air with room humidity of < 35 %.

5.2 Zn-doped TiO_2 ETLs

Doping of TiO_2 with varieties of ions, both metallic and non-metallic, has been widely applied in DSSCs[10] and photocatalysts[17], and has also attracted research interests in perovskite solar cells[18–20]. But the effects of the doping on the photoelectric properties of TiO_2 are still poorly understood.[21,22] Here, the Zn^{2+} ion was investigated as a dopant for TiO_2 compact layers by the introduction of $Zn(NO_3)_2$ in the precursor solution at a concentration of 2 mol%.

XRD patterns of the pristine and Zn-doped TiO_2 films deposited on silicon wafers are illustrated in **Fig. 5.2**. All the films showed the pure anatase structure, with the peaks at 25.4 °, 48.2 ° and 55.3 ° assigned to the (101), (200) and (211) facets respectively. The absence of diffraction peaks for ZnO indicated the Zn^{2+} dopant ions were incorporated into the TiO_2 lattices, rather than forming an oxide phase of its own.

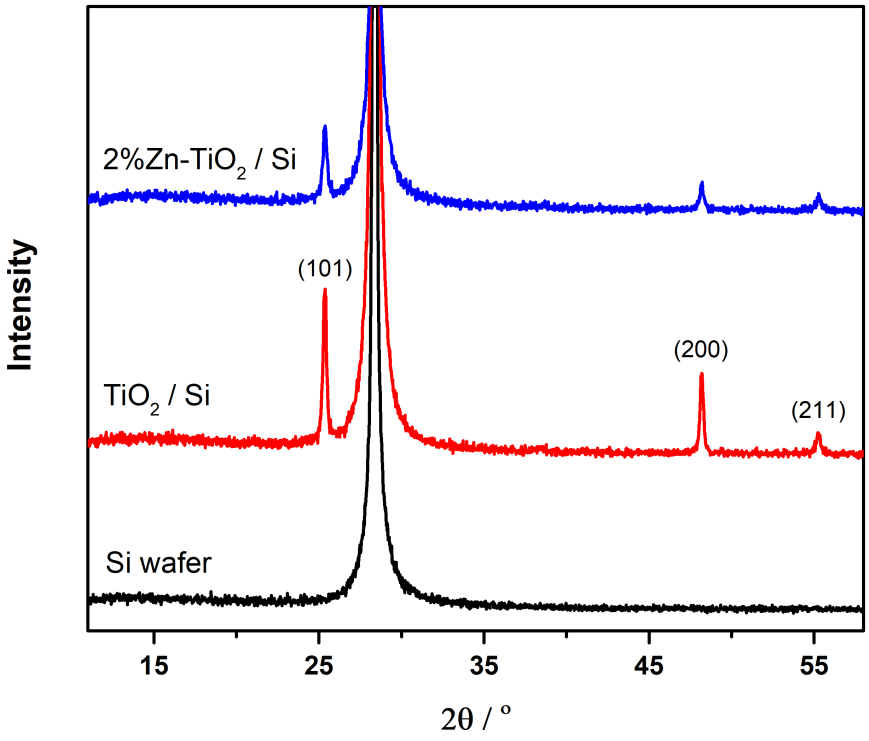

Fig. 5.2 XRD patterns of pristine and Zn-doped TiO_2 films deposited on silicon wafers.

The incorporation of the Zn^{2+} ions was further confirmed by the XPS spectra of the films. As shown in **Fig. 5.3**a, the pristine TiO_2 films showed the presence of C, Ti and O, and additional Zn peaks were observed in the Zn^{2+} doped samples. The presence of C might be caused by the absorption of carbon sources in the atmosphere on the surface of the films[23]. The ratio of Zn:Ti was estimated to be 6:94, higher than the 2% in the precursor solution, indicating the accumulation of Zn^{2+} ions on the surface. The high-resolution Ti 2p spectra in **Fig. 5.3**b showed the doublet Ti $2p_{3/2}$ and Ti $2p_{1/2}$ peaks at binding energies of 458.6 eV and 464.2 eV in the pristine TiO_2 film. The Ti 2p peaks were slightly shifted lower to 458.4 eV and 464.1 eV respectively after Zn-doping. The shifts of the Ti 2p peaks match those found in literature reports[24,25], indicating that Zn ions replaced some of the titanium ions and changed the chemical envionment. **Fig. 5.3**c shows the doublet peaks of Zn $2p_{3/2}$ and Zn $2p_{1/2}$ at 1021.1 eV and 1044.1 eV in the Zn−TiO_2 sample, which were absent in the pristine TiO_2 film. These peaks suggested the existence of Zn^{2+}, mainly in the form of Zn-O.

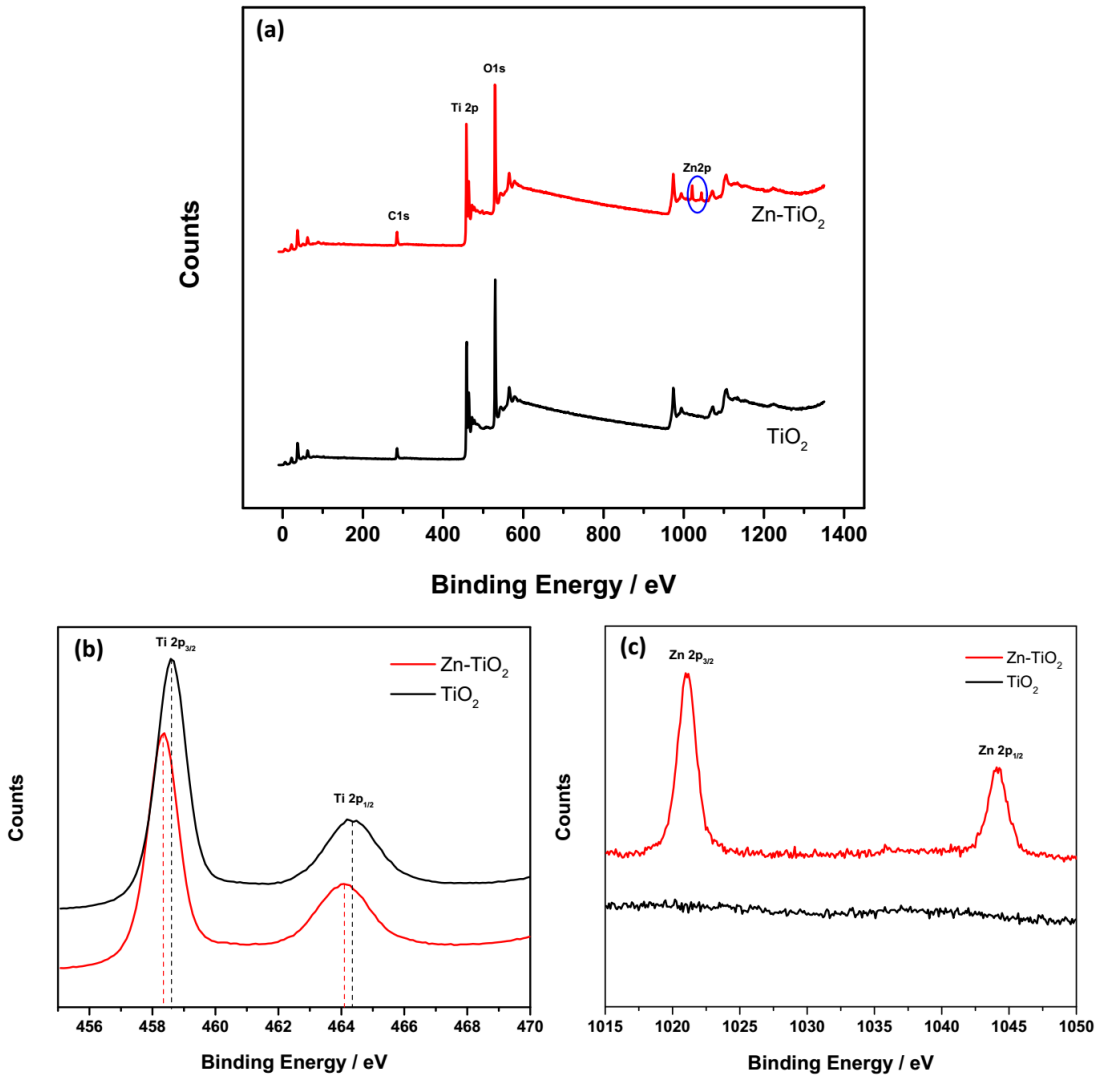

Fig. 5.3 Full profile XPS spectra of the pristine and Zn-doped TiO_2 films (a), and the corresponding high-resolution spectra of Ti 2p (b), Zn 2p (c).

Table 5.1 Elemental contents in the pristine and Zn-doped TiO_2 films from the XPS spectra.

Samples	Element contents (atomic %)			
	Ti2p	O1s	C1s	Zn2p3
TiO_2	24.1	60.9	15.0	-
Zn-TiO_2	22.2	58.6	17.7	1.6

AFM images of the pristine and Zn-doped TiO_2 films are shown in **Fig. 5.4**. The morphologies of the films were quite similar, with the area roughness both in the range of 6-7 nm. The particle sizes were 140-160 nm for both the samples, which however are

more likely to be the morphological properties of the underlying TEC15 FTO substrates. Due to the fine structure and small thickness, the TiO_2 smooths the FTO surface, but its crystal morphology is very difficult to detect using AFM[26,27].

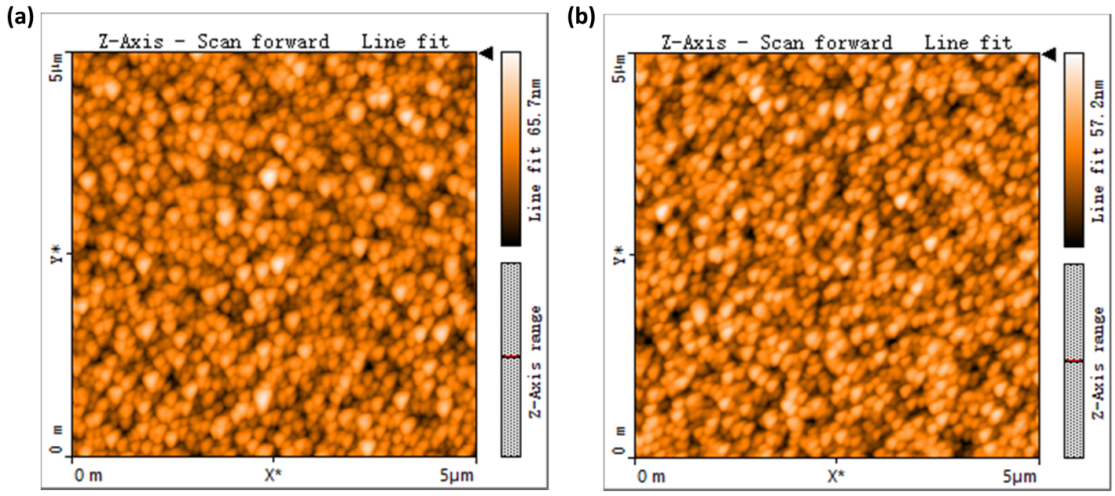

Fig. 5.4 AFM images of the pristine (a) and doped Zn-doped TiO_2 films (b) deposited on FTO substrates.

The surface wetability of the TiO_2 films were also investigated, as perovskite layers were spin-coated right on the top of the TiO_2 layers during cell fabrication and the wetability of the TiO_2 layers would impact the spread of the perovskite precursor solution and consequently the film homogeneity of the perovskite layers. However, no valid contact angle data were obtained with the static sessile drop method, because all the films were very hydrophilic, and the water drops completely spread out once being dropped onto the surfaces and could hardly be distinguished from the substrates, giving contact angles of almost 0°. Previously Wentao in our lab has shown that the contact angle of TiO_2 films can be greatly increased from near zero to 47° in 5 days if the surface becomes coated with organics from the atmosphere during storage[27]. This measurement confirms that the fresh blocking layers are very hydrophilic if used immediately.

Given that the surface properties including the morphology and the wetability of the TiO_2 films after doping with Zn^{2+} stayed unchanged, the morphologies of the perovskite films deposited on top would be expected to be unaffected, which was confirmed by the AFM images shown in **Fig. 5.5**. High surface coverages were exhibited in perovskite film on both the doped and undoped TiO_2 layers, which are essential for efficient perovskite solar

cells. Both of the films showed surface roughness as low as ~65 nm, and no obvious changes were observed in the particle sizes.

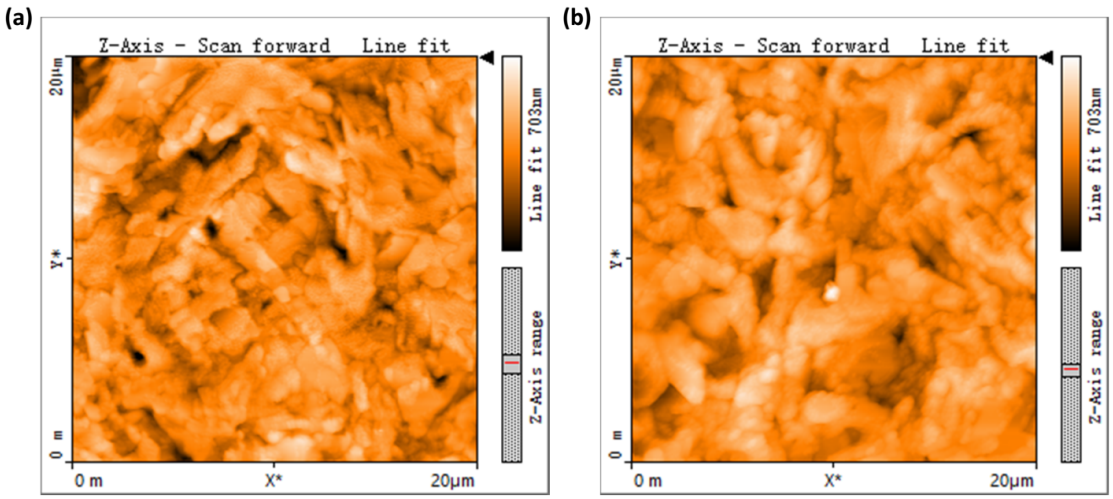

Fig. 5.5 AFM images of $MAPbI_{3-x}Cl_x$ perovskite films deposited on the pristine (a) and Zn-doped (b) TiO_2 films.

In the n-i-p structured perovskite solar cells shown in **Fig. 4.1**, the light illuminates through the FTO substrates and the TiO_2 ETLs, and gets absorbed by the perovskite layers to generate electron-hole charge pairs. Therefore, high transmittance of the ETL is a necessity. **Fig. 5.6** shows the transmittance of the pristine and Zn-doped TiO_2 films on FTO. Similiar transmission spectra were obtained for the pristine and Zn-doped TiO_2 films, with the high transmittance of 65-75 % over the whole range of 400-850 nm. Considering the transmittance of the FTO substrates of 82-84.5 % (provided by Sigma-Aldrich), the light loss caused by the TiO_2 ETLs are quite small.

The UV-vis spectra of perovskite films on the pristine and Zn-doped TiO_2 films are shown in **Fig. 5.7**. The absorption of the films were almost identical, with well-defined optical onsets of ~800 nm and strong absorption of around 90 % over wide wavelength ranges. The excellent light absorbing properties were due to the high surface coverage and uniformity of the perovskite films as shown in the AFM images in **Fig. 5.5**, and the very small differences in the absorption spectra of the films on pristine and Zn-doped TiO_2 layers indicated that Zn-doping of TiO_2 layers had negligible impact on the optical properties of the perovskite layers.

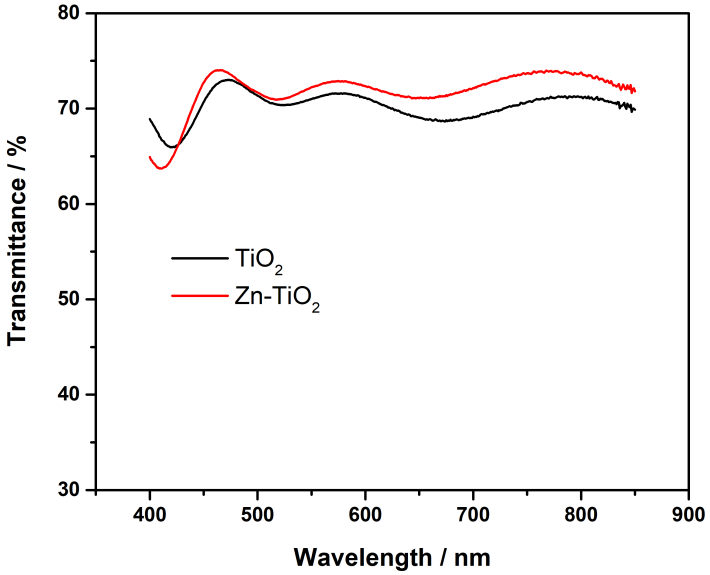

Fig. 5.6 Transmittance of the pristine and Zn-doped TiO_2 films on FTO substrates over the wavelength range of 400-850 nm.

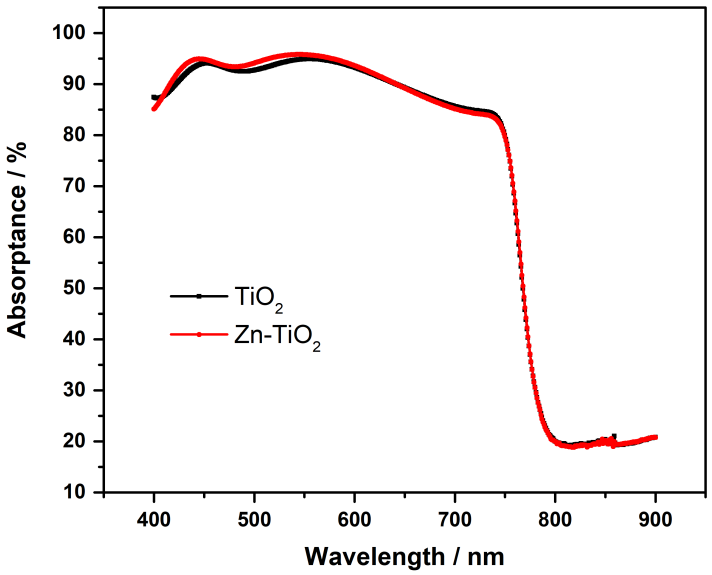

Fig. 5.7 UV-vis absorption spectra of perovskite films deposited on top of the pristine and Zn-doped TiO_2 films. The absorptance A% is calculated through A%=1-T%-R%.

Since good morphological and optical properties have been achieved for both the TiO_2 and perovskite layers, complete devices of FTO/c-TiO_2/perovskite/Spiro-OMeTAD/Au perovskite solar cells were made with the pristine and doped TiO_2 layers as ETLs, and the cell performances are illustrated in **Fig. 5.8** and **Table 5.2**. All the cells showed PCEs of over 10 % with good reproducibility. However, compared with the 12.0 ± 1.0 % of the

cells with undoped TiO_2 blocking layers, the PCEs dropped for the cells with Zn-doped TiO_2 to $10.7 \pm 0.6\,\%$, mainly arising from the decreased FF of 0.55 ± 0.02 compared to 0.60 ± 0.03 for the pristine cells. The V_{OC} and J_{SC} were basically unchanged. The series resistance R_s is one of the major factors influencing the FF of solar cells. R_s of the devices are estimated from the slope of the J-V curves at the open-circuit voltage point[28] as illustrated in **Fig. 5.9**. The Zn-TiO_2 device showed a higher R_s of $12.5\,\Omega\,cm^2$ compared with the $9.3\,\Omega\,cm^2$ for the TiO_2 device, which is in accordance with the decreased FF.

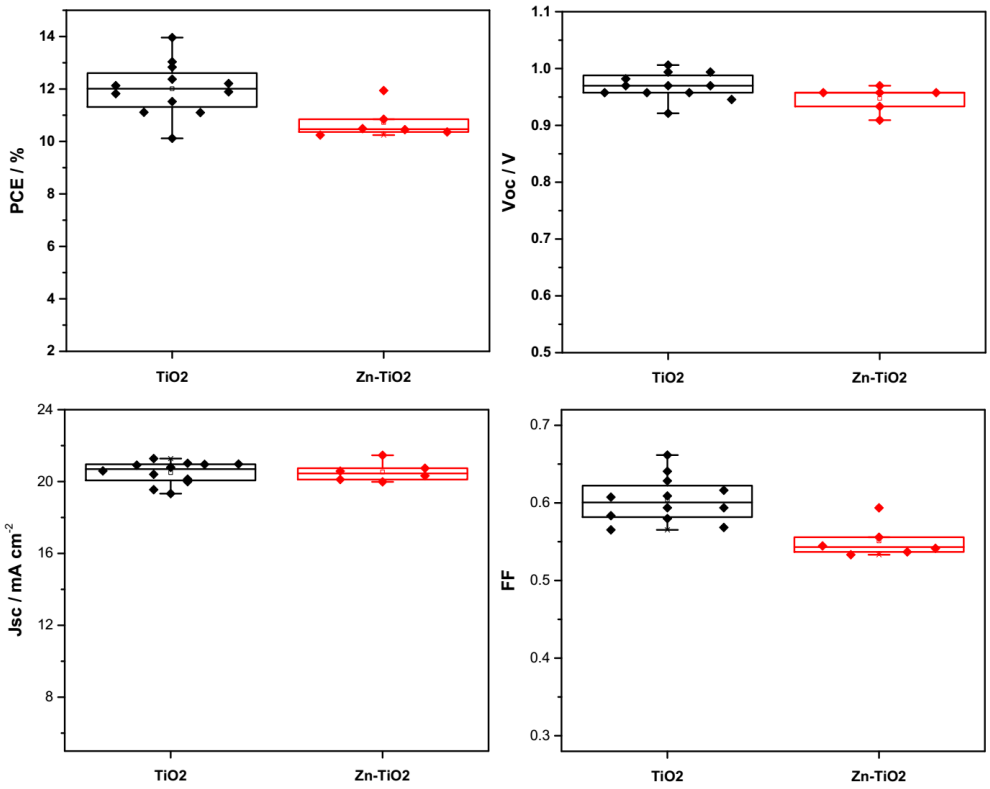

Fig. 5.8 Box plots of the device performances with the pristine and Zn-doped TiO_2 films as ETLs.

Table 5.2 Performance parameters for cells with pristine and Zn-doped TiO_2 layers as ETLs.

ETLs	V_{OC} [V]	J_{SC} [$mA \cdot cm^{-2}$]	FF	PCE [%]
TiO_2	0.97 ± 0.02	20.5 ± 0.6	0.60 ± 0.03	12.0 ± 1.0
$2\,\%\,Zn{-}TiO_2$	0.95 ± 0.02	20.5 ± 0.5	0.55 ± 0.02	10.7 ± 0.6

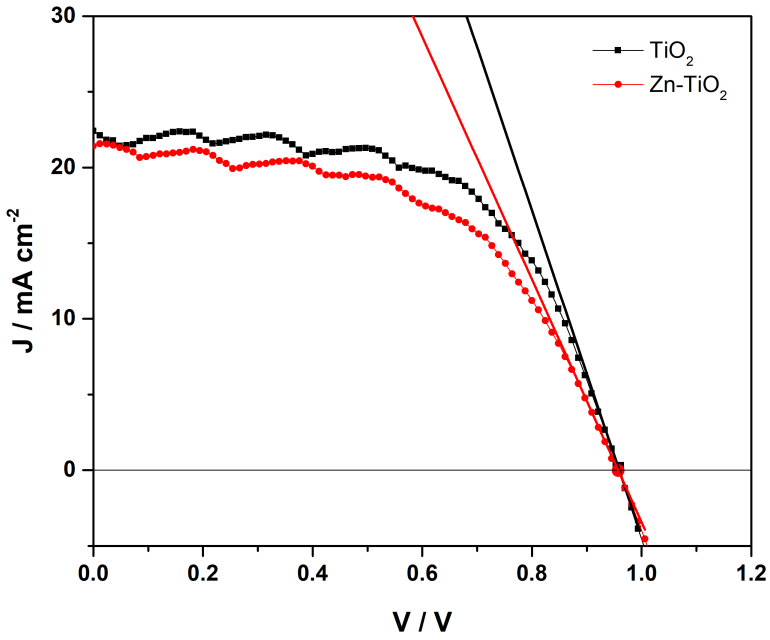

Fig. 5.9 J-V curves of the devices with the pristine and Zn-doped TiO_2 films as ETLs. The straight lines are the tangents at the open circuit voltage point.

As it has been shown that Zn-doping of the TiO_2 layers barely affected the morphological and optical properties of the TiO_2 and perovskite layers, the differences in the cell performances are believed to be due to the differences in the semiconductive electronic properties of the TiO_2 layers and the interfacial properties between the TiO_2 and perovskite layers. To investigate the impact of Zn-doping on the semiconductive electronic properties of the TiO_2 layers, Mott-Schottky plots were measured, as illustrated in **Fig. 5.10**. The films showed the typical Mott-Schottky responses of n-type semiconductors. Linear regions were observed which correspond to the formation of depletion layers above the flat band potential at the semiconductor-electrolyte junction. When the potential was swept more positive, the plot flattened off, as the depletion layer extended across the TiO_2 layer and started to probe the FTO layer. The n-type nature of the TiO_2 films could be due to defects sites, such as oxygen vacancies[29,30], in the matrix. Doping densities N_d and flat band potentials V_{FB} of the TiO_2 films were calculated through linear regressions of the linear regions, as listed in **Table 5.3**, assuming a relative permittivity of 40 for TiO_2[31].

After Zn-doping, the doping density of TiO_2 was decreased slightly from 4.07×10^{18} cm^{-3} to 1.06×10^{18} cm^{-3}, which could suggest a decreased conductivity and could explain the lower FF of the Zn-TiO_2 devices. But it also should be understood that the difference

was not significant and could potentially lie within the margin of error considering the uncertainty caused by the film roughness and porosity and the error in the surface area measurement of the electrodes. However the V_{FB} was shifted significantly to a more negative value of -0.11 V from 0.13 V. The negative shift of the V_{FB} may suggest an upward shift of the E_F [32], which can occur following n-type doping as shown in **Fig. 5.1**b, but this is a surmise, since we have no idea whether the distribution of trap states changes after Zn-doping, and the V_{OC} of the devices was not increased as seen in **Fig. 5.8**. Another factor affecting the V_{OC} is recombination. To compare the recombination of cells with pristine and Zn-doped TiO_2 ETLs, impedance spectra of the devices were measured at open circuit, as illustrated in **Fig. 5.11**. Well defined semicircles were observed in the Nyquist plots for both the cells, consistent with literature reports [33]. The high frequency semicircle is attributed to the geometric capacitance C_{geo} and the recombination resistance R_{rec}. By fitting the semicircles with a simple circuit shown in the inset, the R_{rec} was obtained. The R_{rec} at different V_{OC} induced by different light intensities are shown in **Fig. 5.11**b. Good linearity is observed in the semilogarithmic plots of R_{rec} vs. V_{OC} for both the TiO_2 and Zn-TiO_2 devices, consistent with Pockett's report [33]. The ideality factor m of the devices can be calculated from the slope of the plots using the equation

$$\frac{\partial \log \mathrm{R_{rec}}}{\partial V_{OC}} = -\frac{q}{2.303 m k_B T} \tag{5.1}$$

where q is the elementary charge, k_B is the Boltzmann constant and T is temperature. The m values for the TiO_2 and Zn-TiO_2 cells are calculated to be 2.6 and 5.3 respectively, which are also similar to those found previously by Pockett. The ideality factor of a solar cell is normally 1 when only radiative recombination occurs, whereas the trap-assisted recombination gives an ideality factor of 2 [34,35]. The reason for the large differences in ideality factors of our devices are not clear, the cells studied by Pockett et al. had similar efficiencies at 1 Sun and had been made in an identical preparation process. From **Fig. 5.11**b, the R_{rec} is expected to be higher for the Zn-TiO_2 devices than the TiO_2 devices under one sun where the V_{OC} is 0.9-1 V, suggesting less recombination in the Zn-TiO_2 devices at operating conditions. The reason for the unchanged V_{OC} though the V_{FB} was negatively shifted and recombination was reduced is not clear yet. Mott-Schottky plots were carried out on isolated semi-conductor films dipped into electrolyte solution, it is very possible that in a complete device the interface of the TiO_2 layers experiences a

different environment and the shifts in V_{FB} are not the same.

In addition, the R_s for the Zn-TiO_2 device is fitted from the impedance spectra to be 46 Ω, slightly higher than the 41 Ω for the Zn-TiO_2 device, which is consistent with the J-V curves and explains the lower FF of the Zn-TiO_2 devices.

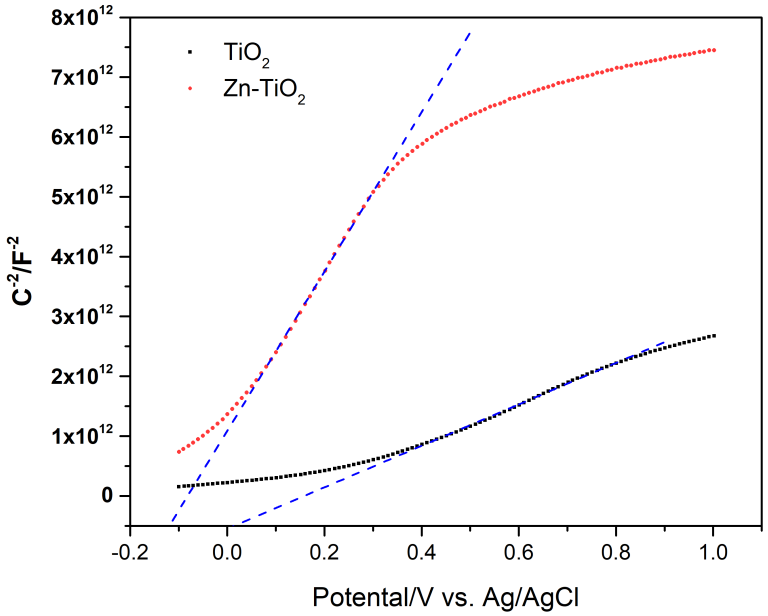

Fig. 5.10 Mott-Schottky plots of the pristine and Zn-doped TiO_2 films on FTO.

Table 5.3 Doping densities and V_{FB} of the pristine and Zn-doped TiO_2 ETLs calculated from their Mott-Schottky plots.

ETLs	Doping Density [cm^{-3}]	V_{FB} [V] vs. Ag/AgCl
TiO_2	4.07×10^{18}	0.13
$Zn{-}TiO_2$	1.06×10^{18}	-0.11

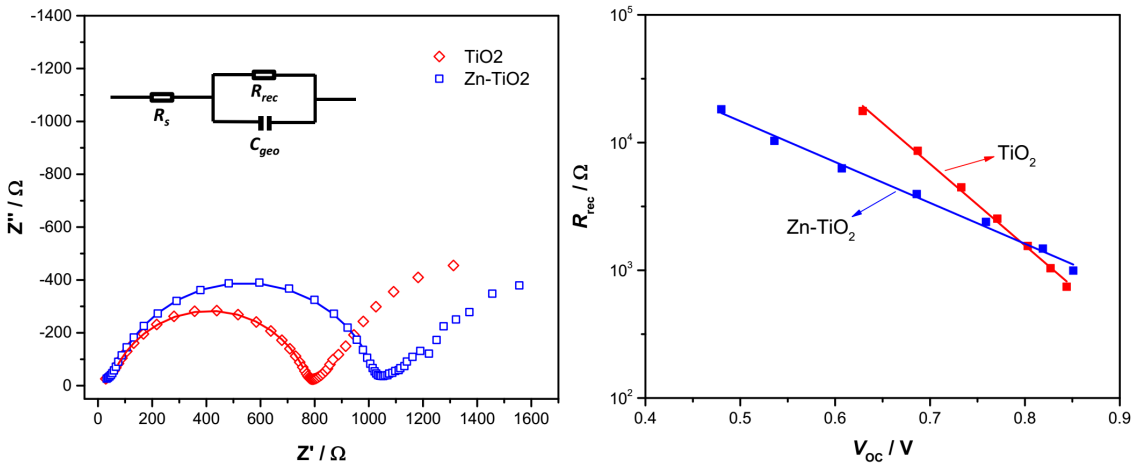

Fig. 5.11 Impedance spectra of devices employing pristine and Zn-doped TiO_2 ETLs. The dots are the experimental data points, and the line curves are the fittings with the circuit shown in the inset.

5.3 Double TiO_2 electron-transporting layers

As discussed above, doping TiO_2 ETLs with Zn ions barely affected their optical and morphological properties, but there was a change in the V_{FB} and a slight decrease in the doping density of TiO_2. In addition the total recombination in the device was reduced after Zn-doping. However the series resistance of the device was increased, possibly due to an decreased conductivity of the Zn-TiO_2, as a result, the FF was decreased, resulting in poorer cell performances. It has been reported that a bilayer of ZnO on top of TiO_2 as ETL could facilitate the electron transport and improve the performance of both dye-sensitised solar cells[36] and perovskite solar cells[37]. Besides, efficient perovskite solar cells with very thin insulating layers between the ETL and perovskite layers have been reported[38], suggesting electrons transport hindrance can be avoided by reducing the thickness of the layer. Therefore, here an electron-transporting bilayer comprised of a thin Zn-doped TiO_2 layer on top of a pristine TiO_2 layer was constructed, so that the negative effects (i.e. higher series resistance) can be minimised by decreasing the thickness of the Zn-TiO_2 layer while the positive effect of Zn-doping (negative shift of V_{FB} and reduced recombination) might be retained.

The performance of the cells employing the bilayer ETLs are shown in **Fig. 5.12** and **Table 5.4**, and different ratios of TiO_2 : $Zn{-}TiO_2$ were compared. The ratios were controlled

by spraying the TiO_2 and $Zn{-}TiO_2$ for different numbers of sprays while a total of 10 sprays were maintained so that the whole thickness of the ETLs were kept the same. For the purpose of comparison, the cell performance of the single $Zn{-}TiO_2$ ETL based devices shown in previous section are reproduced. All the cells showed narrow distributions in all the parameters of PCE, V_{OC}, J_{SC} and FF, indicating their excellent reproducibility. With TiO_2 single layer as the ETL, the control cells showed the PCE of $12.0 \pm 1.0\,\%$, with the V_{OC} of 0.97 ± 0.02 V, the J_{SC} of $20.5 \pm 0.6\,mA \cdot cm^{-2}$ and the FF of 0.60 ± 0.03. While with $Zn{-}TiO_2$ single layer as the ETL, the cells showed inferior PCEs of $10.7 \pm 0.6\,\%$, with decreased FF of 0.55 ± 0.02 as discussed in the previous section. However, with $TiO_2/Zn{-}TiO_2$ bilayer ETLs, interesting results were observed. When a thin layer of $Zn{-}TiO_2$ was deposited on top of pristine TiO_2 layer with the $Zn{-}TiO_2 : TiO_2$ ratio of $3:7$ (3 sprays for Zn-TiO_2 and 7 sprays for TiO_2), the PCE of the devices was improved to $12.6\,\%$. As the content of $Zn{-}TiO_2$ was further increased, the PCEs dropped. The same trend was seen for the FF of the devices. The best FF of 0.62 ± 0.02 was obtained at the $Zn{-}TiO_2 : TiO_2$ ratio of $3:7$, and decreased as the content of $Zn{-}TiO_2$ further increased. The V_{OC} also showed improvements with bilayer ETLs that decreased as the $Zn{-}TiO_2$ content went too high. The best V_{OC} happened in devices with the $Zn{-}TiO_2 : TiO_2$ ratio of $5:5$.

The differences in cell performances with the bilayer ETLs suggested that the thin layer of the $Zn{-}TiO_2$ between the pristine TiO_2 and perovskite layers might serve the role of interface engineering, and the negative effect on the conductivity could be minimised by decreasing the thickness of the Zn-TiO_2 layer while the positive effects of a negatively shifted V_{FB} and reduced recombination might be retained. As a result the V_{OC} and FF were both enhanced, leading to the improvement of cell performance, just as expected. Whereas when the thickness of the Zn-TiO_2 increased too much, the negative effects came up again and reduced the cell performance.

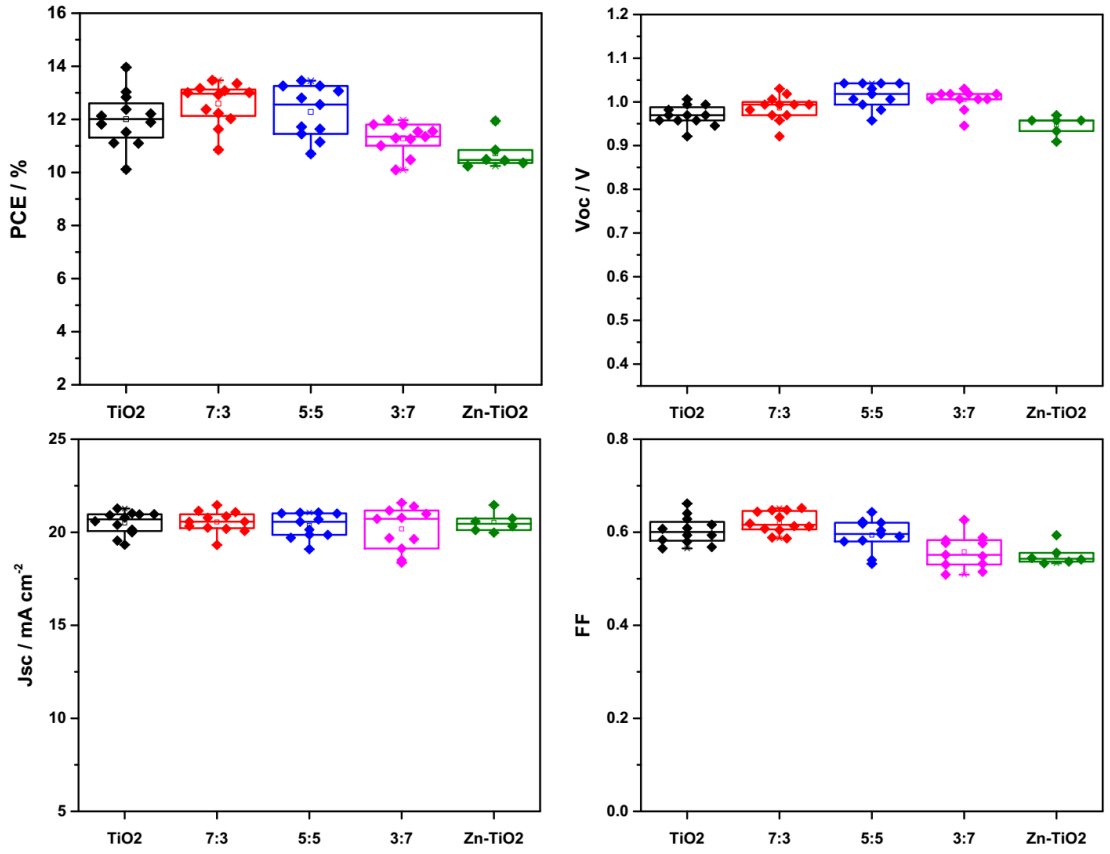

Fig. 5.12 Box plots of the device performances with bilayer ETLs comprised of pristine and doped TiO_2 films with different ratios.

Table 5.4 Performance parameters for cells employing bilayer ETLs comprised of pristine and doped TiO_2 films with different ratios.

$TiO_2 : Zn{-}TiO_2$	V_{OC} [V]	J_{SC} [$mA \cdot cm^{-2}$]	FF	PCE [%]
10 : 0	0.97 ± 0.02	20.5 ± 0.6	0.60 ± 0.03	12.0 ± 1.0
7 : 3	0.98 ± 0.03	20.6 ± 0.5	0.62 ± 0.02	12.6 ± 0.8
5 : 5	1.01 ± 0.03	20.4 ± 0.6	0.59 ± 0.04	12.3 ± 1.0
3 : 7	1.00 ± 0.02	20.2 ± 1.2	0.56 ± 0.03	11.3 ± 0.6
0 : 10	0.95 ± 0.02	20.5 ± 0.5	0.55 ± 0.02	10.7 ± 0.6

As it has been shown that Zn-doping had no influences on the morphological and optical properties of the TiO_2 ETLs, the morphological and optical properties of the bilayer ETLs would be not changed from the TiO_2 layer. Therefore, to figure out the origin of the dif-

ferences in cell performances, the morphological and optical properties of the perovskite layers were compared.

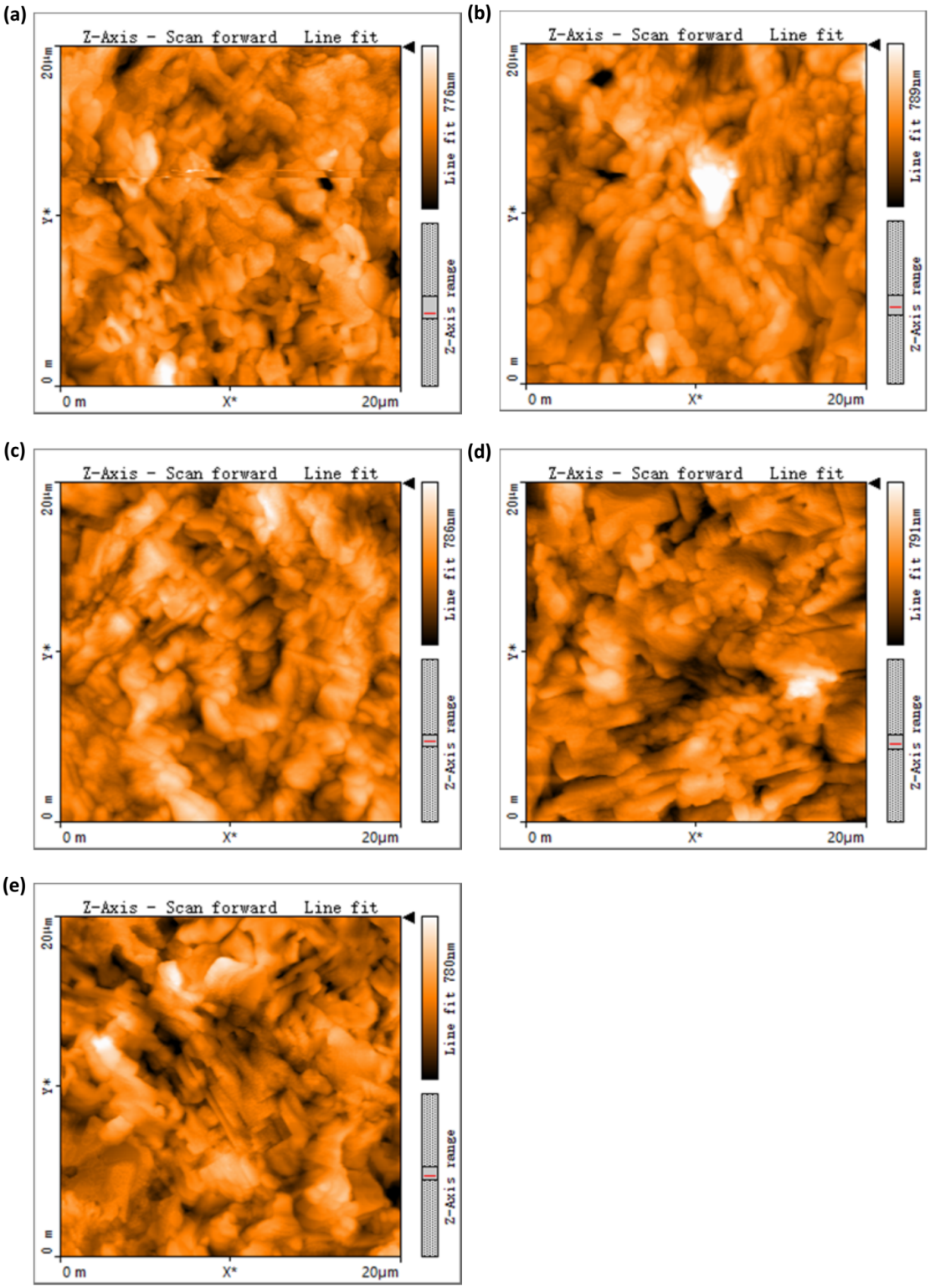

Fig. 5.13 AFM images of perovskite layers on top of dual ETLs with different ratios of TiO_2 : $Zn{-}TiO_2$: (a) 10:0; (b) 7:3; (c) 5:5; (d) 3:7; and (e) 0:10.

The morphologies of the perovskite layers are shown in **Fig. 5.13**. No obvious differences were observed for the perovskite films, which all showed high surface coverages on TiO_2 / Zn−TiO_2 bilayer ETLs with different ratios of TiO_2 : Zn−TiO_2. All of the films showed low surface roughnesses of 80-90 nm, and no obvious changes were observed in the particle sizes.

Optical property of the films were compared in the UV-vis spectra shown in **Fig. 5.14**. All the films showed well-defined optical onsets of ~ 800 nm, corresponding to the optical band-gap of ~ 1.55 eV, and strong absorption of around 90 % over wide wavelength ranges. The excellent light absorbing properties are attributed to the high coverage of the films as shown in the AFM images, and are responsible for the high J_{SC} of over 20 mA·cm^{-2} of the cells. The spectra of the films deposited on TiO_2 / Zn−TiO_2 bilayer ETLs with different ratios of TiO_2 : Zn−TiO_2 were very similar, with only small differences in the range of 400-600 nm. Considering the very similar J_{SC} of the cells, the small changes are believed to be due to the contamination on the back of the glass introduced during the spray pyrolysis process. Therefore, as might be expected, a second layer of lightly Zn-doped TiO_2 layers had negligible impact on the optical properties of the perovskite layers.

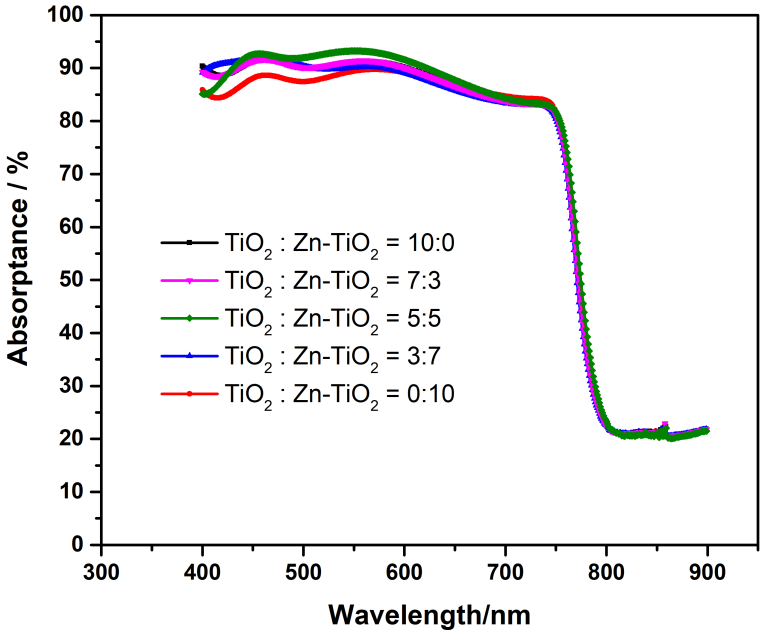

Fig. 5.14 UV-vis absorption spectra of perovskite films on top of bilayer ETLs with different ratios of TiO_2 : Zn-TiO_2 from 10:0 to 0:10.

Now that the morphological and optical properties of the perovskite layers were not affected, the semiconductive electronic properties of the bilayer ETLs were investigated by Mott-Schottky measurements. As shown in the Mott-Schottky plots in **Fig. 5.15**, all the films showed the typical Mott-Schottky responses of n-type semiconductors. With bilayers of $Zn{-}TiO_2$ on top of pristine TiO_2 with different ratios of $TiO_2 : Zn{-}TiO_2$, the films showed similar doping densities of 7-9 $\times 10^{18}$ cm^{-3}, indicating the overall doping density was not significantly changed when the films being partly light doped with Zn. Moreover, similar negative shifts of the V_{FB} with in the previous section were also observed, and the shift became more profound as the Zn content increased. The negative shift of the V_{FB} explains the increase of V_{OC} when the thickness of the $Zn{-}TiO_2$ is small. While with the further increase of the $Zn{-}TiO_2$ content in the bilayer, the V_{OC} decreases, the reason for which is still not clear.

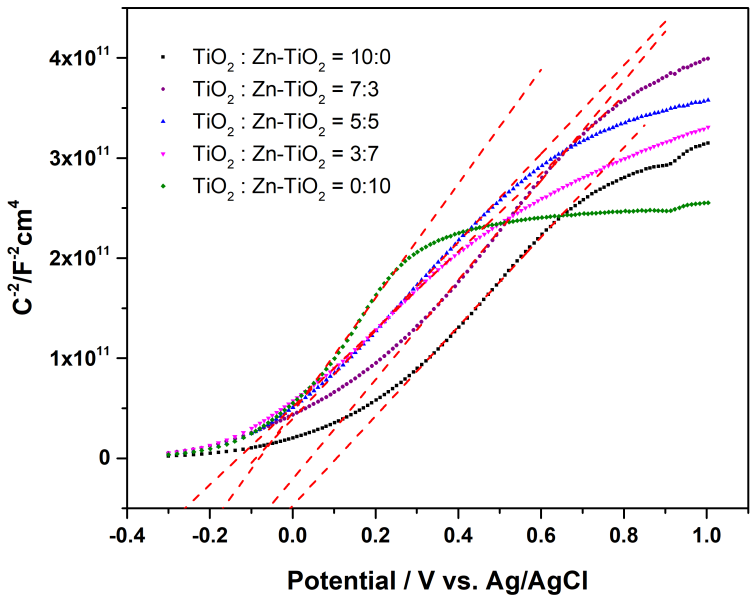

Fig. 5.15 Mott-Schottky plots of the dual ETLs with different ratios of $TiO_2 : Zn{-}TiO_2$ from 10:0 to 0:10.

Table 5.5 Doping densities and V_{FB} of the TiO_2 ETLs calculated from their Mott-Schottky plots.

$TiO_2 : Zn{-}TiO_2$	Doping Density [cm^{-3}]	V_{FB} [V] vs. Ag/AgCl
10:0	7.88×10^{18}	0.08
7:3	7.09×10^{18}	0.02
5:5	7.99×10^{18}	-0.12
3:7	9.07×10^{18}	-0.16
0:10	7.09×10^{18}	-0.11

5.4 Doped TiO_2 ETLs with other metal ions

As shown in the discussions above, the effect of doping of TiO_2 ETLs with Zn^{2+} ion on the cell performance was insignificant, though small differences were observed. In this part, other different metal ions of Sn^{4+} and Nb^{5+} are studied as dopants for TiO_2 layers. As the valence state of Sn^{4+} ion is the same with, while the valence state of Nb^{5+} ion is higher than Ti^{4+} in the TiO_2 lattice, which are different from the case of Zn^{2+}, their impacts on the electronic properties of TiO_2 layers would be different from Zn-doping.

As illustrated in the XRD patterns of the pristine, Sn-doped and Nb-doped TiO_2 films deposited on silicon wafers in **Fig. 5.16**, all the films showed high phase purity of anatase TiO_2, with the absence of the oxide phases of SnO_2 and Nb_2O_5. All the diffraction peaks at 25.4 °, 48.2 ° and 55.3 ° are assigned to the (101), (200) and (211) facets respectively. Therefore the doping ions were also incorporated into the TiO_2 lattices, rather than forming the oxide phase of their own.

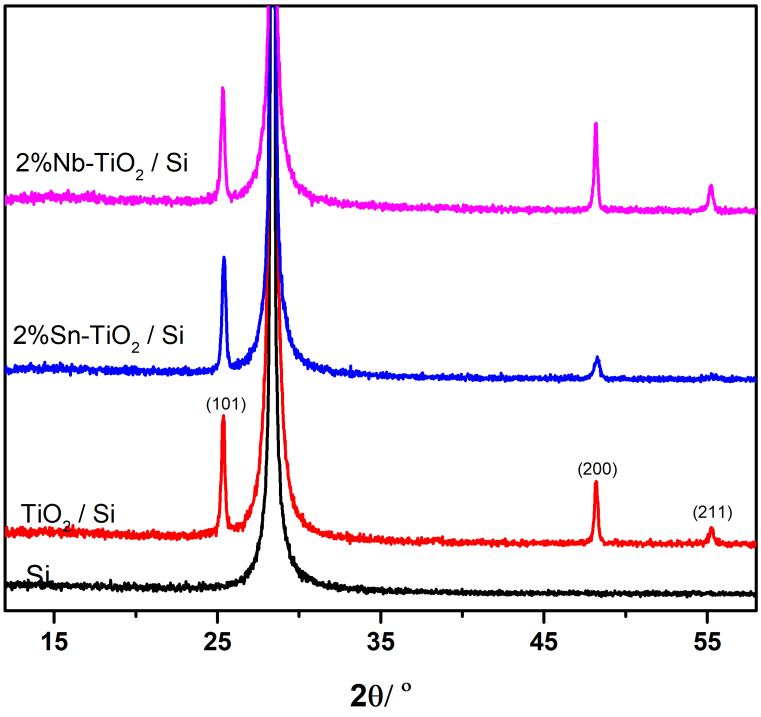

Fig. 5.16 XRD patterns of pristine and doped TiO_2 films with Sn and Nb.

The successful incorporation of the dopant ions was also confirmed by the XPS spectra of the films. As shown in **Fig. 5.17**a, additional Sn and Nb peaks were present in the spectra after Sn and Nb doping respectively. The ratio of Sn:Ti and Nb:Ti were estimated to be 3:97 and 7:93, higher than the 1% for Sn and 2% for Nb in the precursors, indicating that the Sn^{4+} and Nb^{5+} ions were also accumulated at the surface of the films. The high-resolution Ti 2p spectra in **Fig. 5.17**b showed the doublet Ti $2p_{3/2}$ and Ti $2p_{1/2}$ peaks for all the films. Compared with the pristine TiO_2 sample, The Ti 2p peaks were slightly shifted lower to 458.4 eV and 464.1 eV respectively for Sn−TiO_2, and higher to 458.7 eV and 464.5 eV for Nb−TiO_2, suggesting that Sn and Nb ions replaced some of the Ti ions and change the chemical environment. **Fig. 5.17** c and d showed the doublet peaks of Sn $3d_{5/2}$ and Sn $3d_{3/2}$ at 486.0 eV and 494.5 eV in the Sn−TiO_2 sample, and the doublet peaks of Sn $3d_{5/2}$ and Sn $3d_{3/2}$ at 207.2 eV and 210.2 eV in the Nb−TiO_2 sample, which are absent in the pristine TiO_2 film. These peaks suggested the existence of Sn^{4+} mainly in the Sn−TiO_2 film and Nb^{5+} in the Nb−TiO_2 film.

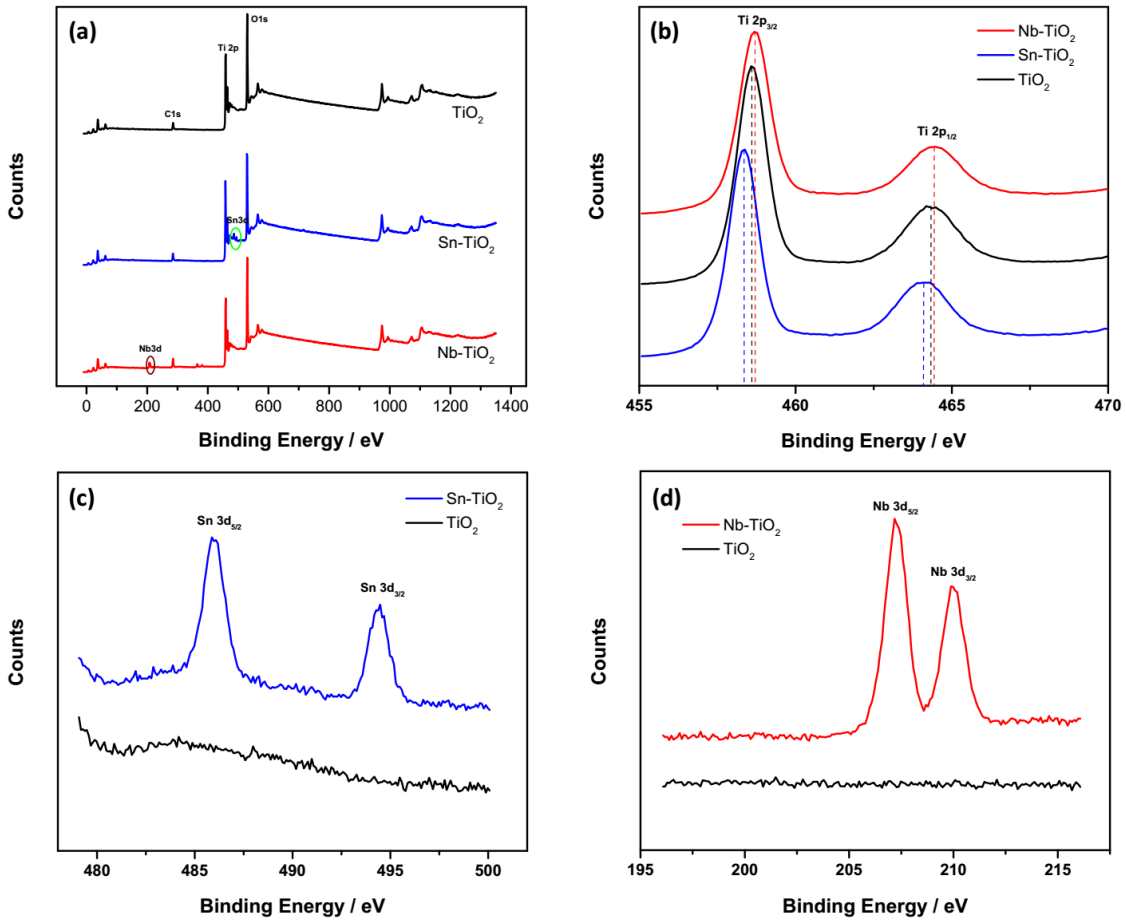

Fig. 5.17 Full profile XPS spectra of the pristine and doped TiO_2 films (a); and the corresponding high-resolution spectra of Ti 2p (b), Sn 3d (c), Nb 3d (d).

Table 5.6 Elemental contents in the pristine and doped TiO_2 films from the XPS spectra.

Samples	Element contents (atomic %)				
	Ti2p	O1s	C1s	Nb3d	Sn3d
TiO_2	24.1	60.9	15.0	-	-
Nb-TiO_2	21.0	58.0	19.4	1.6	-
Sn-TiO_2	22.7	60.1	16.5	-	0.7

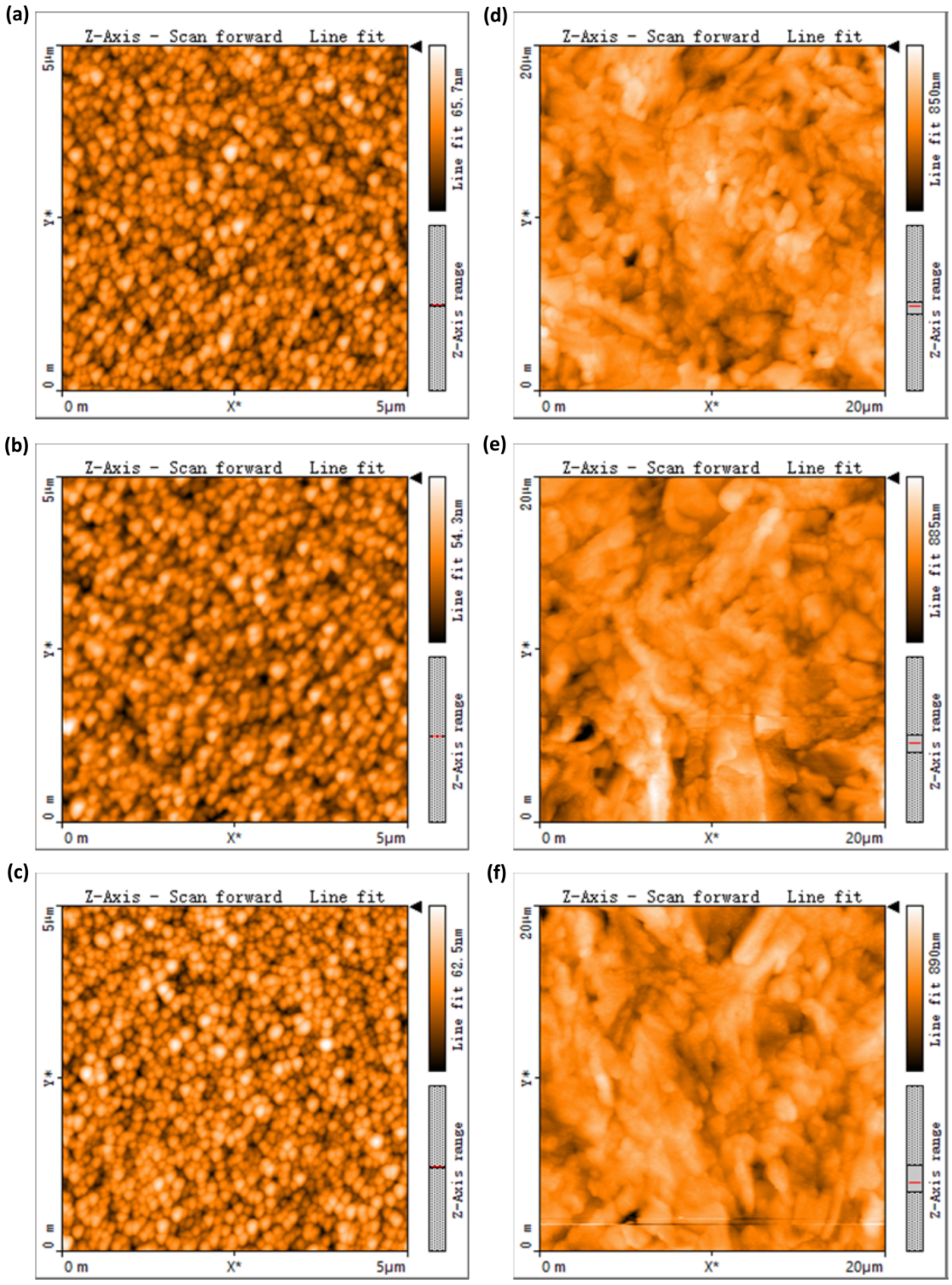

Fig. 5.18 AFM images of TiO_2 films: (a) pristine; (b) Sn-doped; (c) Nb-doped; and (d-f) perovskite films on top.

AFM images of the pristine and doped TiO_2 films with Sn and Nb ions and the perovskite layers on top are shown in **Fig. 5.18**. All the TiO_2 films showed compact and smooth morphologies with high surface coverages, and no noticeable changes in the morphologies

of the films were observed with the incorporation of Sn^{4+} and Nb^{5+} dopants. The particle sizes stayed 140-160 nm for all the samples and the roughness of the films were all in the range of 6-7 nm, indicating the light doping of TiO_2 films with these ions also had no impact on the film morphology. Besides, for the perovskite films on top, high surface coverages were also exhibited in all the films, as shown in **Fig. 5.18**d-f. All of the films showed surface roughness of as low as ~ 80 nm, and no obvious changes were observed in the particle sizes. Therefore, the light doping with Sn and Nb also had negligible impact on the morphological properties of of TiO_2 films and the perovskite films on top.

Also, the doping of TiO_2 ETLs with Sn or Nb ions had no impact on the optical properties of the perovskite films deposited on top, as illustrated in the UV-vis spectra in **Fig. 5.19**. The perovskite film showed almost identical absorption spectra in the wavelength range of 400-900 nm, with well defined absorption onset of ~ 800 nm and strong absorption of around 90% within visible region. The strong absorption of the films are due to their high surface coverage and film uniformity as illustrated in their AFM images.

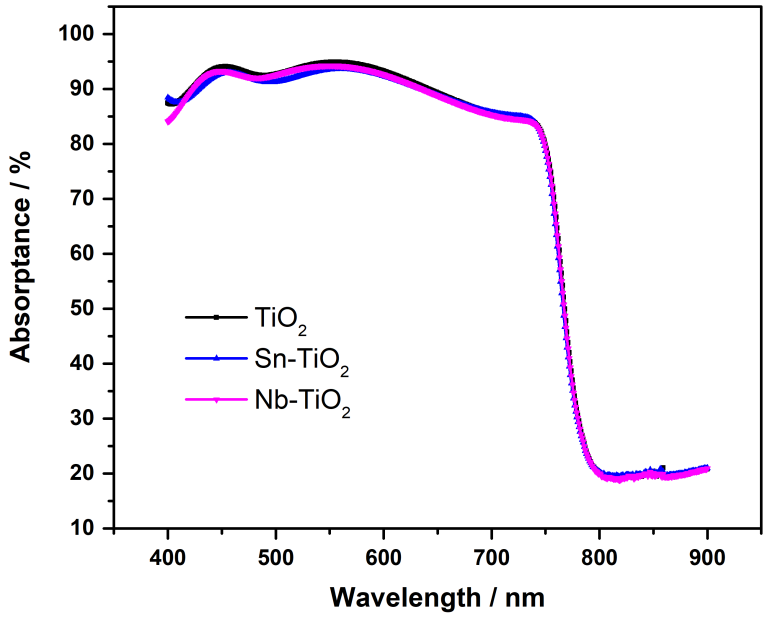

Fig. 5.19 UV-vis absorption spectra of perovskite films on top of pristine and doped TiO_2 ETLs with Sn and Nb ions.

The influences of doping of TiO_2 ETLs with Sn and Nb ions on the cell performances are shown in **Fig. 5.20** and **Table 5.7**. All the cells showed PCEs of above 10 % with good reproducibility. However, compared with the 11.6 ± 1.6 % of the cells with un-

doped TiO_2 blocking layers, the PCEs dropped for all the cells with doped TiO_2. For the $Sn-TiO_2$ based devices, the V_{OC} was slightly increased to 1.00 ± 0.01 V, whereas the J_{SC} was decreased to $17.5 \pm 2.1\,mA \cdot cm^{-2}$, leading to a slightly decreased PCE of $11.0 \pm 1.5\,\%$. While for the $Nb-TiO_2$ based devices, the V_{OC} dropped to 0.95 ± 0.05 V and the FF was decreased to 0.6 ± 0.02, causing the decrease of the PCE to $10.8 \pm 1.1\%$ though the J_{SC} was slightly enhanced to $19.0 \pm 0.8\,mA \cdot cm^{-2}$.

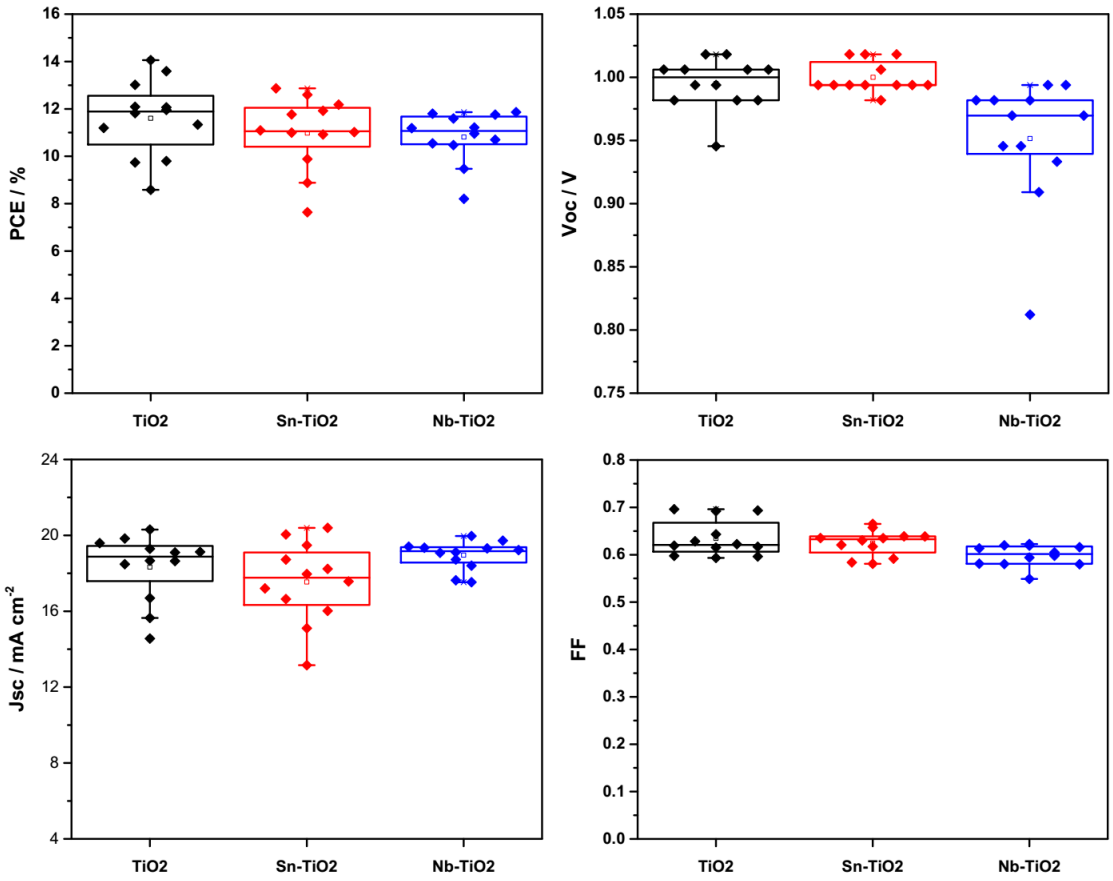

Fig. 5.20 Box plots of cell performances with Sn and Nb doped TiO_2 as ETLs.

Table 5.7 Performance parameters for cells with pristine and Sn-doped and Nb-doped TiO_2 layers as ETLs.

ETLs	V_{OC} [V]	J_{SC} [$mA \cdot cm^{-2}$]	FF	PCE [%]
TiO_2	0.99 ± 0.02	18.3 ± 1.8	0.63 ± 0.04	11.6 ± 1.6
$Sn-TiO_2$	1.00 ± 0.01	17.5 ± 2.1	0.62 ± 0.03	11.0 ± 1.5
$Nb-TiO_2$	0.95 ± 0.05	19.0 ± 0.8	0.60 ± 0.02	10.8 ± 1.1

To figure out the cause of the cell performance change, the semiconductive electronic properties of the pristine and doped TiO_2 with Sn and Nb ions were also measured, as illustrated in the Mott-Schottky plots in **Fig. 5.21**. With Nb-doping, the doping density of TiO_2 was slightly increased to $1.59 \times 10^{19}\,cm^{-3}$, and on the contrary to the case of Zn-doped TiO_2, the V_{FB} was positively shifted to 0.23 V, which explains the decrease in the V_{OC} of the devices. Sn doping, on the other hand, showed very small influence on the semiconducting electronic properties of TiO_2. The V_{FB} was unchanged, and the change in doping density was also insignificant, only from $4.07 \times 10^{18}\,cm^{-3}$ to $6.81 \times 10^{18}\,cm^{-3}$. As a result, the cell performance was essentially unchanged as shown in **Fig. 5.20**.

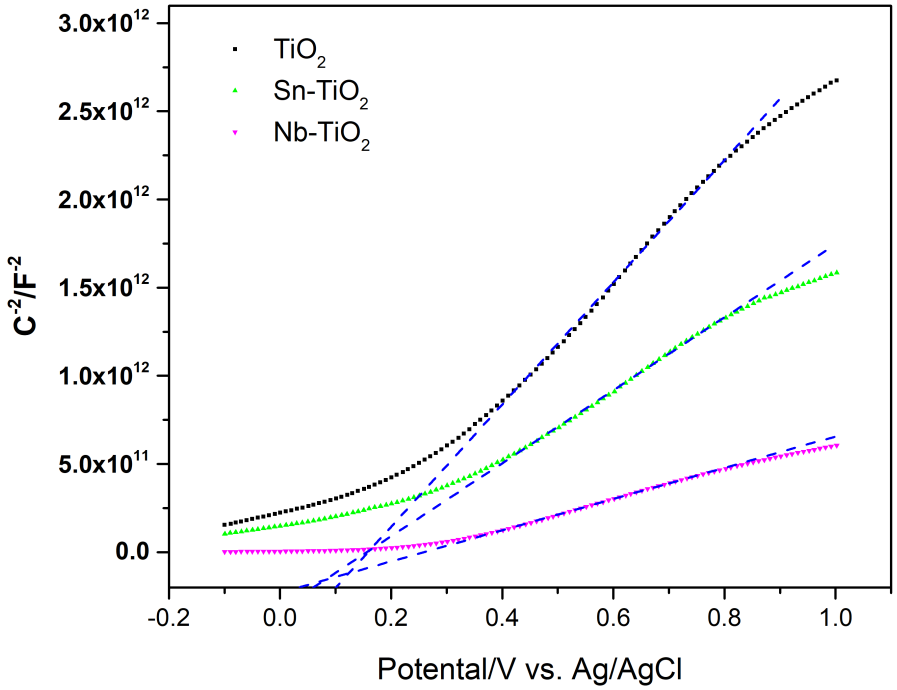

Fig. 5.21 Mott-Schottky plots of the pristine and doped TiO_2 films with different dopant ions on FTO.

Table 5.8 Doping densities and V_{FB} of the pristine and doped TiO_2 ETLs with Sn and Nb calculated from their Mott-Schottky plots.

ETLs	Doping Density [cm^{-3}]	V_{FB} [V] vs. Ag/AgCl
TiO_2	4.07×10^{18}	0.13
$Sn{-}TiO_2$	6.81×10^{18}	0.13
$Nb{-}TiO_2$	1.59×10^{19}	0.23

5.5 Conclusion

In this chapter, different metal ions of Zn^{2+}, Sn^{4+} and Nb^{5+} with different valence states were investigated as dopants for TiO_2 ETLs. Their impacts on the morphological, optical and semiconductive electronic properties of the TiO_2 layers were studied, and the performances of planar perovskite solar cells employing the ETLs were compared.

Due to the similar sizes of the doping ions with Ti^{4+}, the doping ions were successfully incorporated into the lattice through a simple spray pyrolysis process.

Zn-doping had negligible impacts on the morphological and optical properties of both the TiO_2 ETLs and the perovskite layers on top. The doping density of the TiO_2 was decreased very slightly, but the V_{FB} was largely negatively shifted. Recombination in the device under operating conditions was decreased after Zn-doping. On the other hand, the FF was decreased due to an increase of the series resistance, leading to decreased PCEs of the planar cells with the Zn-doped TiO_2 ETLs. To minimise the negative effect of the Zn-doping while retaining the positive side, a bilayer ETL was constructed by depositing a thin layer of Zn-TiO_2 on top of the pristine TiO_2. When the thickness of the Zn-TiO_2 is very small, it works as interface engineering with the drawbacks in series resistance being minimised, so the V_{OC} and FF of the device are improved, resulting the enhanced PCE of the cells. As the thickness of the Zn$-TiO_2$ layer further increased, the negative effects become profound again, and cell performance decreases.

Sn and Nb doping, on the other hand, worked differently from Zn-doping. They also showed insignificant impact on the morphology and optical properties of the TiO_2 and perovskite layers, but they influenced the electronic properties of TiO_2 differently from Zn-doping. The doping density of the TiO_2 was also not changed much, but the V_{FB} was shifted quite obviously. Sn-doping showed the smallest effect on the V_{FB}, and the cell performance showed the least changes. Nb-doping, however, positively shifted the V_{FB} of TiO_2, contrary to the case of Zn-doping. As a result, the V_{OC} dropped, leading to the decrease of the PCE.

Finally, the metal ion doping of TiO_2 ETLs showed some effects on the cell performance

of planar perovskite solar cells, but the differences are quite small, typically $\sim 1\,\%$ in PCE at most, which is unlike reports by other research groups[12,13]. It is believed to be due to the fact that the quality of the perovskite films play the most important role in the cell performances, and differences between cells could be due to differences in perovskite morphology if it is not tightly controlled to make it directly comparable.

Reference

[1] H.J. Snaith and M. Grätzel. Electron and hole transport through mesoporous TiO_2 infiltrated with Spiro-MeOTAD. *Advanced Materials*, 19(21):3643–3647, 2007.

[2] D. Yang, X. Zhou, R. Yang, Z. Yang, W. Yu, X. Wang, C. Li, S. Liu, and R.P.H. Chang. Surface optimization to eliminate hysteresis for record efficiency planar perovskite solar cells. *Energy & Environmental Science*, 9(10):3071–3078, 2016.

[3] J. You, L. Meng, T.B. Song, T.F. Guo, Y.M. Yang, W.H. Chang, Z. Hong, H. Chen, H. Zhou, Q. Chen, Y. Liu, N. De Marco, and Y. Yang. Improved air stability of perovskite solar cells via solution-processed metal oxide transport layers. *Nature Nanotechnology*, 11(1):75–81, 2016.

[4] G. Xing, B. Wu, S. Chen, J. Chua, N. Yantara, S. Mhaisalkar, N. Mathews, and T.C. Sum. Interfacial electron transfer barrier at compact TiO_2/$CH_3NH_3PbI_3$ heterojunction. *Small*, 11(29):3606–3613, 2015.

[5] H.P. Dong, Y. Li, S.F. Wang, W.Z. Li, N. Li, X.D. Guo, and L.D. Wang. Interface engineering of perovskite solar cells with PEO for improved performance. *Journal of Materials Chemistry A*, 3(18):9999–10004, 2015.

[6] C. Tao, S. Neutzner, L. Colella, S. Marras, A.R.S. Kandada, M. Gandini, M. De Bastiani, G. Pace, L. Manna, M. Caironi, C. Bertarelli, and A. Petrozza. 17.6% stabilized efficiency in low-temperature processed planar perovskite solar cells. *Energy & Environmental Science*, 8(8):2365–2370, 2015.

[7] Y. Li, J.K. Cooper, W. Liu, C.M. Sutter-Fella, M. Amani, J.W. Beeman, A. Javey, J.W. Ager, Y. Liu, F.M. Toma, and I.D. Sharp. Defective TiO_2 with high photo-

conductive gain for efficient and stable planar heterojunction perovskite solar cells. *Nature Communications*, 7:12446, 2016.

[8] Y.C. Ho, M.N.F. Hoque, E. Stoneham, J. Warzywoda, T. Dallas, and Z.Y. Fan. Reduction of oxygen vacancy related traps in TiO_2 and the impacts on hybrid perovskite solar cells. *Journal of Physical Chemistry C*, 121(43):23939–23946, 2017.

[9] J. Nowotny, T. Bak, M.K. Nowotny, and L.R. Sheppard. Titanium dioxide for solar-hydrogen ii. Defect chemistry. *International Journal of Hydrogen Energy*, 32(14):2630–2643, 2007.

[10] B. Roose, S. Pathak, and U. Steiner. Doping of TiO_2 for sensitized solar cells. *Chemical Society Reviews*, 44(22):8326–8349, 2015.

[11] H. Zhou, Q. Chen, G. Li, S. Luo, T. b. Song, H.-S. Duan, Z. Hong, J. You, Y. Liu, and Y. Yang. Interface engineering of highly efficient perovskite solar cells. *Science*, 345(6196):542–546, 2014.

[12] F. Giordano, A. Abate, J.P. Correa Baena, M. Saliba, T. Matsui, S.H. Im, S.M. Zakeeruddin, M.K. Nazeeruddin, A. Hagfeldt, and M. Grätzel. Enhanced electronic properties in mesoporous TiO_2 via lithium doping for high-efficiency perovskite solar cells. *Nature Communications*, 7:10379, 2016.

[13] J. Peng, T. Duong, X. Zhou, H. Shen, Y. Wu, H.K. Mulmudi, Y. Wan, D. Zhong, J. Li, T. Tsuzuki, K.J. Weber, K.R. Catchpole, and T.P. White. Efficient indium-doped TiO_x electron transport layers for high-performance perovskite solar cells and perovskite-silicon tandems. *Advanced Energy Materials*, 7(4):1601768, 2017.

[14] F. Zhu, P. Zhang, X. Wu, L. Fu, J. Zhang, and D. Xu. The origin of higher open-circuit voltage in Zn-doped TiO_2 nanoparticle-based dye-sensitized solar cells. *ChemPhysChem*, 13(16):3731–3737, 2012.

[15] K.-P. Wang and H. Teng. Zinc-doping in TiO_2 films to enhance electron transport in dye-sensitized solar cells under low-intensity illumination. *Physical Chemistry Chemical Physics*, 11(41):9489–9496, 2009.

[16] Q. Liu, Y. Zhou, Y. Duan, M. Wang, and Y. Lin. Improved photovoltaic performance of dye-sensitized solar cells (DSSCs) by Zn+Mg co-doped TiO_2 electrode. *Electrochimica Acta*, 95:48–53, 2013.

[17] Y.N. Tan, C.L. Wong, and A.R. Mohamed. An overview on the photocatalytic activity of nano-doped-TiO_2 in the degradation of organic pollutants. *ISRN Materials Science*, 2011:1–18, 2011.

[18] H.-H. Wang, Q. Chen, H. Zhou, L. Song, Z.S. Louis, N.D. Marco, Y. Fang, P. Sun, T.-B. Song, H. Chen, and Y. Yang. Improving the TiO_2 electron transport layer in perovskite solar cells using acetylacetonate-based additives. *Journal of Materials Chemistry A*, 3(17):9108–9115, 2015.

[19] B. Roose, K.C. Gdel, S. Pathak, A. Sadhanala, J.P.C. Baena, B.D. Wilts, H.J. Snaith, U. Wiesner, M. Grätzel, U. Steiner, and A. Abate. Enhanced efficiency and stability of perovskite solar cells through nd-doping of mesostructured TiO_2. *Advanced Energy Materials*, 6(2):1501868, 2016.

[20] H. Tan, A. Jain, O. Voznyy, X. Lan, F.P. Garcia de Arquer, J.Z. Fan, R. Quintero-Bermudez, M. Yuan, B. Zhang, Y. Zhao, F. Fan, P. Li, L.N. Quan, Y. Zhao, Z.H. Lu, Z. Yang, S. Hoogland, and E.H. Sargent. Efficient and stable solution-processed planar perovskite solar cells via contact passivation. *Science*, 355(6326):722–726, 2017.

[21] M.-C. Wu, S.-H. Chan, M.-H. Jao, and W.-F. Su. Enhanced short-circuit current density of perovskite solar cells using Zn-doped TiO_2 as electron transport layer. *Solar Energy Materials and Solar Cells*, 157(Supplement C):447–453, 2016.

[22] M. Lv, W. Lv, X. Fang, P. Sun, B. Lin, S. Zhang, X. Xu, J. Ding, and N. Yuan. Performance enhancement of perovskite solar cells with a modified TiO_2 electron transport layer using Zn-based additives. *RSC Advances*, 6(41):35044–35050, 2016.

[23] C.E. Taylor, S.D. Garvey, and J.E. Pemberton. Carbon contamination at silver surfaces: Surface preparation procedures evaluated by raman spectroscopy and x-ray photoelectron spectroscopy. *Analytical Chemistry*, 68(14):2401–2408, 1996.

[24] K. Wu and J. Cui. Synthesis of TiO_2 nanocrystals with exposed 001 facets and improved photocatalytic activity. *Optik*, 164:556–560, 2018.

[25] S.K. Md Saad, A.A. Umar, H.Q. Nguyen, C.F. Dee, M.M. Salleh, and M. Oyama. Porous (001)-faceted Zn-doped anatase TiO_2 nanowalls and their heterogeneous photocatalytic characterization. *RSC Advances*, 4(100):57054–57063, 2014.

[26] K.D. Han, W. Mariah, L. Kyoungmi, and P.G. N. Atomic layer deposition of high performance ultrathin TiO_2 blocking layers for dyesensitized solar cells. *ChemSusChem*, 6(6):1014–1020, 2013.

[27] Wentao Deng. Small molecules for applications in solar cells, 2017.

[28] F. Hao, C.C. Stoumpos, D.H. Cao, R.P.H. Chang, and M.G. Kanatzidis. Lead-free solid-state organicinorganic halide perovskite solar cells. *Nature Photonics*, 8(6):489–494, 2014.

[29] B.J. Morgan and G.W. Watson. Intrinsic n-type defect formation in TiO_2: A comparison of rutile and anatase from GGA+U calculations. *The Journal of Physical Chemistry C*, 114(5):2321–2328, 2010.

[30] R. Beranek. (photo) electrochemical methods for the determination of the band edge positions of TiO_2-based nanomaterials. *Advances in Physical Chemistry*, 2011:1–20, 2011.

[31] H. Tang, K. Prasad, R. Sanjins, P.E. Schmid, and F. Lvy. Electrical and optical properties of TiO_2 anatase thin films. *Journal of Applied Physics*, 75(4):2042–2047, 1994.

[32] F. Xinjian, S. Karthik, P. Maggie, and G.C. A. Tantalumdoped titanium dioxide nanowire arrays for dyesensitized solar cells with high opencircuit voltage. *Angewandte Chemie. International Edition in English*, 121(43):8239–8242, 2009.

[33] A. Pockett, G.E. Eperon, T. Peltola, H.J. Snaith, A. Walker, L.M. Peter, and P.J. Cameron. Characterization of planar lead halide perovskite solar cells by impedance spectroscopy, open-circuit photovoltage decay, and intensity-modulated photovoltage/photocurrent spectroscopy. *The Journal of Physical Chemistry C*, 119(7):3456–3465, 2015.

[34] W.G.J.A. H., S. Max, S.A. Miquel, M. Cristina, . Jorge, and B.H. J. Trap-assisted non-radiative recombination in organic-inorganic perovskite solar cells. *Advanced Materials*, 27(11):1837–1841, 2015.

[35] K.H. Do, O. Hideo, B. Hiroaki, and I. Shinzaburo. Photovoltaic performance of perovskite solar cells with different grain sizes. *Advanced Materials*, 28(5):917–922, 2016.

[36] R.S. Mane, W.J. Lee, H.M. Pathan, and S.-H. Han. Nanocrystalline TiO_2/Zno thin films: Fabrication and application to dye-sensitized solar cells. *The Journal of Physical Chemistry B*, 109(51):24254–24259, 2005.

[37] X. Xu, H. Zhang, J. Shi, J. Dong, Y. Luo, D. Li, and Q. Meng. Highly efficient planar perovskite solar cells with a TiO_2/ZnO electron transport bilayer. *Journal of Materials Chemistry A*, 3(38):19288–19293, 2015.

[38] Q. Wang, Q. Dong, T. Li, A. Gruverman, and J. Huang. Thin insulating tunneling contacts for efficient and water-resistant perovskite solar cells. *Advanced Materials*, 28(31):6734–6739, 2016.

Chapter 6

Synthesis of perovskite nanocrystals

As is discussed in previous chapters, the crystallisation of perovskite within thin films is highly influenced by the processing conditions such as humidity, temperature, atmosphere and even light, which makes the fabrication of perovskite films hard to control. The preparation of perovskite solar cells has to be conducted under strictly-controlled conditions, typically with the assistance of glove boxes, and reproducibility can be a challenge, which greatly hinders their practical production and application. Therefore, it would be very interesting if the crystallisation and film formation processes of perovskites could be separated and a robust method could be developed for the synthesis of perovskite crystals.

Currently, the synthesis of $APbX_3$ perovskite nanocrystals (NCs) is mainly based on two methods: ligand-assisted reprecipitation (LARP)[1] which involves the reprecipitation of perovskite NCs when the precursor dissolved in a solvent (typically DMF or DMSO) is injected into an anti-solvent (e.g. toluene, hexane), and hot injection (HI)[2] in which a Cs-oleate solution is injected into a PbX_2 solution at elevated temperature. In LARP, bulk material is formed as a by-product together with the NCs, which limits the synthetic yield[1]. While the HI method normally requires temperatures of over 100 °C, and is most commonly used for the synthesis of Cs-based perovskites and rarely for $MAPbX_3$ NCs[3]. Although these two methods can both result in the formation of highly emissive perovskite NCs, the syntheses are typically carried out in batch systems which are characterized by poor heat and mass transport, making the large-scale production difficult due to the limitations in their scale-up.

In this work, a facile continuous flow method was developed for the synthesis of $MAPbX_3$

perovskite NCs at room temperature with no requirement for pre-degassing steps. The resulting perovskite NCs showed narrow size distribution, excellent emissive properties and high stability, and ultra-high reproducibility was achieved. The band-gap of the NCs was easily tuned by changing the halide composition to achieve emissions covering a wide range of visible and near infrared wavelength region.

6.1 Experimental

The flow synthesis of $MAPbX_3$ NCs was conducted in a flow reactor as illustrated in **Fig.3.3**, and details of the procedure can be found in the main experimental **Chapter 3**. Briefly, PbX_2 and MAX solutions were injected by syringe pumps separately into PTFE tubes and mixed in a PFA T-junction. The mixture flowed through a PTFE flow reactor immersed in a 30 °C water bath with a residence time of 10 min. The reaction between MAX and PbX_2 was very fast, with a typical rate constant of $\sim 2.5 \times 10^{-3}$ min^{-1} at 75 °C[4]. The perovskite NCs were observed to nucleate quickly, forming small crystals that created a visible colour change from yellow to brown in the tube a few seconds after mixing. The product was collected in a container inside an ice bath. The resulting mixture was centrifuged and the pellet of solid material obtained was resuspended in toluene. The suspension was then centrifuged again to remove any bulky aggregates. The toluene supernatant solution was stored in a glass vial with a screwed lid in the dark for further characterisations. The post-treatment process for the product after collection is illustrated in **Fig. 6.1**. On the basis of the standard procedure, to study the effect on the size of the NCs, different reaction temperatures (20 °C, 30 °C and 50 °C), different residence time (5 min, 10 min and 20 min by changing the flow rate), and different ligand amounts (one fold, halved and doubled) were compared.

Deposition of films of $MAPbX_3$ NCs was carried out by immersing clean substrates of FTO glass or silicon wafers into the toluene solution of the $MAPbX_3$ NCs prepared using the flow reactor, which were kept in the dark at room temperature for 24 h before being taken out and blow dried with nitrogen. The films were used for XRD and PL measurements to study the crystal structure of the NCs and test their possibility in thin film applications.

Synthesis of bulk $MAPbI_3$ powder and films. 576 mg/mL PbI_2 and 199 mg/mL CH_3NH_3I were dissolved in DMF and stirred at 60 °C for an hour. To make the $MAPbI_3$ powder, the solution was cast onto a clean glass petri dish at 100 °C and left for an hour. To prepare the $MAPbI_3$ films, the solution was spin-coated onto clean 2.5 cm × 2.5 cm FTO substrates at 3000 rpm for 30 s followed by annealing/curing at 100 °C for 30 min.

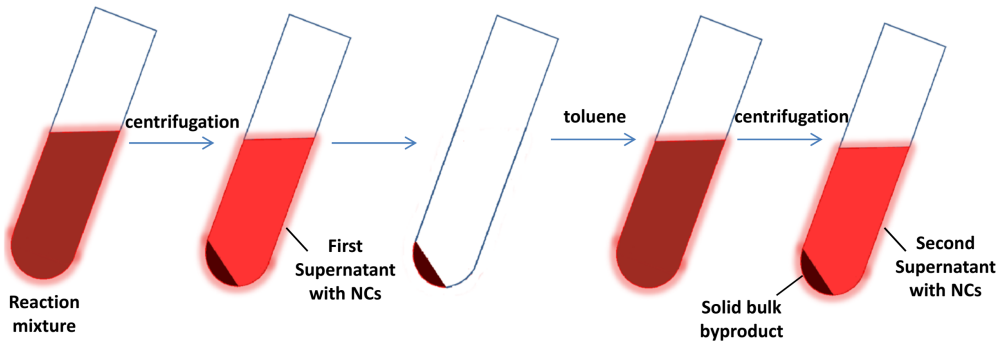

Fig. 6.1 Schematic diagram of the post-treatment for the product after collection of the reaction mixture.

6.2 Synthesis of $MAPbI_3$ NCs

There have been quite a few reports about the synthesis of perovskite NCs, but mainly based on inorganic $CsPbX_3$ perovskite[5–7] or $MAPbBr_3$ perovskite[3,8,9]. The synthesis of $MAPbI_3$ NCs has rarely been reported, and their poor stability is blamed[8,10,11]. In this work, we showed that $MAPbI_3$ NCs could be successfully synthesized using the flow method at low temperature, giving NCs with excellent optical properties and high stability.

TEM images of $MAPbI_3$ NCs are shown in **Fig. 6.2**. The NCs had a cubic morphology with sizes of 10.5 ± 1.5 nm, as shown in the size distribution histogram in **Fig. 6.2**b. The interplanar spacing was measured to be 3.2 Å, which is consistent with the (220) plane of tetragonal phase $MAPbI_3$ perovskite[12]. The perovskite structure of the crystals was further confirmed by X-ray diffraction (XRD) spectra taken for NCs coated onto a piece of silicon wafer, as shown in **Fig. 6.3**. Diffraction peaks at 14.0 ° and 28.3 ° were observed, corresponding to the (110) and (220) planes of the tetragonal perovskite phase. Notably, the peaks are much broader compared with the film of bulk material (see the inset of **Fig. 6.3**), confirming the small crystal sizes. Scherrers equation was used to calculate the

average crystal size.

$$\beta = \frac{K\lambda}{B\cos\theta} \tag{6.1}$$

where β is the mean crystal size, K is the Scherrer constant $K = 0.89$, λ is the wavelength of the X-ray, B is the full width at half maximum (FWHM) of the diffraction peak, and θ is the angle of the diffraction peak. Using this equation, the average crystal size was estimated to be 9.4 ± 0.1 nm, which is in good agreement with the TEM results.

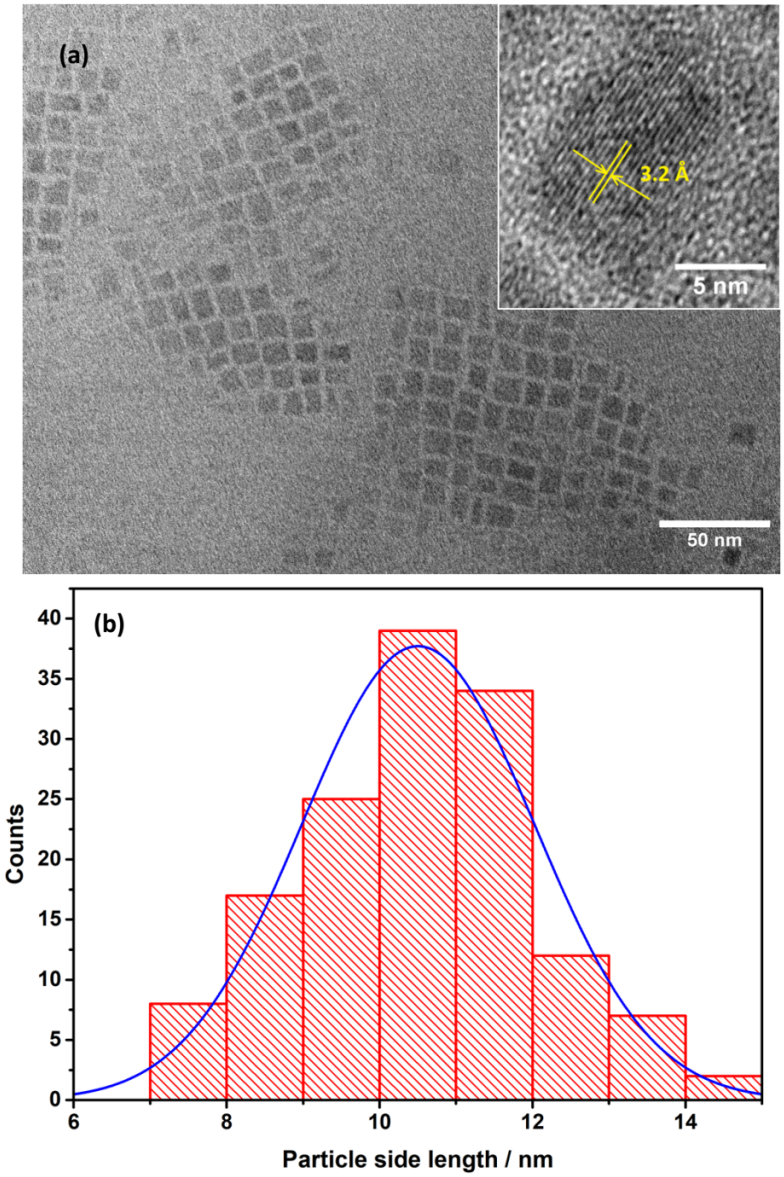

Fig. 6.2 (a) TEM image of the $MAPbI_3$ NCs. The inset is the high resolution TEM of a typical $MAPbI_3$ NC. (b) Size distribution histogram of the $MAPbI_3$ NCs measured from the TEM image. The side lengths of the NCs were obtained by square rooting the areas of the NCs in the TEM image, under the approximation of their shape to be square.

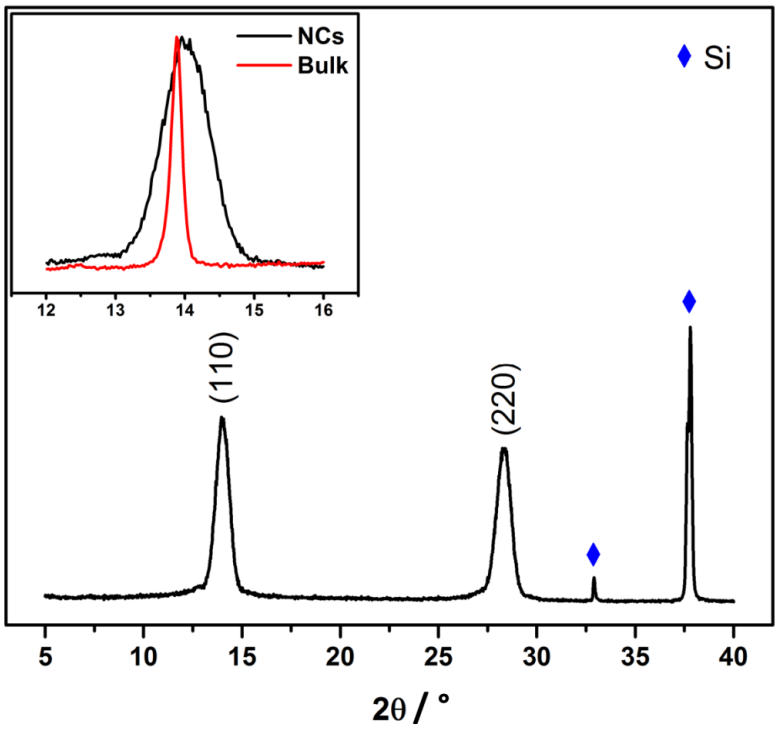

Fig. 6.3 XRD patterns of $MAPbI_3$ NCs coated on a silicon wafer. The inset is the comparison of the (110) peak of the $MAPbI_3$ NCs with that of the bulk film.

The $MAPbI_3$ NCs in toluene solution showed bright red colour under UV light, and exhibited strong optical absorption and emission properties as illustrated in the UV-vis and photoluminescence (PL) spectra in **Fig. 6.4**. The absorption onset is at 740 nm, and the emission peaks sharply at 745 nm, indicating an optical band-gap of 1.66 eV. The absorption and emission are both blue-shifted compared to the bulk material[13] (spectrum shown in **Fig. 6.4**b), which could be due to the quantum confinement effect since the exciton Bohr radius a_B is calculated to be $\sim$ 22 nm using Equation.2.36 (the relative permittivity of $MAPbI_3$ ε=70 according to Meredith[14], and the reduced mass of the exciton μ=0.17m_e according to Yamashita[15]), and the sizes of the NCs as shown in the TEM image are well below a_B. Using the band-gap of 1.60 eV of the bulk material (PL at 775 nm), the band-gap of the NCs with size of 10 nm is calculated from Equation.2.44 to be 1.68 eV, corresponding to a PL peak of 738 nm, which is reasonably close to the 745 nm we obtained. The PL emission peak was sharp, with a narrow FWHM of 39 nm. As quantum confinement effect makes the band-gap size-dependent, the narrow PL peak is believed to a result of a narrow size distribution of the NCs, as confirmed in **Fig. 6.2**b.

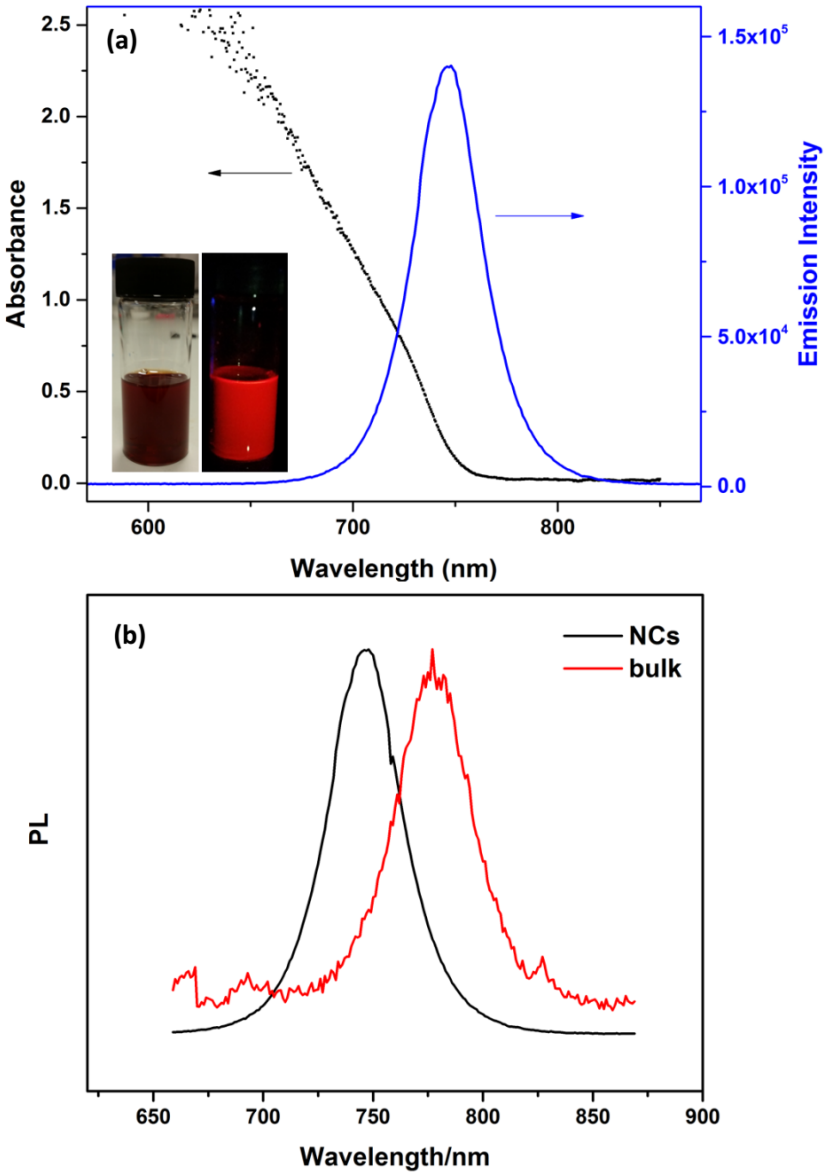

Fig. 6.4 (a) UV-vis and PL spectra of $MAPbI_3$ NCs solution in toluene. The insets show the solution under ambient and UV light. (b) Comparison of the PL spectra of the NCs and bulk powders of $MAPbI_3$ dispersed in toluene. Excitation wavelength: 365 nm.

Stability is an important problem for perovskite NCs, especially MA-based perovskite NCs[3,5]. As is the case with all NCs, they are prone to aggregation which has to be prevented by stabilising ligands, which are oleic acid and oleylamine in our case. $MAPbX_3$ perovskites can also be easily decomposed into PbI_2 [16] in the presence of polar solvents such as water through reaction 1.2. To investigate the long term stability of the $MAPbI_3$ NCs in toluene solution, PL emission spectra were measured at regular intervals for more than one month, as shown in **Fig. 6.5**a. No position shift or width broadening was observed in the emission peak for the $MAPbI_3$ NC solution over 39 days, as seen in **Fig. 6.5**b.

Actually the PL intensity increased with time during storage, which could be related to a decrease in the concentration of the NCs in the solution due to their adhesion on the wall of the vial container, as thin films of the NCs can be clearly observed on the inner wall of the vial. As the solution was highly concentrated, which is evidenced by the deep colour and strong absorption in **Fig. 6.4**a, the emission could be self-quenched, self-absorbed or scattered by the NCs to some extent. Therefore, when the concentration was decreased, these effects were reduced and the emission intensity was enhanced. The stability of the $MAPbI_3$ NCs was also confirmed by the TEM images shown in **Fig. 6.5**c and d. After being kept for over 8 months, the cubic morphology of the NCs was retained and the size showed no obvious changes. The high stability of the $MAPbI_3$ NCs are believed to be due to the presence of hydrophobic long-chain ligands, which not only prevented the NCs from aggregating, but also acted as a barrier to slow moisture reaching the perovskite core.

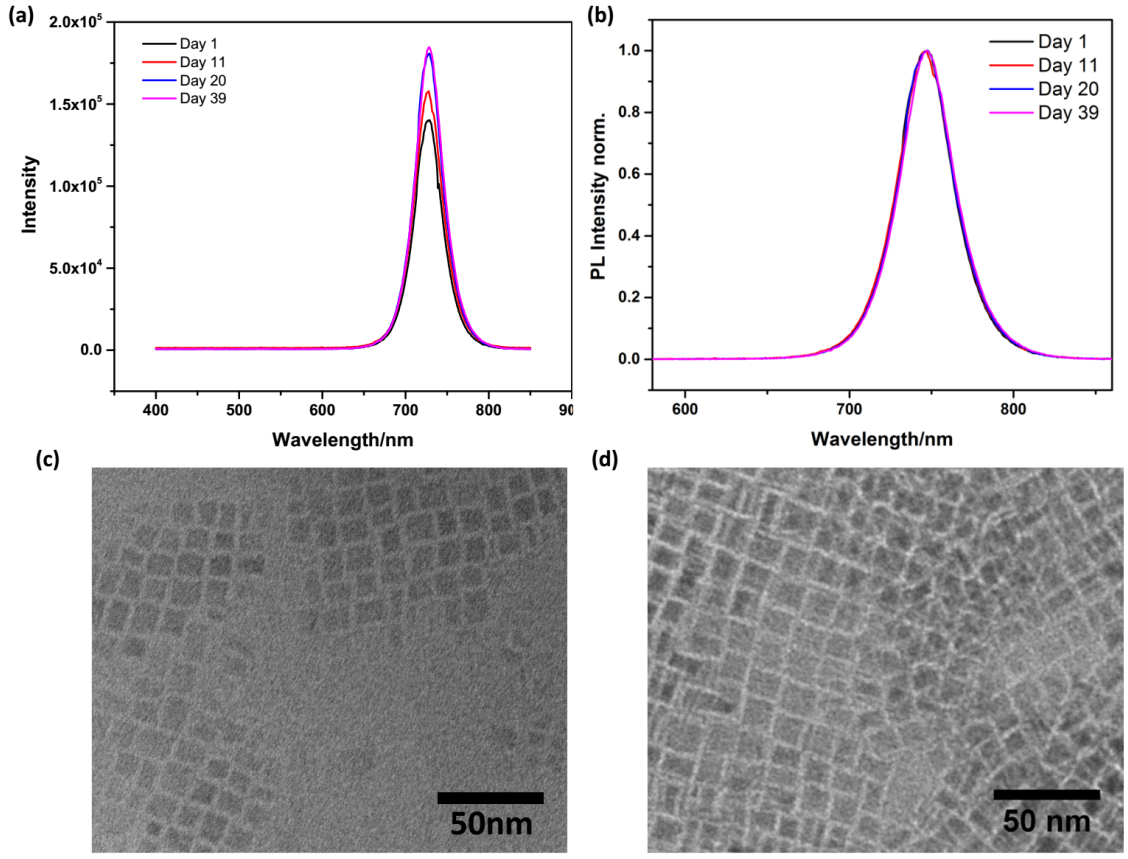

Fig. 6.5 Stability of the $MAPbI_3$ NCs. (a) PL spectra and (b) normalised PL spectra taken for the $MAPbI_3$ NC solution over 39 days; TEM images of the NCs: (c) as-prepared and (d) after over 8 months. The solution was stored in a glass vial with screwed lid at room temperature in the dark.

Notably, the flow synthesis showed outstanding reproducibility, as shown in the PL spectra of eleven independent repeats in **Fig. 6.6**. The emission peaks showed high conformity, centering at 742.4 ± 1.6 nm, with the FWHM of 39.8 ± 0.3 nm. The small deviations indicated the high robustness of the method. The reproducibility of the NCs are much better than the films of the $MAPbI_3$ bulk material discussed in previous chapters, which may be due to the fact that the crystallisation occurs in the solution and does not contact directly with air. Therefore the crystallisation of the NCs are less affected by humidity and atmosphere than in the films and much easier to control.

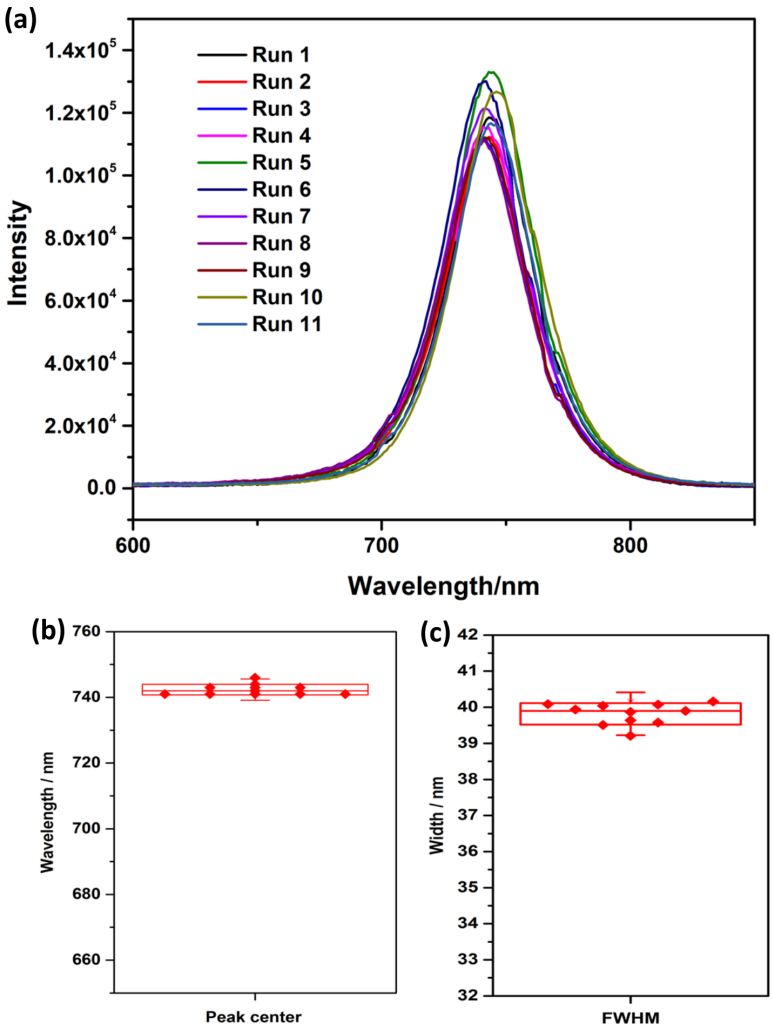

Fig. 6.6 (a) PL spectra of $MAPbI_3$ NCs obtained in 11 different runs and the box plots of the (b) peak positions and (c) FWHM.

For NCs, a very important advantage is their size-dependent band-gap which makes it feasible to tune their optical properties by controlling their sizes. Therefore, tuneability is an important aspect in the synthesis of NCs. In this work, to investigate the tuneability of

the flow synthesis of perovskite NCs, a few process conditions that we think are important in size control, including temperature, residence time, ligand concentration and washing liquid, are investigated.

6.2.1 Temperature

As the rates of nucleation and crystal growth, which determine the size of colloid nanocrystals, are both temperature-dependent[17], temperature has been an important factor for tuning the particle size during quantum dots syntheses, especially in hot injection method[18–20]. The crystallisation process involves nucleation, only occuring when the concentration of the solute is above the critical nucleation concentration C_{min}^{nu}, followed by growth of the particles, as shown in **Fig. 6.7**[21]. At higher temperature, since the solubility of the solute normally increases, both the saturation concentration C_S and the critical nucleation concentration C_{min}^{nu} would increase as well, which would result in the suppress of the nucleation process and consequently bigger particle sizes. Therefore, to study the tunability of the NC sizes in the flow synthesis, different temperatures of 20 °C, 30 °C and 50 °C were investigated.

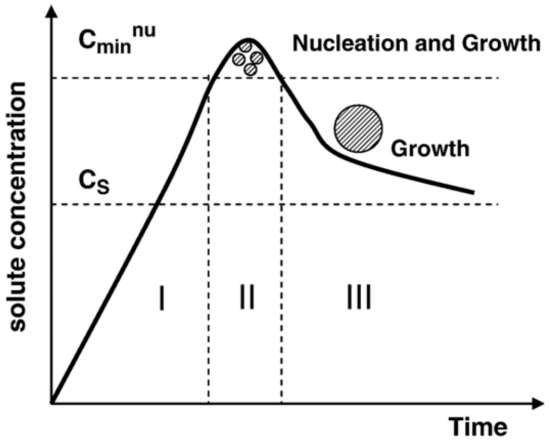

Fig. 6.7 Schematic diagram showing the nucleation and growth processes during crystallisation.[21]

As seen in **Fig. 6.8**a, small shifts in the PL peak positions of the NCs in toluene prepared at different temperatures were observed. However, when the temperature was raised to 50 °C, or lowered to 20 °C, the PL spectra showed properties of multiple peaks, which indicated particles of different sizes. What exactly toluene washing does to the NCs to cause

the changes in their sizes is still uncertain. It could be due to the incomplete removal of the reactants through centrifugation, which reprecipitate and form smaller crystals when added into toluene. Or it could be due to the change in the morphology of the NCs upon dispersion in toluene. Urban and coworkers have reported[22] an obvious blue-shift in PL of $MAPbBr_3$ NCs upon dilution in toluene. The large NCs are fragmentated due to osmotic swelling, forming different morphologies, and the excess ligands in the solution quickly passivate the new surfaces and stabilize the smaller NCs. In order to get rid of the affect of the toluene washing and obtain the direct information about temperature on the particle sizes, the PL spectra of our NCs in the first supernatant of the as-prepared mixtures were retrieved. As seen from **Fig. 6.8**b, the position of the PL peak maximum was basically the same for the NCs synthesised at different temperature, but peak broadening was observed for the NCs made at higher temperatures, as evidenced by the tails at shorter wavelength in the PL spectra. The asymmetry of the emission peaks suggested the formation of more smaller particles at higher temperature, which is contrary to literature reports where bigger particles were normally obtained at higher temperature[19,23]. The reason of the anomalous change in particle sizes with temperature still needs more investigations to figure out.

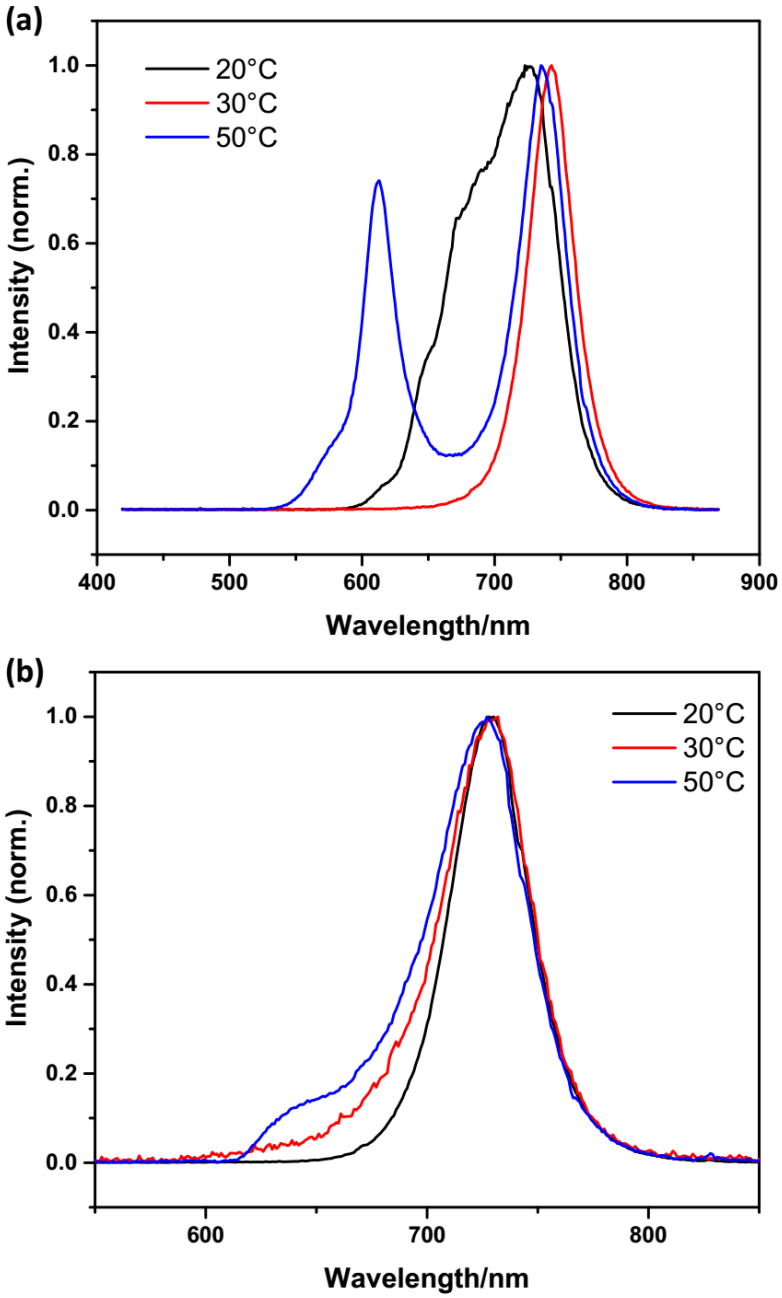

Fig. 6.8 PL spectra of the $MAPbI_3$ NCs synthesised at different temperatures: (a) the second supernatant in toluene and (b) the first supernatant of the as-prepared reaction mixture.

6.2.2 Residence time

In flow chemistry, the residence time is a most important parameter, as it is the reaction time of the reactants in the tubing. In the case of NC synthesis, the residence time affects the extent of crystal growth, and therefore has great impact on the size of the NCs. Longer residence time potentially results in larger crystal sizes. Thus, in this work, while the tube

length and diameter were kept constant, the flow rates of the reactants were doubled or halved to achieve different residence times of 5 min, 10 min and 20 min, and the impact on the NC sizes were investigated.

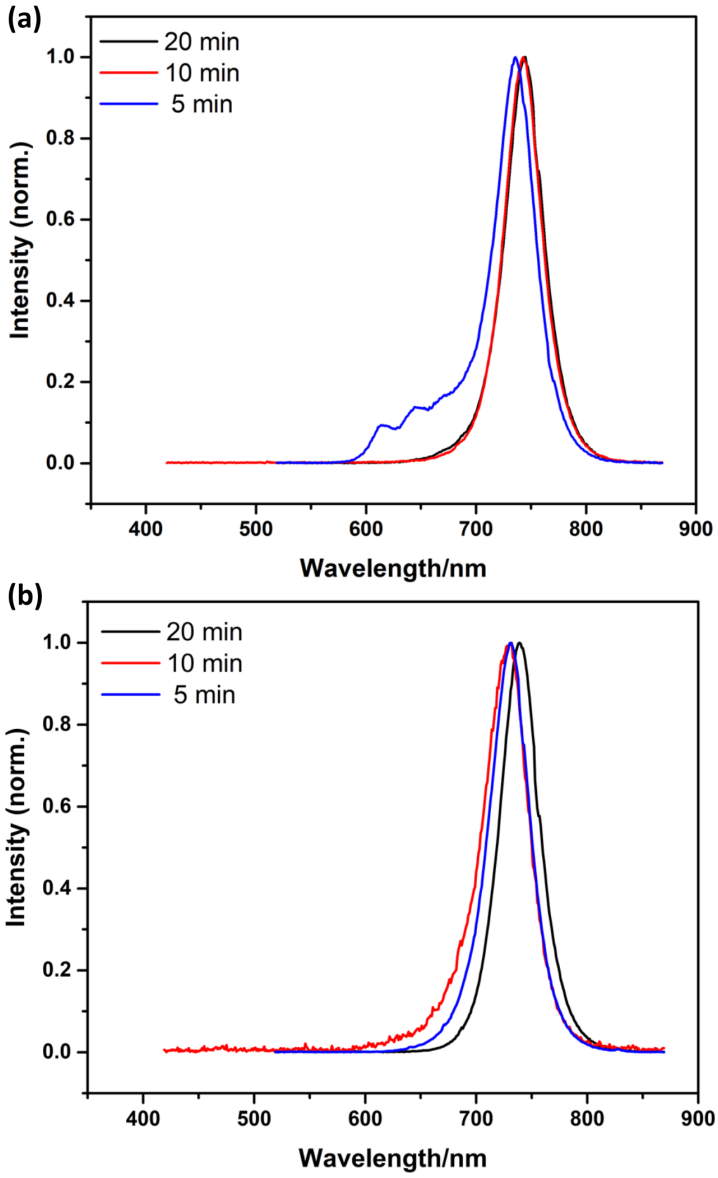

Fig. 6.9 PL spectra of the $MAPbI_3$ NCs synthesised with different residence time: (a) the second supernatant in toluene and (b) the first supernatant of the as-prepared reaction mixture.

The $MAPbI_3$ NCs in toluene prepared with the residence time of 10 min and 20 min showed almost identical PL spectra, as shown in **Fig. 6.9**a, while multiple PL peaks were again observed for the sample made with the residence time of 5 min. Again, to get rid of the affect of the toluene washing, the PL spectra of the NCs in the first supernatant of the as-prepared mixtures were compared, as seen in **Fig. 6.9**b. The PL emission peak became

sharper when the flow rate was doubled, which could be ascribed to the improved mixing of the reactants at higher flow rate. While the peak shifted slightly to longer wavelength as the flow rate was halved, indicating a slight increase of the particle size with longer residence time. The insignificance of the changes in the PL spectra with the different residence time of 5 min, 10 min and 20 min could be due to the fast kinetics of the reaction, which can be seen from the fast colour change of the mixture in the tube, so that a plateau of the particle size has been reached after 5 min.

6.2.3 Ligand concentration

In the synthesis of perovskite NCs, the ligands are very important, which not only control the kinetics of crystallisation, but also suppress the aggregation of the NCs[1]. More ligand used in the synthesis can potentially stabilize the nanocrystals at earlier stage of the crystallisation, and consequently result in smaller crystal size. Therefore, ligand concentration could be another important factor for the tuning of the size of the NCs. In this work, 1.2 mL OLA and 2.2 mL OA were used as standard, which were also halved and doubled, for the synthesis of $MAPbI_3$ NCs, and the PL spectra were compared.

Again, multiple peaks were observed in the PL spectra of $MAPbI_3$ NCs in toluene prepared with different ligand concentrations, as shown in **Fig. 6.10**a. To get rid of the affect of the toluene washing, the the PL spectra of the NCs in the first supernatant of the as-prepared mixtures were also compared, as seen in **Fig. 6.10**b. An obvious blue shift of the PL emission peak was observed when the ligand concentration was increased, indicating the particle size of the NCs was decreased. As the role of the ligands is to stick on the surface of the NCs to suppress their growth into bulk material, higher concentration of the ligands would be able to stabilise the NCs at earlier stage of the crystal growth, and therefore could result in the form of smaller crystals.

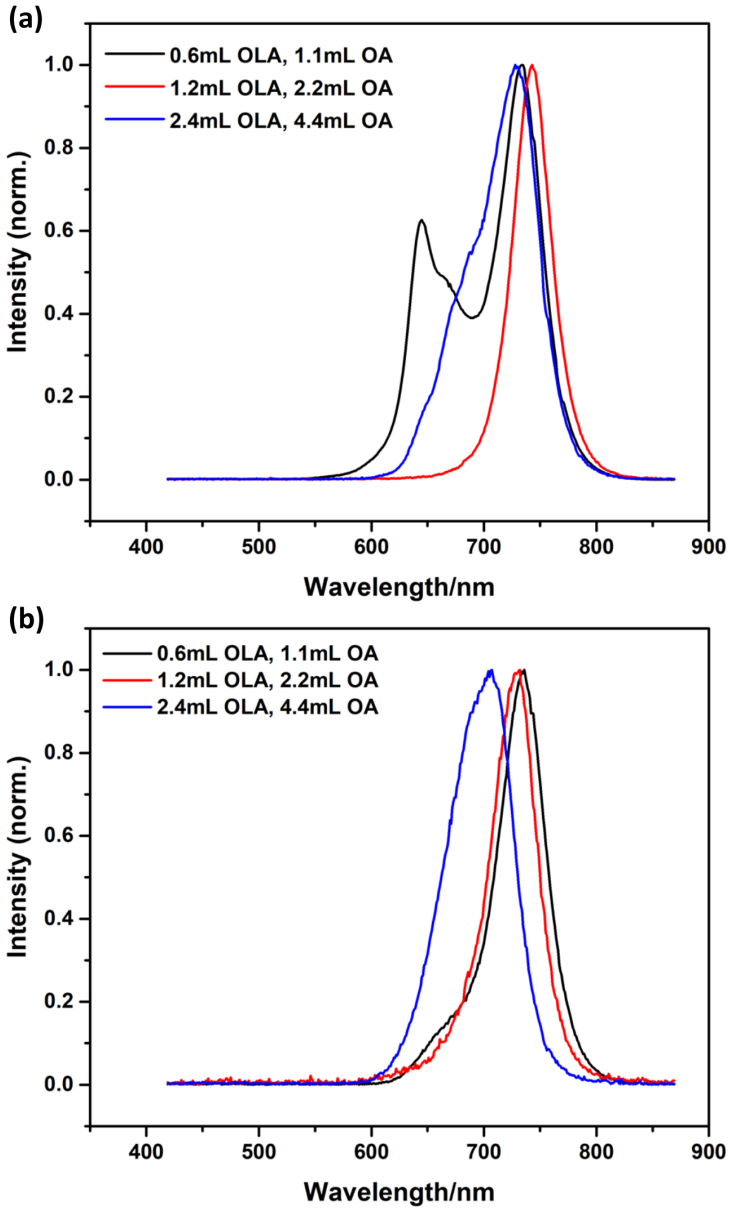

Fig. 6.10 PL spectra of the $MAPbI_3$ NCs synthesised with different ligand amount while all other conditions being kept the same: (a) the second supernatant in toluene and (b) the first supernatant of the as-prepared mixture.

6.2.4 Washing solvent

As discussed in **6.2.1**, the washing-out of the $MAPbI_3$ NCs using toluene caused changes to the NCs, which changed their sizes and resulted in the multiple peaks in the PL spectra, possibly due to the reprecipitation of the incompletely removed reactants when added into toluene, or the fragmentation of the NCs due to osmotic swelling upon dispersion in toluene, which resulted in the formation of smaller crystals. In the hope of addressing

this problem, different solvents were compared for the washing-out of the NCs. **Fig. 6.11** showed the PL spectra of $MAPbI_3$ NCs synthesised at standard condition with toluene, hexane and diethyl ether as the washing solvent respectively. All these solvents worked well for the re-suspension of the $MAPbI_3$ NCs at standard condition, as seen from the sharp emission peaks in the PL spectra. All the peaks showed narrow FWHMs of below 40 nm. Comparing with the first supernatant (729 nm), all the washed-out solutions showed notable red shift in their PL, which is reasonable as the NCs in the solutions were washed out from the pellets and are expected to be slightly bigger in size than that remained in the first supernatant. Moreover, the PL peaks was shifted differently with the different washing solvents. Toluene washing exhibited the smallest red shift to 748 nm, while hexane and diethyl ether washing shifted the PL to 752 nm and 759 nm respectively. The difference in the peak positions could be due to the different dispersibility of the NCs which resulted in the washing out of NCs with different sizes.

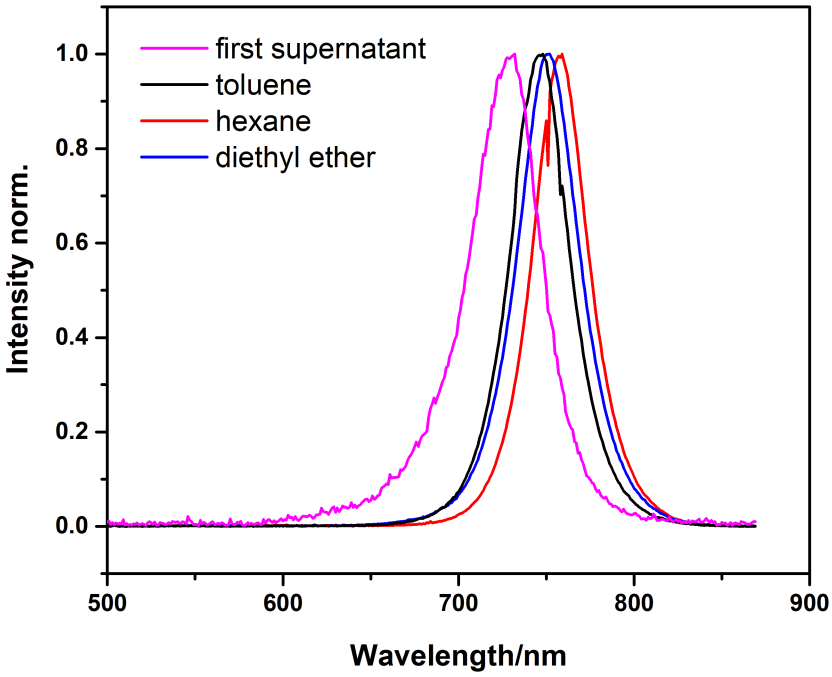

Fig. 6.11 PL spectra of the $MAPbI_3$ NCs washed out with different solvents. All other conditions are kept the same as standard.

These solvents were further used for the synthesis of the $MAPbI_3$ NCs with doubled ligand concentration, as the PL spectra of the NCs in the first supernatant of the as-prepared mixture showed obvious blue shift compared with that obtain at standard condition, as shown in **Fig. 6.10**b. The PL spectra peaked at the same wavelength of 739 nm for all

the samples with the three solvents, as seen in **Fig. 6.12**, blue shifted compared with the 745 nm of the NCs made with standard ligand concentration. However, multiple peaks were still observed, though less pronounced for the sample in diethyl ether. Therefore, diethyl ether might be a slightly better washing solvent in terms of size tuning of the $MAPbI_3$ NCs, but better understanding of what solvent washing does to the NCs is still needed in order to fully solve the problem.

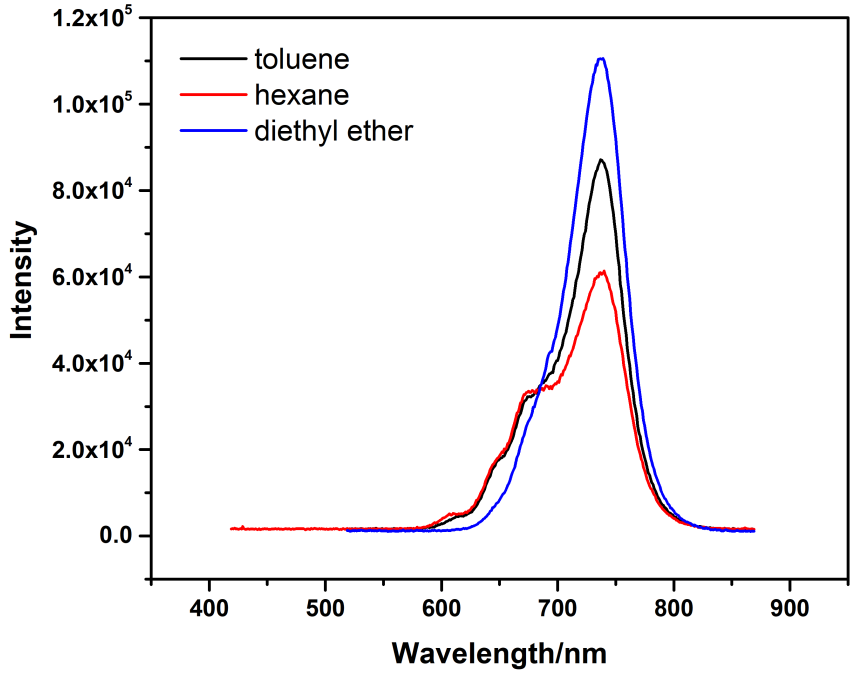

Fig. 6.12 PL spectra of the $MAPbI_3$ NCs synthesised with doubled ligand concentration using different solvents as washing solvents.

6.3 Synthesis of $MAPbX_3$ NCs with different halide compositions

As has been well understood, the band-gap of organolead halide perovskites can be effectively tuned by changing the halide composition[24,25]. The band-gap becomes larger when the halide is changed from iodine to bromine and further to chlorine, and continuous tuneability can be achieved by using the binary mixture of adjacent halides with different ratios. The easy tuneability of the band-gap makes perovskites very promising

for applications in LEDs and lasers. NCs of $CsPbX_3$, $MAPbI_3$ and $FAPbX_3$ Perovskites with different halide compositions have also been prepared[1,5,26], which showed luminescences covering wide wavelength ranges in visible region, with high quantum yield and colour purity. To investigate the feasibility of the flow method in the synthesis of perovskite NCs with different halide compositions, a range of $MAPbI_xBr_{3-x}$ NCs were also prepared with the facile flow reactor.

As shown in **Fig. 6.13**, the addition of bromine shifted the emission peak to lower wavelengths, indicating a larger band-gap with an increase of bromine content. A wide range of $MAPbI_xBr_{3-x}$ compositions were investigated, allowing us to tune the emission between 485 nm and 745 nm. It was a larger range than has previously been reported for $CsPbX_3$ quantum dots[19], and also slightly wider than that for $MAPbX_3$ NCs reported by Zhang[1] made by the LARP method in a batch process. The NCs prepared by Zhang showed tuneable emission between 515-734 nm when the halide composition was changed from $MAPbBr_3$ to $MAPbI_3$. For all of our compositions, excellent colour purity was observed with FWHMs of below 50 nm, which suggests a narrow size distribution of the NCs and means the NCs have the potential to be used for LED and lasing applications.

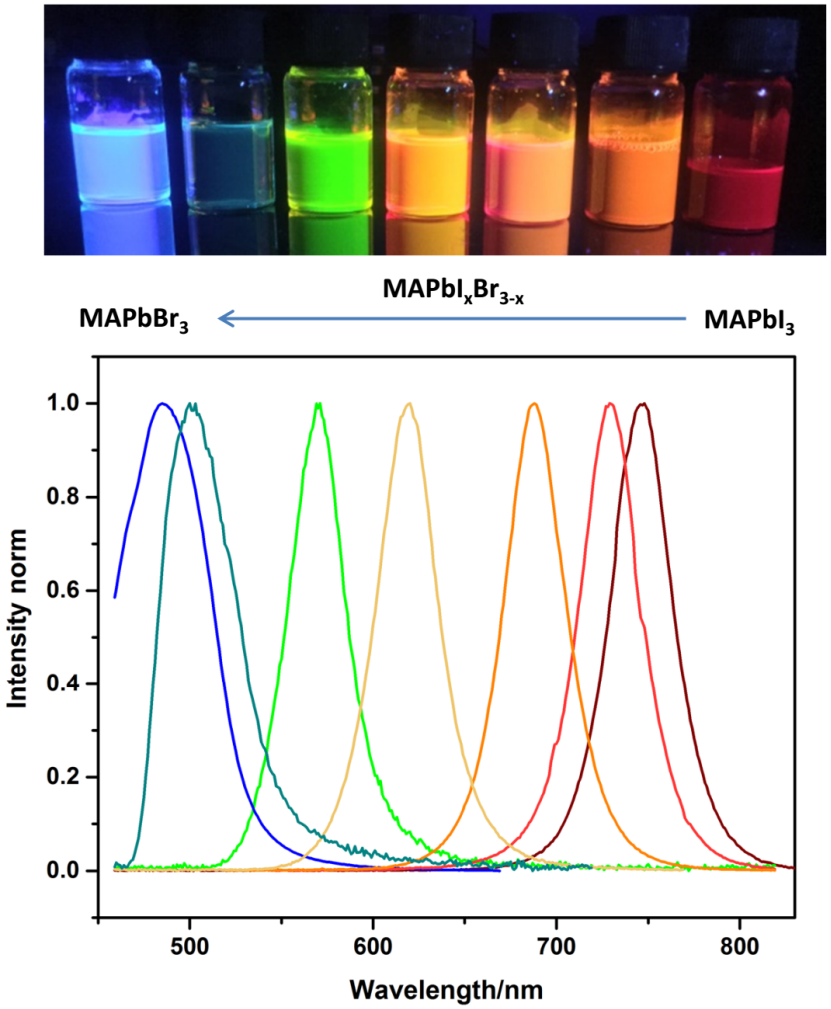

Fig. 6.13 Photograph of sample vials under UV illumination and PL spectra of $MAPbI_xBr_{3-x}$ perovskite NCs in toluene with different halide compositions.

Interestingly, the NCs with different halide compositions showed different morphologies. As shown in **Fig. 6.14**, in addition to cubes of ~ 10 nm, the $MAPbIBr_2$ NCs also presented small dots of 2-5 nm in diameter, while $MAPbBr_3$ NCs were all tiny dots with diameters of 2.8 ± 0.3 nm. It was quite surprising to see mixed morphology in the $MAPbIBr_2$ sample as a single narrow peak was observed in the PL as seen in **Fig. 6.13**. It is possible that the number of the dots are very small compared to the cubes so that the fluorescence signal from them are too low to be distinguished in the spectrum. Also the smaller nanoparticle could have been formed during the sample preparation for TEM. Future work is needed to understand the morphology evolution from cubes to dots between the I^- and Br^- perovskites. The ultra small size of the $MAPbBr_3$ NCs is believed to be responsible for the emission below 500 nm.

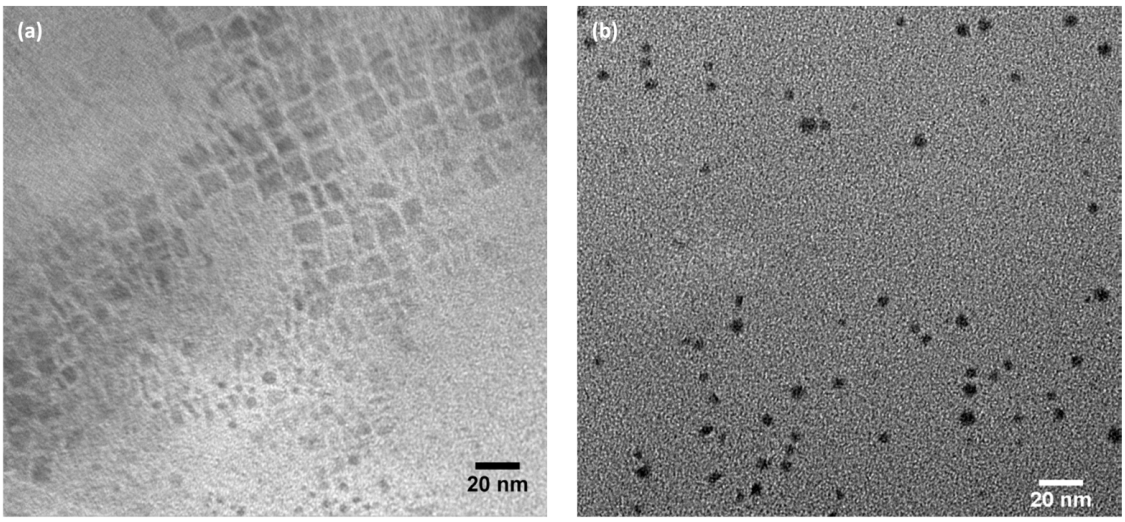

Fig. 6.14 TEM images of the (a) $MAPbIBr_2$ and (b) $MAPbBr_3$ NCs.

The mixed halide NCs also showed high stability, as shown in the long term PL spectra for $MAPbIBr_2$ and $MAPbBr_3$ NCs displayed in **Fig. 6.15**. The $MAPbIBr_2$ NCs showed very high stability over a time span of 26 days, showing almost identical PL spectra in terms of peak position and peak shape. The $MAPbBr_3$ NCs also showed reasonably high stability, though the peak position of the PL was slightly red shifted from 485 nm to 492 nm over 7 days, indicating the moderate growth of the particle size which then stabilised, evidenced by no further shifting of the peak in the next 100 days. The slightly poorer stability of the $MAPbBr_3$ NCs may also be related to their ultra small sizes which make them ultimately active to agglomeration.

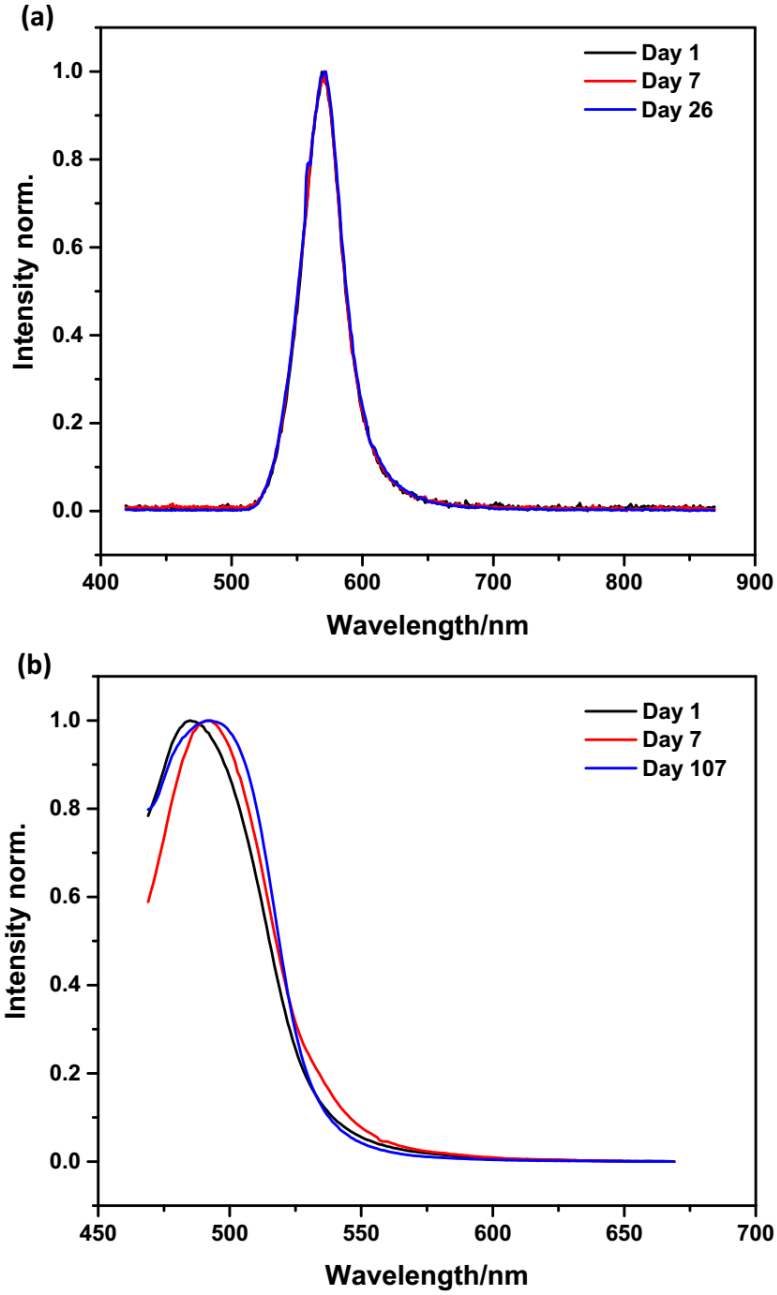

Fig. 6.15 PL spectra of (a) $MAPbIBr_2$ and (b) $MAPbBr_3$ NCs in toluene over 26 days and 107 days respectively.

To investigate the possibility of the NCs to be applied in display or photovoltaic devices, films of $MAPbI_3$, $MAPbIBr_2$ and $MAPbBr_3$ NCs showing light emissions in red, green and blue colours were made using a dip-coating method. The photographs and PL spectra of the films are illustrated in **Fig. 6.16**. The PL properties of the NCs were well retained after they were made into films. Bright emission is visible in the photographs under UV light, and sharp emission peaks were recorded at 736 nm, 527 nm, 461 nm respectively.

The peak positions of the films were slightly blue shifted compared with the solution in toluene (745 nm, 570 nm and 485 nm respectively as shown in **Fig. 6.13**), which could be due to the interaction with solvents in the solution and the orientation of the NCs in the solid state[27,28]. The emission peaks also showed small FWHMs, demonstrating their high colour purity, especially the $MAPbBr_3$ NCs, indicating they could be suitable for display applications. Notably, the signal of the $MAPbIBr_2$ film was very noisy, which was due to the low intensity of the spectrum. For one thing, it was partly because of the low resolution of the spectrometer on solid samples without the assistance of an integrating sphere, for another, it also indicated the low quantum yield of the $MAPbIBr_2$ NCs compared with NCs with other halide compositions.

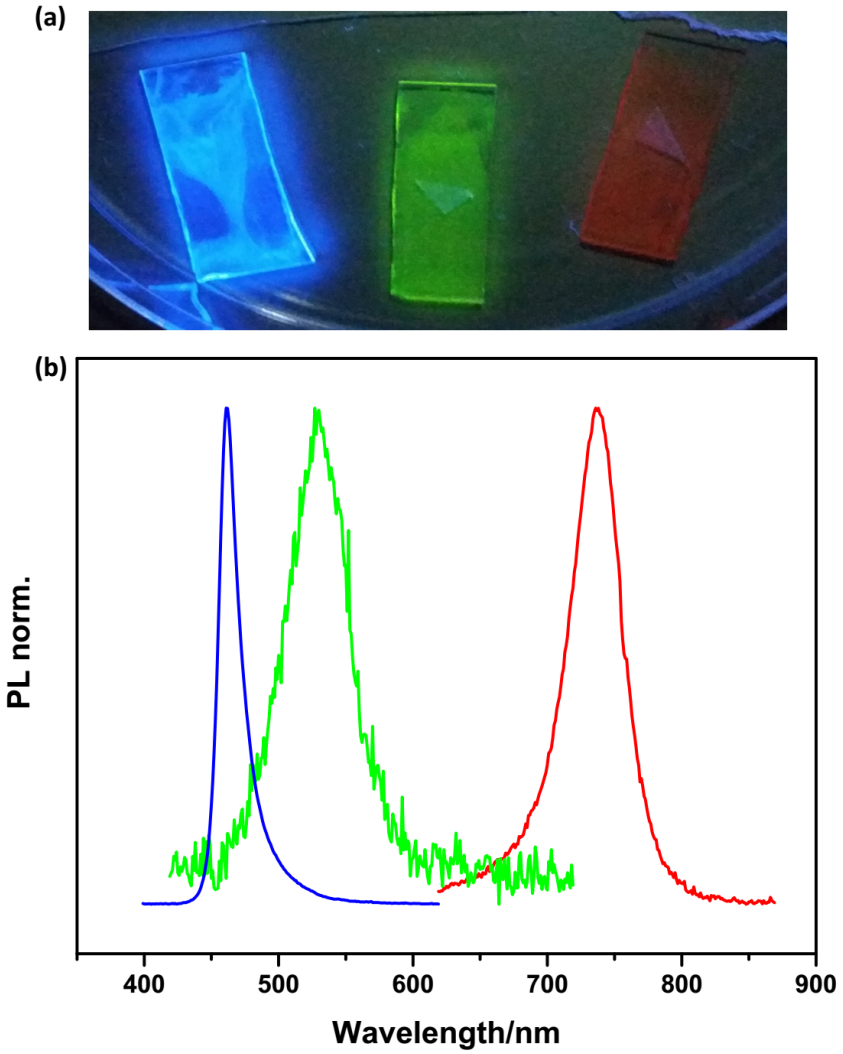

Fig. 6.16 (a) Optical image and (b) PL spectra of films of $MAPbI_3$, $MAPbIBr_2$ and $MAPbBr_3$ perovskite NCs on glass substrates showing red, green and blue emissions respectively.

6.4 Synthesis of $APbI_3$ NCs with different organic cations

Apart from halide composition, different cations at the A site have also been widely investigated[29] to explore other new potential 3D or 2D perovskite materials, such as formamidinium (FA)[30,31], aminovaleric acid (AVA)[32] and tetrabutylammonium[33] lead halides. Previous work in our group has revealed an orange phase of azetidinium lead iodide ($AzPbI_3$)[34] with a possible structure between 2D and 3D perovskite. The substitution of up to 5% Az cations in $MAPbI_3$ solar cells showed improved cell performance and reduced hysteresis. It has also been reported that n-butylammonium (BA) ions can be incorporated into $MAPbI_3$ perovskite and form a Ruddlesden-Popper layered perovskite structure $(BA)_2(MA)_{n-1}Pb_nI_{3n+1}$[35], where the $MAPbI_3$ perovskite layers are isolated from one another by the BA spacer cations and the value of n determines the thickness of each perovskite layer. The layered perovskite structure has showed improved stability compared with their three-dimensional counterparts in stress tests of light, humidity and heat. Therefore, in this work, azetidinium and tert-butylammonium (tBA, which is an isomer of n-butylammonium) are investigated as A site cations for the synthesis of $APbI_3$ NCs.

Fig. 6.17 shows the PL spectra of $AzPbI_3$ NCs. Unlike $MAPbI_3$ NCs, the toluene washing liquid showed almost negligible fluorescent response, as also seen in the very weak emission under UV light. But interestingly, the first supernatant of the as-prepared mixture showed blue emission peaking at the wavelength of 429 nm, corresponding to a band-gap of 2.89 eV. The band-gap is much higher than the 2.15 eV reported for $AzPbI_3$ bulk films[34]. For comparison, PL spectra of both the AzI and PbI_2 reactants were also measured. No fluorescence signals were observed, which confirmed the blue emission is likely to be from the $AzPbI_3$ product rather than residual reactants. The significant blue-shift of the PL emission was believed to result from the quantum confinement effect due to the small size of the NCs. The absence of fluorescence response in the toluene washing liquid suggests that the NCs could not be separated by centrifugation, also an indication of the ultra small size of the NCs. However, due to the high boiling point of the octadecene solvent in the first supernatant, no TEM or XRD data could be obtained. For further characterisations and applications, proper methods for the isolation of the NCs from the liquid need to be developed.

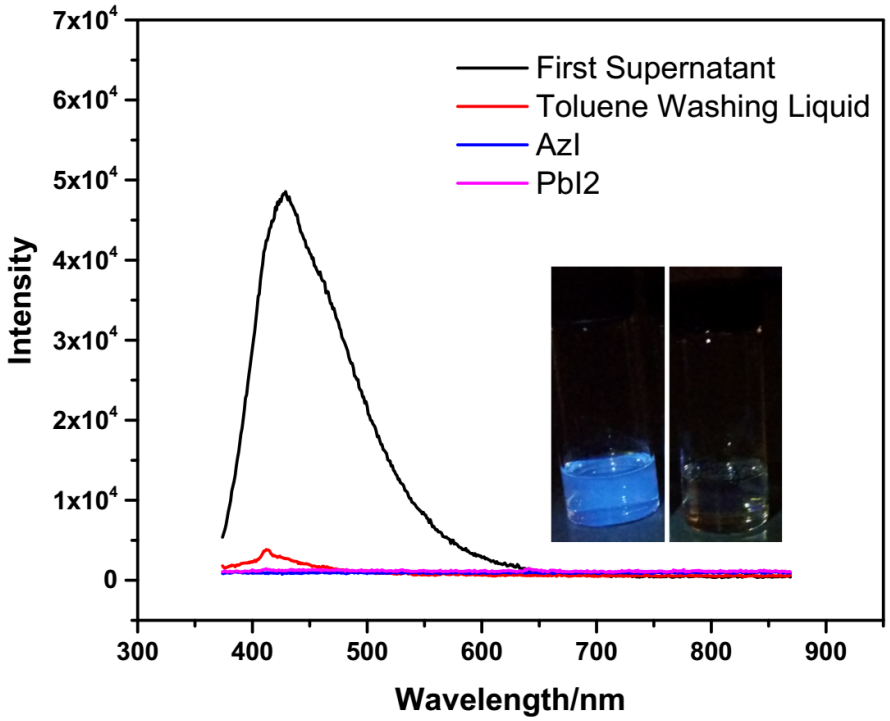

Fig. 6.17 PL spectra of $AzPbI_3$ NCs in the first supernatant and in toluene. The insets are their photo images under UV light: first supernatant on the left and toluene washing liquid on the right.

Synthesis of perovskite NCs with tBA as the A site organic cation was also attempted with the MAI solution being replaced by tBAI. However, no colour change or solid precipitation was observed when PbI_2 solution was mixed with the pure solution of tBAI. It indicated no $tBAPbI_3$ perovskite was formed with the direct reaction of PbI_2 and tBAI. Therefore, a mixture of tBAI : MAI = 1 : 2 was used instead. PL spectra of perovskite NCs with the mixed ammonium cations are shown in **Fig. 6.18**. Both the first supernatant and the toluene washing liquid showed strong PL emission, with peak maxima of 703 nm and 716 nm respectively. The blue-shift of the first supernatant compared with the toluene washing liquid was similar to that observed for $MAPbI_3$ NCs, as discussed in **6.2.4**, due to the selection effect of the centrifugation process. The spectra of the $MAPbI_3$ NCs are also reproduced for comparison. After the incorporation of tBA ions, the PL of both the first supernatant and the toluene washing liquid were blue-shifted, indicating a larger band-gap in the mixed cation perovskite $MA_{2/3}tBA_{1/3}PbI_3$ than $MAPbI_3$, which is similar to the case of BA incorporation[35]. However, broad peaks with long tails at lower wavelength were seen for the $MA_{2/3}tBA_{1/3}PbI_3$ NCs in both the first supernatant and toluene

washing liquid, suggesting the uneven size distribution, which might be due to a different crystallisation kinetics for the mixed cation perovskite.

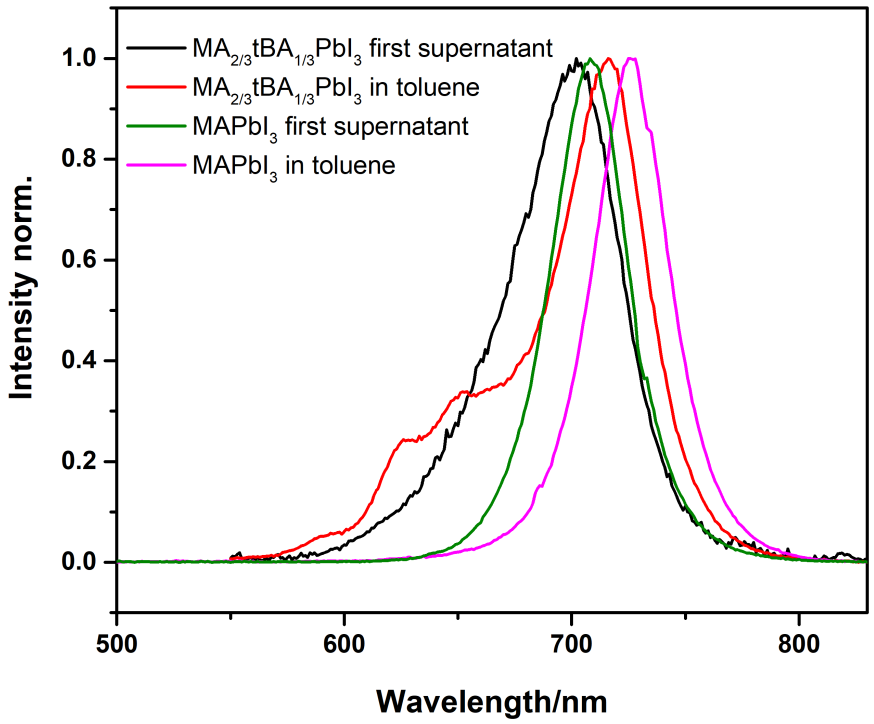

Fig. 6.18 PL spectra of (MA tBA)PbI_3 NCs prepared from MAI : tBAI = 2 : 1 in the first supernatant and in toluene and that of $MAPbI_3$.

6.5 Conclusion

In this chapter, a facile flow reactor was developed for the continuous synthesis of organo-lead halideperovskite NCs at low temperature. The process was very simple and highly reproducible, and avoided the use of high temperature and complex degassing treatment used in most conventional methods. It is easy to scale up, and particularly suitable for mass production.

$MAPbI_3$ NCs were successfully synthesised with the flow method. The NCs showed small sizes of ~ 10 nm with narrow size distribution and exhibited obvious quantum confinement effect compared with $MAPbI_3$ bulk material. The NCs also showed high stability and excellent emissive properties. The $MAPbI_3$ NCs gave a sharp emission peak at 745 nm in their PL spectrum, with narrow FWHM of 39 nm. Notably, the morphological

and emissive properties of the $MAPbI_3$ NCs remained stable for over 8 months. The exceptional stability of the $MAPbI_3$ NCs could be ascribed to the presence of hydrophobic long-chain ligands, which not only prevented the NCs from aggregating, but also acted as a barrier to slow moisture reaching the perovskite core.

The PL of the $MAPbI_3$ NCs can be tuned by changing the temperature, flow rate and ligand concentration, especially for the NCs in the first supernatant of the as-prepared mixture. Different temperatures of 20 °C, 30 °C and 50 °C did not change the peak position, but peak broadening was observed for the NCs made at higher temperatures. Lower flow rate resulted in the formation of NCs giving emissions at longer wavelength, indicating their larger sizes with longer residence time, but the effect was not significant when the residence time was tuned from 5 min to 20 min, probably due to the fast reaction kinetics such that a plateau of the particle size was already reached after 5 min. Higher ligand concentration obviously shifted the fluorescence peak of the $MAPbI_3$ NCs to shorter wavelength, suggesting the smaller crystal size of the NCs, due to the ligands' role of suppressing the growth of the NCs in the synthesis. However the impacts of these process parameters on the NCs washed out in toluene were more complex due to the appearance of multiple peaks in the PL spectra. It was speculated that toluene washing caused the formation of smaller NCs due to the reprecipitation of incompletely removed reactants when added into toluene, or the fragmentation of the NCs upon dispersion in toluene, but better understanding is still needed.

The flow synthesis was adapted to the synthesis of perovskite NCs $MAPbI_xBr_{3-x}$ with different halide compositions. A series of perovskite NCs with halides of pure iodine to pure bromine were successfully prepared, and showed tuneable emissions between 485-745 nm, covering a wide wavelength range of visible and near infrared regions. The PL spectra of the NCs showed narrow FWHMs of below 50 nm, indicating the high colour purities, and the emission peoperties was well retained after being made into thin films with a dip-coating method, which are very promising for LED applications.

Different organic cations of azetidinium and tert-butylammonium were attempted as A site cations for the synthesis of $APbI_3$ perovskite NCs. $AzPbI_3$ NCs showed the emission peak of 429 nm, much blue-shifted than their bulk films. Tert-butylammonium ions were incorporated into $MAPbI_3$ NCs with the ratio of tBA : MA = 1 : 2. The mixed cation per-

ovskite $MA_{2/3}tBA_{1/3}PbI_3$ NCs showed blue shift than $MAPbI_3$ NCs in their PL spectra, but broad peaks with long tails were observed, indicating the uneven size distribution.

Finally, perovskite NCs were successfully synthesised through a continuous solution process, in which their crystallisation are easier to control and less dependent on atmosphere conditions. It could also provide a new idea for the preparation of perovskite thin films, which can separate the crystallisation and film formation processes and potentially achieve better control to the quality of the films. It could be beneficial for the large scale fabrication of perovskite solar cells in terms of reproducibility.

Reference

[1] F. Zhang, H. Zhong, C. Chen, X. g. Wu, X. Hu, H. Huang, J. Han, B. Zou, and Y. Dong. Brightly luminescent and color-tunable colloidal $CH_3NH_3PbX_3$ (X = Br, I, Cl) quantum dots: Potential alternatives for display technology. *ACS Nano*, 9(4):4533–4542, 2015.

[2] L. Protesescu, S. Yakunin, M.I. Bodnarchuk, F. Krieg, R. Caputo, C.H. Hendon, R.X. Yang, A. Walsh, and M.V. Kovalenko. Nanocrystals of cesium lead halide perovskites ($CsPbX_3$, X = Cl, Br, and I): Novel optoelectronic materials showing bright emission with wide color gamut. *Nano Letters*, 15(6):3692–3696, 2015.

[3] O. Vybornyi, S. Yakunin, and M.V. Kovalenko. Polar-solvent-free colloidal synthesis of highly luminescent alkylammonium lead halide perovskite nanocrystals. *Nanoscale*, 8(12):6278–6283, 2016.

[4] B. Wang, K. Young Wong, X. Xiao, and T. Chen. Elucidating the reaction pathways in the synthesis of organolead trihalide perovskite for high-performance solar cells. *Scientific Reports*, 5:10557, 2015.

[5] X. Li, Y. Wu, S. Zhang, B. Cai, Y. Gu, J. Song, and H. Zeng. $CsPbX_3$ quantum dots for lighting and displays: Room-temperature synthesis, photoluminescence superiorities, underlying origins and white light-emitting diodes. *Advanced Functional Materials*, 26(15):2435–2445, 2016.

[6] Y. Wang, X. Li, X. Zhao, L. Xiao, H. Zeng, and H. Sun. Nonlinear absorption and low-threshold multiphoton pumped stimulated emission from all-inorganic perovskite nanocrystals. *Nano Letters*, 16(1):448–453, 2016.

[7] A. Swarnkar, R. Chulliyil, V.K. Ravi, M. Irfanullah, A. Chowdhury, and A. Nag. Colloidal $CsPbBr_3$ perovskite nanocrystals: Luminescence beyond traditional quantum dots. *Angewandte Chemie International Edition*, 54(51):15424–15428, 2015.

[8] L.C. Schmidt, A. Pertegs, S. Gonzlez-Carrero, O. Malinkiewicz, S. Agouram, G. Mnguez Espallargas, H.J. Bolink, R.E. Galian, and J. Prez-Prieto. Nontemplate synthesis of $CH_3NH_3PbBr_3$ perovskite nanoparticles. *Journal of the American Chemical Society*, 136(3):850–853, 2014.

[9] Y. Ling, Z. Yuan, Y. Tian, X. Wang, J.C. Wang, Y. Xin, K. Hanson, B. Ma, and H. Gao. Bright light-emitting diodes based on organometal halide perovskite nanoplatelets. *Advanced Materials*, 28(2):305–311, 2016.

[10] A. Merdasa, M. Bag, Y. Tian, E. Kllman, A. Dobrovolsky, and I.G. Scheblykin. Super-resolution luminescence microspectroscopy reveals the mechanism of photoinduced degradation in $CH_3NH_3PbI_3$ perovskite nanocrystals. *The Journal of Physical Chemistry C*, 120(19):10711–10719, 2016.

[11] H. Huang, M.I. Bodnarchuk, S.V. Kershaw, M.V. Kovalenko, and A.L. Rogach. Lead halide perovskite nanocrystals in the research spotlight: Stability and defect tolerance. *ACS Energy Letters*, 2(9):2071–2083, 2017.

[12] T. Oku. *Crystal structures of $CH_3NH_3PbI_3$ and related perovskite compounds used for solar cells*, page Ch. 03. InTech, Rijeka, 2015.

[13] D. Shi, V. Adinolfi, R. Comin, M. Yuan, E. Alarousu, A. Buin, Y. Chen, S. Hoogland, A. Rothenberger, K. Katsiev, Y. Losovyj, X. Zhang, P.A. Dowben, O.F. Mohammed, E.H. Sargent, and O.M. Bakr. Low trap-state density and long carrier diffusion in organolead trihalide perovskite single crystals. *Science*, 347(6221):519–522, 2015.

[14] Q. Lin, A. Armin, R.C.R. Nagiri, P.L. Burn, and P. Meredith. Electro-optics of perovskite solar cells. *Nature Photonics*, 9(2):106–112, 2014.

[15] G. Giorgi, J.-I. Fujisawa, H. Segawa, and K. Yamashita. Small photocarrier effective masses featuring ambipolar transport in methylammonium lead iodide perovskite: A density functional analysis. *The Journal of Physical Chemistry Letters*, 4(24):4213–4216, 2013.

[16] G. Niu, W. Li, F. Meng, L. Wang, H. Dong, and Y. Qiu. Study on the stability of $CH_3NH_3PbI_3$ films and the effect of post-modification by aluminum oxide in all-solid-state hybrid solar cells. *Journal of Materials Chemistry A*, 2(3):705–710, 2014.

[17] Principles of glass formation. In James E. Shelby, editor, *Introduction to Glass Science and Technology (2)*, pages 7–25. The Royal Society of Chemistry, 2005.

[18] Y. Bekenstein, B.A. Koscher, S.W. Eaton, P. Yang, and A.P. Alivisatos. Highly luminescent colloidal nanoplates of perovskite cesium lead halide and their oriented assemblies. *Journal of the American Chemical Society*, 137(51):16008–16011, 2015.

[19] J. Song, J. Li, X. Li, L. Xu, Y. Dong, and H. Zeng. Quantum dot light-emitting diodes based on inorganic perovskite cesium lead halides ($CsPbX_3$). *Advanced Materials*, 27(44):7162–7167, 2015.

[20] I. Lignos, S. Stavrakis, G. Nedelcu, L. Protesescu, A.J. deMello, and M.V. Kovalenko. Synthesis of cesium lead halide perovskite nanocrystals in a droplet-based microfluidic platform: Fast parametric space mapping. *Nano Letters*, 16(3):1869–1877, 2016.

[21] SeJin Ahn, KiHyun Kim, YoungGab Chun, and KyungHoon Yoon. Nucleation and growth of Cu(In,Ga)Se_2 nanoparticles in low temperature colloidal process. *Thin Solid Films*, 515(7-8):4036–4040, 2007.

[22] Y. Tong, F. Ehrat, W. Vanderlinden, C. Cardenas-Daw, J.K. Stolarczyk, L. Polavarapu, and A.S. Urban. Dilution-induced formation of hybrid perovskite nanoplatelets. *ACS Nano*, 10(12):10936–10944, 2016.

[23] I. Moreels, Y. Justo, B. De Geyter, K. Haustraete, J.C. Martins, and Z. Hens. Size-tunable, bright, and stable pbs quantum dots: A surface chemistry study. *ACS Nano*, 5(3):2004–2012, 2011.

[24] E.T. Hoke, D.J. Slotcavage, E.R. Dohner, A.R. Bowring, H.I. Karunadasa, and M.D. McGehee. Reversible photo-induced trap formation in mixed-halide hybrid perovskites for photovoltaics. *Chemical Science*, 6(1):613–617, 2015.

[25] S.A. Kulkarni, T. Baikie, P.P. Boix, N. Yantara, N. Mathews, and S. Mhaisalkar. Band-gap tuning of lead halide perovskites using a sequential deposition process. *Journal of Materials Chemistry A*, 2(24):9221–9225, 2014.

[26] D.N. Minh, J. Kim, J. Hyon, J.H. Sim, H.H. Sowlih, C. Seo, J. Nam, S. Eom, S. Suk, S. Lee, E. Kim, and Y. Kang. Room-temperature synthesis of widely tunable formamidinium lead halide perovskite nanocrystals. *Chemistry of Materials*, 29(13):5713–5719, 2017.

[27] Y. Sun, Y. Sun, S. Zhao, D. Cao, R. Guan, Z. Liu, X. Yu, and X. Zhao. Efficient solution- and solid-state fluorescence for a series of 7-diethylaminocoumarin amide compounds. *Asian Journal of Organic Chemistry*, 7(1):197–202, 2018.

[28] Q.A. Akkerman, M. Gandini, F. Di Stasio, P. Rastogi, F. Palazon, G. Bertoni, J.M. Ball, M. Prato, A. Petrozza, and L. Manna. Strongly emissive perovskite nanocrystal inks for high-voltage solar cells. *Nature Energy*, 2(2):16194, 2016.

[29] C. Li, X. Lu, W. Ding, L. Feng, Y. Gao, and Z. Guo. Formability of ABX_3 (X = F, Cl, Br, I) halide perovskites. *Acta Crystallographica Section B*, 64(6):702–707, 2008.

[30] W.S. Yang, J.H. Noh, N.J. Jeon, Y.C. Kim, S. Ryu, J. Seo, and S.I. Seok. High-performance photovoltaic perovskite layers fabricated through intramolecular exchange. *Science*, 348(6240):1234–1237, 2015.

[31] T.M. Koh, K. Fu, Y. Fang, S. Chen, T.C. Sum, N. Mathews, S.G. Mhaisalkar, P.P. Boix, and T. Baikie. Formamidinium-containing metal-halide: An alternative material for near-ir absorption perovskite solar cells. *The Journal of Physical Chemistry C*, 118(30):16458–16462, 2014.

[32] G. Grancini, C. Roldan-Carmona, I. Zimmermann, E. Mosconi, X. Lee, D. Martineau, S. Narbey, F. Oswald, F. De Angelis, M. Grätzel, and M.K. Nazeeruddin.

One-year stable perovskite solar cells by 2D/3D interface engineering. *Nature Communications*, 8:15684, 2017.

[33] I. Poli, S. Eslava, and P. Cameron. Tetrabutylammonium cations for moisture-resistant and semitransparent perovskite solar cells. *Journal of Materials Chemistry A*, 5(42):22325–22333, 2017.

[34] S.R. Pering, W. Deng, J.R. Troughton, P.S. Kubiak, D. Ghosh, R.G. Niemann, F. Brivio, F.E. Jeffrey, A.B. Walker, M.S. Islam, T.M. Watson, P.R. Raithby, A.L. Johnson, S.E. Lewis, and P.J. Cameron. Azetidinium lead iodide for perovskite solar cells. *Journal of Materials Chemistry A*, 5(39):20658–20665, 2017.

[35] H. Tsai, W. Nie, J.-C. Blancon, C.C. Stoumpos, R. Asadpour, B. Harutyunyan, A.J. Neukirch, R. Verduzco, J.J. Crochet, S. Tretiak, L. Pedesseau, J. Even, M.A. Alam, G. Gupta, J. Lou, P.M. Ajayan, M.J. Bedzyk, M.G. Kanatzidis, and A.D. Mohite. High-efficiency two-dimensional ruddlesden–popper perovskite solar cells. *Nature*, 536(7616):312–316, 2016.

Chapter 7

Applications of perovskite nanoparticles in solar cell fabrication

Due to their size-tunable band-gap, solution processability and high monodispersity, quantum dots of a variety of semiconductor materials such as PbS, PbSe, PbTe, CdSe et al. have been widely investigated for photovoltaic applications[1,2]. Their photovoltaic performance have been boosted from less than 1 % in 2005 to a recently certified record of 11.3%[3,4]. Due to the easy tunability of their band-gap, quantum dots could be very promising for the construction of multijunction solar cells which can achieve high power conversion efficiencies[5] .

Perovskite nanocrystals have also attracted significant interests. $MAPb(Br_{0.3}I_{0.7})_3$ NCs have been used as interlayers[6] for perovskite solar cells, placed between a $MAPbI_3$ layer and a hole-transporting layer (HTL). The NCs improved the device performance and the increase in efficiency was attributed to improved hole transfer at the interface. $CsPbI_3$ NCs have been used as the absorber layer for solar cells[7,8] delivering an efficiency of 10.77%, high stability and an open-circuit voltage as high as 1.23 V.

As discussed in previous chapters, preparation of perovskite thin films using nanoparticles could potentially provide a way of separating the crystallisation and film formation processes, which makes the film fabrication much easier to control and improves the reproducibility of the devices. Therefore, on the basis of the flow synthesis of perovskite NCs as discussed in **Chapter 6**, the application of the $MAPbI_3$ NCs and their powder bulk by-products in perovskite solar cell making was attempted.

7.1 Experimental

Synthesis of $MAPbI_3$ NCs has been mentioned in previous chapter and the details can be found in the main experimental **Chapter 3**. The NCs were kept in toluene for further use.

Cell preparation employing $MAPbI_3$ NCs was conducted under ambient conditions with no control over the humidity or atmosphere. The cells were based on the mesoporous structure with TiO_2 as a scaffold layer. Deposition of the $MAPbI_3$ NCs were carried out via dip-coating and spin-coating methods. In dip-coating, the substrates were soaked in the NC solutions in toluene and kept still for 24 h in the dark before being taken out, and blow dried with nitrogen at room temperature. In spin-coating, 100 μL of the NC solution was spin cast onto the substrates at 1000 rpm for 20 s, followed by blow drying at room temperature for 5 min. The spin-coating process was repeated 5 times. The pretreatment of the substrates and deposition of other layers were the same as in the preparation of standard mesoporous devices, and can be found in **Chapter 3**.

The application of $MAPbI_3$ NCs for interface engineering was performed with two different methods in a nitrogen filled dry box:

Method 1 The standard perovskite precursor solutions were prepared by dissolving MAI, PbI_2 and $PbCl_2$ in DMF to get 40w% solution ($MAI : PbI_2 : PbCl_2 = 4 : 1 : 1$). 100 μL of precursor solution was spun onto the substrate at 4000 rpm for 30 seconds, then dried at 100 °C for 90 minutes. The $MAPbI_3$ NCs dispersed in toluene was spun coated onto the above perovskite layer at 4000 rpm for 30 s followed by annealing at 100 °C for 2 min, forming the perovskite/MAPI NCs film. In the control perovskite film, no MAPI NCs dispersed in toluene were spin-coated on top.

Method 2 The standard perovskite precursor solutions were prepared by dissolving MAI and PbI_2 in DMSO/GBL (3:7 vol ratio)to get 40w% solution ($MAI : PbI_2 = 1 : 1$). 100 mL of precursor solution was spun onto the substrate at 5000 rpm for 50 seconds. At the 25th second 1 mL of $MAPbI_3$ NCs dispersed in toluene was fast dropped onto the center of the substrate and then dried at 100 °C for 10 minutes. The reference perovskite film was fabricated using pure toluene as anti-solvent.

Cell preparation employing $MAPbI_3$ bulk powders was also attempted. The $MAPbI_3$ bulk powder by-products of the flow synthesis were dispersed in hexane, forming inks of ~ 20 mg/mL after being sonicated for 10 min. 100 μL of the $MAPbI_3$ ink was spin cast onto the substrates at 2000 rpm for 30 s, followed by annealing at 70 °C for 5 min. The spin-coating process was repeated different times to control the thickness of the films. Deposition of other layers were the same with the preparation of standard devices.

7.2 Perovskite solar cells based on $MAPbI_3$ NCs

$MAPbI_3$ NCs in toluene were used for the preparation of perovskite absorbing layers for mesoporous perovskite solar cells. Spin-coating and dip-coating are two main methods used for the deposition of quantum dots thin film[9,10]. In this section, these two methods were both investigated for the deposition of the perovskite NC films. **Fig. 7.1** shows the UV-vis absorption and PL emission spectra of perovskite films made using the spin-coating method. The film was quite transparent as can be seen in the photograph in **Fig. 7.1**a, which indicated very thin films had been formed. The emissive properties of the $MAPbI_3$ NCs were retained after being deposited onto the substrates. A PL peak at 738 nm was observed for the NC film, slightly blue-shifted from the 748 nm found for the NCs in toluene, which could be due to the different orientations of the NCs in the solid state and the interaction with solvent in solution. For applications in solar cells, the light absorbing ability of the films is very important. However, the films made with the $MAPbI_3$ NCs showed very weak light absorption, as seen from **Fig. 7.1** a, especially in the wavelength range of 600-750 nm. The low light absorption is likely due to the small thickness of the films and a poor surface coverage, which could be detrimental for the cell performance.

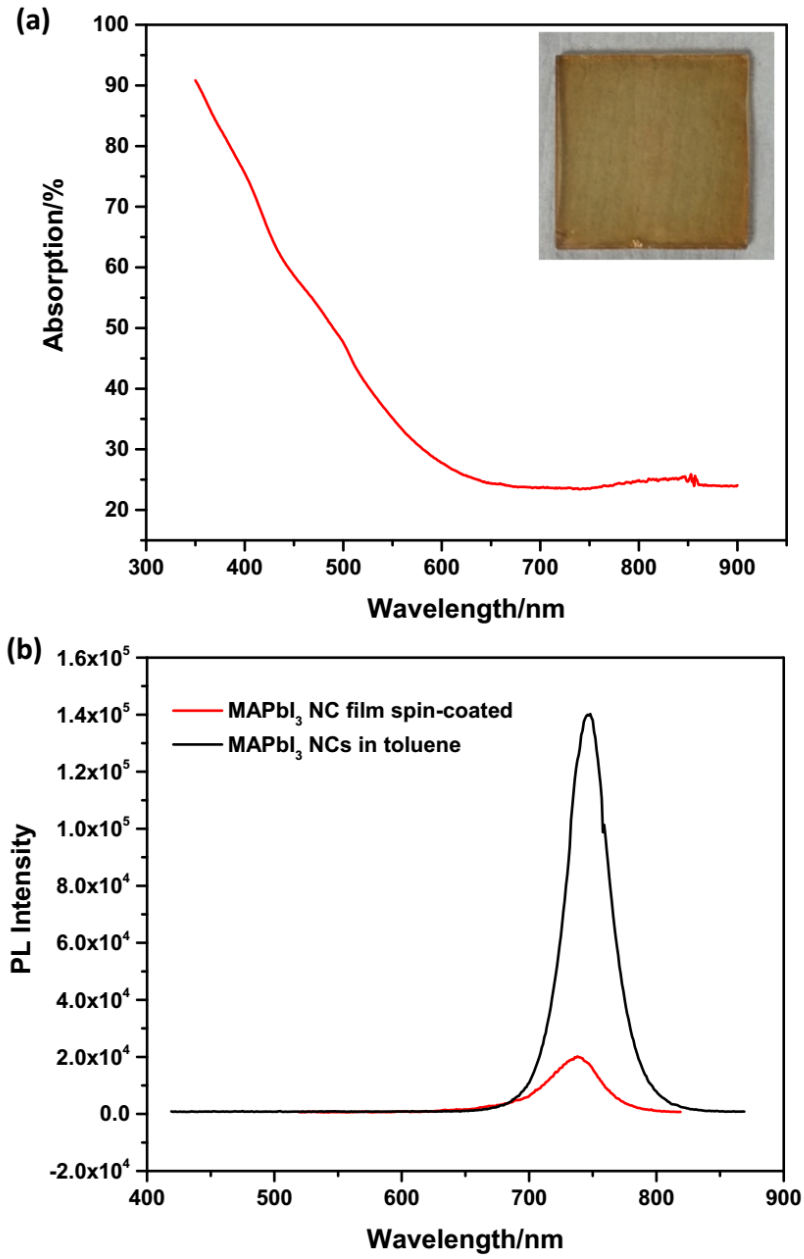

Fig. 7.1 (a) UV-vis and (b) PL spectra of the $MAPbI_3$ films spin-coated with $MAPbI_3$ NCs. The inset is the photograph of the film.

The films prepared with the $MAPbI_3$ NCs were made into perovskite solar cells, and J-V curves of average-working cells employing perovskite layers made with the spin-coating and dip-coating methods were illustrated in **Fig. 7.2**. Both the cells showed well-defined J-V responses, though the curves were very noisy, which were due to the small current signals. The J_{SC} of the devices were only around $1\,mA \cdot cm^{-2}$. The very low current response were believed to be due to the low light absorption as shown in **Fig. 7.1**. The existence of capping layers of long chain ligands which potentially hindered the charge

transfer could also be another reason. To dissolve the reactants and stabilise the NCs, long chain ligands, in our case OA and OLA, are normally added during the synthesis of the NCs. As a results, the as-prepared nanocrystals are shielded by these long chain ligands, which act as an electrically insulating layer (1-2 nm) that impedes efficient charge transfer[11,12]. Therefore, ligand exchange treatments to remove or replace the long chain ligands with short length chemicals are normally required during the applications of QDs in photovoltaics[13,14]. However due to the poor stability of the perovskite NCs in various solvents, no ligand exchange was carried out herein.

The cells with dip-coated perovskite layers showed much better performances compared to those with spin-coated perovskite layers, in terms of the J_{SC}, V_{OC} and FF. As shown in the box plots in **Fig. 7.3**, the dip-coated cells showed PCEs of $0.51 \pm 0.06\,\%$, much higher than the $0.19 \pm 0.05\,\%$ for the spin-coated cells. More specifically, the cells with dip-coated perovskite layers showed J_{SC} of $1.31 \pm 0.10\,\mathrm{mA \cdot cm^{-2}}$, V_{OC} of $0.65 \pm 0.01\,\mathrm{V}$ and FF of 0.60 ± 0.06, all better than the cells with spin-coated perovskite layers (J_{SC} of $0.77 \pm 0.11\,\mathrm{mA \cdot cm^{-2}}$, V_{OC} of $0.58 \pm 0.08\,\mathrm{V}$ and FF of 0.45 ± 0.15). The better performance of the cells made with dip-coating method might be due to the better loading of $MAPbI_3$ NCs on top of mesoporous TiO_2 layers by dip-coating, probably with higher film thickness films and better surface coverage.

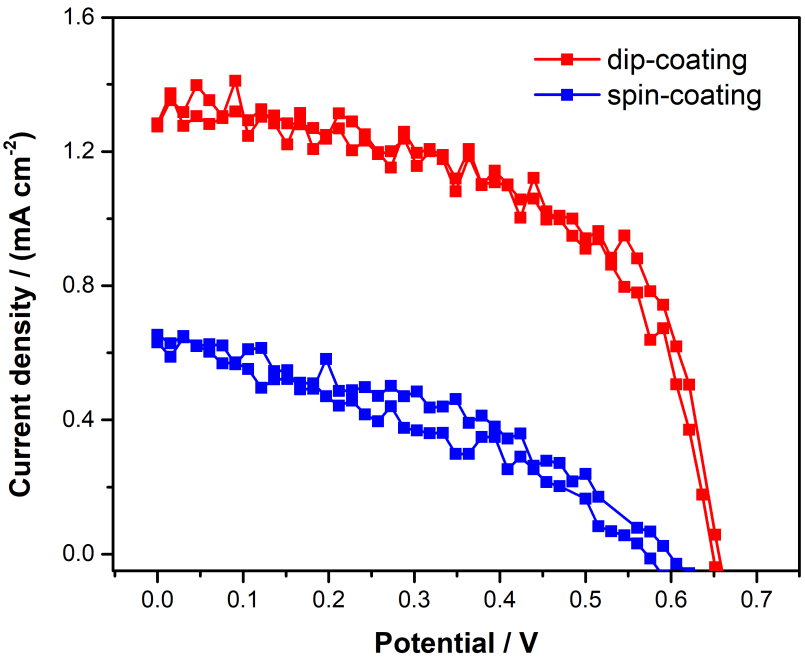

Fig. 7.2 J-V curves of cells employing perovskite films prepared with $MAPbI_3$ NCs.

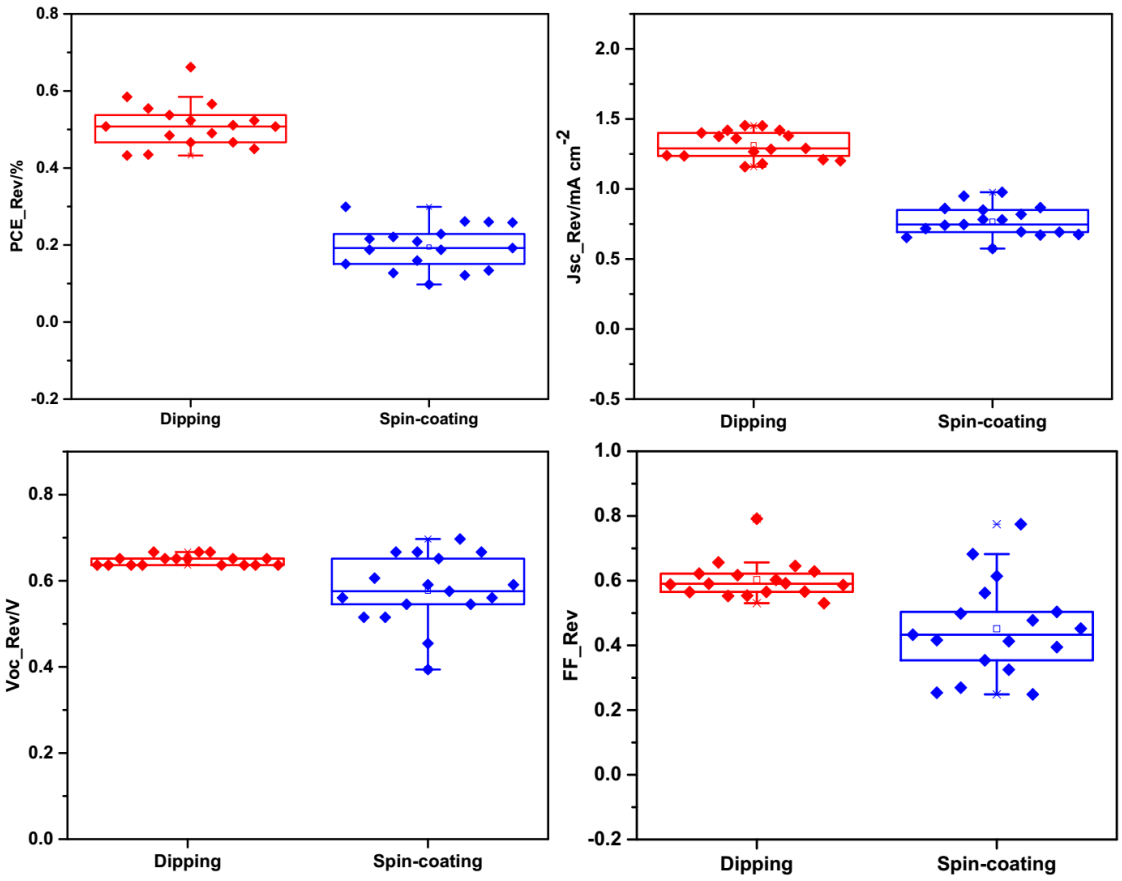

Fig. 7.3 Box plots of the cell performances employing perovskite films prepared with $MAPbI_3$ NCs.

Table 7.1 Performance parameters for cells employing spin-coated and dip-coated perovskite layers from $MAPbI_3$ NCs.

	J_{SC} $[mA \cdot cm^{-2}]$	V_{OC} [V]	FF	PCE [%]
Spin−coating	0.77 ± 0.11	0.58 ± 0.08	0.45 ± 0.15	0.19 ± 0.05
Dip−coating	1.31 ± 0.10	0.65 ± 0.01	0.60 ± 0.06	0.51 ± 0.06

Though the cells were not very efficient, the result is still promising considering the low thickness and high transparency of the perovskite layers and the existence of large amount of ligands on the surface of the NCs. To improve their performance, an increase in the film thickness and ligand exchange treatments for the removal of the ligands need to be done.

7.3 $MAPbI_3$ NCs for interface engineering

It has been shown that making efficient cells with the $MAPbI_3$ NCs is very challenging. Effective methods of making films thick enough and ligand exchange strategies for the removal of the long chain ligands are still to be explored. On the other hand, interface engineering could be a simple way of applying the NCs in perovskite solar cells. A variety of thin layers have been studied as interlayers at perovskite-ETL or perovskite-HTL interfaces[15], either to modify band energy offsets at interfaces or to improve the morphology of the absorber layer or to increase the long-term stability of the device. There have been reports about the use of QDs in perovskite solar cells to improve the cell performance. $CuInS_2$ QDs were applied on TiO_2 nanorod arrays, facilitating electron injection from the perovskite absorber layer to the TiO_2 scaffold[16]. $MAPbBr_{0.9}I_{2.1}$ QDs were incorporated at the $MAPbI_3$-HTM interface, facilitating hole transfer[6]. Therefore, in this work, the $MAPbI_3$ NCs were also studied as the interlayer between perovskite and Spiro HTM layers, as shown in **Fig. 7.4**, via two methods (**method 1**: direct spin-coating on top of $MAPbI_xCl_{3-x}$ layers; **method 2**: anti-solvent treatment for $MAPbI_3$ layers, see experimental in **7.1**), and the impacts on the performance and stability of the cells were investigated.

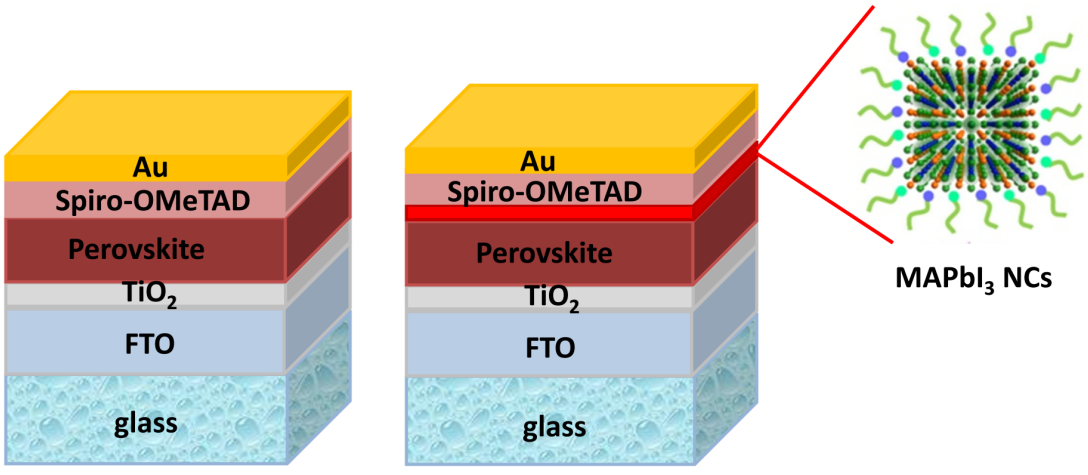

Fig. 7.4 Diagram of cell structures without (left) and with (right) the NC interlayer.

Cell performances with and without the $MAPbI_3$ NCs as interlayers are shown in **Fig. 7.5**. For the control cells without the NC interlayers, PCEs of around 10 % were achieved

for both the direct spin-coating (**method 1**) and toluene dripping (**method 2**) methods, with small deviations. The control cells made with **method 1** showed slightly better performance (J_{SC} of $19.9 \pm 0.6\,mA \cdot cm^{-2}$, V_{OC} of $0.75 \pm 0.02\,V$ and FF of 0.71 ± 0.03, leading to the PCE of $10.6 \pm 0.6\,\%$) than the cells made with **method 2** (J_{SC} of 18.1 ± 1.9 $mA \cdot cm^{-2}$, V_{OC} of $0.76 \pm 0.02\,V$ and FF of 0.70 ± 0.09, resulting the PCE of $9.5 \pm 0.8\,\%$). The improved performance could be due to larger grain sizes in the $MAPbI_xCl_{3-x}$ films compared with the anti-solvent treated $MAPbI_3$ films. Larger grains are believed to reduce recombination at the grain boundaries[17–19]. However, the incorporation of $MAPbI_3$ NC interlayers by both directly spin-coating the NC solution and adding the NCs in the toluene antisolvent decreased the performance of the cells. The PCEs decreased to $9.6 \pm 0.6\,\%$ and $7.2 \pm 0.4\,\%$ respectively. The decrease in the cell performance was mainly due to the decreased J_{SC} while the V_{OC} and FF were fairly similar. The reduction in J_{SC} could be due to changes in film morphology, or problems with charge extraction through the long chain ligands capped NC layer.

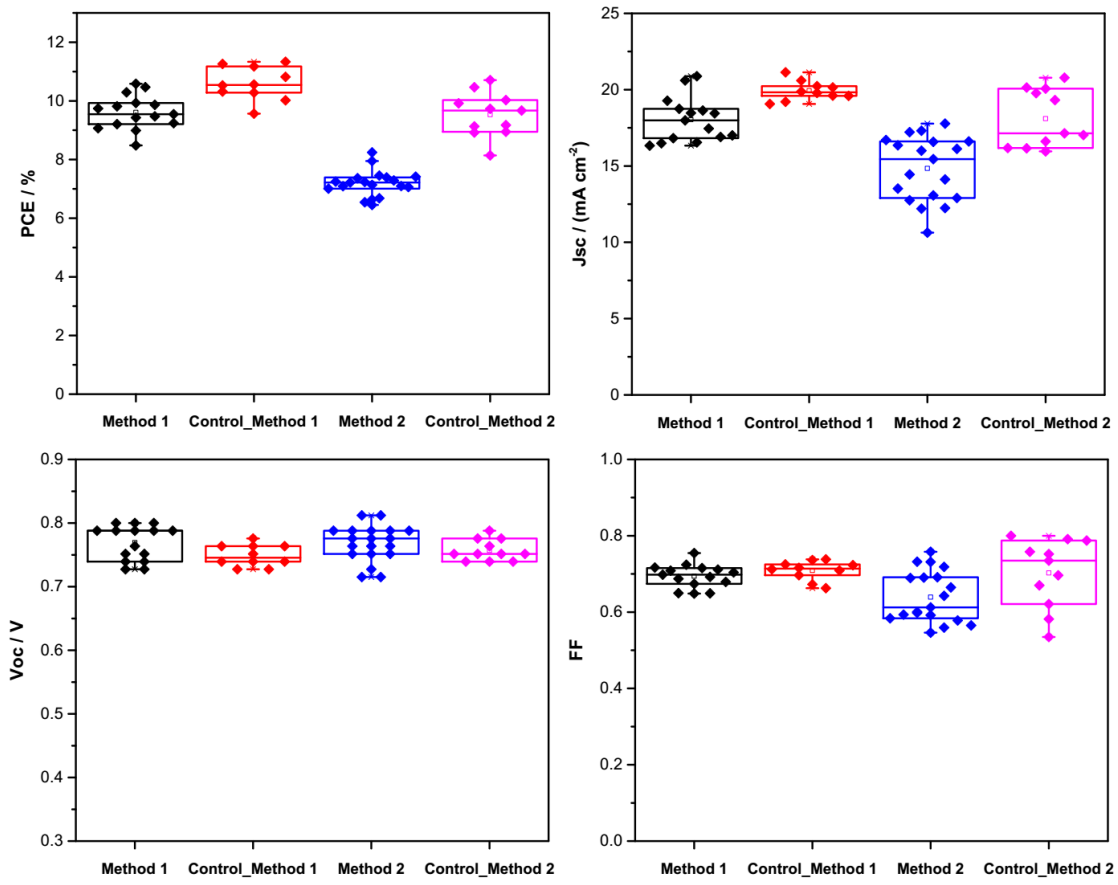

Fig. 7.5 Box plots of the cell performances with and without the $MAPbI_3$ NCs as interlayers.

Table 7.2 Performance parameters for cells with and without the $MAPbI_3$ NCs as interlayers.

	J_{SC} $[mA \cdot cm^{-2}]$	V_{OC} [V]	FF	PCE [%]
Method 1 control	19.9 ± 0.6	0.75 ± 0.02	0.71 ± 0.03	10.6 ± 0.6
Method 1 with NCs	17.0 ± 1.5	0.77 ± 0.03	0.69 ± 0.03	9.6 ± 0.6
Method 2 control	18.1 ± 1.9	0.76 ± 0.02	0.70 ± 0.09	9.5 ± 0.8
Method 2 with NCs	14.8 ± 2.1	0.77 ± 0.03	0.64 ± 0.07	7.2 ± 0.4

Though the cells with the NC interlayers showed slightly decreased cell performance compared with the controls, the perovskite films showed much improved hydrophobicity, as seen from the contact angles of the films shown in **Fig. 7.6**. The control perovskite films made with the two standard methods showed contact angles of 23.2° and 53.8° respectively, which were greatly increased to over 90° when the $MAPbI_3$ NCs were incorporated. A value as high as 100.5° was achieved for the film made with **method 1**. The outstanding hydrophobicity of the films is believed to be due to the presence of the hydrophobic ligands OA and OLA bound to the surface of the NCs. Unlike in quantum dot solar cells where the organic ligand are normally removed to avoid an insulating layer that reduces charge transport[20], the ligands were kept on the surface of our NCs in this work, as the interlayer is very thin and the impediment to carrier transport is very limited. The high hydrophobicity of perovskite film is highly favoured for photovoltaic applications as the poor water stability of perovskites is a big challenge[21] and the high hydrophobicity could lead to higher water resistance.

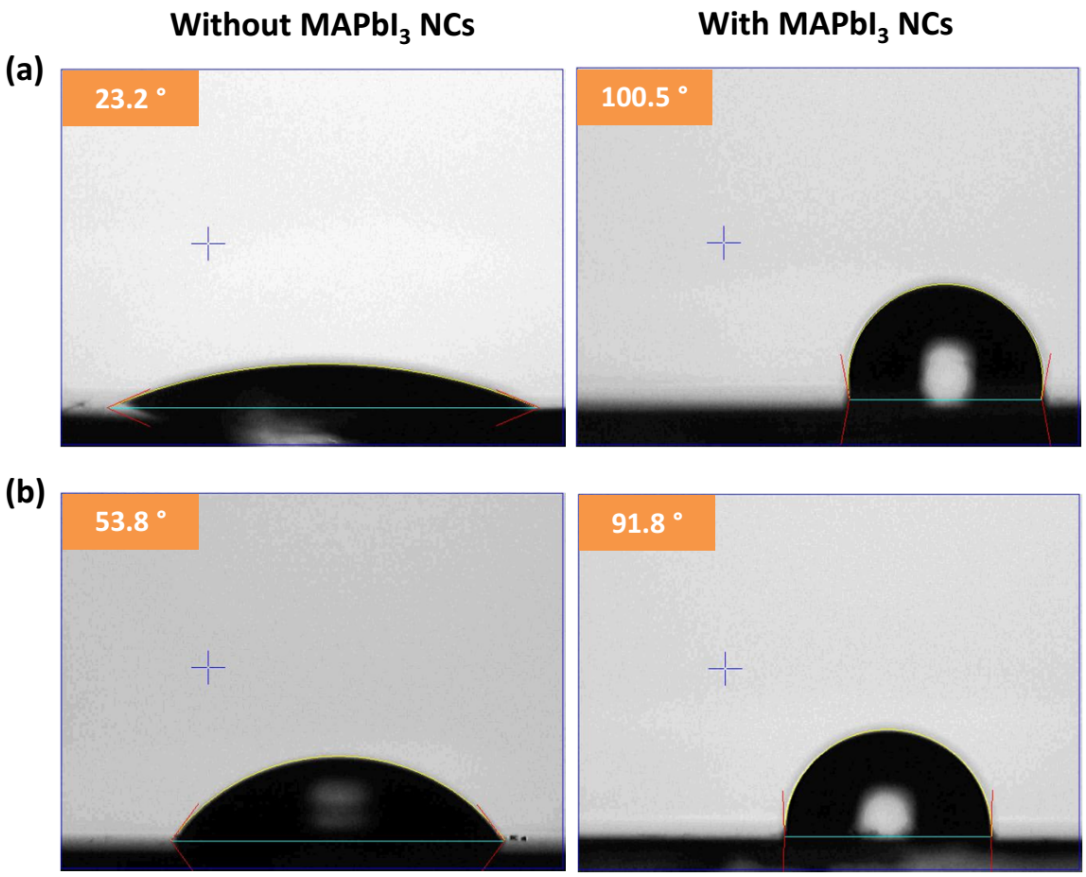

Fig. 7.6 Contact angles of perovskite film with and without the $MAPbI_3$ NC interlayers, made with (a) method 1 and (b) method 2.

The high water resistance of the perovskite films with the $MAPbI_3$ NCs were further confirmed by dipping the films in water for 10 seconds. **Fig. 7.7** shows the XRD patterns of the films made with **method 1** before and after 10 s being dipped in water. Both the films showed typical XRD patterns of perovskite phase with the strong diffraction peak of (110) facet at 14.7° before water immersion. As soon as being immersed in water, however, the control film without the NCs underwent a rapid colour change from dark brown to yellow, and the characteristic peak for PbI_2 at 13.2° became the main and only diffraction peak. No $MAPbI_3$ phase could be detected, indicating a complete dissociation of the $MAPbI_3$ phase into the PbI_2 phase. In contrast, the film with integrated NCs remained dark brown after being immersed in water for 10s. The tetragonal $MAPbI_3$ phase of the film was still detected and its characteristic peak at 14.7° remained as the dominant diffraction peak, though a small peak due to the PbI_2 phase was observed.

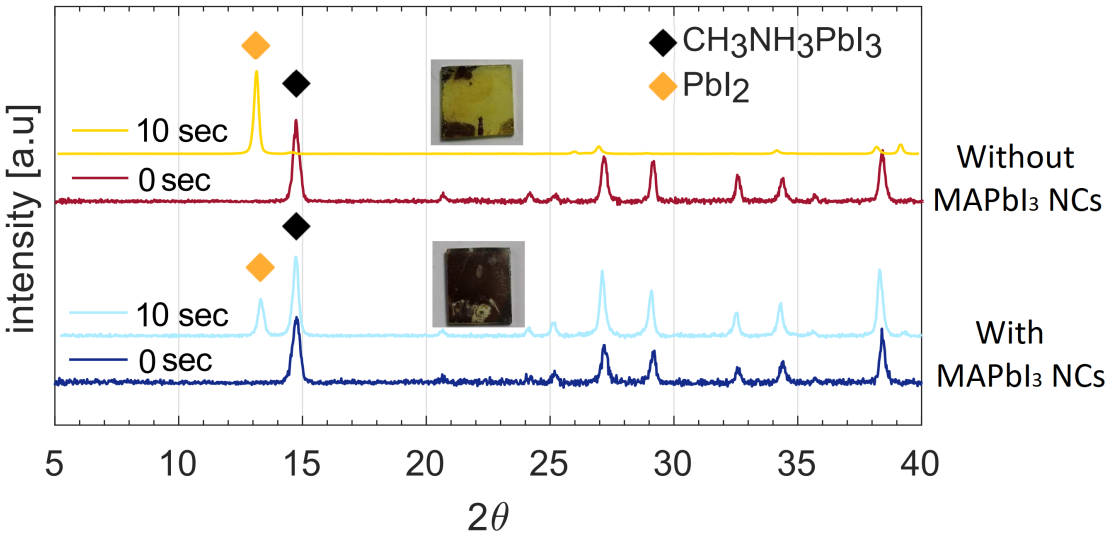

Fig. 7.7 XRD patterns of perovskite films with and without the $MAPbI_3$ NC interlayers before and after being immersed in water for 10 s. The insets are the photo images of the films after water immersion.

To investigate the stability of the perovskite solar cells, J-V curves were measured 70 days after fabrication for two devices with and without the NC interlayers. Over this period of time, the cells were left in ambient atmosphere with room humidity measured to be $60 \pm 10\%$. The cells were made on the same day and exposed to the same ageing process. Two solar cells with similar initial PCEs were evaluated. The PCE of the reference cell decreased by over 40%, from 9.56 % to 5.81 %. The reduction in PCE mainly arose from the decrease in current density from 19.2 $mA \cdot cm^{-2}$ to 13.3 $mA \cdot cm^{-2}$. This is believed to be due to a degradation of the perovskite $MAPbI_3$ to PbI_2 due to the presence of moisture which caused a decreased light harvesting. In contrast, the cell with integrated $MAPbI_3$ NCs only suffered a slight decrease in PCE from 9.93 % to 9.17 %, with 92.3% of the initial efficiency retained, showing greatly enhanced stability towards moisture.

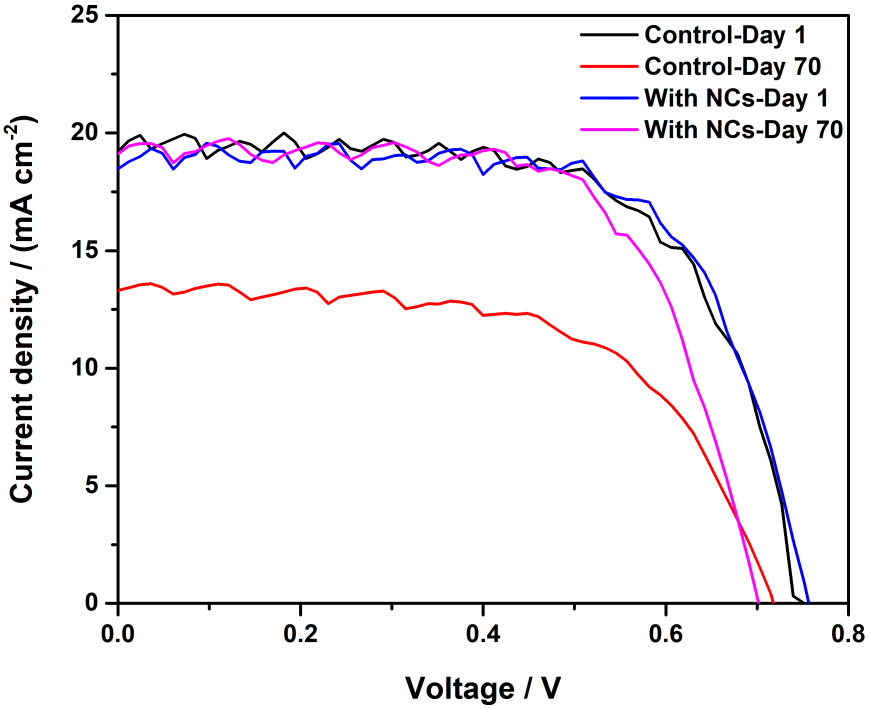

Fig. 7.8 J-V curves of solar cells with and without $MAPbI_3$ NCs as soon as fabricated and after 70 days of ageing in ambient atmosphere.

7.4 Perovskite solar cells based on $MAPbI_3$ powders

As discussed in **7.2**, it is difficult to make films that are thick enough for efficient light absorption in solar cell applications using $MAPbI_3$ NCs only. As a different approch, the bulk solid by-product of the flow synthesis dipersed in hexane was used as precursor material to make the absorber layers. This approach uses directly the $MAPbI_3$ solid powders for film making, potentially leading to higher control over cell reproducibility by separating the crystallisation and the film formation steps. In addition, due to the bigger particle size of the perovskite solid powder compared to the NCs, grain boundaries can be reduced when made into films, which is more favourable due to reduced recombination, as grain boundaries are normally companied with defects which have been believed to cause recombination[22]. Hung-Ju Yen[23] reported the use of perovskite single crystals for the preparation of perovskite films with large grain sizes. The cells showed improved reproducibility and stability, but as the single crystals were dissolved to form the precursor solution, the crystal could not be retained and further crystallisation process was still

needed.

Therefore, a perovskite ink was made by re-dispersing the perovskite solid powders coming from the flow synthesis after they had been washed twice with toluene. The solid showed excellent dispersibility in hexane and an ink with the concentration of ~ 15 mg/mL showed high homogeneity as shown in **Fig. 7.9** a. The ink was spin-coated onto TiO_2 layers on FTO substrates to form perovskite light-absorbing layers. The film had a dark brown colour and high uniformity as seen in **Fig. 7.9** b. SEM images of the perovskite film were taken to investigate the quality of the film. As shown in **Fig. 7.9** c, the film exhibited high surface coverages, with only a couple of small pin-holes present. The film was made of particles with different sizes. A large portion of the particles are very small particles of tens of nanometres packing densely, while there are also a large amount of big cubes of hundreds of nanometres. The solid powders were the by-products of the flow synthesis of perovskite NCs, thus the bulky size of the particles were due to the over growth and aggregation of the small NCs, which also caused the differences in the sizes. The presence of the large cubes could also be seen in the cross-sectional SEM image shown in **Fig. 7.9** d. The compactness of the perovskite film was observed, with the thickness of generally 250 - 300 nm, but at positions where the large cubes were present the thickness of the perovskite layer could be as large as 400 - 450 nm. The non-uniformity in the thickness of the perovskite film could be a problem when it is applied as the light-absorbing layer for perovskite solar cells, as a thin film could cause the insufficient absorption towards light incidence whereas too thick films could result in the increase of recombination[24].

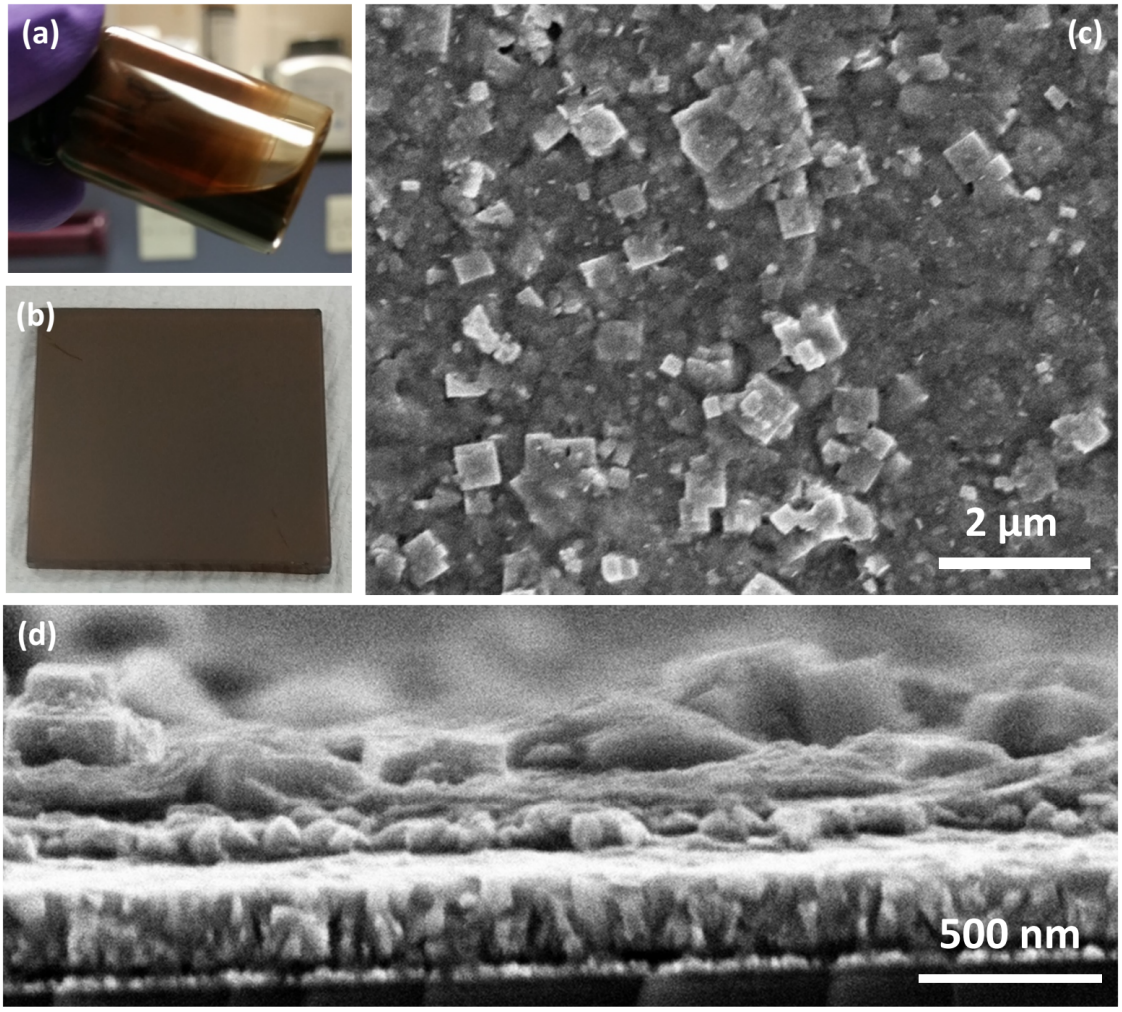

Fig. 7.9 . Photo images of (a) the perovskite ink in hexane; (b) the film spin-coated from the ink; and SEM images of the film: (c) top view; (d) cross-sectional.

UV-vis and photoluminescence spectra of the $MAPbI_3$ films are illustrated in **Fig. 7.10**. The absorption onset was seen at ~ 800 nm, consistent with that of bulk perovskite films. The film showed reasonably good light absorption, especially in the range of 300-500 nm, with a high absorption of over 80 % was observed, which is comparable with the films made with standard perovskite precursor solution as shown in **Fig. 5.7**. However, in the range of 500-750 nm, the absorption of the film gradually decreased to only ~ 45 %, much lower than that of the standard solution processed films. The relatively poor light absorbing ability of the films suggested that thicker film might be needed for sufficient light absorption. Moreover, unlike the bulk film whose PL responses were normally very weak in our basic fluorometer without an integrating sphere, the film made with the ink showed an strong peak at 754 nm, which could be due to the existence of small $MAPbI_3$ NCs in

the film which gave much stronger fluorescence.

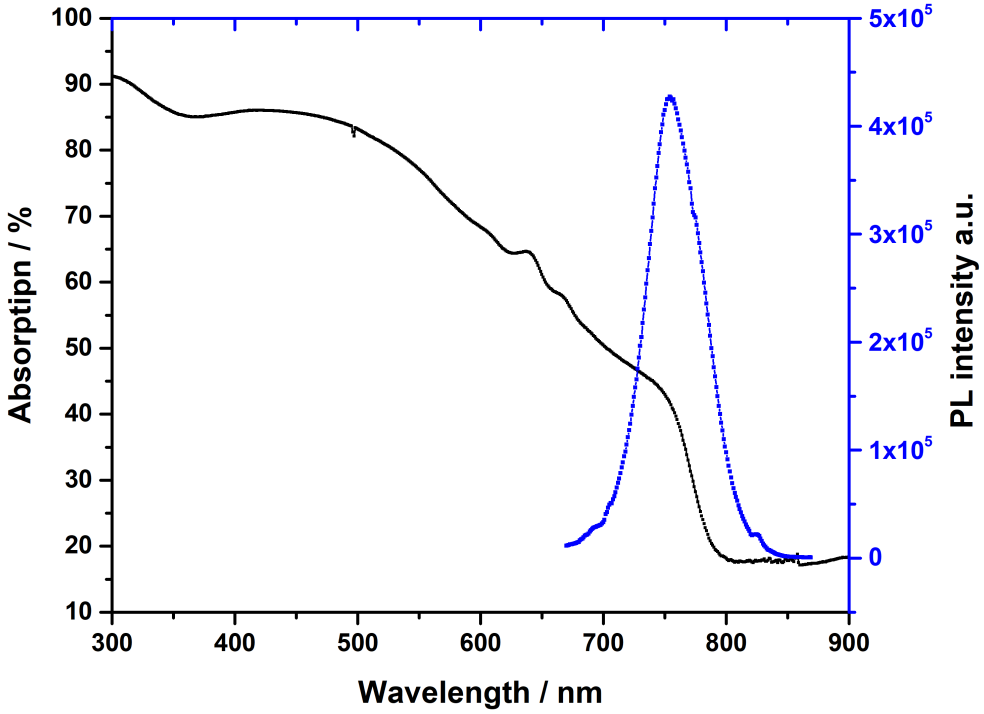

Fig. 7.10 . UV-vis and PL spectra of the perovskite film made with the $MAPbI_3$ solid powders.

The perovskite films were used for the fabrication of perovskite solar cells, and the performances of planar and mesoporous cells were compared. As shown in the J-V curves in **Fig. 7.11**, the mesoporous cell showed well-defined J-V response of a photovoltaic device, with the J_{SC} of 3.76 mA $\cdot$ cm^{-2}, the V_{OC} of 0.73 V and the FF of 0.45, leading to a PCE of 1.22 %. However the planar cell barely worked. The PCE was as low as 0.09 %, and the J_{SC} greatly dropped to 0.41 mA $\cdot$ cm^{-2}, and the V_{OC} and FF also decreased to 0.57 V and 0.40 respectively. The much better performance of the mesoporous cells than the planar ones can also be seen in the box plots in **Fig. 7.12**. The mesoporous cells showed PCEs of 1.18 ± 0.08 %, much higher than the 0.08 ± 0.02 % of the planar cells. More specifically, the mesoporous cells showed J_{SC} of 3.64 ± 0.72 mA $\cdot$ cm^{-2}, V_{OC}s of 0.74 ± 0.02 V and FF of 0.45 ± 0.08, all better than the planar cells (J_{SC} of 0.48 ± 0.32 mA $\cdot$ cm^{-2}, V_{OC}s of 0.53 ± 0.16 V and FF of 0.38 ± 0.04). The mesoporous cells only showed the PCE of ~ 1 %, which could be due to the improper thickness of the perovskite layer and the hindered charge transfer caused by the presence of the long chain ligands, but it is still very promising, considering the non-uniformity of the particle sizes and that none of the processing parameters have been optimised yet. The ultra low PCE of ~ 0.1 % for the

planar cells could be due to the poor contact of the perovskite layers with the compact TiO_2 electron-transporting layers without the presence of a mesoporous layer.

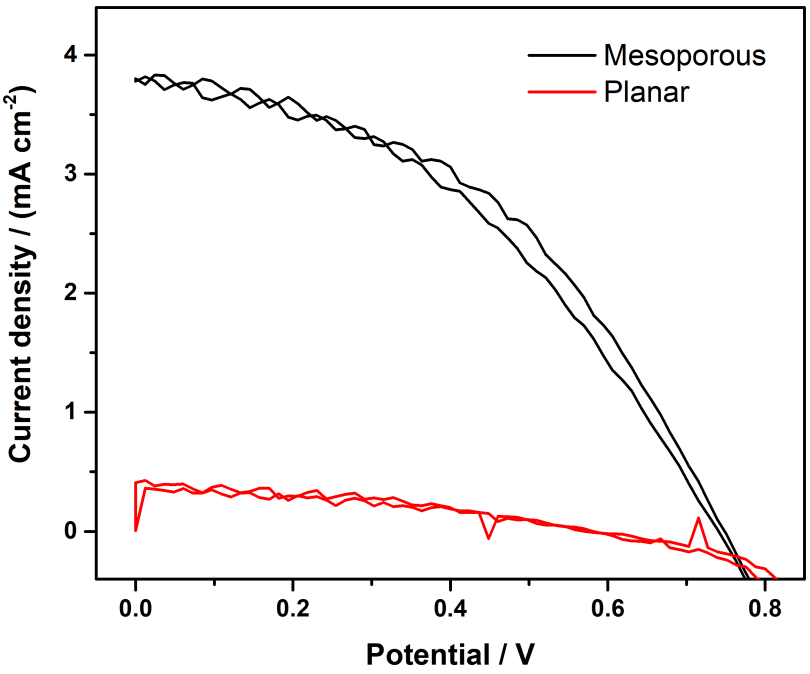

Fig. 7.11 J-V curves of planar and mesoporous cells employing perovskite films spin-coated from the ink of $MAPbI_3$ solid powders in hexane.

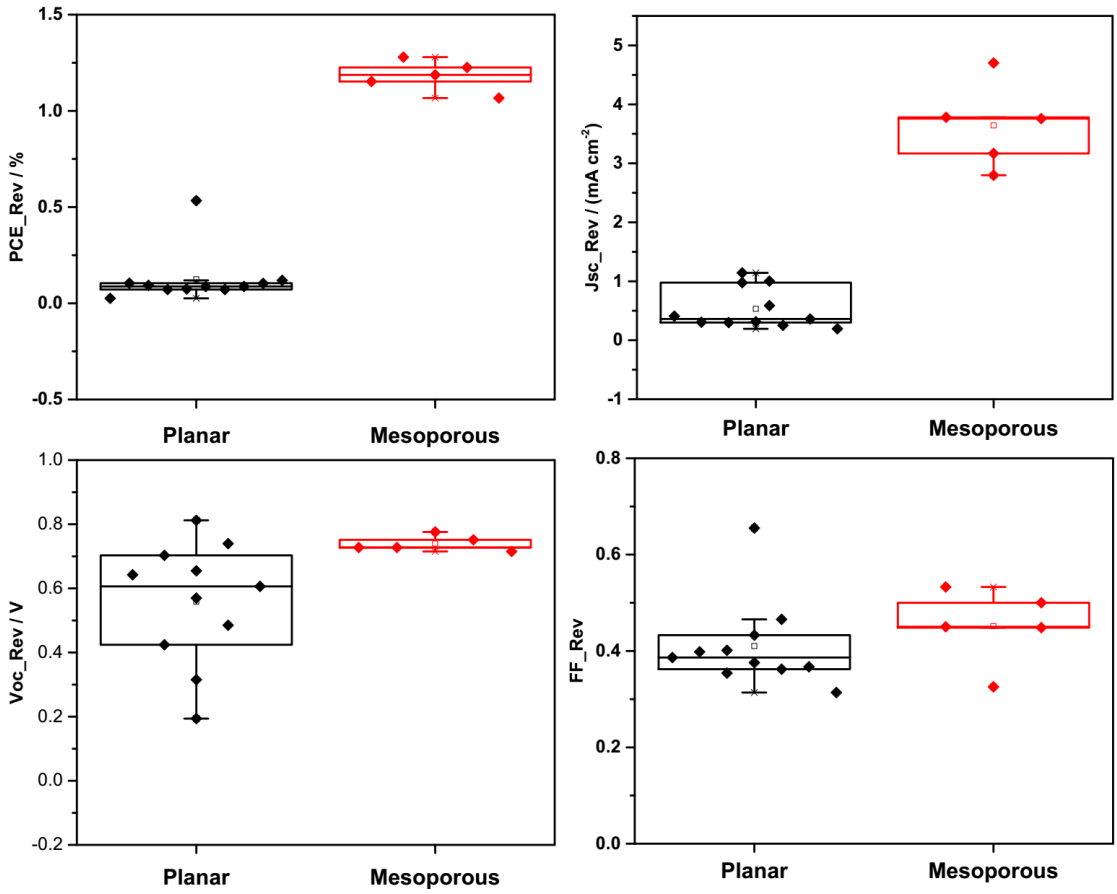

Fig. 7.12 Box plots of the performances of the planar and mesoporous cells employing perovskite films prepared with $MAPbI_3$ solid powders.

Table 7.3 Performance parameters for planar and mesoporous cells employing spin-coated perovskite layers from $MAPbI_3$ solid powders.

	J_{SC} [$mA \cdot cm^{-2}$]	V_{OC} [V]	FF	PCE [%]
Planar	0.48 ± 0.32	0.53 ± 0.16	0.38 ± 0.04	0.08 ± 0.02
Mesoporous	3.64 ± 0.72	0.74 ± 0.02	0.45 ± 0.08	1.18 ± 0.08

However, interestingly, the cells made with the $MAPbI_3$ solid powders showed high water resistance. As shown in **Fig. 7.13**, no colour change was seen after the complete cell made with the $MAPbI_3$ solid powder was dripped with water, whereas drastic colour change from dark brown to yellow was observed soon after water was dropped on to the surface of the standard cell made with perovskite precursor solution, indicating the fast decomposition of perovskite into PbI_2 which is fatal for the photovoltaic performance of

perovskite solar cells. Notably, the outstanding water resistance was also seen on the bare perovskite film made with the $MAPbI_3$ solid powder, without the protection of either spiro or gold layers. The brown colour was well retained after water dripping as shown in **Fig. 7.13** e, whereas the normal perovskite film made with $MAPbI_3$ precursor solution turned yellow very rapidly as demonstrated in **Fig. 7.13** f. As the instability of perovskite towards water is a serious problem for the application of perovskite solar cells[21], this result is really exciting. The high water resistance of the perovskite film made with the $MAPbI_3$ solid powder is likely to be due to the presence of the long chain hydrophobic ligands on the particles which resisted the infiltration of water, however these ligands can also act to insulate the nanoparticles and hinder charge transfer.

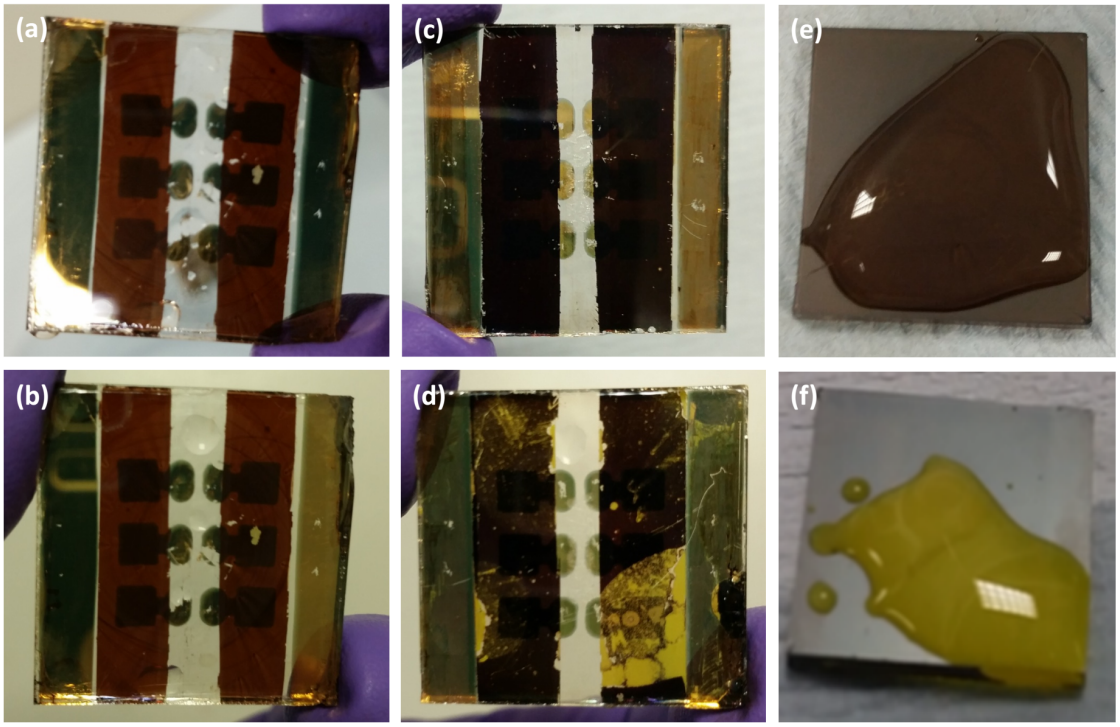

Fig. 7.13 Photo images of: the cell made with the $MAPbI_3$ solid powder (a) before and (b) after water dripping; the cell made with $MAPbI_3$ solution (c) before and (d) after water dripping; the bare perovskite films made with (e) the $MAPbI_3$ solid powder and (f) $MAPbI_3$ precursor solution being dripped with water.

To investigate the impact of thickness of the perovskite layer on the cell performance, the spin-coating process of the $MAPbI_3$ ink was conducted for different number of cycles to tune the thickness, and the cell performance of the devices thereof are illustrated in **Fig. 7.14**. The cells with perovskite layers spin-coated from the $MAPbI_3$ ink for 5 cycles exhibited the best performances, with the J_{SC} of $1.46 \pm 0.53\,mA \cdot cm^{-2}$, the V_{OC} of

0.74 ± 0.02 V, and the FF of 0.78 ± 0.06, giving the PCEs of 0.83 ± 0.28. The cell performance deteriorated as the thickness of the perovskite layer was increased by increasing the number of spin-coating cycles. PCEs of 0.58 ± 0.21 % and 0.54 ± 0.26 % were obtained for the cells spin-coated for 7 and 10 cycles respectively. The deteriorating cell performance was mainly caused by the decreased J_{SC} while the V_{OC} and FF were fairly similar. The decreased photocurrent could be due to the increased recombination when the thickness of the perovskite layer was increased. The thickness of the perovskite layers were investigated by cross-sectional SEM as shown in **Fig. 7.15**. Well-defined different layers were observed from the SEM images and labelled as different colours. The perovskite layer spin-coated for 5 cycles showed an average thickness of ~ 300 nm with variations at positions with and without big particles, while for the film spin-coated for 10 cycles, the thickness was roughly doubled to ~ 600 nm. It has been reported that the best thickness of perovskite layer for solar cells is around 330 nm[24], so further increasing the thickness by spin-coating the films for more than 5 cycles could be unfavourable due to the increased recombination. Besides, the cell performance of all the devices showed wide variation, especially the J_{SC}, which might be resulted from the non-evenness of the film thickness caused by the existence of large cubic particles as shown in **Fig. 7.9** d.

Therefore, thickness is not the parameter that limited the cell performance of the devices employing perovskite layers made with the $MAPbI_3$ solid powders. The poor performance is most likely due to the poor charge transfer caused by the long chain ligands bound to the surface of the perovskite particles. To date several ligand exchange treatments such as pyridine, hydrazine and 1,4-benzenedithiol have been demonstrated to be effective for the removal of long chain ligands on the surface of inorganic colloidal QDs[13,14,25]. However due to the poor stability of perovskite towards various solvents, effective ligand exchange treatment for perovskite NCs is still a challenge and needs to be investigated further.

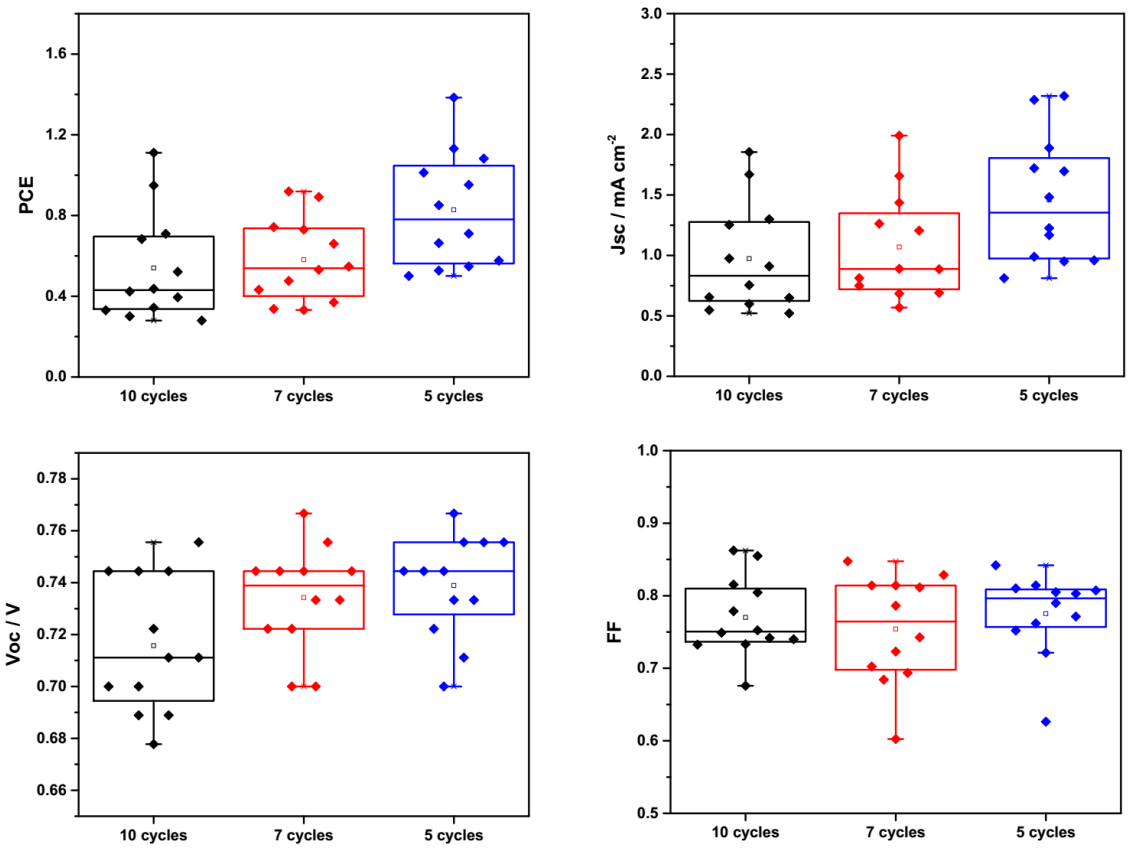

Fig. 7.14 Box plots of performances of cells employing perovskite layers spin-coated from the $MAPbI_3$ ink for different cycles.

Table 7.4 Performance parameters for cells employing perovskite layers spin-coated from the $MAPbI_3$ ink for different cycles.

	J_{SC} $[mA \cdot cm^{-2}]$	V_{OC} [V]	FF	PCE [%]
5 cycles	1.46 ± 0.53	0.74 ± 0.02	0.78 ± 0.06	0.83 ± 0.28
7 cycles	1.07 ± 0.44	0.73 ± 0.02	0.75 ± 0.08	0.58 ± 0.21
10 cycles	0.97 ± 0.45	0.72 ± 0.03	0.77 ± 0.05	0.54 ± 0.26

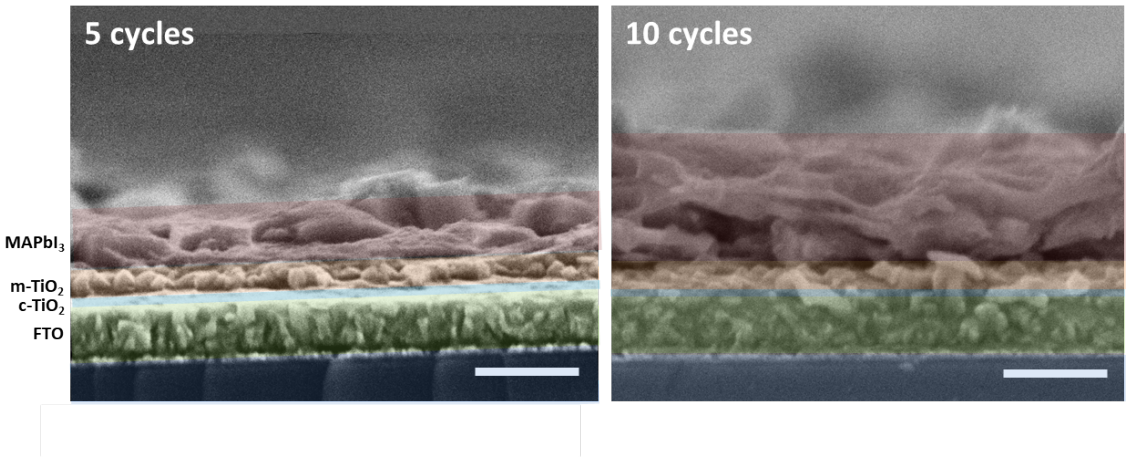

Fig. 7.15 Cross-sectional SEM images of the $MAPbI_3$ films made with different spin-coating cycles on top of mesoporous TiO_2 layers. The scale bars shown are 500 nm.

7.5 Conclusion

In this chapter, flow synthesised $MAPbI_3$ NCs and the bulk by-product were tested in perovskite solar cells. Making films with these nanoparticles avoided the in-situ crystallisation of perovskite phase, and thus is less dependent on environment conditions and easier to control.

The fluorescent properties of the $MAPbI_3$ NCs were well retained after being made into thin films, but the light absorption was very weak due to their low thickness. As a result, the cells made with the films showed poor performance suffering from low photocurrents. Cells with dip-coated perovskite films gave the PCE of 0.51 %, better than the 0.19 % for the spin-coated devices, showing dip-coating is better for the loading of the NCs.

The NCs were also applied as interlayers at the perovskite-HTM interface through direct spin-coating on perovskite layers and antisolvent dripping during the preparation of perovskite layers. The cell performances were both slightly decreased after the incorporation of the NC interlayers, but the films showed outstanding hydrophobicity and water resistance, even being immersed in water. The cells with the NC interlayers showed much improved stability towards moisture, with a high retention of 92.3% of the PCE after being kept for 70 days in ambient with humidity of 60 ± 10 %.

The $MAPbI_3$ solid powder by-products showed excellent dipersibility in hexane, forming homogeneous inks for the preparation of perovskite thin films. The films made by spin-coating for 5 cycles gave the thickness of 250-300 nm and showed reasonable light absorbing ability, and the mesoporous cells employing them showed the PCE of over 1 %. Further increasing the thickness of the films by increasing the number of spin-coating cycles did not improve the cell performance, probably due to the increased recombination caused by the excessive thickness of the films. Though the cells are still not very efficient, outstanding water resistance were obtained, with no obvious colour change when the cell being dripped with water, which could be very useful for applications such as water splitting.

Lastly, the cells with the $MAPbI_3$ NCs and solid powders are still far from efficient enough, and one of the most important causes is believed to be the hindered charge transfer due to the existence of insulating long chain ligands. For the improvement in the cell performance, effective ways of ligand exchange treatments for the removal of the ligands have to be developed in the future work.

Reference

[1] Z. Yang, J.Z. Fan, A.H. Proppe, F.P.G.d. Arquer, D. Rossouw, O. Voznyy, X. Lan, M. Liu, G. Walters, R. Quintero-Bermudez, B. Sun, S. Hoogland, G.A. Botton, S.O. Kelley, and E.H. Sargent. Mixed-quantum-dot solar cells. *Nature Communications*, 8(1):1325, 2017.

[2] S. Emin, S.P. Singh, L. Han, N. Satoh, and A. Islam. Colloidal quantum dot solar cells. *Solar Energy*, 85(6):1264–1282, 2011.

[3] S.A. McDonald, G. Konstantatos, S. Zhang, P.W. Cyr, E.J.D. Klem, L. Levina, and E.H. Sargent. Solution-processed pbs quantum dot infrared photodetectors and photovoltaics. *Nature Materials*, 4(2):138–142, 2005.

[4] M. Liu, O. Voznyy, R. Sabatini, F.P. Garca de Arquer, R. Munir, AhmedH. Balawi, X. Lan, F. Fan, G. Walters, AhmadR. Kirmani, S. Hoogland, F. Laquai, A. Amassian,

and EdwardH. Sargent. Hybrid organicinorganic inks flatten the energy landscape in colloidal quantum dotsolids. *Nature Materials*, 16(2):258–263, 2016.

[5] E.H. Sargent. Colloidal quantum dot solar cells. *Nature Photonics*, 6(3):133–135, 2012.

[6] M. Cha, P. Da, J. Wang, W. Wang, Z. Chen, F. Xiu, G. Zheng, and Z.-S. Wang. Enhancing perovskite solar cell performance by interface engineering using $CH_3NH_3PbBr_{0.9}I_{2.1}$ quantum dots. *Journal of the American Chemical Society*, 138(27):8581–8587, 2016.

[7] Q.A. Akkerman, M. Gandini, F. Di Stasio, P. Rastogi, F. Palazon, G. Bertoni, J.M. Ball, M. Prato, A. Petrozza, and L. Manna. Strongly emissive perovskite nanocrystal inks for high-voltage solar cells. *Nature Energy*, 2(2):16194, 2016.

[8] A. Swarnkar, A.R. Marshall, E.M. Sanehira, B.D. Chernomordik, D.T. Moore, J.A. Christians, T. Chakrabarti, and J.M. Luther. Quantum dotinduced phase stabilization of α-$CsPbI_3$ perovskite for high-efficiency photovoltaics. *Science*, 354(6308):92–95, 2016.

[9] W. Deng, X. Xu, X. Zhang, Y. Zhang, X. Jin, L. Wang, S.-T. Lee, and J. Jie. Organometal halide perovskite quantum dot light-emitting diodes. *Advanced Functional Materials*, 26(26):4797–4802, 2016.

[10] L. Qian, Y. Zheng, J. Xue, and P.H. Holloway. Stable and efficient quantum-dot light-emitting diodes based on solution-processed multilayer structures. *Nature Photonics*, 5(9):543–548, 2011.

[11] J. Seo, W.J. Kim, S.J. Kim, K.-S. Lee, A.N. Cartwright, and P.N. Prasad. Polymer nanocomposite photovoltaics utilizing CdSe nanocrystals capped with a thermally cleavable solubilizing ligand. *Applied Physics Letters*, 94(13):133302, 2009.

[12] N.C. Greenham, X. Peng, and A.P. Alivisatos. Charge separation and transport in conjugated-polymer/semiconductor-nanocrystal composites studied by photoluminescence quenching and photoconductivity. *Physical Review B*, 54(24):17628–17637, 1996.

[13] H. W.U., D. J.J., L. W.C., W. G.L., and A. A.P. Controlling the morphology of nanocrystalpolymer composites for solar cells. *Advanced Functional Materials*, 13(1):73–79, 2003.

[14] G.I. Koleilat, L. Levina, H. Shukla, S.H. Myrskog, S. Hinds, A.G. Pattantyus-Abraham, and E.H. Sargent. Efficient, stable infrared photovoltaics based on solution-cast colloidal quantum dots. *ACS Nano*, 2(5):833–840, 2008.

[15] W. Deng, X. Liang, P.S. Kubiak, and P.J. Cameron. Molecular interlayers in hybrid perovskite solar cells. *Advanced Energy Materials*, 8(1):1701544, 2018.

[16] F. Gao, H. Dai, H. Pan, Y. Chen, J. Wang, and Z. Chen. Performance enhancement of perovskite solar cells by employing TiO_2 nanorod arrays decorated with $CuInS_2$ quantum dots. *Journal of Colloid and Interface Science*, 513:693–699, 2018.

[17] Q. Chen, H. Zhou, Y. Fang, A.Z. Stieg, T.-B. Song, H.-H. Wang, X. Xu, Y. Liu, S. Lu, J. You, P. Sun, J. McKay, M.S. Goorsky, and Y. Yang. The optoelectronic role of chlorine in $CH_3NH_3PbI_3$(Cl)-based perovskite solar cells. *Nature Communications*, 6(1):7269, 2015.

[18] N.J. Jeon, J.H. Noh, Y.C. Kim, W.S. Yang, S. Ryu, and S.I. Seok. Solvent engineering for high-performance inorganic-organic hybrid perovskite solar cells. *Nature Materials*, 13(9):897–903, 2014.

[19] W. Nie, H. Tsai, R. Asadpour, J.-C. Blancon, A.J. Neukirch, G. Gupta, J.J. Crochet, M. Chhowalla, S. Tretiak, M.A. Alam, H.-L. Wang, and A.D. Mohite. High-efficiency solution-processed perovskite solar cells with millimeter-scale grains. *Science*, 347(6221):522–525, 2015.

[20] J. Peng, Y. Chen, X. Zhang, A. Dong, and Z. Liang. Solid-state ligand-exchange fabrication of $CH_3NH_3PbI_3$ capped pbs quantum dot solar cells. *Advanced Science*, 3(6):1500432, 2016.

[21] G. Niu, W. Li, F. Meng, L. Wang, H. Dong, and Y. Qiu. Study on the stability of $CH_3NH_3PbI_3$ films and the effect of post-modification by aluminum oxide in all-solid-state hybrid solar cells. *Journal of Materials Chemistry A*, 2(3):705–710, 2014.

[22] D.W. deQuilettes, S.M. Vorpahl, S.D. Stranks, H. Nagaoka, G.E. Eperon, M.E. Ziffer, H.J. Snaith, and D.S. Ginger. Impact of microstructure on local carrier lifetime in perovskite solar cells. *Science*, 348(6235):683–686, 2015.

[23] H.-J. Yen, P.-W. Liang, C.-C. Chueh, Z. Yang, A.K.Y. Jen, and H.-L. Wang. Large grained perovskite solar cells derived from single-crystal perovskite powders with enhanced ambient stability. *ACS Applied Materials & Interfaces*, 8(23):14513–14520, 2016.

[24] D. Liu, M.K. Gangishetty, and T.L. Kelly. Effect of $CH_3NH_3PbI_3$ thickness on device efficiency in planar heterojunction perovskite solar cells. *Journal of Materials Chemistry A*, 2(46):19873–19881, 2014.

[25] S.J. Kim, W.J. Kim, Y. Sahoo, A.N. Cartwright, and P.N. Prasad. Multiple exciton generation and electrical extraction from a PbSe quantum dot photoconductor. *Applied Physics Letters*, 92(3):031107, 2008.

Chapter 8

Conclusion and future work

8.1 Conclusion

In this work, a reliable fabrication of perovskite solar cells was developed though the optimisation to the perovskite layer deposition methods and the metal ion doping to the TiO_2 electron transporting layers. After optimising the device fabrication, nanocrystals of perovskite were synthesised using a facile flow reactor, and their applications in solar cells were investigated.

Vapour-assisted sequential method, sequential spin-coating method and one-step spin-coating method were used for the deposition of perovskite absorbing layers for perovskite solar cells, and the effects of solvent, temperature, lead source, recipe and antisolvent dripping were investigated. One-step spin-coating of MAI:$PbCl_2$=3:1 solution gave the best cell performance, with the PCE of 12.1 ± 0.7 % in air with controlled humidity of $< 35\%$ and 10.8 ± 0.9 % in a dry box filled with nitrogen, respectively, showing high reliability and reproducibility.

In order to improve the charge-transporting properties of the compact TiO_2 ETLs, different metal ions with different valence states were introduced into the TiO_2 films as dopants, and their effects on the TiO_2 layers and the cell performances were investigated. All the ions were successfully introduced into the lattice of TiO_2 through a simple spray pyrolysis route, and the doping had negligible influences on the morphological and optical properties of the TiO_2 layers. The doping density of the TiO_2 was changed very slightly after the introduction of these dopant ions, but the flat band potential was changed quite signif-

icantly. Zn^{2+} ions negatively shifted the V_{FB} from 0.13 V to -0.11 V, whereas Nb^{5+} ions positively shifted the V_{FB} to 0.23 V, and Sn^{4+}-doping showed the smallest effect on the V_{FB}.

Zn-doping decreased the PCE of the planar devices though the V_{FB} was negatively shifted, mainly due to an decreased FF caused by an increased series resistance. However, when a very thin layer of Zn-doped TiO_2 was deposited on top of the pristine TiO_2 layer forming a bilayer ETL, the negative effects of the Zn-doping was minimised while the advantage of negatively shifted V_{FB} was retained, thus the V_{OC} and FF were both enhanced, and the PCE was slightly improved.

A facile flow reactor was developed for the continuous synthesis of $MAPbX_3$ perovskite NCs at low temperature. The obtained $MAPbI_3$ NCs showed small sizes of ~ 10 nm with narrow size distribution. The NCs also showed excellent emissive properties and high stability. The $MAPbI_3$ NCs gave a sharp emission peak at 745 nm in the PL spectrum, with narrow FWHM of 39 nm. Notably, the morphological and emissive properties of the $MAPbI_3$ NCs remained stable for over 8 months. The synthesis also exhibited excellent reproducibility, with very small deviations in the PL spectra in 11 independent repeats.

A series of $MAPbI_3$ perovskite NCs with different halide compositions were successfully prepared using the flow reactor, showing tuneable emissions between 485-745 nm, covering a wide wavelength range of visible and near infrared regions. The PL spectra of the NCs showed narrow FWHMs of below 50 nm, indicating the high colour purities, and the emission peoperties was well retained after being made into thin films with a dip-coating method, which are very promising for LED applications.

The PL of the $MAPbI_3$ NCs in the first supernatant of the as-prepared mixture can be tuned by changing the temperature, flow rate and ligand concentration. However, toluene washing changes the PL response of the NCs, forming multiple peaks in the PL spectra, indicating different sizes of the NCs, possibly due to the fragmentation of the NCs as a result of osmotic swelling during toluene washing[1].

The continuous solution process provides better control to the crystallisation of perovskite NCs, which is less dependent on atmosphere conditions. It could thus provide a new

idea for the preparation of perovskite thin films by separating the crystallisation and film formation processes, so that better control to the film quality and consequently better reproducibility can be achieved.

The synthesised $MAPbI_3$ NCs and the bulk byproduct were tested in perovskite solar cells, both as interlayers at the perovskite-HTM interface and active light-absorbing layers. The NCs as interlayer slightly decreased the cell performances, but the stability of the cells towards moisture was greatly improved. 92.3% of the initial PCE was retained after the cells being kept for 70 days in ambient with humidity of 60 ± 10 %. As light-absorbing layers, the NCs and the bulk by-product gave the champion PCEs of 0.51% and 1.2% respectively. The lower efficiency can be ascribed to the hindered charge transfer due to the existence of insulating long chain ligands on the surface of the NCs, and effective ways of ligand exchange treatment is still to be discovered. But all the cells showed outstanding water resistance, with no obvious colour change being dripped with water, which could be very useful for applications such as water splitting.

8.2 Future work

Current work has been focused on the optimisation of planar perovskite solar cells, the synthesis of perovskite nanocrystals and their applications in perovskite solar devices. Future work can be carried on the following aspects of the project:

The influence of doping on the electronic properties of TiO_2 can be modelled computationally, and ultraviolet photoelectron spectra can be measured, which together will give direct insight into the band shifts of the TiO_2 after ion doping.

The flow strategy has been shown to be effective for the synthesis of perovskite nanocrystals with high size uniformity, but toluene washing does something to the nanocrystals resulting in multiple PL peaks, and the mechanism is still not fully clear yet. More investigation into the toluene washing should be done so that better tunablity of the size of the nanocrystals can be achieved. Moreover, since the nanocrystals show highly emissive properties, it would be also interesting to investigate their applications in electroluminescent devices.

The perovskite nanocrystals synthesised using the flow reactor and their bulk byproducts have been used in perovskite solar cells, but the efficiencies are rather low. The main problem is believed to be the existence of long chain ligands on the surface which hinder the charge transfer. Therefore, future work needs be done on the development of effective ligand exchange strategies. Besides, the applications in a carbon based cell configuration could be also interesting, as charge transport could be enhanced by the interpenetrating interface between perovskite and carbon electrodes[2].

Reference

[1] Y. Tong, F. Ehrat, W. Vanderlinden, C. Cardenas-Daw, J. K. Stolarczyk, L. Polavarapu, and A. S. Urban. Dilution-Induced Formation of Hybrid Perovskite Nanoplatelets. *ACS Nano*, 10(12):10936–10944, 2016.

[2] Haining Chen and Shihe Yang. Stabilizing and scaling up carbon-based perovskite solar cells. *Journal of Materials Research*, 32(16):3011–3020, 2017.